Ministry of Education and Science of the Russian Federation
Saint Petersburg National Research University of Information
Technologies, Mechanics, and Optics

NANOSYSTEMS:

PHYSICS, CHEMISTRY, MATHEMATICS

2013, volume 4(2)

Наносистемы: физика, химия, математика
2013, том 4, № 2

NANOSYSTEMS:

PHYSICS, CHEMISTRY, MATHEMATICS

ADVISORY BOARD MEMBERS

Chairman: V.N. Vasiliev *(St. Petersburg, Russia)*,
V.M. Ievlev *(Voronezh)*, P.S. Kop'ev*(St. Petersburg, Russia)*,
V.N. Parmon *(Novosibirsk)*, A.I. Rusanov *(St. Petersburg, Russia)*.

EDITORIAL BOARD

Editor-in-Chief: N.F. Morozov *(St. Petersburg, Russia)*
Deputy Editor-in-Chief: I.Yu. Popov *(St. Petersburg, Russia)*

Section Co-Editors:
Physics – V.M. Uzdin *(St. Petersburg, Russia)*,
Chemistry, material science –V.V. Gusarov *(St. Petersburg, Russia)*,
Mechanics – A.K. Belyaev *(St. Petersburg, Russia)*,
Mathematics – I.Yu. Popov *(St. Petersburg, Russia)*.

Editorial Board Members:
V.M. Adamyan *(Odessa, Ukraine)*; O.V. Al'myasheva *(St. Petersburg, Russia)*; S. Bechta *(Stockholm, Sweden)*; V.G. Bespalov *(St. Petersburg, Russia)*; A. Chatterjee (*Hyderabad, India)*; S.A. Chivilikhin *(St. Petersburg, Russia)*; A.V. Chizhov *(Dubna, Russia)*; P.P. Fedorov *(Moscow, Russia)*; E.A. Gudilin *(Moscow, Russia)*; D.A. Indeitsev *(St. Petersburg, Russia)*; A.L. Ivanovskii *(Ekaterinburg, Russia)*; H. Jónsson *(Reykjavik, Iceland)*; A.A. Kiselev *(Madison, USA)*; Yu.S. Kivshar *(Canberra, Australia)*; S.A. Kozlov *(St. Petersburg, Russia)*; Yu.B. Kudasov *(Sarov, Russia)*; S.E. Kul'kova *(Tomsk, Russia)*; P.A. Kurasov *(Stockholm, Sweden)*; A.V. Lukashin *(Moscow, Russia)*; V.A. Margulis *(Saransk, Russia)*; I.V. Melikhov *(Moscow, Russia)*; G.P. Miroshnichenko *(St. Petersburg, Russia)*; H. Neidhardt *(Berlin, Germany)*; K. Pankrashkin *(Orsay, France)*; B.S. Pavlov *(Auckland, New Zealand)*; A.V. Ragulya *(Kiev, Ukraine)*; V. Rajendran *(Tamil Nadu, India)*; V.P. Romanov *(St. Petersburg, Russia)*; V.Ya. Rudyak *(Novosibirsk, Russia)*; V.M. Talanov *(Novocherkassk, Russia)*; A.Ya. Vul' *(St. Petersburg, Russia)*.

Editors:
I.V. Blinova; A.I. Popov; M.A. Skryabin; A.I. Trifanov; E.S. Trifanova *(St. Petersburg, Russia)*, R. Simoneaux *(USA)*.

Address: University ITMO, Kronverkskiy pr., 49, St. Petersburg 197101, Russia.
Phone: +7(812)232-67-65, **Journal site:** http://nanojournal.ifmo.ru/,
E-mail: popov1955@gmail.com

AIM AND SCOPE

The scope of the journal includes all areas of nano-sciences. Papers devoted to basic problems of physics, chemistry, material science and mathematics inspired by nanosystems investigations are welcomed. Both theoretical and experimental works concerning the properties and behavior of nanosystems, problems of its creation and application, mathematical methods of nanosystem studies are considered.

The journal publishes scientific reviews (up to 30 journal pages), research papers (up to 15 pages) and letters (up to 5 pages). All manuscripts are peer-reviewed. Authors are informed about the referee opinion and the Editorial decision.

Content

MATHEMATICS

PHYSICS

CHEMISTRY AND MATERIAL SCIENCE

Papers, presented at MAM-12

FROM THE EDITORIAL BOARD

In this issue we start to publish works presented at 6th International Symposium on Macro- and Supramolecular Architectures and Materials; Special Theme: Nano Systems and Applications (MAM-12).

Scope of the Conference

As novel materials will play a key role in science and technology in the 21st century, the objectives of this symposium series are in providing an interdisciplinary forum for scientists engaged in the full spectrum of research, development, application, and to discuss the current status and recent developments of these materials with a focus on the chemistry and practical approaches. In addition, the meeting will provide an opportunity to overview the field by covering a wide range of topics. Themes have selected to accommodate a wide range of interests to facilitate interdisciplinary interaction in both academic fields and industrial science and technology.

MAM is a series of conferencies which is organized by Prof. Dr. Dr. K.E. Geckeler. MAM-12 is 6th conference in this series which was held at Coimbatore, India during 21-25 November 2012. Chairman of MAM-12 is Dr. V. Rajendran, Director, R&D and Centre for Nanoscience and Technology K.S.R. College of Technology, India.

Steering committee

Chairs:

K.E. Geckeler (Gwangju, South Korea)
V. Rajendran (Coimbatore, India)

Members:

Kahwa (Kingston, West Indies); **H. Nishide (**Tokyo, Japan); **H. Ritter** **(**Dusseldorf, Germany); **B. Rivas (**Concepcion, Chile); **E. Rosenberg** **(**Missoula, USA).

NANOSYSTEMS: PHYSICS, CHEMISTRY, MATHEMATICS, 2013, 4 (2), P. 166–172

NOTE ON 2D SCHRÖDINGER OPERATORS WITH δ-INTERACTIONS ON ANGLES AND CROSSING LINES

V. Lotoreichik

Technische Universität Graz, Institut für Numerische Mathematik
Steyrergasse 30, 8010 Graz, Austria

lotoreichik@math.tugraz.at

PACS 03.65.-w

In this note we sharpen the lower bound previously obtained by Lobanov et al [LLP10] for the spectrum of the 2D Schrödinger operator with a δ-interaction supported on a planar angle. Using the same method we obtain the lower bound on the spectrum of the 2D Schrödinger operator with a δ-interaction supported on crossing straight lines. The latter operators arise in the three-body quantum problem with δ-interactions between particles.

Keywords: Schrödinger operators, δ-interactions, spectral estimates.

1. Introduction

Self-adjoint Schrödinger operators with δ-interactions supported on sufficiently regular hypersurfaces can be defined via closed, densely defined, symmetric and lower-semibounded quadratic forms using the first representation theorem, see [BEKS94], [BLL13].

δ-interactions on angles. In our first model the support of the δ-interaction is the set $\Sigma_\varphi \subset \mathbb{R}^2$, which consists of two rays meeting at the common origin and constituting the angle $\varphi \in (0, \pi]$ as in Figure 1.

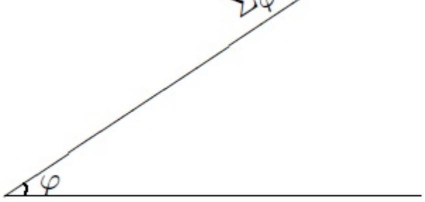

Fig. 1. The angle Σ_φ of degree $\varphi \in (0, \pi]$

The quadratic form in $L^2(\mathbb{R}^2)$

$$\mathfrak{a}_\varphi[f] := \|\nabla f\|^2_{L^2(\mathbb{R}^2;\mathbb{C}^2)} - \alpha\|f|_{\Sigma_\varphi}\|^2_{L^2(\Sigma_\varphi)}, \qquad \operatorname{dom}\mathfrak{a}_\varphi := H^1(\mathbb{R}^2), \tag{1}$$

is closed, densely defined, symmetric and lower-semibounded, where $f|_{\Sigma_\varphi}$ is the trace of f on Σ_φ, and the constant $\alpha > 0$ is called the strength of interaction. The corresponding self-adjoint operator in $L^2(\mathbb{R}^2)$ we denote by A_φ. Known spectral properties of this operator include explicit representation of the essential spectrum $\sigma_{\text{ess}}(A_\varphi) = [-\alpha^2/4, +\infty)$ and some information on the discrete spectrum: $\sharp\sigma_{\rm d}(A_\varphi) \geqslant 1$ if and only if $\varphi \neq \pi$. These two statements can be deduced from more general results by Exner and Ichinose [EI01]. They are complemented by Exner and Nemčová [EN03] with the limiting property $\sharp\sigma_{\rm d}(A_\varphi) \to +\infty$ as $\varphi \to 0+$.

In [LLP10] the author obtained jointly with Igor Lobanov and Igor Yu. Popov a general result, which implies the lower bound on the spectrum of A_φ

$$\inf \sigma(A_\varphi) \geqslant -\frac{\alpha^2}{4\sin^2(\varphi/2)}. \tag{2}$$

This bound is close to optimal for φ close to π, whereas in the limit $\varphi \to 0+$ the bound tends to $-\infty$. In the present note we sharpen this bound. Namely, we obtain

$$\inf \sigma(A_\varphi) \geqslant -\frac{\alpha^2}{(1+\sin(\varphi/2))^2}. \tag{3}$$

The new bound yields that the operators A_φ are uniformly lower-semibounded with respect to φ and

$$\inf \sigma(A_\varphi) \geqslant -\alpha^2$$

holds for all $\varphi \in (0,\pi]$. This observation agrees well with physical expectations. Note that separation of variables yields that $\inf\sigma(A_\pi) = -\alpha^2/4$ and in this case the lower bound in (3) coincides with the exact spectral bottom.

For sufficiently sharp angles upper bounds on $\inf\sigma(A_\varphi)$ were obtained by Brown, Eastham and Wood [BEW08]. See also Open Problem 7.3 [E08] related to the discrete spectrum of A_φ for φ close to π.

δ-interactions on crossing straight lines. We also consider an analogous model with the δ-interaction supported on the set $\Gamma_\varphi = \Gamma_1 \cup \Gamma_2$, where Γ_1 and Γ_2 are two straight lines, which cross at the angle $\varphi \in (0,\pi)$ as in Figure 2.

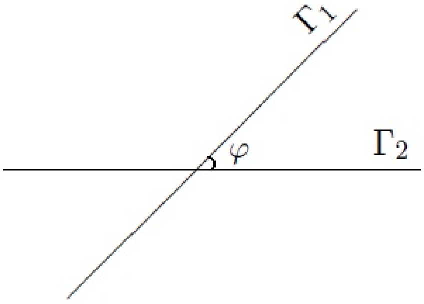

Fig. 2. The straight lines Γ_1 and Γ_2 crossing at the angle of degree $\varphi \in (0,\pi)$

The corresponding self-adjoint operator B_φ in $L^2(\mathbb{R}^2)$ can be defined via the closed, densely defined, symmetric and lower-semibounded quadratic form in $L^2(\mathbb{R}^2)$

$$\mathfrak{b}_\varphi[f] := \|\nabla f\|^2_{L^2(\mathbb{R}^2;\mathbb{C}^2)} - \alpha\|f|_{\Gamma_\varphi}\|^2_{L^2(\Gamma_\varphi)}, \qquad \operatorname{dom}\mathfrak{b}_\varphi := H^1(\mathbb{R}^2), \tag{4}$$

where $\alpha > 0$ is the strength of interaction. According to [EN03] it is known that $\sigma_{\rm ess}(B_\varphi) = [-\alpha^2/4, +\infty)$ and that $\sharp\sigma_{\rm d}(B_\varphi) \geqslant 1$.

In this note we obtain the lower bound

$$\inf \sigma(B_\varphi) \geqslant -\frac{\alpha^2}{1+\sin\varphi}, \tag{5}$$

using the same method as for the operator A_φ. Separation of variables yields $\inf\sigma(B_{\pi/2}) = -\alpha^2/2$, and in this case the lower bound in the estimate (5) coincides with the exact spectral bottom.

Upper bounds on $\inf\sigma(B_\varphi)$ were obtained in [BEW08, BEW09]. The operators of the type B_φ arise in the one-dimensional quantum three-body problem after excluding the center of mass, see Cornean, Duclos and Ricaud [CDR06, CDR08] and the references therein.

We want to stress that our proofs are of elementary nature and we do not use any reduction to integral operators acting on interaction supports Σ_φ and Γ_φ.

2. Sobolev spaces on wedges

In this section $\Omega \subset \mathbb{R}^2$ is a wedge with an angle of $\varphi \in (0, 2\pi)$. The Sobolev space $H^1(\Omega)$ is defined as usual, see [McL, Chapter 3]. For any $f \in H^1(\Omega)$ the trace $f|_{\partial\Omega} \in L^2(\partial\Omega)$ is well-defined as in [McL, Chapter 3] and [M87].

Proposition 2.1. *[LP08, Lemma 2.6] Let Ω be a wedge with angle of degree $\varphi \in (0,\pi]$. Then for any $f \in H^1(\Omega)$ the estimate*

$$\|\nabla f\|^2_{L^2(\Omega;\mathbb{C}^2)} - \gamma\|f|_{\partial\Omega}\|^2_{L^2(\partial\Omega)} \geqslant -\frac{\gamma^2}{\sin^2(\varphi/2)}\|f\|^2_{L^2(\Omega)}$$

holds for all $\gamma > 0$.

Proposition 2.2. *[LP08, Lemma 2.8] Let Ω be a wedge with angle of degree $\varphi \in (\pi, 2\pi)$. Then for any $f \in H^1(\Omega)$ the estimate*

$$\|\nabla f\|^2_{L^2(\Omega;\mathbb{C}^2)} - \gamma\|f|_{\partial\Omega}\|^2_{L^2(\partial\Omega)} \geqslant -\gamma^2\|f\|^2_{L^2(\Omega)}$$

holds for all $\gamma > 0$.

Propositions 2.1 and 2.2 are variational equivalents of spectral results from [LP08].

3. A lower bound on the spectrum of A_φ

In the next theorem we sharpen the bound (2) using only properties of the Sobolev space H^1 on wedges and some optimization.

Theorem 3.1. *Let the self-adjoint operator A_φ be associated with the quadratic form given in* (1)*. Then the estimate*

$$\inf\sigma(A_\varphi) \geqslant -\frac{\alpha^2}{\big(1+\sin(\varphi/2)\big)^2}$$

holds.

Proof. The angle Σ_φ separates the Euclidean space $\mathbb{R}^2$ into two wedges Ω_1 and Ω_2 with angles of degrees φ and $2\pi - \varphi$, see Figure 3.

The underlying Hilbert space can be decomposed as

$$L^2(\mathbb{R}^2) = L^2(\Omega_1) \oplus L^2(\Omega_2).$$

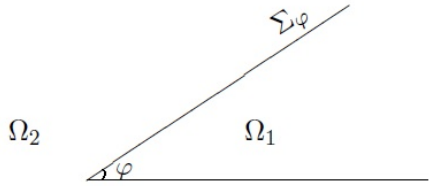

Fig. 3. The angle Σ_φ separates the Euclidean space $\mathbb{R}^2$ into two wedges Ω_1 and Ω_2

Any $f \in \operatorname{dom} \mathfrak{a}_\varphi$ can be written as the orthogonal sum $f_1 \oplus f_2$ with respect to that decomposition of $L^2(\mathbb{R}^2)$. Note that $f_1 \in H^1(\Omega_1)$ and that $f_2 \in H^1(\Omega_2)$. Clearly,

$$\begin{aligned} \|f\|^2_{L^2(\mathbb{R}^2)} &= \|f_1\|^2_{L^2(\Omega_1)} + \|f_2\|^2_{L^2(\Omega_2)}, \\ \|\nabla f\|^2_{L^2(\mathbb{R}^2;\mathbb{C}^2)} &= \|\nabla f_1\|^2_{L^2(\Omega_1;\mathbb{C}^2)} + \|\nabla f_2\|^2_{L^2(\Omega_2;\mathbb{C}^2)}. \end{aligned} \tag{6}$$

The coupling constant can be decomposed as $\alpha = \beta + (\alpha - \beta)$ with some optimization parameter $\beta \in [0, \alpha]$ and the relation

$$\alpha \|f|_{\Sigma_\varphi}\|^2_{L^2(\Sigma_\varphi)} = \beta \|f_1|_{\partial\Omega_1}\|^2_{L^2(\partial\Omega_1)} + (\alpha - \beta)\|f_2|_{\partial\Omega_2}\|^2_{L^2(\partial\Omega_2)}. \tag{7}$$

holds. According to Proposition 2.1

$$\|\nabla f_1\|^2_{L^2(\Omega_1;\mathbb{C}^2)} - \beta\|f_1|_{\partial\Omega_1}\|^2_{L^2(\partial\Omega_1)} \geqslant -\tfrac{\beta^2}{\sin^2(\varphi/2)}\|f_1\|^2_{L^2(\Omega_1)}, \tag{8}$$

and according to Proposition 2.2

$$\|\nabla f_2\|^2_{L^2(\Omega_2;\mathbb{C}^2)} - (\alpha - \beta)\|f_2|_{\partial\Omega_2}\|^2_{L^2(\partial\Omega_2)} \geqslant -(\alpha - \beta)^2\|f_2\|^2_{L^2(\Omega_2)}. \tag{9}$$

The observations (6), (7) and the estimates (8), (9) imply

$$\mathfrak{a}_\varphi[f] \geqslant -\max\left\{\tfrac{\beta^2}{\sin^2(\varphi/2)}, (\alpha - \beta)^2\right\}\|f\|^2_{L^2(\mathbb{R}^2)}.$$

Making optimization with respect to β, we observe that the maximum between the two values in the estimate above is minimal, when these two values coincide. That is

$$\tfrac{\beta^2}{\sin^2(\varphi/2)} = (\alpha - \beta)^2,$$

which is equivalent to

$$\beta = \tfrac{\alpha \sin(\varphi/2)}{(1+\sin(\varphi/2))}, \tag{10}$$

resulting in the final estimate

$$\mathfrak{a}_\varphi[f] \geqslant -\tfrac{\alpha^2}{(1+\sin(\varphi/2))^2}\|f\|^2_{L^2(\mathbb{R}^2)}.$$

This final estimate implies the desired spectral bound. □

Remark 3.2. Note that the previously known lower bound (2) was derived from the proof of the last theorem if we choose $\beta = \alpha/2$, which is the optimal choice in our proof only for $\varphi = \pi$ as we see from (10).

4. A lower bound on the spectrum of $\mathbf{B}_\varphi$

In the next theorem we obtain a lower bound on the spectrum of the self-adjoint operator B_φ using the same idea as in Theorem 3.1.

Theorem 4.1. *Let the self-adjoint operator B_φ be associated with the quadratic form given in* (4). *Then the estimate*

$$\inf \sigma(B_\varphi) \geqslant -\frac{\alpha^2}{1+\sin\varphi}$$

holds.

Proof. The crossing straight lines Γ_1 and Γ_2 separate the Euclidean space $\mathbb{R}^2$ into four wedges $\{\Omega_k\}_{k=1}^4$. Namely, the wedges Ω_1 and Ω_2 with angles of degree φ and the wedges Ω_3 and Ω_4 with angles of degree $\pi-\varphi$, see Figure 4.

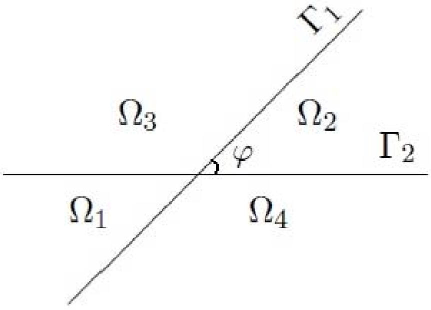

Fig. 4. The crossing straight lines Γ_1 and Γ_2 separate the Euclidean space $\mathbb{R}^2$ into four wedges $\{\Omega_k\}_{k=1}^4$

The underlying Hilbert space can be decomposed as

$$L^2(\mathbb{R}^2) = \bigoplus_{k=1}^{4} L^2(\Omega_k).$$

Any $f \in \operatorname{dom}\mathfrak{b}_\varphi$ can be written as the orthogonal sum $\oplus_{k=1}^4 f_k$ with respect to that decomposition of $L^2(\mathbb{R}^2)$. Note that $f_k \in H^1(\Omega_k)$ for $k=1,2,3,4$. Clearly,

$$\|f\|^2_{L^2(\mathbb{R}^2)} = \sum_{k=1}^{4} \|f_k\|^2_{L^2(\Omega_k)}, \quad \|\nabla f\|^2_{L^2(\mathbb{R}^2;\mathbb{C}^2)} = \sum_{k=1}^{4} \|\nabla f_k\|^2_{L^2(\Omega_k;\mathbb{C}^2)}. \tag{11}$$

The coupling constant can be decomposed as $\alpha = \beta + (\alpha-\beta)$ with some optimization parameter $\beta \in [0,\alpha]$ and the relation

$$\begin{aligned}\alpha\|f|_{\Gamma_\varphi}\|^2_{L^2(\Gamma_\varphi)} = \beta\|f_1|_{\partial\Omega_1}\|^2_{L^2(\partial\Omega_1)} + \beta\|f_2|_{\partial\Omega_2}\|^2_{L^2(\partial\Omega_2)}& \\ + (\alpha-\beta)\|f_3|_{\partial\Omega_3}\|^2_{L^2(\partial\Omega_3)} + (\alpha-\beta)\|f_4|_{\partial\Omega_4}\|^2_{L^2(\partial\Omega_4)}&\end{aligned} \tag{12}$$

holds. According to Proposition 2.1

$$\begin{aligned}\|\nabla f_1\|^2_{L^2(\Omega_1;\mathbb{C}^2)} - \beta\|f_1|_{\partial\Omega_1}\|^2_{L^2(\partial\Omega_1)} &\geqslant -\tfrac{\beta^2}{\sin^2(\varphi/2)}\|f_1\|^2_{L^2(\Omega_1)},\\ \|\nabla f_2\|^2_{L^2(\Omega_2;\mathbb{C}^2)} - \beta\|f_2|_{\partial\Omega_2}\|^2_{L^2(\partial\Omega_2)} &\geqslant -\tfrac{\beta^2}{\sin^2(\varphi/2)}\|f_2\|^2_{L^2(\Omega_2)}.\end{aligned} \tag{13}$$

Also according to Proposition 2.1

$$\begin{aligned} \|\nabla f_3\|^2_{L^2(\Omega_3;\mathbb{C}^2)} - (\alpha-\beta)\|f_3|_{\partial\Omega_3}\|^2_{L^2(\partial\Omega_3)} &\geqslant -\tfrac{(\alpha-\beta)^2}{\cos^2(\varphi/2)}\|f_3\|^2_{L^2(\Omega_3)},\\ \|\nabla f_4\|^2_{L^2(\Omega_4;\mathbb{C}^2)} - (\alpha-\beta)\|f_4|_{\partial\Omega_4}\|^2_{L^2(\partial\Omega_4)} &\geqslant -\tfrac{(\alpha-\beta)^2}{\cos^2(\varphi/2)}\|f_4\|^2_{L^2(\Omega_4)}. \end{aligned} \tag{14}$$

The observations (11), (12) and the estimates (13), (14) imply

$$\mathfrak{b}_\varphi[f] \geqslant -\max\left\{\tfrac{\beta^2}{\sin^2(\varphi/2)}, \tfrac{(\alpha-\beta)^2}{\cos^2(\varphi/2)}\right\}\|f\|^2_{L^2(\mathbb{R}^2)}.$$

Making optimization with respect to β, we observe that the maximum between the two values in the estimate above is minimal, when these two values coincide. That is

$$\tfrac{\beta^2}{\sin^2(\varphi/2)} = \tfrac{(\alpha-\beta)^2}{\cos^2(\varphi/2)},$$

which is equivalent to

$$\beta = \tfrac{\alpha\tan(\varphi/2)}{(1+\tan(\varphi/2))}, \tag{15}$$

resulting in the final estimate

$$\mathfrak{b}_\varphi[f] \geqslant -\tfrac{\alpha^2}{1+\sin(\varphi)}\|f\|^2_{L^2(\mathbb{R}^2)}.$$

This final estimate implies the desired spectral bound. □

Remark 4.2. The result of Theorem 4.1 complements [CDR08, Theorem 4.6 (iv)], where the bound

$$\inf\sigma(B_\varphi) \geqslant -\alpha^2.$$

for all $\varphi \in (0,\pi)$ was obtained.

Acknowledgements

The author is grateful to Jussi Behrndt, Sylwia Kondej, Igor Lobanov, Igor Yu. Popov, and Jonathan Rohleder for discussions. The work was supported by Austrian Science Fund (FWF): project P 25162-N26 and partially supported by the Ministry of Education and Science of Russian Federation: project 14.B37.21.0457.

References

[BLL13] J. Behrndt, M. Langer, and V. Lotoreichik, Schrödinger operators with δ and δ'-potentials supported on hypersurfaces, *Ann. Henri Poincaré*, **14**, P. 385–423 (2013).

[BEKS94] J.F. Brasche, P. Exner, Yu.A. Kuperin, and P. Šeba, Schrödinger operators with singular interactions, *J. Math. Anal. Appl.*, **184**, P. 112–139 (1994).

[BEW08] B.M. Brown, M. S. P. Eastham, and I. Wood, An example on the discrete spectrum of a star graph, in *Analysis on Graphs and Its Applications*, Proceedings of Symposia in Pure Mathematics, American Mathematical Society (2008).

[BEW09] B.M. Brown, M. S. P. Eastham, and I. Wood, Estimates for the lowest eigenvalue of a star graph, *J. Math. Anal. Appl.*, **354**, P. 24–30 (2009).

[CDR06] H. Cornean, P. Duclos, and B. Ricaud, On critical stability of three quantum charges interacting through delta potentials, *Few-Body Systems*, **38**, P. 125–131 (2006).

[CDR08] H. Cornean, P. Duclos, and B. Ricaud, On the skeleton method and an application to a quantum scissor, in *Analysis on graphs and its applications, Proc. Sympos. Pure Math.* Amer. Math. Soc. Providence (2008).

[E08] P. Exner, Leaky quantum graphs: a review, in *Analysis on graphs and its applications, Proc. Sympos. Pure Math.* Amer. Math. Soc. Providence (2008).

[EI01] P. Exner and I. Ichinose, Geometrically induced spectrum in curved leaky wires, *J. Phys. A*, **34**, P. 1439–1450 (2001).

[EN03] P. Exner and K. Němcová, Leaky quantum graphs: approximations by point-interaction Hamiltonians, *J. Phys. A*, **36**, P. 10173–10193 (2003).

[LP08] M. Levitin and L. Parnovski, On the principal eigenvalue of a Robin problem with a large parameter, *Math. Nachr.*, **281**, P. 272–281 (2008).

[LLP10] I. Lobanov, V. Lotoreichik, and I. Yu. Popov, Lower bound on the spectrum of the two-dimensional Schrödinger operator with a delta-perturbation on a curve, *Theor. Math. Phys.*, **162**, P. 332–340 (2010).

[M87] J. Marschall, The trace of Sobolev-Slobodeckij spaces on Lipschitz domains, *Manuscripta Math.*, **58**, P. 47–65 (1987).

[McL] W. McLean, *Strongly elliptic systems and boundary integral equations*. Cambridge University Press, Cambridge (2000).

NANOSYSTEMS: PHYSICS, CHEMISTRY, MATHEMATICS, 2013, 4 (2), P. 173–181

MULTI PARTICLE STATES CALCULATIONS AND PARTICLES STORAGE IN PERTURBED NANOLAYERS

S. I. Popov

Saint Petersburg National Research University of Information Technologies,
Mechanics and Optics, 49 Kronverkskiy, Saint Petersburg, 197101, Russia
popov1955@gmail.com

PACS 02.30.Tb, 73.21.Ac, 03.65.Ge

The problem of particle storage in nanolayered structures will be considered. Local perturbations of nanolayers can lead to the appearanceof eigenvalues of the corresponding one-particle Hamiltonian. To study particle storage it is necessary to deal with the multi-particle problem. This problem faces essential computational difficulties due to the great increase of the spatial dimension. Using a composite of natural physical models, analytical methods and computational approaches allows one to simplify the problem and to obtain useful results for application. Particularly, the Hartree method and Finite Elements Method (FEM) are used. The discrete spectrum of the Hamiltonian for two interacting particles is considered. Two different types of perturbation are considered: deformation of the layer boundary and a small window in a wall between two layers. The relation between the system parameters (interaction intensity - waveguide deformation) ensuring the existence of a non-empty discrete spectrum is studied. A comparison of particle storage efficiencies is made for these two cases.

Keywords: discrete spectrum; few-particle problem; quantum waveguide.

1. Introduction

It is known that curved quantum layers can store particles. From a mathematical point of view, it is related with the existence of eigenvalues for the corresponding Hamiltonian. Increased curvature leads to larger eigenvalues figures. This question is important in various physical problems. For example, to do two-qubit operation in a quantum computer based on coupled quantum waveguides (see, e.g., [1], [2]), it is necessary to store two electrons in some bounded domain during the operation time. Another interesting application is related to the storage of hydrogen (or protons) in nanolayered structures. Storing hydrogen in this manner can give a safe and effective fuel container for a hydrogen engine. One can note that layers with curved boundaries are more effective for particle storage because increasing the curvature (or boundary perturbation amplitude) leads to an increase of the discrete spectrum cardinality. Hence, the amount of hydrogen stored in the layered structure will be greater. Note that the Hamiltonian for the corresponding plane layered structure has an empty discrete spectrum.

To solve the problem it is necessary to consider the multi-body system, which is the main source of difficulty. Many-particle problems appear in various situations. These problems have been studied by using a variety of different methods (see, e.g., [3], [4]). For the quantum waveguide multi-body problem, the majority of results concerns the use of one-dimensional wires. Many of these methods for dealing with this particular problem have been reported previously [5]. Interesting approaches are also based on scattering theory [6], operator extensions theory [7] and reducing the problem to a 2D diffraction [8].

In the discrete spectrum problem for curved or deformed 2D (3D) quantum waveguides, rigorous mathematical results are only available for the one-particle Hamiltonian (if we deal with non-interacting particles or interaction is taken into account as some mean field only, then we really deal with a one-particle problem). As for the many-particle problem for quantum waveguides, only approximated results have been obtained [9], [10], [11], [12]. For example, Exner estimates the number of neutral fermions which can be stored near the distortion of the layer as the dimension of the discrete spectrum subspace [10]. For charged (repulsing) particles, only rough variational estimation for the maximum number of stored particles can be obtained (the analogous rough variational results for attracting particles have been described [12]). Namely, consider 2D layer Σ – strip in $\mathbb{R}^2$ of width $2a$. Let Γ be the axis of Σ. The strip is determined by the semi-width a and the curvature $s \to \gamma(s)$, defined on Γ. Here s is the curve length. Assume that the following regularity conditions take place: a) Σ is non self-intersecting curve, b) $a\|\gamma\|_\infty < 1$, c) γ has bounded support and $\gamma \in C^2$, γ, γ' are bounded.

Let us first choose a system of units for which $\hbar = 2m = c = 1$, c is the speed of light, m is the particle mass. Using natural waveguide coordinates (s, u) in Σ, one reduces the one-particle Hamiltonian to the following operator:

$$H = -\partial_s(1+u\gamma)^{-2}\partial_s - {\partial_u}^2 + V(s,u)$$

in $L^2(\mathbb{R} \times (-a,a))$ with the potential

$$V(s,u) = -\frac{\gamma(s)^2}{4(1+u\gamma(s))^2} + \frac{u\gamma''(s)}{2(1+u\gamma(s))^3} - \frac{5u\gamma''(s)^2}{4(1+u\gamma(s))^4}.$$

The operator is defined and essentially self-adjoint on $D(H) = \{f : f \in C^\infty, f(s,\pm a) = 0, Hf \in L^2\}$. By means of the modes expansion, one reduces the problem to a one-dimensional case [13–15], for which we use the Birman-Shwinger estimations. The potential V is majorized by:

$$W = \frac{\gamma(s)^2}{4\delta_-^2} + \frac{a|\gamma''(s)|}{2\delta_-^3} + \frac{5a^2\gamma''(s)^2}{4\delta_-^4}, \quad \delta_\pm = 1 \pm a\|\gamma\|_\infty.$$

Let us introduce W_j, $j = 2, 3, \ldots$

$$W_j(s) = \begin{cases} 0, & \left(\frac{\pi}{2a}\right)^2(j^2-1) > \|W\|_\infty, \\ W(s), & \left(\frac{\pi}{2a}\right)^2(j^2-1) \leqslant \|W\|_\infty. \end{cases}$$

Then the number N of neutral fermions, with spins S, which can be bounded near the perturbation of the layer is estimated [10] as:

$$N \leqslant (2S+1)\left(1 + \delta_+^2 \frac{\int\limits_{\mathbb{R}^2} W(s)\,|s-t|\,W(t)dsdt}{\int\limits_{\mathbb{R}} W(s)ds} + \sum_{j=2}^{\infty} \delta_+^2 \int\limits_{\mathbb{R}} W(s)ds\right).$$

Here we assume the Dirichlet condition. The Neumann and Robin conditions are analogous. As for the semi-transparent surface, it is possible to consider it as $\delta-$potential supported by curve [16], [17], [18].

In the case of charged particles (electrons, protons) it is necessary to consider their interaction. The simplest approximation was discussed previously [10], and some variational estimations were obtained. The discrete spectrum of a N-particle Hamiltonian can be empty. A sufficient condition for this is as follows:

$$T_\beta(N) + \frac{e^2N(N-1)}{2\beta\sqrt{7}} \geqslant \|W\|_\infty N + \left(\frac{\pi}{2a}\right)^2 N + \frac{e^2}{18\beta\sqrt{2}}$$

for some $\beta \geqslant \max\{2b, 596e^{-2}\}$, where $2b$ is the diameter of the support of function γ, e is the particle charge,

$$T_\beta(N) = \begin{cases} 2\sum\limits_{m=1}^{n} \lambda_m, & N = 2n, \\ 2\sum\limits_{m=1}^{n} \lambda_m + \lambda_m, & N = 2n+1, \end{cases}$$

λ_m are ordered eigenvalues of the Dirichlet Laplacian for the domain $\left[-\frac{3}{2}\beta\delta_+, \frac{3}{2}\beta\delta_+\right] \times [-a, a]$.

The computational problem for an $N-$particle state is rather difficult due to the essential increasing of the space dimension (N times). To simplify the problem, it is possible to use natural physical models and some preliminary analytical considerations. Particularly, the Hartree method permits the reduction of the problem to a sequence of one-particle problems. By using analytically obtained asymptotics, one can choose an initial approximation more effectively. Such a combination of analytical and computational methods seems to be the most promising approach to this problem.

2. One-particle problem for waveguide with deformed boundary

Variational estimates for the eigenvalues of the problem were obtained [19]. The domain is determined as follows:

$$\Omega = \{(x, y) \in R^2 : \ 0 < y < a(1 + \lambda f(x))\}, \text{supp} f = [-b, b], f \in C_0^\infty(R).$$

The trial function is sought in the form

$$\psi = \begin{cases} (1 + \lambda\eta f(x))\chi_1(y), & |x| \leqslant b, \\ e^{-h|x \mp b|}\chi_1(y), & |x| > b. \end{cases}$$

Let

$$z = \frac{\pi^2}{a^2}\frac{\|f\|^2}{\|f'\|^2},$$

The parameter η is chosen by the condition

$$\eta^2 - 2\eta z + 3z + K^2 < 0, \ \ K = \sqrt{\sum_{n=2}^{\infty}\left(\frac{2n}{n^2 - 1}\right)} = \sqrt{\frac{\pi^2}{3} + \frac{1}{4}},$$

which can be valid if $z^2 - 3z - K^2 > 0$, particularly, one can take $\eta = z$, that corresponds to the parabola minimum.

$$\chi_n = \sqrt{\frac{2}{a}}\sin\frac{\pi n y}{a}.$$

$$h = \frac{1}{2}\lambda^2 d_1 \|f\|^2, d_1 = \frac{\pi^2}{a^2 z}(z^2 - 3z - K^2).$$

The eigenvalue distance from the bottom of the continuous spectrum is estimated as follows;

$$-\lambda^4 {d_0}^2 \|f\|^4 + O(\lambda^5) \leqslant E - \frac{\pi^2}{a^2} \leqslant -\frac{1}{4}\lambda^4 {d_1}^2 \|f\|^4 + O(\lambda^5),$$

$$d_0 = \left(\frac{4\pi b}{a^2}\right)^2 - 3\frac{\pi^2}{a^2}.$$

The eigenvalue problem is solved numerically by the Finite Elements Method (FEM). Namely, we consider the minimization problem for the functional (in natural system of units)

$$a(\psi, \phi) = \int_\Omega \left(\frac{\hbar^2}{2m}(\frac{\partial\psi}{\partial x}\frac{\partial\phi}{\partial x} + \frac{\partial\psi}{\partial y}\frac{\partial\phi}{\partial y}) + E\psi\phi\right) d\Omega \tag{1}$$

in the waveguide domain of length $2k$, width $2a$ with sine-like deformation of height d and width $2b$, $b \ll k$: $f(x) = d \sin\left(\frac{(x-b)\pi}{2b}\right)$, $|x| \leqslant b$. In real physical systems the thickness (width L) of the layer is about the de Broglie wavelength (few nanometers for the electron) The Dirichlet condition are valid at the waveguide boundaries, while Neumann conditions are assumed at the waveguide ends ("formal" boundaries). One can use "non-reflecting" conditions at the ends, but this type of this condition doesn't influence the results. The reason is very simple — the corresponding eigenfunction decays exponentially outside of the perturbation region. To find the numerical solution, we used FreeFem++ with the library ARPACK to search for the matrix eigenvalues. Domain was Ω is divided into triangular subdomains with determined quadratic functions (see Fig. 1). The dependence of the eigenvalue (energy level) on the height of the deformation is shown on Fig. 2. Note that the eigenvalue is less than the threshold, i.e. the bottom of the continuous spectrum, $E/E_0 = \pi^2$. Our results are in good correlation with Exner's estimations.

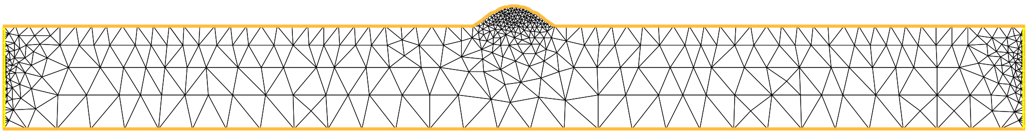

Fig. 1. Triangulation of the domain

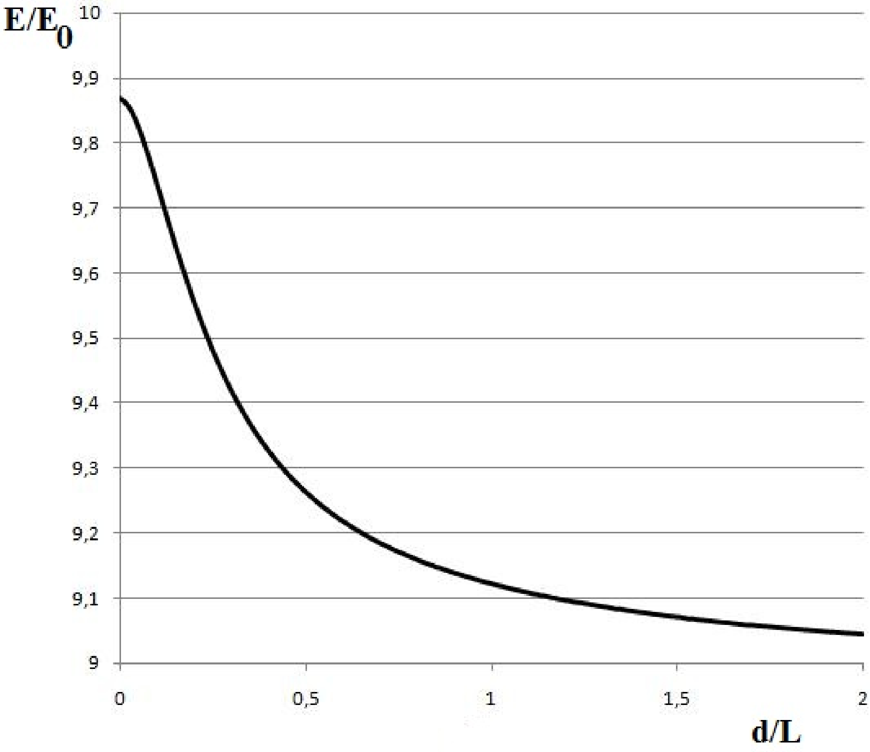

Fig. 2. Dependence of the eigenvalue (energy level) E/E_0 on the height d/L of the deformation (in dimensionless form); $L = 2a$, $E_0 = \frac{\hbar^2}{2mL^2}$, $b = 0.4L$

3. Two-particle problem for waveguide with deformed boundary

Consider two interacting particles in 2D waveguide with a perturbed boundary, i.e. we deal with the two-particle Schrödinger equation

$$-\frac{\hbar^2}{2m}\Delta\psi(r_1,r_2)+U(r_1,r_2)\psi(r_1,r_2)=E\psi(r_1,r_2).$$

The one-particle Hamiltonian for aquantum waveguide exhibits bound states if it is bent, protruded or allowing a leak to another duct [19], [20], [21], and the discrete spectrum depends substantially on the shape of the channel. The same is true for non-interacting particles. The most interesting question is whether the discrete spectrum's non-emptiness is preserved if we switch on the interaction between particles. A search was begun for system parameters that ensured this. Working with the Hartree approximation, the wavefunction is sought in the form

$$\psi(r_1,r_2)=\psi_1(r_1)\psi_2(r_2), \tag{2}$$

where ψ_1 and ψ_2 are one-particle functions and r_1 and r_2 are coordinate vectors of the corresponding particles. Using conventional methods, one obtains the following system for ψ_1 and ψ_2:

$$\left\{\begin{array}{l} -\frac{\hbar^2}{2m}\Delta\psi_1(r_1)+U_1(r_1)\psi_1(r_1)=E_1\psi_1(r_1),\\ -\frac{\hbar^2}{2m}\Delta\psi_2(r_2)+U_2(r_2)\psi_2(r_2)=E_2\psi_2(r_2), \end{array}\right. \tag{3}$$

where

$$U_n(r_n)=\int_\Omega|\psi_{3-n}(r_{3-n})|^2\,u(r_1,r_2)dr_{3-n}, \tag{4}$$

$u(r_1,r_2)$ is the interaction potential, e.g., for Coulomb repulsion it has the form $u(r_1,r_2)=\frac{e^2}{|r_1-r_2|}$. The simplest type of interaction is a $\delta-$potential (see, e.g., [22], [23], [24]). For this case, $U_n(r_n)$ takes the form:

$$U_n(r_n)=\int_\Omega|\psi_{3-n}(r_{3-n})|^2\,U_0\delta(r_1,r_2)dr_{3-n}=U_0\,|\psi_{3-n}(r_n)|^2\,,$$

where U_0 describes the intensity of the interaction. As a result, we get the following system:

$$\left\{\begin{array}{l} -\frac{\hbar^2}{2m}\Delta\psi_1(r_1)+U_0\,|\psi_2(r_1)|^2\,\psi_1(r_1)=E_1\psi_1(r_1),\\ -\frac{\hbar^2}{2m}\Delta\psi_2(r_2)+U_0\,|\psi_1(r_2)|^2\,\psi_2(r_2)=E_2\psi_2(r_2). \end{array}\right. \tag{5}$$

To find eigenvalues of the two-particle Hamiltonian, FEM is used. For this purpose, the problem needs reformulation in order to study the variational problem. At this stage, the system of differential equations (5) is replaced by integral relations:

$$\begin{array}{l} \int_\Omega\left(\frac{\hbar^2}{2m}\nabla\psi_1\cdot\nabla\phi_1+U_0\,|\psi_2|^2\,\psi_1\phi_1\right)dr_1-E_1\int_\Omega\psi_1\phi_1dr_1=0,\\ \int_\Omega\left(\frac{\hbar^2}{2m}\nabla\psi_2\cdot\nabla\phi_2+U_0\,|\psi_1|^2\,\psi_2\phi_2\right)dr_2-E_2\int_\Omega\psi_2\phi_2dr_2=0. \end{array} \tag{6}$$

The algorithm for the solution begins by taking as the first approximation the following functions $\psi_1=\psi_2=0$leading naturally, to a one-particle problem. Once the one-particle problem is solved, that solution (approximation for the one-particle eigenfunction) is inserted into (5) (or (4) in the general case), then, problem (6) is solved with the obtained potential. The solution is inserted into (5), and the procedure is repeated. Due to spatial symmetry, the values of E_1 and E_2 should coincide, so, the algorithm is made up to the instant when coincidence with the chosen accuracy appears. Bound states corresponds to values less than the lower bound of the continuous spectrum (π^2). For fixed geometry, the convergence deteriorates when the interaction intensity U_0 increases. Values of U_0 are found which guarantee the existence of the bound state. Increasing U_0 leads to the destruction of the two-particles eigenstate. Conversely, increasing the boundary deformation d leads to an increase of the "eigenvalue-threshold" distance (the only reason for the eigenvalue's existence is this deformation, as plane waveguides have no eigenvalues). It is interesting to find the correlation between the intensity and deformation, for which there exists a two-particle bound state. This corresponds to the domain on the parameter plane. The boundary of this domain (in dimensionless form) is found (see Fig. 3). The domain in question is below the curve on the Figure. One can use this curve to predict the possibility of particle storage, and consequently, to create systems with the proper parameters (proper deformation should correlates with the intensity of the particle's interaction).

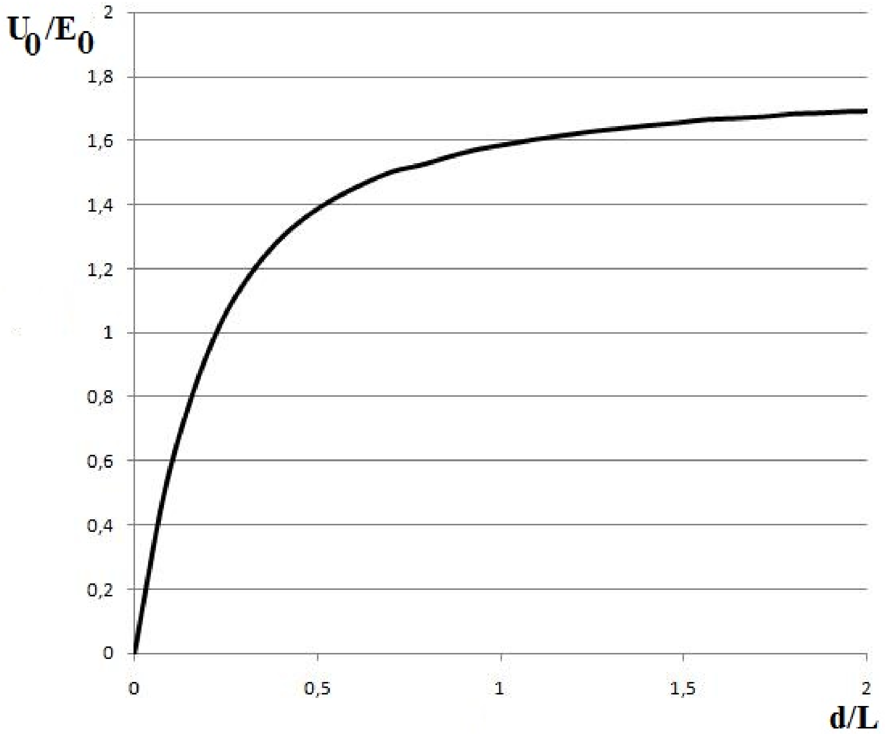

Fig. 3. Domain on the dimensionless parameters plane $(d/L, U_0/E_0)$ corresponding to the existence of eigenvalues of the two-particle Hamiltonian (below the curve); $2a = L$, $E_0 = \frac{\hbar^2}{2mL^2}$, $b = 0.4L$; the domain is below the curve

4. Layers coupled through window

Local perturbation of the layered structure boundary isn't a unique one that leads to the appearance of bound states below the continuous spectrum. Consider two nanolayers coupled through a narrow slot. It can be considered as a two-dimensional system, i.e. two strips coupled through window. The Dirichlet Laplacian for such system is known to have an eigenvalue below the threshold. The eigenvalue tends to the lower bound of the continuous spectrum when the window width tends to zero. Let d and a be the widths of the strip and the window, correspondingly. Exner and Vugalter [25] obtained an estimation of the eigenvalue distance from the threshold for a small window. The asymptotics (in the width of coupling window) of the eigenvalue were obtained by matching the asymptotic expansions for solutions to the boundary value problem [26], [27]:

$$\lambda_a = \frac{\pi^2}{d^2} - \left(\frac{\pi^3}{2d^3}\right)^2 a^4 + o(a^4). \tag{7}$$

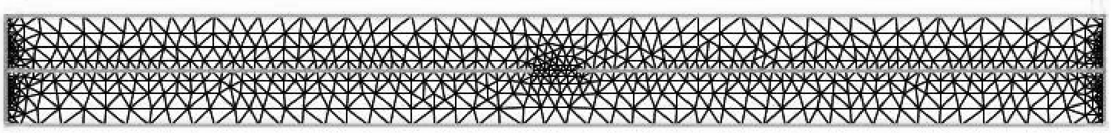

Fig. 4. Triangulation of coupled layers

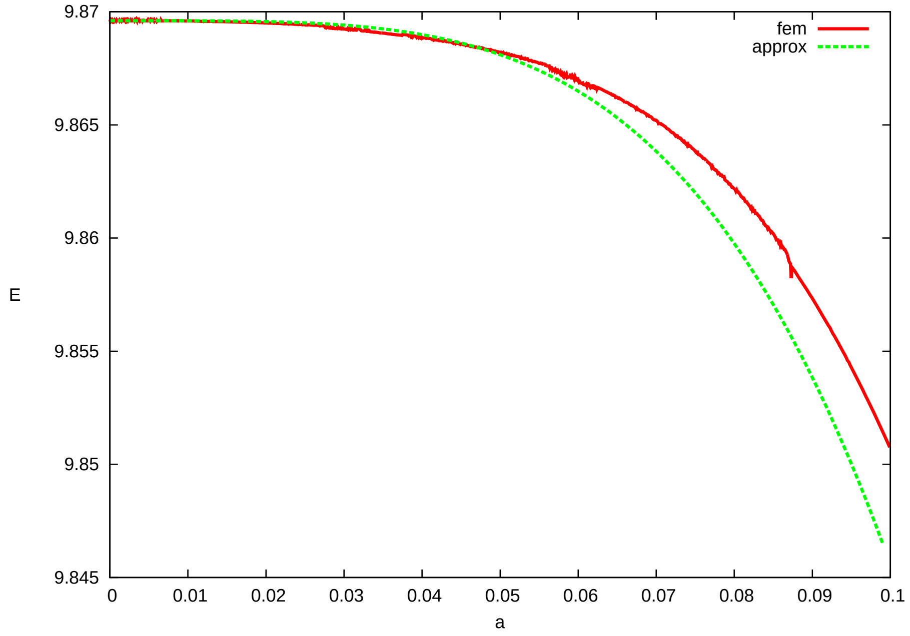

Fig. 5. Comparison of eigenvalue asymptotics (“approx”) (7) and exact eigenvalue (“fem”) for small coupling window

These results concern the one-particle Hamiltonian. As for the corresponding two-particle problem, there are no results. In the present paper, as a first step, we consider the one-particle problem for the system of arbitrary window size. Computations are made by FEM. Triangulation is made as shown on Fig. 4 One can see (Fig. 5) that for a small window, the results are in good correlation with the asymptotics. The main subject of this section is the two-particle problem for this system. We consider the delta-interaction between the particles. Delta-repulsion leads to the destruction of the one-particle bound state. We found the domain on the parameter’s plane (“interaction intensity - window width”), which corresponds to the existence of the two-particle bound state. The results are shown on Fig.6. It is interesting to compare these results with the analogous one obtained for the deformed boundary layer. One can see that two layers with a coupling window is essentially more effective for the storage of two particles than the nanolayer with a deformed boundary (the destroying electrostatic repulsion intensity is many times greater). The result becomes clear if we look through the distributions of electron density (Fig. 7).

Acknowledgements

The work was supported by Federal Targeted Program “Scientific and Educational Human Resources for Innovation-Driven Russia” (contracts P689 NK-526P, 14.740.11.0879, 16.740.11.0030), grant 11-08-00267 of Russian Foundation for Basic Researches.

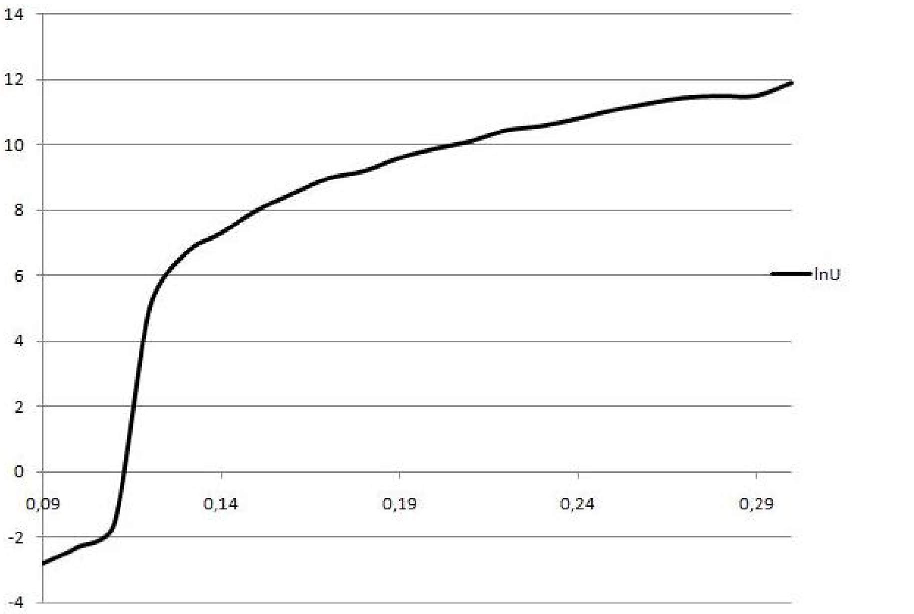

Fig. 6. Domain on the dimensionless parameters plane $(d/L, \log U_0/E_0)$ corresponding to the existence of eigenvalues of the two-particle Hamiltonian (below the curve)

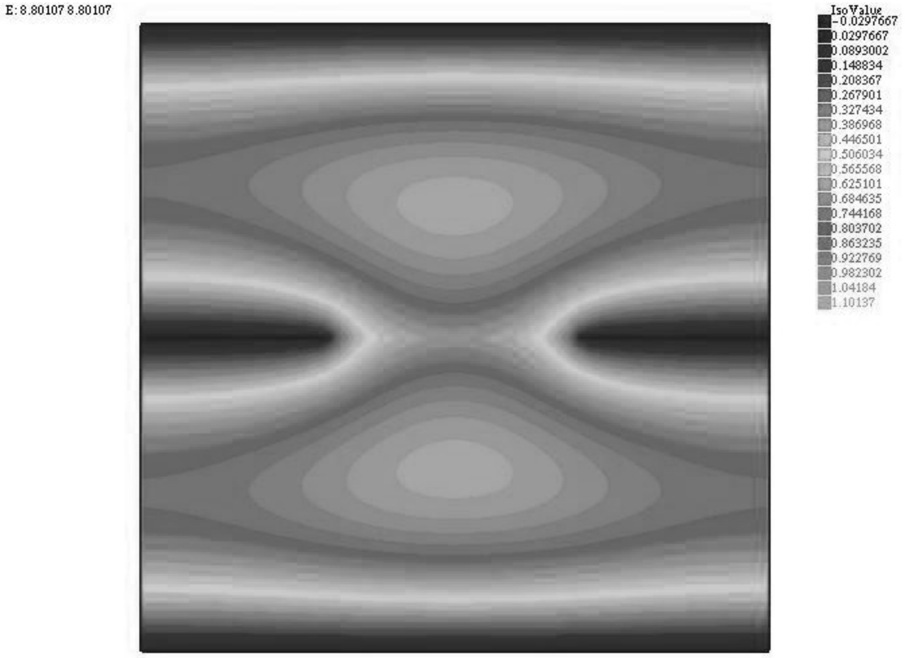

Fig. 7. electron density distribution of two-particle state for layers coupled through window

References

[1] Gavrilov M., Gortinskaya L., Pestov A., Popov I. and Tesovskaya E. *Phys. Part. Nucl. Lett.*, **4**(2), P. 137 (2007).

[2] Pavlov B.S., Popov I.Yu., Geyler V.A. and Pershenko O.S. *Europhys. Lett.*, **52**(2), P. 196 (2000).

[3] Roemer R.A. and Raikh M.E. *Phys. Rev.B*, **62**(11), P. 7045 (2000).

[4] Shepelyansky D.L. *Phys. Rev. Lett.*, **73**(19), P. 2607 (1994).

[5] Sutherland B. *Beautiful Models. 70 Years of Exactly Solved Quantum Many-body Problems* (World Scientific, Singapore, 2004).

[6] Shen J.-T. and Fan Sh. *New J. Phys.*, **11**, P. 113024 (2009).

[7] Langmann G., Laptev A. and Paufler C. *J. Phys. A: Math. Gen.*, **39**, P. 1057 (2006).

[8] Buslaev V.S., Levin S.B., Neittaanmaki P. and Ojala T. *J. Phys. A: Math. Theor.*, **43**, P. 285205 (2010).

[9] Nogami Y., Toyama F.M. and Varshni Y.P. *Phys. Lett. A*, **207**, P. 355 (1995).

[10] Exner P. and Vugalter S.A. *J. Math. Phys.*, **40**(10), P. 4630 (1999).

[11] Exner P. and Zagrebnov V.A. *J. Phys. A: Math. Gen.*, **38**, P. L463 (2005).

[12] Linde H. *J. Phys. A: Math. Gen.*, **39**, P. 5105 (2006).

[13] Newton R.G. *J. Operator Theory*, **10**, P. 119 (1983).

[14] Klaus M. *Annals Phys.*, **108**(2), P. 288 (1977).

[15] Seto N. *Publ. RIMS*, **9**, P. 429 (1974).

[16] Popov I.Yu. *J. Math. Phys.,* **33**(5), P. 1685 (1992).

[17] Popov I.Yu. *Math. Proc. Cambridge Phil. Soc.,* **118**(3), P. 555 (1995).

[18] Lobanov I.S., Lotoreichik V.Yu. and Popov I.Yu. *Theor. Math. Phys.*, **162**(3), P. 397 (2010).

[19] Exner P. and Vugalter S.A. *Lett. Math. Phys.,* **39**(1), P. 59 (1997).

[20] Duclos P. and Exner P. *Rev. Math. Phys.*, **7**, P. 73 (1995).

[21] Bulla W., Gesztesy F., Renger W. and Simon B. *Proc. Am. Math. Soc.,* **125**, P. 1487 (1997).

[22] Okopinska A. *J. Phys.: Conf. Series,* **213**(1), P. 012004 (2010).

[23] Block I., Dalibard J. and Zwerger W. *Rev. Mod. Phys.,* **80**(3), P. 885 (2008).

[24] Cornean H., Duclos P. and Ricaud B. *Few-Body Systems*, **38**(2-4), P. 125 (2006).

[25] Exner P. and Vugalter S., *Ann. I.H.P. Phys. Theor.*, **65**, P. 109–123 (1996).

[26] Popov I.Yu. *Appl. Math. Lett.*, **14**, P. 109–113 (2001).

[27] Popov I.Yu. *J.Math.Phys.*, **43**(1), P. 215–234 (2002).

NANOSYSTEMS: PHYSICS, CHEMISTRY, MATHEMATICS, 2013, 4 (2), P. 182–189

NEAR-FIELD RADIO-FREQUENCY PROBING METHOD CAPABILITIES FOR THE STUDY OF WATER STRUCTURAL DYNAMIC

Y. Baloshin[1], A. Drozdov[2], A. Volchenko[1]

[1] Saint Petersburg National Research University of Information Technologies, Mechanics and Optics, Saint Petersburg, Russia

[2] Institute for Analytical Instrumentation Russian Academy of Science, Saint Petersburg, Russia

baloshin1940@mail.ru, av@biophys.ru, wolf2684@mail.ru

PACS 84.40.-x

Living systems and free water were studied with the help of near-field radio-frequency (NFRF) probing methods. The results of this analysis suggest that processes within biological systems are comparable with those in ordinary water. The presented data suggest that near-field radio-frequency probing can be a useful diagnostic tool for the analysis of the radio-frequency fields generated by biological objects.

Keywords: radio-frequency near-field probing method, permittivity, generator frequency, wavelet transform.

1. Introduction

Recent progress in the development of radio-frequency and microwave medical equipment suggests that such instrumentation can be a useful diagnostic tool applicable in the area of internal medicine, traumatology and musculoskeletal disorders. Diagnostics based on radio-frequency and microwave probing methods offer advantages over conventional diagnostic tools e.g. probing methods offer a noninvasive diagnostic approach that allows the studying of biological tissue heterogeneity and such methods offer spatial analysis of biological organs, including the analysis of tissues located on the surface or within biological organs, as well as help define the special dimensions of these biological organs.

Despite recent progress, there is a growing understanding that new diagnostic approaches need to be transformed into more sophisticated tools which not only target symptoms of inflammatory processes, but are also successfully integrated into mainstream clinical laboratory and instrumental analyses.

Living biological objects have a complex structure of physical fields inside and outside the biological borders of the object. Spatial distribution and time dynamics of these physical fields carry important biological information that could be used for medical diagnosis.

One of the most important characteristics that describes interaction between probing electromagnetic radiation (PER) and a biological object is the complex permittivity, that is, in turn, connected with conductivity and the tangent of dielectric loss. Conductivity and dielectric loss, in turn, depend upon the physicochemical parameters of the biological object, such as water content, protein hydration, temperature, etc.

Recent studies suggest a strong connection between protein hydration and the activity of a biological system [1].

This paper presents data from the near-field radio-frequency (NFRF) probing study of biological objects as compared to ordinary water. Data suggest that the NFRF probing method is sensitive to the dynamic state of the water in a biological object, and therefore, can be used to analyze the state of that biological object.

2. The equipment and the methodology of the experiment

The main purpose of this method is to glean information about any inner structure (biological or physical) which can be surveyed from its surface. The NFRF probing method is based on the following assumptions: first, the electrodynamic state of the surface is connected with processes inside object through its dielectric permittivity (ε) and specific conductivity (σ), and second, the connection between the surface parameters and processes inside the object can be monitored by means of a compact electric antenna (sensor) that is working in the active mode.

There is one distinct property that characterizes our approach and sets it apart from conventional methods of radio-frequency (RF) diagnostics, namely, the choice of frequency for the antenna-sensor. We have previously presented the analysis of the known dispersive dependences for (ε), (σ) and full impedance (Z) which demonstrated that frequencies between 1-10 MHz were very sensitive to processes in biological systems [2]. Based on those results, 4 MHz was selected as the working frequency for the antenna-sensor.

All experiments were conducted with the help of diagnostic equipment [3] presented in Figure-1.

a) **b)**

Fig. 1. Diagnostic radio-frequency near-field probing equipment: a) general overview of the equipment in full assembly; b) overview of the antenna-sensor with circuit board of the RF generator

The main element of the electronic equipment is the highly sensitive detector comprised of the compact antenna connected to the RF generator oscillatory circuit with geometry presented on Figure-2-a.

During operation, the generator's aperture creates a quasi-static electric field (near-field zone) in the air. Figure-3 presents the results of the quasi-static electric field analysis conducted with the help of certified software package CST Studio Suite 2012 designated for electrodynamic modeling within a wide range of frequencies.

When the sensor is placed in contact with the surface of the physical or biological object, a quasi-static electric field generated by the sensor works as a connector between

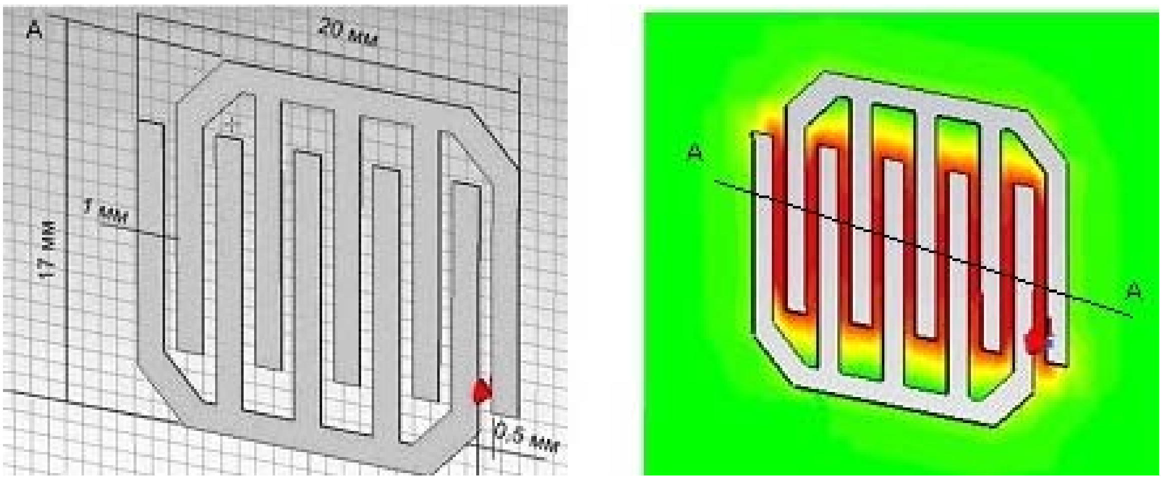

a) **b)**

Fig. 2. Radio-frequency antenna-sensor: a) Overview of the antenna geometry; b) Quasi-static field (near-field zone) at the antenna aperture

the antenna's impedance and object's surface impedance. As a result of that connection, the general impedance of the radio-frequency generator's oscillating circuit and its frequency value ($\delta\nu$) are changed. The difference between frequencies is described according to the following equation: ($\delta\nu = \nu_0 - \nu_1$), where ($\nu_0$) is the generator's frequency when antenna is placed in air, and (ν_1) is the generator's frequency, when antenna is placed on the object's surface. During NFRF probing, the frequency difference ($\delta\nu$), recorded through computer interface, represents an analytical signal that follows the changes in the object of interest.

After an analytical signal $\delta\nu = \nu_0 - \nu_1$ is obtained by the antenna, the signal is digitized through a "frequency-code" transformation and analyzed with the help of a designated software package.

3. Experimental design

The goal of the study was to compare the NFRF probing of a healthy subject's hand and water samples.

As previously mentioned, the frequency difference ($\delta\nu$) is the main source of diagnostic information of the proposed method, which allows an estimation of the object's internal structural organization.

Prior to use, the sensor was subjected to an initial calibration procedure that comprised of two processes: the first included 20 minutes of sensor operation in the air until the working temperature of the sensor was stabilized; the second process included 20 minutes of operation during which the sensor was wrapped in a plastic film and placed in water. After that, the device was re-calibrated and the frequency of the sensor was tuned in.

The initial calibration procedure was set up using the software option "Tune in" that expressed the sensor's frequency (ν_0) in relative units, and allowed the sensor's frequency to be tuned to either the "air" or "water" option. The selection between "air" and "water" options was determined by the goals of the particular experiment, since the sensor's tuning and calibration process could be carried out using any other object or different place on the object.

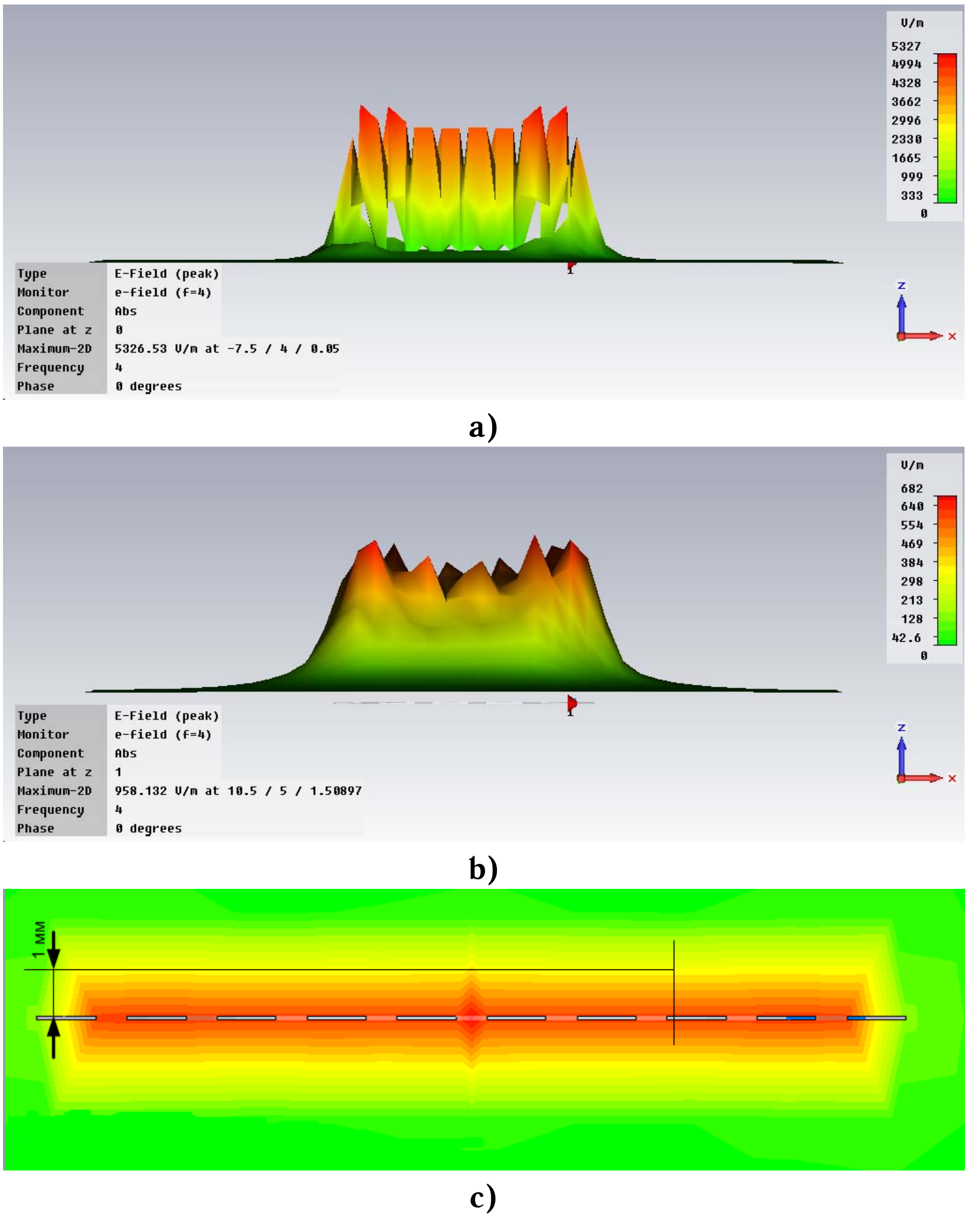

a)

b)

c)

Fig. 3. Quasi-static electric field distribution at the antenna aperture (near-field zone): a) field distribution at A-A cross-section (Figure 2-b). b) Distribution of the same field (a) 1mm away from antenna's aperture. Note that field amplitude is decreased by approx. 10 times. c) field distribution at 90 degrees

In order to conduct the first set of experiments (Figure-4), the sensor was tuned in the air for 20 minutes. After tuning, the sensor was placed on the volunteer's hand and the sensor's signal was recorded every three minutes for two hours without changing the position of the sensor.

The second set of experiments (Figure-5) was conducted using the same tuning in the air (20 minutes), but the sensor was then wrapped in plastic film and placed in the water ($\sigma = 4\times10^{-6}$ mOhm/cm, pH$\sim$5.6). The plastic film did not change the parameters of the sensor.

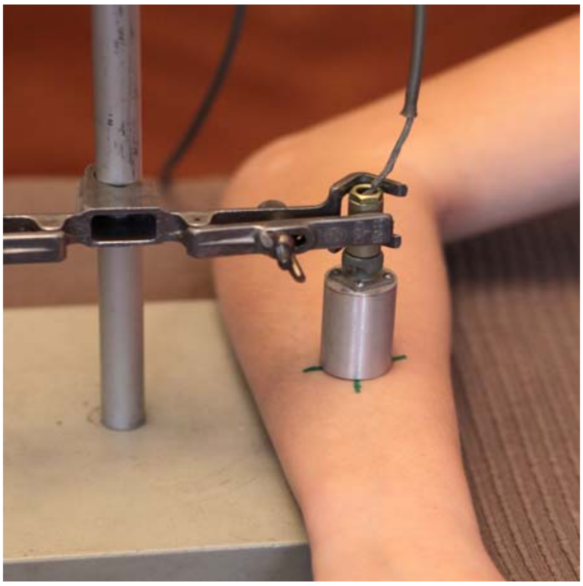

Fig. 4. The arm experiment

Fig. 5. The distilled water experiment

The final experimental step included the time-frequency analysis of the measured parameters. This analysis was carried out with the help of wavelet transformation. The wavelet transformation was chosen over a Fourier transformation because it offers two dimensional evolvement of a one-dimensional process where frequency and time values are considered to be independent variables. Therefore, this transformation allows simultaneous frequency and time analysis of the same process. The Morlet wavelet was used as the basic function.

4. Results and Discussion

Figure 6 presents data obtained with the help of radio-frequency near-field probing of the hand (a) and wavelet analysis of the data (b). Method is described in the experimental design section.

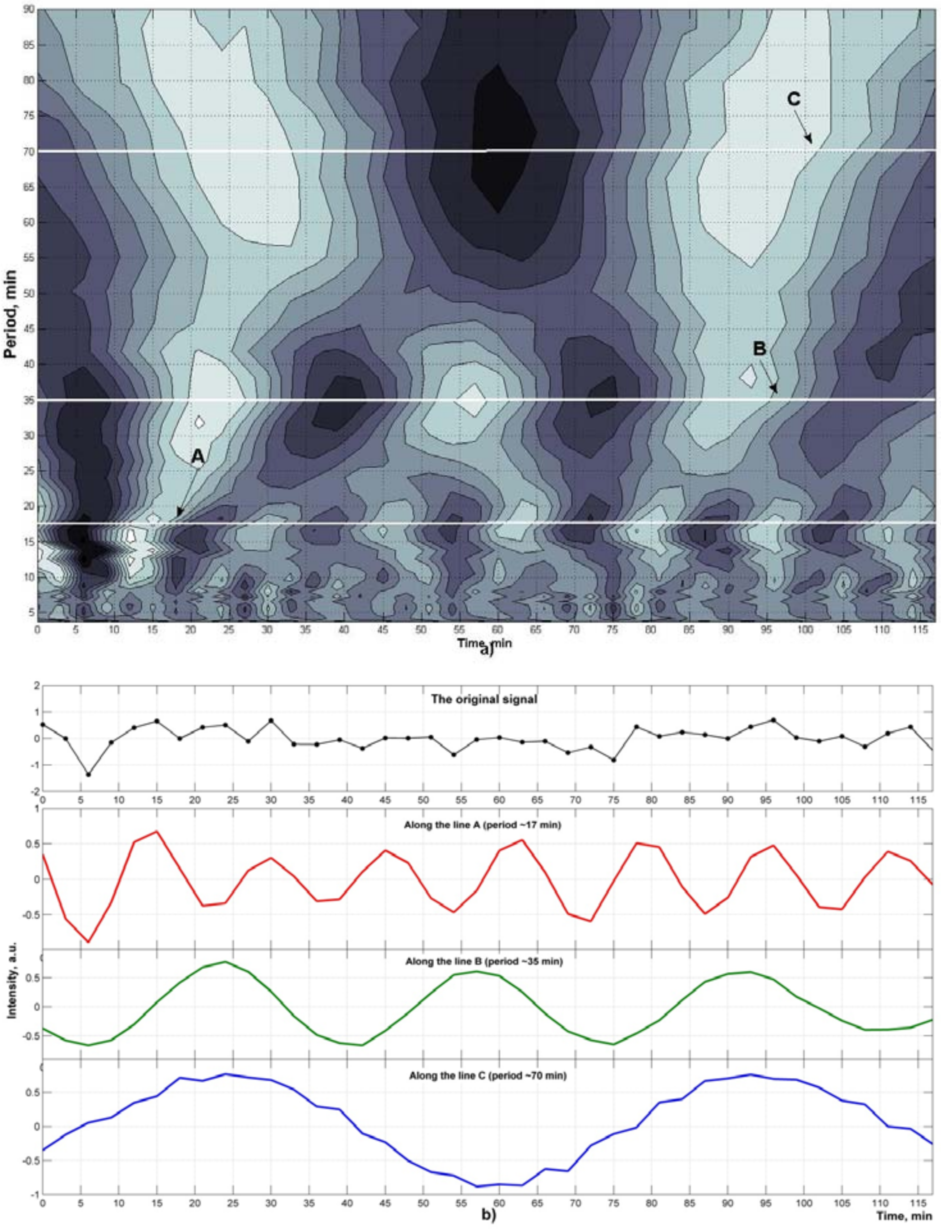

Fig. 6. Wavelet analysis of the NFRF probing signal recorded from the surface of the hand: a) wavelet transformation of the initial signal. Horizontal lines are labeled with letters A, B, and C. b) Initial signal harmonics along the lines A, B, and C on the Figure 6-a

Figure 7 presents data obtained with the help of radio-frequency near-field probing of the water. Method is described in the experimental design section.

Analysis of the experimental data allows us to conclude that, regardless of the nature of studied object, all observed dynamic changes in the NFRF probing signal showed

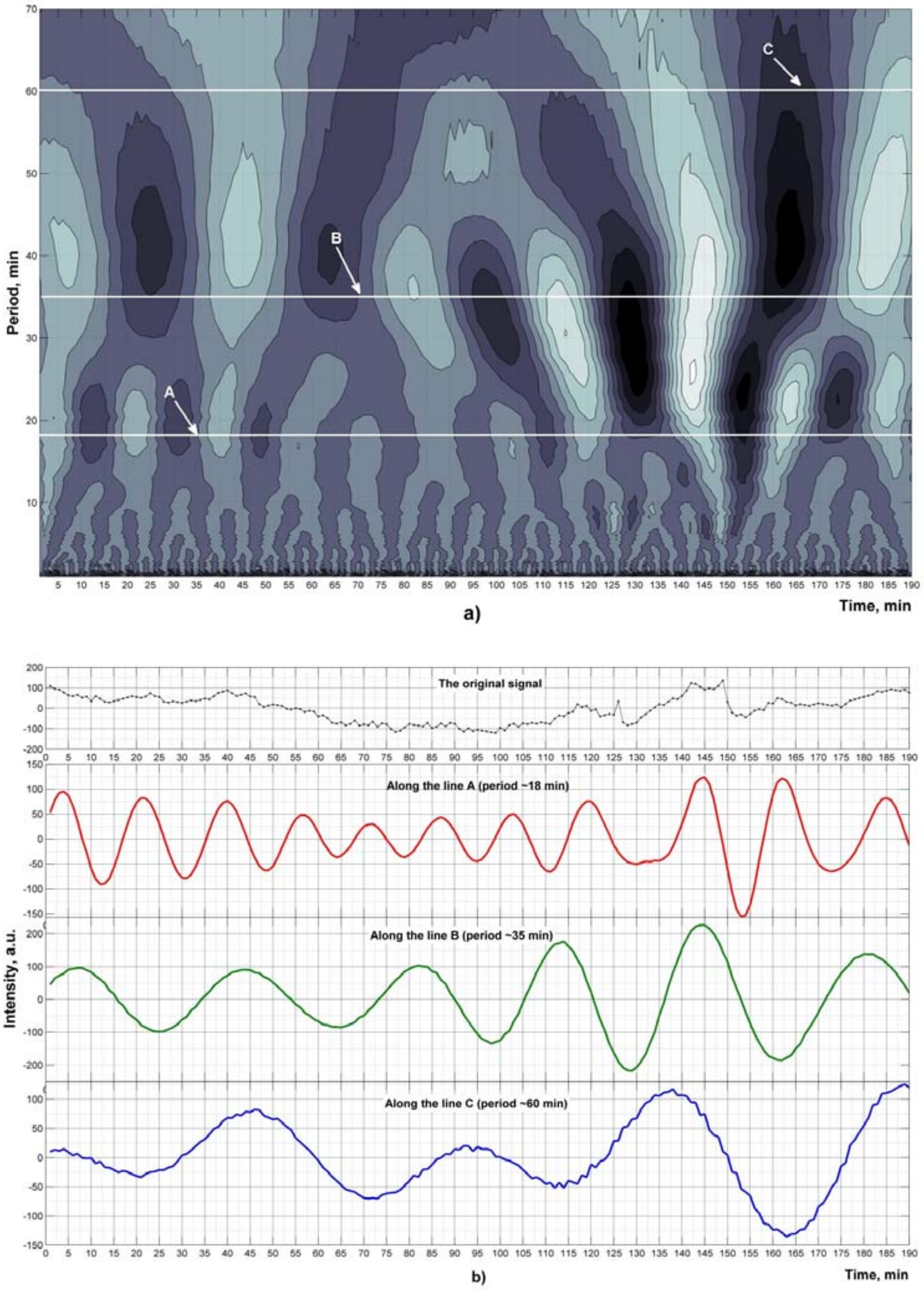

Fig. 7. Wavelet analysis of the radio-frequency near-field probing signal recorded from the sensor placed in the water: a) wavelet transformation of the initial signal. Horizontal lines are labeled with letters A, B, and C. b) Initial signal harmonics along the lines A, B, and C on the Figure 6-a

very reproducible time patterns, within which the magnitude of the changes varied up to 10% (11-19 min, 25-35 min, and 60-70 min). Similarity between patterns obtained from biological object and from ordinary water pointed out that, perhaps, NFRF probing signal was very sensitive to the degree of protein hydration, namely, the changes of the dispersive dependences for ε, σ and Z were determined by hydration shells around proteins.

Therefore, the main hypothesis is that processes within biological system are comparable with the processes in the ordinary natural water. Presented analysis of the dynamic changes of the radio-frequency near-field probing signal can be used for the development of a diagnostic method.

References

[1] O. Samoylov. *The structure of water solution electrolyte and ions hydration*. AS USSR, Moscow (1957).

[2] Y. Baloshin, A. Sorokin, A. Arsen'ev, A. Volchenko. Diagnosis method of functional activity tissue and organs of biological objects and its realization device. *The universities — Instrument*, **54**(3), P. 37–43 (2011).

[3] V. Samoylov. *Medical biophysics* (textbook for universities). Special Literature, Saint Petersburg, 558 pp. (2007).

NANOSYSTEMS: PHYSICS, CHEMISTRY, MATHEMATICS, 2013, 4 (2), P. 190–195

ANALYSIS OF A SIDEBANDS-BASED QUANTUM CRYPTOGRAPHY SYSTEM WITH DIFFERENT DETECTOR TYPES

V. I. Egorov[1], D. N. Vavulin[1], I. Z. Latypov[2], A. V. Gleim[1], A. V. Rupasov[1]
[1] Saint Petersburg National Research University
of Information Technologies, Mechanics and Optics, St. Petersburg, Russia
[2] Zavoisky Physical-Technical Institute, Kazan, Russia
egorovvl@gmail.com, dima-vavulin@mail.ru

PACS 03.67.-a

We performed theoretical analysis of a sidebands-based quantum cryptography system with two types of detectors: an avalanche photodiode and a superconducting photon counter. The influence of detector parameters on eavesdropper “Intercept-resend” attack efficiency was investigated.

Keywords: quantum cryptography, intercept-resend, avalanche photodiodes, superconducting single photon detectors.

1. Introduction

Quantum cryptography is a method of secure communications based on using single-photons in the process of secret key generation [1]. Therefore, information security is granted on a physical level by the fundamentals of quantum physics. The principal advantage of this technology is its ability to allow legitimate users (Alice and Bob) to always detect eavesdropping in the secure channel based on the increase in error level during transmission. In practice, quantum key distribution security is limited by the amount of losses in communication channel and the quantum bit error rate (QBER). It is known that the eavesdropper (Eve) can conceal their activity under errors which inevitably appear during the key distribution process [2]. The QBER value is dependent upon both the optical scheme and device parameters. In particular, detector characteristics make the largest contribution, especially at shorter distances (<50 km). In these studies, two detector types: an avalanche photodiode (APD) and a superconducting single-photon detector (SSPD) were analyzed. APD-detectors are used in most quantum cryptography experiments [2]. Their main drawback is a high rate of dark counts, resulting in high QBER. Superconducting detectors [3] have high count rates and fewer dark counts, however, they are more operationally complex, requiring the use of liquid helium to maintain cryogenic temperatures (2–4 K).

Today many types of QKD systems are known [2]. Merolla et al. [4] suggested a method of quantum key distribution using sidebands modulation of light (SQKD). Among its advantages are simplicity of optical phase introduction, matching and maintenance, high bitrate and low error rate, achieved by unidirectionality and frequency separation of quantum and classical signals, as well as in principal, the possibility of implementing wavelength division multiplexing.

In this paper the informational characteristics of an SQKD system with APD and SSPD detectors (raw key generation rate and QBER) were investigated. We also performed theoretical analysis of the system’s ability to resist Intercept-resend attacks [2], the efficiency of which was defined by its QBER value.

2. Experimental Setup

Figure 1 shows a schematic diagram of an SQKD system. The laser emitted monochromatic radiation. The spectrum of signal in frequency scale include only one component. In a sender block phase modulator PMA performed sinusoidal modulation on a high frequency from radio range. If the index of modulation is low enough, in addition to the central frequency, two sidebands will appear in the spectrum at PMA output (Fig. 1b). The spectral shift of the sidebands from the central frequency was equal to the modulation frequency. Optical phase shift of sidebands was determined by the phase of the modulating wave. The index of modulation can be chosen low enough so that the radiation on the sidebands can be regarded as a single stream of photons.

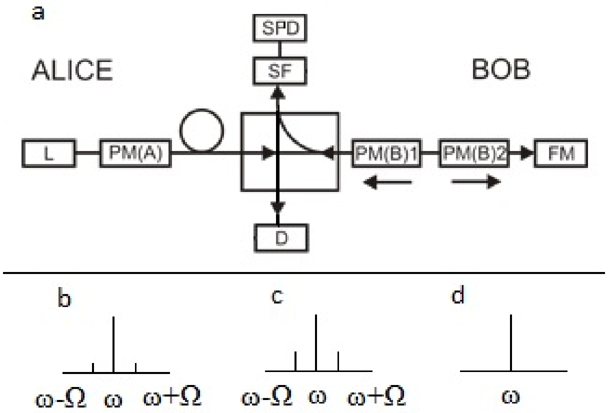

FIG. 1. Principal scheme of a sidebands-based quantum key distribution system (a). L — light source. PMA, PMB — phase modulators, FM — Faradey mirror, SF — spectral filter, D — detector, SPD — single photon detector. At the bottom — spectra of optical signals after modulation at the Alice block and Bob's block with relative phase shift 2π (c) and π (d)

The modulated optical signal, which consisted of central and side frequencies with a given relative phase was transmitted over the communication line to Bob's device, which contain ed similar modulators PMB1 and PMB2. Two modulators were necessary to compensate for polarization distortion in the optical system. At the receiving unit a phase shift was added without reference to the sender. The second modulation resulted in sideband amplitude changes depending on the relative phase shift of Alice and Bob. After passing through modulators the light was reflected off the Faraday mirror and passed to the spectral filter. This filter separated quantum and classical signal components, which were detected by a single photon counter SPD and detector D respectively. The SQKD system also included an optical subsystem of synchronization between the sender and the receiver (not shown on the figure).

3. Operational Parameters of the System with Different Detector Types

One of the main parameters of a quantum key distribution system is the ultimate raw key generation rate F_{raw}, which was, in our case, limited by the maximum detector count rate on the receiver side and is defined as:

$$F_{raw} = \frac{1}{2} f_{bit}\, \mu\, a_{\text{loss}}\, \eta,$$

where 1/2 refers to probability of coincidence between Alice and Bob modulator phase shifts in the B92 protocol [1]; f_{bit} is the phase change frequency (i.e. the frequency of signals sent by the transmitter); μ — mean number of photons per pulse ($\mu \sim 0.2$), η — quantum efficiency of a single photon detector. Coefficient a_{loss} represents the probability of a photon to achieve the detector and is defined through the value of total optical losses in the channel α:

$$a_{\text{loss}} = 10^{-\alpha/10}.$$

For the investigated SQKD system, the total losses were defined as the sum of losses in optical fiber and other optical elements. The latter included losses on a multiplexer (1.2 dB), circulator (2.21 dB), Bob modulators (10 dB after two passes) and a Faraday mirror (0.6 dB), totalling 14.01 dB. The attenuation rate in single mode fiber (SMF-28) was assumed to be 0.2 dB/km.

Modeling was conducted for the following detector parameters: f_{bit} = 100 MHz, η = 10% (APD, IdQuantique [5]); f_{bit} = 100 MHz, η = 25% (APD, IdQuantique [5]); f_{bit} = 500 MHz, η = 16% (SSPD, Scontel [3]). Fig. 2 illustrates calculated values of raw key generation rate depending on fiber optics line length for the SSQKD system with APD and SSPD detectors.

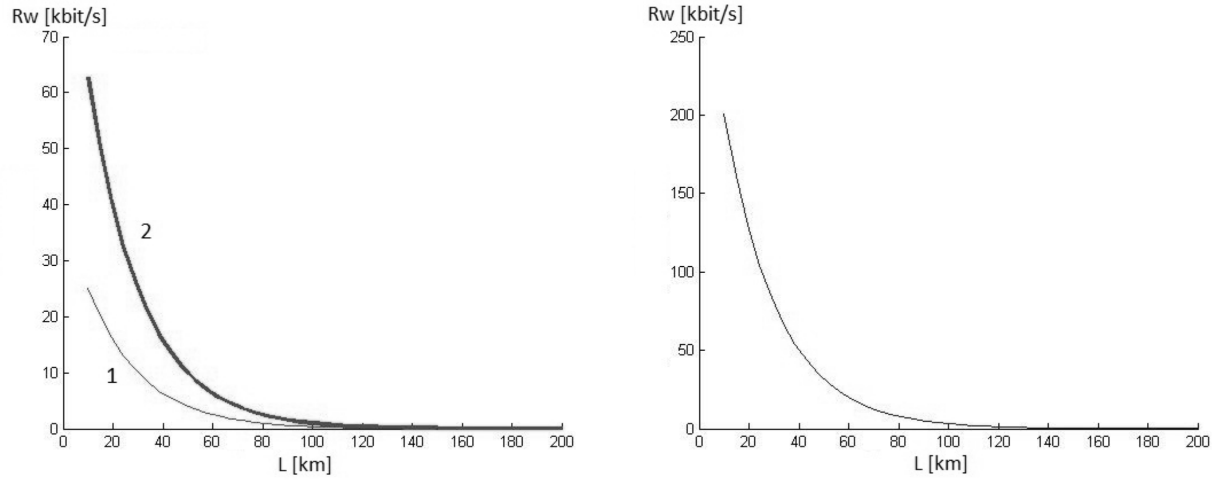

FIG. 2. Raw key generation rate in the SSQKD system with APD (a) and SSPD (b) detectors

Quantum bit error rate (QBER) is another important parameter of any QKD system. It is defined as:

$$QBER = \frac{F_{err}}{F_{raw} + F_{err}},$$

where F_{err} is the frequency of error bits that appear in the process of key distribution. This quantity consisted of two components: optical error frequency F_{opt} and detector dark count rate F_{dark}. For an SSPD detector, the F_{dark} value may be as low as 10 Hz [6], and for an APD — 1 kHz for η = 10% and 5 kHz for η = 25% [5]. Optical error frequency F_{opt} is defined as:

$$F_{opt} = F_{raw} \cdot p_{err},$$

where p_{err} is the optical error probability, that in the current setup, includes Fabry–Perot based filter noise ($1.85 \cdot 10^{-4}$), probability of error induced by Rayleigh reflection, back reflection, circulator directivity ($1.63 \cdot 10^{-3}$), and noise from multiplexer cross-coupling ($1.93 \cdot 10^{-3}$). Multiplexer errors decay in optical fiber. Computational results are given on Fig. 3.

One may notice that QBER suffers a slight decay in a system with an SSPD detector for communication line length 10–40 km. This is due to errors introduced by optical elements

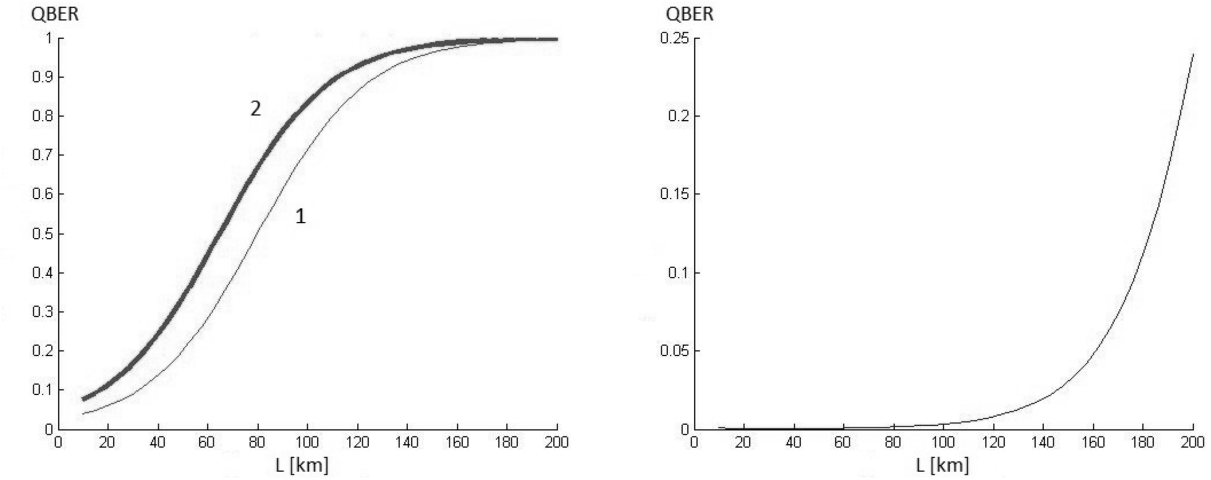

FIG. 3. QBER values in SQKD system with an APD (a) and SSPD (b) detectors

of Alice (they are represented by multiplexer errors in our model). This noise component is quickly attenuated over longer distances.

In order to estimate the efficiencies of different detectors, we introduced a parameter D_{Eff}, defining it as:

$$\mathrm{D}_{\mathrm{Eff}} = \frac{\mathrm{QBER}_{\mathrm{APD}} \;/\; \mathrm{QBER}_{\mathrm{SSPD}}}{F_{raw}\ \mathrm{APD} \;/\; F_{raw}\ \mathrm{SSPD}}.$$

The curves for APD's with different quantum efficiencies are shown on Fig. 4. It can be seen that for optical channel length between 20 to 100 km, SSPD detectors demonstrated the most considerable advantage. In particular, at 60 km the signal-to-noise ratio of an SSPD is more than three orders of magnitude higher than for the studied APDs.

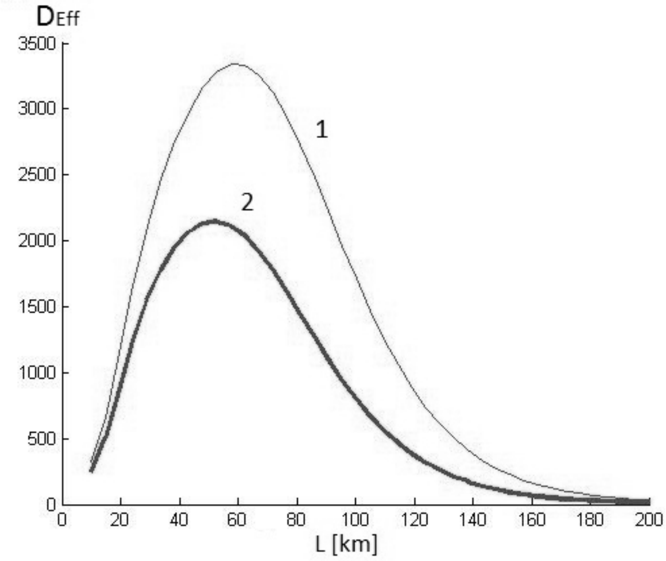

FIG. 4. Relative efficiency of SQKD systems with APD and SSPD detectors

TABLE 1. Probability analysis of Intercept-Resend strategy. Probabilities calculated for two symmetric cases are marked with an asterisk. Cases not shown are parenthesized

Phase used by Alice	0		π		0		π	
Phase used by Eve	0		π		π		0	
Probability of photon detection for Eve	$\mu/4$		$\mu/4$		0		0	
Phase detected by Eve	0		π		—		—	
Phase used by Eve for transmission	0		π		0	(π)	0	(π)
Probability of this event	$\mu/4$		$\mu/4$		$1/4 - \mu/8$*		$1/4 - \mu/8$*	
Phase used by Bob for detection	0	π	0	π	0	π	0	π
Probability of photon detection for Bob	$\mu^2/8$	0	0	$\mu^2/8$	$\mu/8 - \mu^2/16$*	0	$\mu/8 - \mu^2/16$*	0

4. "Intercept-resend" Attack Resistance

Intercept-resend eavesdropping strategy, e.g. when Eve imitates Bob's and Alice's behavior [1] is based upon the principal ability of an intruder to conceal their activity under optical errors, numerically estimated by the QBER value. Implementing this strategy, Eve connects to the quantum channel and measures the results of interference between prepared photons and Alice's pulses. If Eve receives a detector count, she sends a photon with the same phase value as the one used for measurement. Otherwise, if she doesn't receive a count, she sends a pulse with a random phase. Table 1 shows the probability analysis of this strategy. We assume that Eve possesses a detector with $\eta = 100\%$, no dark counts and a light source equal to Alice with $\mu \sim 0.2$.

An important advantage of this strategy is the fact that Bob's total detection probability ($\mu/2$ for B92 protocol) doesn't change. According to the table, the probability of a disagreement between Alice's and Bob's raw key bits is close to 50% for low μ. It is certain that such a high error rate is unsatisfactory, but Eve still possesses another opportunity. She may sacrifice information about the key, and therefore, linearly reduce the error rate. In order to do this, Eve can perform measurements with a certain rate. Thus, if we assume that random noise fluctuations are 50% of total noise rate, then Eve may stay undetected, adding an amount of errors bounded above by one-half of the QBER value:

$$\left(\frac{\mu}{4} - \frac{\mu^2}{8}\right) \Big/ \frac{\mu}{2} = QBER \cdot n,$$

where n represents the frequency of eavesdropping measurements. The number of bits received by Eve in this case may be estimated as:

$$N_{Eve} = \frac{F_{raw} \cdot t}{n} \cdot \left(\frac{\mu}{4} + \frac{\mu^2}{8}\right) \Big/ \frac{\mu}{2},$$

where t is transmission time. Table 2 shows calculated values for the investigated setup for 40 km fiber distance and $t = 10$ s.

Therefore, at the fiber length of 40 km, Eve is able to perform imperceptible eavesdropping for one of 4600 pulses in an SSPD based system, one of 13 pulses in an APD system with

TABLE 2. "Intercept-Resend" strategy efficiency for systems with different detector types

Detector type	F_{raw}, kbit/s	QBER	n	N_{Eve}, bits	Key fraction, %
SSPD	50.6	$3.9 \cdot 10^{-4}$	4615.4	60.5	0.01
APD, η=10 %	6.3	0.24	7.5	4620	7
APD, η=25 %	15.8	0.14	12.8	6788.6	4

η = 10 % and one of 7 in an APD system with η = 25 %. In ten seconds she will receive 61 (0,01%), 6789 (4%) and 4620 (7%) secret key bits respectively. It may be seen that for efficient detectors QBER grows more slowly than the detection rate, which makes these devices more suitable for QKD, especially at medium distances, which agrees with data from Fig. 4.

5. Conclusion

Thereby, the results of numerical simulations demonstrated the significantly higher efficiency of superconducting detectors relative to APDs for quantum cryptography systems. The values used in the calculations were based on data from the available specifications of commercial single-photon detectors. Both high detection rates and low dark counts of SSPD detectors make them more efficient for quantum cryptography application. The signal-to-noise ratio of an SSPD was found to be more than three orders of magnitude higher than that of the APD for setups with optical fiber several tens of kilometers long. Low dark count values in superconducting devices allowed increasing cryptographic security several times for lines of the same length and additionally facilitated the detection of Intercept-resend attacks. The use of APD made necessary the performance of reconciliation and privacy amplification procedures, [2] even for short optical communication line lengths. The data clearly demonstrated that APD's with higher quantum efficiencies (25% instead of 10%) provided higher security rates. Avalanche photodiodes can be used effectively in one-way cryptographic schemes (in particular, QKD using single-photon interference in sidebands of phase-modulated light for short communication channels (up to 30 km).

Acknowledgments

The study was supported by The Ministry of education and science of Russian Federation, project 14.B37.21.0248.

References

[1] C.H. Bennett. Quantum cryptography using any two nonorthogonal states. *Phys. Rev. Lett.*, **68**, P. 3121–3124 (1992).

[2] V. Scarani, H. Bechmann-Pasquinucci, N.J. Cerf et al. The security of practical quantum key distribution. *Rev. Mod. Phys.*, **81**, P. 1301–1350 (2009).

[3] G. N. Gol'tsman, O. Okunev, et al. Picosecond superconducting single-photon optical detector. *App. Phys. Lett.*, **79** (6), P. 705–707 (2001).

[4] J.-M. Merolla, Y. Mazurenko, J.-P. Goedgebuer, W.T. Rhodes. Single photon interference in sidebands of phase-modulated light for quantum cryptography. *Phys. Rev. Lett.*, **82**, P. 1656 (1999).

[5] IdQuantique id210 series datasheet. `http://www.idquantique.com`.

[6] A.V. Sergienko. Quantum optics: Beyond single-photon counting. *Nature photonics,* **2**, P. 268–269 (2008).

NANOSYSTEMS: PHYSICS, CHEMISTRY, MATHEMATICS, 2013, 4 (2), P. 196–205

X-RAY DIFFRACTION STUDY OF THE PHASE AND MORPHOLOGY CHANGES IN YTTRIUM COMPOUND NANOPARTICLES

R. P. Ermakov, V. V. Voronov, P. P. Fedorov

A. M. Prokhorov General Physics Institute, Russian Academy of Sciences, Moscow, Russia

x-ray_diffraction@mail.ru

In the present experimental study, the precipitation of basic yttrium nitrate from aqueous solutions allowed the optimization of conditions for the preparation of loosely aggregated $Y_2(OH)_5NO_3 \cdot 1.5H_2O$, the thermal decomposition of which, under controlled annealing, permitted the synthesis of yttria nanoparticles with desirable microstructure. The latter material can be widely used to manufacture yttria optical ceramics. $Y_2(OH)_5NO_3 \cdot 1.5H_2O$ thermolysis occurs via the formation of a metastable hexagonal Y_2O_3-based phase ($a = 8.04$, $c = 12.37$ Å).

Keywords: yttrium oxide, optical ceramics, X-ray diffraction phase analysis.

1. Introduction

The preparation of laser nanoceramics with spectral and lasing properties similar to that of single crystals is one of the most important innovations in the field of optical materials in recent years [1]. Advantages of ceramic materials over single crystals include improved mechanical properties, increased laser sustainability, ability to synthesize large samples, monotonous and homogeneous distribution of the high-concentration dopants, opportunity to obtain transparent optical media when the preparation of the single crystals is obstructed, ability to produce multilayered elements, etc. Neodymium- and/or ytterbium-doped yttrium oxide ceramics have spectral and lasing properties very close to the properties of alumoyttrium garnet (YAG) [2]. However, preparation of the former compounds in single crystal form is hindered by the polymorphic phase transition which occurs at temperatures close to its melting point and the high melting temperature of the aforementioned materials. Thus, a shift from single crystal growth to a polycrystalline technology is one of the most promising avenues for the manufacture of yttria-based active laser elements. In fact, the ThO_2-stabilized ceramic Y_2O_3:Nd^{3+} was the first polycrystalline oxide laser material developed [3].

The study of synthetic methods and precursors for the preparation of yttria-based laser ceramics continues at a very accelerated pace [4–12] because these materials possess high chemical stability, high transparency in the IR region, low thermal expansion and high heat conductivity [13]. Activated yttria powders can also be used as luminophores [14].

Transparent oxide ceramics synthesis includes the preparation of precursors with designated composition and morphology. Each step of this procedure is crucially important for the quality of the final product. One should closely monitor and control the size of domains with coherent scattering, narrow size distribution of such domains, low agglomeration, low defect concentration and high chemical purity. These parameters are linked to the sample microstructure, and thus, can be studied by full-profile X-ray diffraction phase analysis.

Therefore, the subject of this paper was the optimization of these conditions for the preparation of the yttria precursor by its precipitation from aqueous nitrate solutions, determination of the correlations between preparation conditions and product microstructure and control over the latter.

2. Experimental

Yttria samples with controlled properties were prepared in two steps. The first step included the synthesis of basic yttrium nitrate. Commercially available 99.99% pure Y_2O_3 was dissolved in a slight excess of diluted nitric acid (15 wt.%; 99.9% pure) under heating. Then the formed solution was carefully titrated with aqueous ammonia (pH = 9.60; prepared by dilution of concentrated 99.9% pure NH_4OH with double-distilled water) under stirring. Precipitation of white jelly-like basic yttrium nitrate during the titration was controlled by the HANNA INSTRUMENT pH-meter (pH = 0.76–9.00). The second step included the thermal decomposition of the obtained precipitate and formation of yttria. Sample thermolysis was performed in SNOL ovens (alumina crucibles; 100 mg specimens). All experiments were performed under air unless specified otherwise.

Thermal decomposition conditions were determined by thermogravimetry (Q-1500D derivatograph; quartz crucibles; 50–100 mg samples (± 0.4 mg); Pt–Pt/Rh thermocouples; heating rate of 10 °C/min in the 25–600 °C range (± 2 °C)).

X-Ray diffraction experiments were done with the use of DRON-4 diffractometer (CuKα radiation; Maud software, RITA/RISTA method [15–19]). We used silicon powder as an internal standard for the evaluation of the instrumentation functions.

Leo 912 AB Omega electron microscope was used for the investigation of the specimen microstructure.

3. Results and Discussion

3.1. Preparation and Analysis of Precursor

As previously mentioned in the Experimental section, preparation of the yttria precursor was carried out in two steps. The first step included dissolution of Y_2O_3 and formation of acidic aqueous nitrate solution:

$$\mathrm{Y_2O_3 + 6HNO_3 = 2Y(NO_3)_3 + 3H_2O.} \tag{1}$$

Then yttrium hydroxynitrate, the precursor of yttria powder with controlled properties, was precipitated by direct titration with aqueous ammonia:

$$\mathrm{2Y(NO_3)_3 + (6-x)NH_4OH + nH_2O = Y_2(OH)_{6-x}(NO_3)_x \cdot nH_2O + (6-x)NH_4NO_3.} \tag{2}$$

A typical titration curve for the reaction of aqueous $Y(NO_3)_3$ and NH_4OH is presented in Fig. 1. It has two low-slope steps “a–b” and “c–d”. Both correspond to the precipitation of yttrium hydroxynitrate $Y_2(OH)_{6-x}(NO_3)_x{\cdot}nH_2O$. $Y_2(OH)_{6-x}(NO_3)_x{\cdot}nH_2O$ precipitates might have had different compositions (i.e., x values) at different steps of the titration curve (Fig. 1). Therefore, we studied properties of $Y_2(OH)_{6-x}(NO_3)_x{\cdot}nH_2O$, formed at each step, separately, i.e., at each step (between points “a” and “b” at pH 6.8, and at the end of titration at point “d”, pH 9.4), precipitates were isolated from the matrix solution and studied separately after filtering, washing and drying.

Concerning the specimens’ flowability, samples prepared at different pH values had different degrees of agglomeration; precipitates obtained at pH 6.8 had rigid agglomerates, whereas specimens precipitated at pH 9.0 had loose agglomerates. We continue to investigate the cause of this difference.

Both types of these samples have identical X-ray diffraction patterns, similar to the pattern of $Y_2(OH)_5NO_3{\cdot}1.5H_2O$ phase (JCPDS card 49-1107) and $Y_2(OH)_{5.14}(NO_3)_{0.86}\ {\cdot}H_2O$ phase

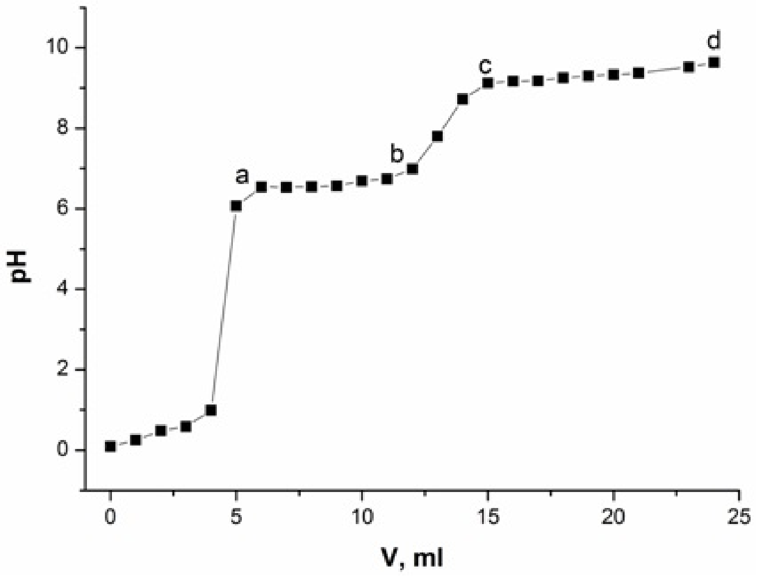

FIG. 1. pH value of the titrated 0.20 M $Y(NO_3)_3$ solution vs. amount of NH_4OH added (ml)

TABLE 1. X-Ray diffraction pattern of $Y_2(OH)_{6-x}(NO_3)_x \cdot nH_2O$ basic nitrate

2Θ, degrees	d, Å	Q_{exp}	I/I_0, a.u.	(hkl)	Q_{calc}	ΔQ
9.63	9.182	118.60	100	(002)	119.95	–1.35
19.53	4.546	483.83	33	(004)	479.81	4.02
20.49	4.335	532.02	13	(113)	529.69	2.33
28.10	3.175	991.79	30	(040)	996.55	–4.75
28.75	3.105	1037.18	60	(220)	1039.18	–2.00
30.24	2.956	1144.71	15	(016)	1141.86	2.85
33.20	2.699	1373.00	9	(231)	1380.59	–7.59
34.62	2.591	1489.18	10	(051)	1587.09	–3.46
35.73	2.513	1583.63	11	(320)	2026.73	3.37
40.65	2.219	2030.10	11	(236)	2430.17	–7.01
44.61	2.031	2423.17	11	(260)	3032.27	–8.46
50.17	1.819	3023.81	19	(139)	3187.12	–13.88
51.48	1.775	3173.24	18	(420)	3409.30	–4.12
53.47	1.714	3405.18	8	(080)	3986.19	–9.24
58.18	1.586	3976.95	8	(440)	4156.71	–3.36

[JCPDS card 32-1435]. These data were indexed in orthorhombic crystal lattice ($a = 17.115(5)$ Å, $b = 12.67(1)$ Å, $c = 18.26(1)$ Å) (Fig. 2, Table 1).

Analysis of the obtained X-ray diffraction patterns confirmed that the precipitates are of a single phase only, but reflections in these patterns have different profiles. Reflections formed by (200) planes are much wider than those formed by (211) planes, perhaps, because of

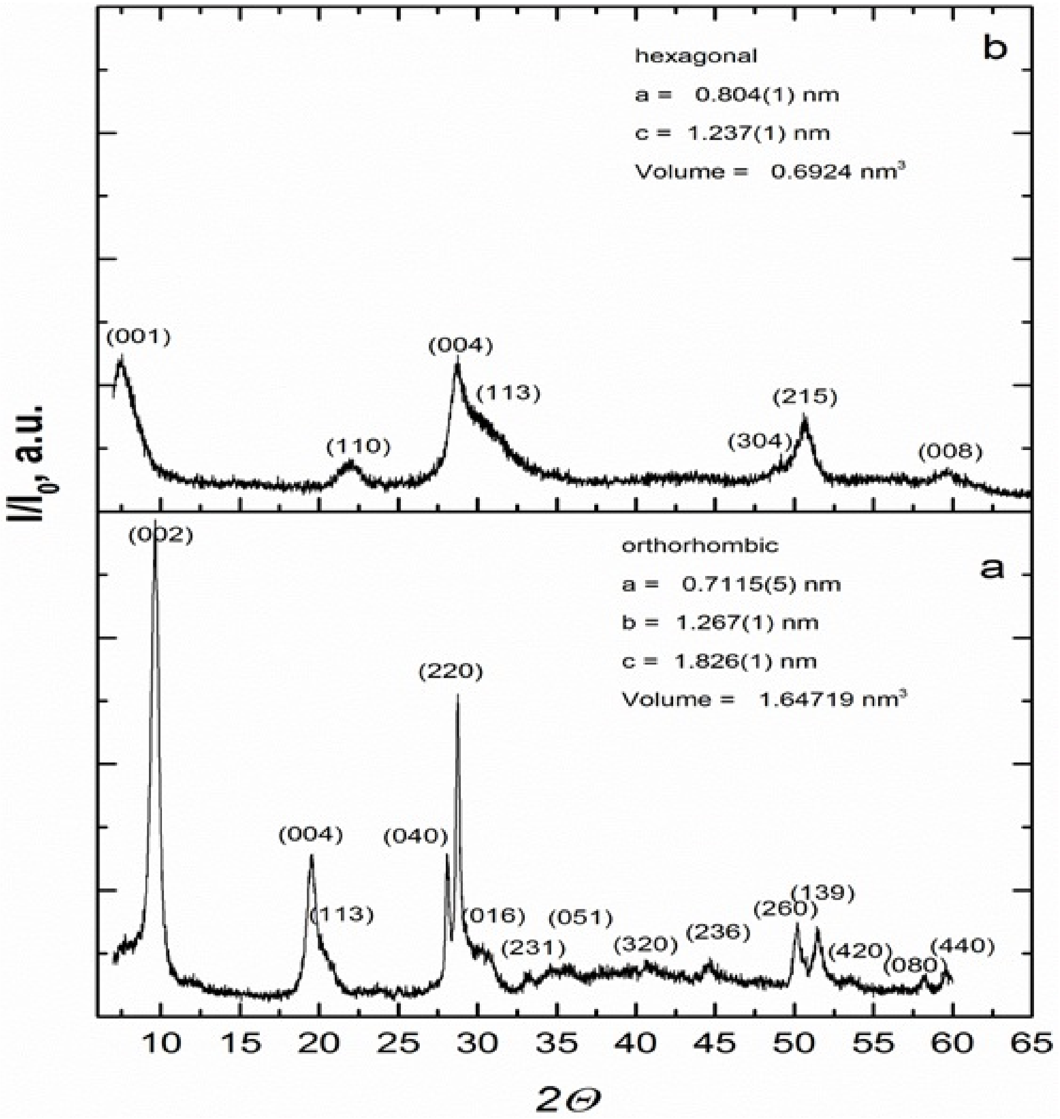

FIG. 2. X-Ray diffraction patterns of $Y_2(OH)_{6-x}(NO_3)_x \cdot nH_2O$ basic nitrate (a) and novel hexagonal Y_2O_3-based phase (b)

anisotropy of the coherent scattering domains. This was confirmed by electron microscopy data (Fig. 3), the particles have planar shape.

3.2. Thermal Decomposition of Basic Yttrium Nitrate with the Formation of Yttria

In order to prepare yttria starting materials which are ready to be used for further ceramics synthesis, the precursor ($Y_2(OH)_{6-x}(NO_3)_x \cdot nH_2O$) is to be thermolyzed to Y_2O_3. Thermolysis of this precursor (precipitated at pH 9.0) yielded the thermogravimetric data shown in Fig. 4.

Thermolysis of $Y_2(OH)_{6-x}(NO_3)_x \cdot nH_2O$ is a multistep process (Fig. 4) that includes five distinguishable endothermic steps which sometimes overlap.

There was no mass loss observed above 600 °C. This is in agreement with data [9].

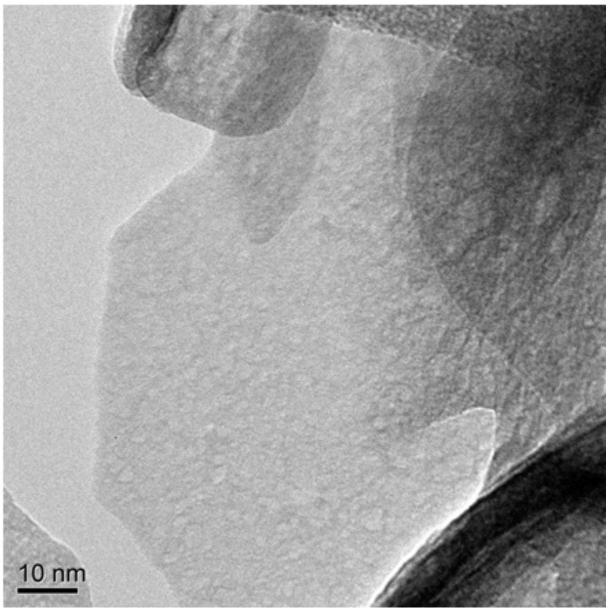

FIG. 3. Electron microscopy image of $Y_2(OH)_{6-x}(NO_3)_x \cdot nH_2O$ basic nitrate precipitate

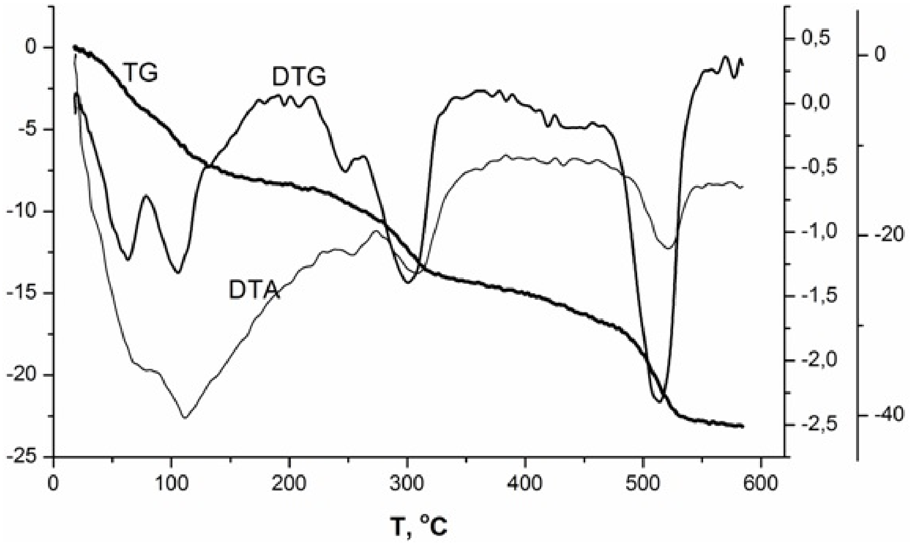

FIG. 4. Thermogravigram of basic yttrium nitrate thermal decomposition

4. Changes in Morphological Properties of Yttria Nanoparticles

4.1. Transformation under Slow Heating

As has already been mentioned, strict control over the microstructure properties of the prepared powders is a must in order to assure the final products will have the proper quality. One widely used means of such control is the thermal treatment of the samples. We used a full-profile X-ray diffraction phase analysis to study the correlation between the sample microstructure and manner of its thermal treatment.

X-Ray diffraction patterns of the samples heated at 2.5 °C/min rate in 20–900 °C interval are presented in Fig. 5 for the samples heated to 500, 600, 700, 800 and 900 °C (please remember that the thermal decomposition of $Y_2(OH)_{6-x}(NO_3)_x{\cdot}nH_2O$ and its conversion to Y_2O_3 should be complete above 500–600 °C (Fig. 4)).

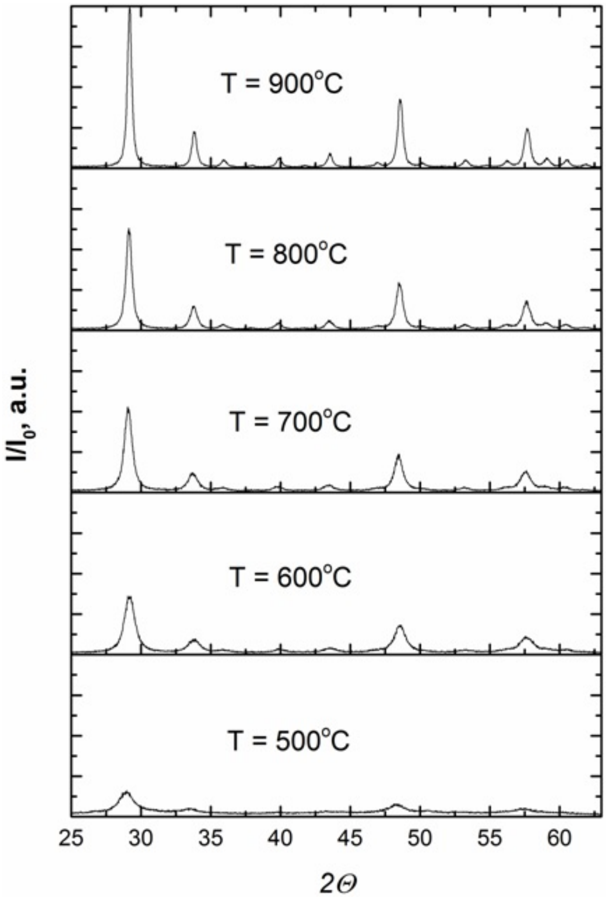

FIG. 5. X-Ray diffraction patterns of yttria samples heated to 500, 600, 700, 800 and 900 °

One can easily notice the changes in the reflection profiles for the X-ray diffraction patterns. The higher the heating temperature, the lower the half-width of the peaks, and the higher the reflection intensity. Correlations between the sizes of the coherent scattering domains and microdeformations as functions of the temperature are presented in Fig. 6. The average size of coherent scattering domains grew linearly, while microdeformations decreased with increasing temperature.

4.2. Isothermal Annealing

A more thorough study of the influence that the heating temperature has on the microstructure changes of yttria nanopowders was performed using isothermal annealing.

With 600 °C annealing (0.5–1.400 min.), the formation of a novel phase similar to $Y_2(OH)_{6-x}(NO_3)_x{\cdot}nH_2O$ basic nitrate was observed. This phase had a simpler X-ray diffraction pattern (Fig. 2b) and can be indexed in the hexagonal system ($a = 8.04(1)$ Å, $c = 12.37(1)$ Å; Table 2). A similar X-ray pattern was observed for the sample of basic yttria nitrate precursor, heated to 500 °C at a rate of 10 °C/min (see Fig. 3d in [9]).

However, for annealing times exceeding 3 minutes, the X-ray diffraction patterns of the thermolysis products contained exclusively reflections of cubic Y_2O_3 phase (Fig. 7). Increasing the annealing times of the latter resulted in an increase in the maximum intensity of the lines

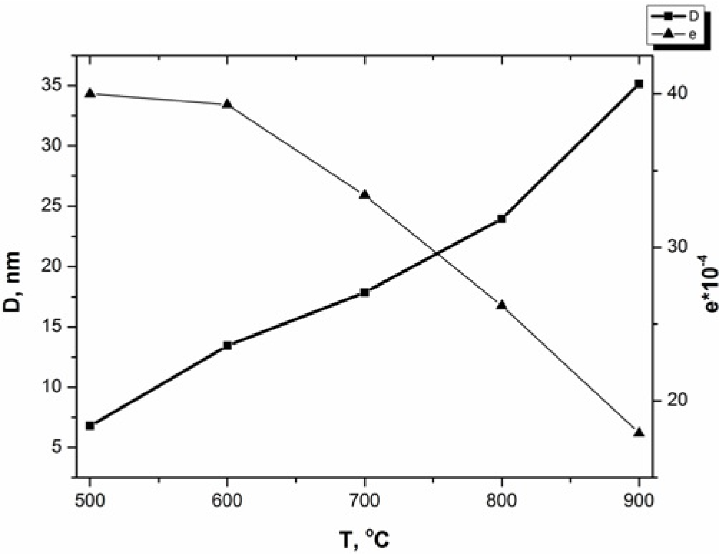

FIG. 6. Correlation between the size of domains of coherent scattering (squares) or microdeformations (triangles) and attained temperature (2.5 °C/min heating rate)

TABLE 2. X-Ray diffraction pattern of the novel Y_2O_3–based phase

2Θ, degrees	d_{exp}, Å	Q_{exp}	I/I_0, a.u.	(hkl)	Q_{calc}	ΔQ
7.49	11.793	71.90	100	(001)	65.46	6.44
21.96	4.044	611.39	30	(110)	618.80	–7.41
28.73	3.105	1037.36	95	(004)	1047.33	–9.97
31.11	2.873	1211.94	50	(113)	1207.92	4.02
49.00	1.858	2898.25	25	(304)	2903.72	–5.47
50.66	1.800	3084.79	55	(215)	3080.31	4.48
59.78	1.546	4185.30	20	(008)	4189.32	–4.02

and a decrease of their half-width (Fig. 7). This means that the sample microstructure changed, with an increase of the crystalline phase content; extension of the annealing time increased the size of the coherent scattering domains (Fig. 8). The average size of these domains changed in a non-linear manner with increased annealing times, doubling in size in the first 5 hours, and then slowing down. (Fig. 8).

Changes in the X-ray diffraction patterns of yttria samples and the corresponding changes in the microstructure parameters are presented in Figs. 9 and 10, respectively. It is worth noting that the sizes of the coherent scattering domains for the samples annealed at 800 °C are more than twice the size of samples heated at 600 °C for the same time. Similarly, samples annealed at 800 °C have three times fewer microdeformations than specimens annealed at 600 °C. These facts unequivocally demonstrate that the microstructure of yttria nanopowders can be controlled by both annealing time and temperature.

5. Conclusions

The present experimental study which examined the precipitation of basic yttrium nitrate from aqueous solutions allowed the optimization of conditions for the preparation of loosely

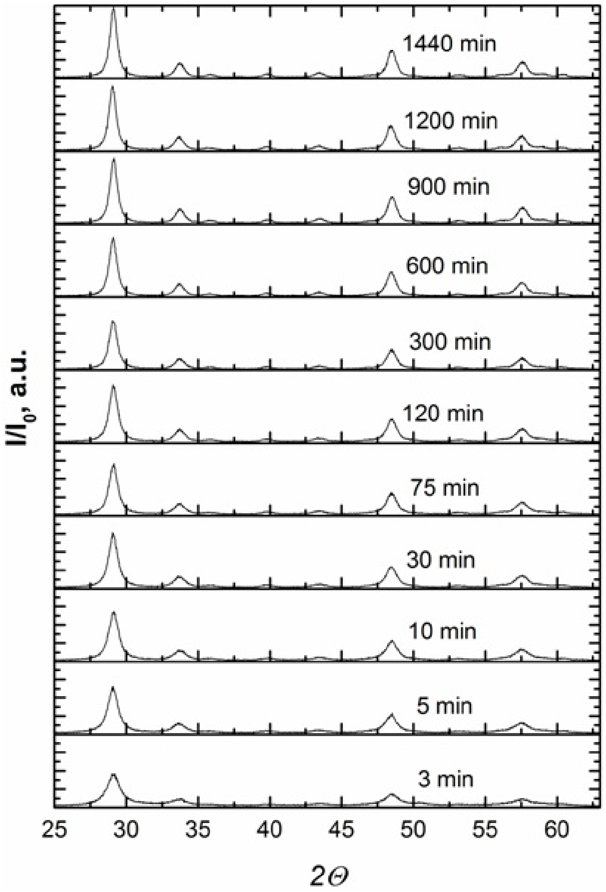

FIG. 7. X-Ray diffraction patterns of Y_2O_3 samples annealed at 600 °C for different times

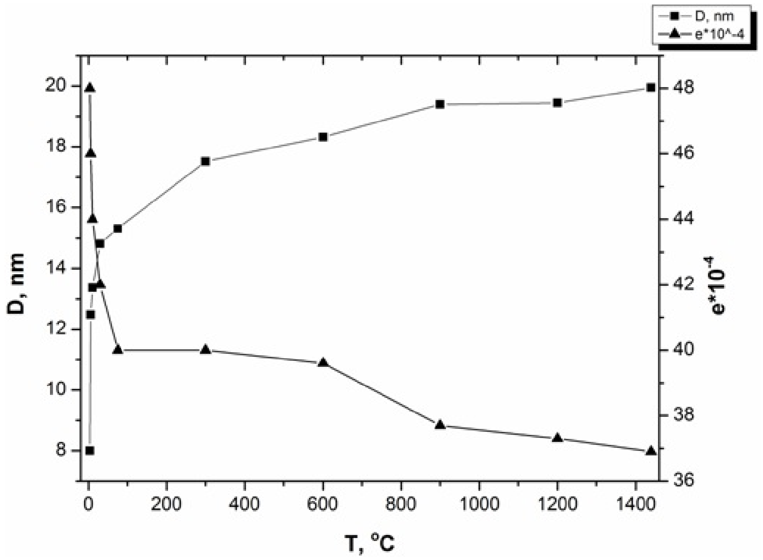

FIG. 8. Changes of microstructure parameters during isothermal annealing at 600 °C (squares — the size of the domains of coherent scattering (nm); triangles — microdeformations)

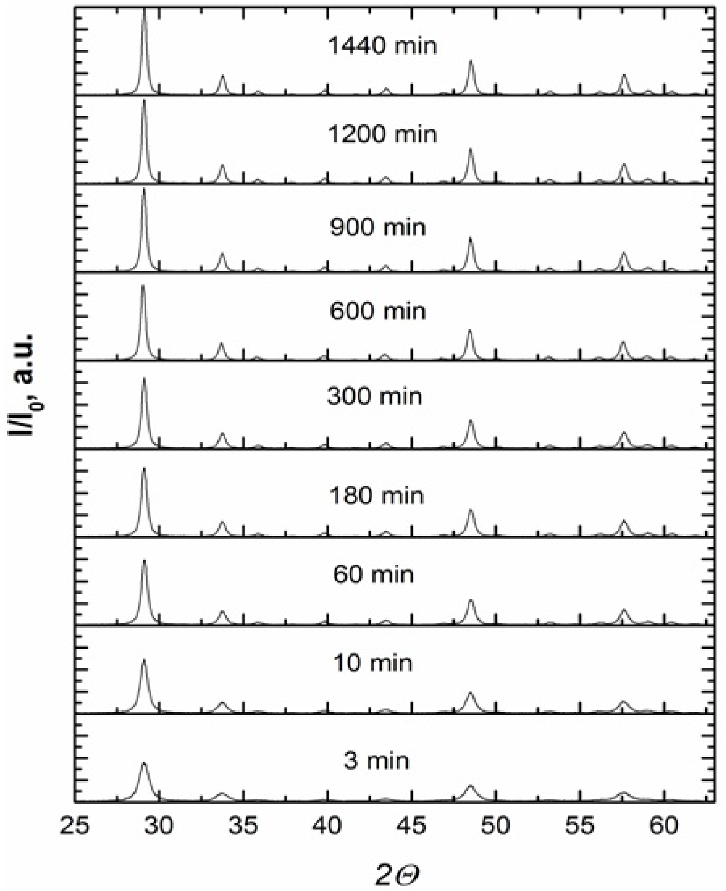

FIG. 9. X-Ray diffraction patterns of Y_2O_3 samples annealed at 800 °C for different time)

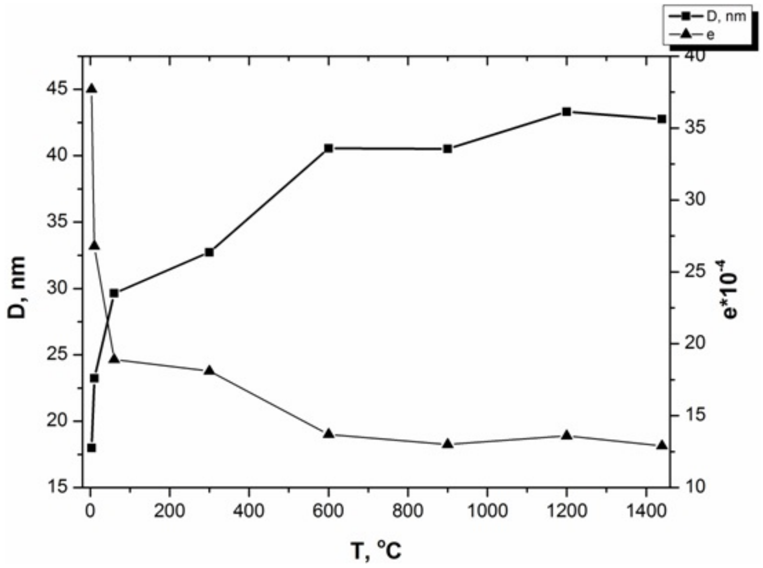

FIG. 10. Changes of the microstructure parameters in the course of isothermal annealing at 800 °C (squares — the size of the domains of coherent scattering (nm); triangles — microdeformations)

aggregated $Y_2(OH)_{6-x}(NO_3)_x \cdot nH_2O$. Thermal decomposition of this compound under controlled annealing permitted the generation of yttria nanoparticles with desirable microstructure, thus making the material widely available for the manufacture of yttria optical ceramics.

References

[1] J. Sanghera, et al. Ceramic laser materials. *Proc. SPIE*, **7912**, P. 79121Q (2011).

[2] V. Lupei, et al. Single crystal and transparent ceramic Nd-doped oxide laser materials: a comparative spectroscopic investigation. *Journal of Alloys and Compounds*, **380**, P. 61–70 (2004).

[3] C. Greskovich, J.P. Chernoch. Polycrystalline ceramic lasers. *J. Appl. Phys.*, **44**, P. 4599–4606 (1973).

[4] T. Ikegami, T. Mori, J. Li, Y. Moriyoshi. Fabrication of transparent yttria ceramics by the low-temperature synthesis of yttrium hydroxide. *J. Amer. Ceram. Soc.*, **85**, P. 1725–1729 (2002).

[5] J. Mouzon. *Synthesis of Yb:Y_2O_3 Nanoparticles and Fabrication of Transparent polycrystalline yttria ceramics*. Lulea University of Technology, Sweden, 126 pp. (2005).

[6] A.E. Baranchikov, V.K. Ivanov, A.V. Dmitriev, et al. Chemical transformations of basic yttrium nitrates during ultrasonic-hydrothermal treatment. *Russian J. Inorg. Chem.*,**51** (11), P. 1689–1695 (2006).

[7] V.K. Ivanov, A.E. Baranchikov, A.S. Vanetsev, et al. Effect of hydrothermal and ultrasonic/hydrothermal treatment on the phase composition and micromorphology of yttrium hydroxocarbonate. *Russian J. Inorg. Chem.*, **52** (9), P. 1321–1327 (2007).

[8] M.A. Uslamina. *Ultradisperse precursors for transparent Y_2O_3:Nd^{3+} ceramics*. Mendeleev Russsian Chemical Technology University, Moscow, 135 pp. (2009). (in Russian).

[9] P.P. Fedorov, V.V. Voronov, et al. Evolution of Yttria nanoparticle ensembles. *Nanotecnologies in Russia*, **5** (9–10), P. 624–634 (2010).

[10] P.P. Fedorov, E.A. Tkachenko, et al. Yttrium Oxide Nanopowders from Carbonate Precursors. *Russian J. Inorg. Chem.*, **55** (6), P. 883–889 (2010).

[11] Yu.I. Pazura, Yu.I. Baumer, et al. Synthesis of Y_2O_3 and Y_2O_3:Nd^{3+} monodisperse crystalline nanospheres by homogenous precipiotation. *Functional Materials*, **17**, P. 107–113 (2010).

[12] M. Ivanov, Y. Kopilov, V. Kravchenko, S. Zayats. Sintering and optical quality of highly transparent Yb doped yttrium lanthanum oxide ceramics. *Physica Status Solidi A*, (2013) (in press).

[13] R.A. Lefever, J. Matsko. Transparent yttrium oxide ceramics. *Mat. Res. Bull.*, **2**, P. 865–869 (1967).

[14] H.S. Roh, Y.C. Kang, H.D. Park, S.B. Park. Eu:Y_2O_3 phosphor particles prepared by spray pyrolysis from a solution containing citric acid and polyethylene glycol. *Appl. Phys. A*, **76**, P. 241–245 (2003).

[15] H.-R. Wenk, S. Matthies, L. Lutterotti. Texture analysis from diffraction spectra. *Mater. Sci. Forum*, **157–162**, P. 473–480 (1994).

[16] M. Ferrari, L. Lutterotti, et al. New opportunities in the texture and stress field by the whole pattern analysis. *Mat. Sci. Forum*, **228–231**, P. 83–88 (1996).

[17] S. Matthies, L. Lutterotti, H.-R. Wenk. Progress in combining Rietveld and QTA Algorithms on Advanced Level. Presented at ICOTOM 11, China, September 1996, P. 146–151 (1996).

[18] M. Ferrari, L. Lutterotti. Method for the simultaneous determination of anisotropic residual stresses and texture by X-ray diffraction. *J. Appl. Phys.*, **76** (11), P. 7246–55 (1994).

[19] L. Lutterotti, P. Scardi. Simultaneous Structure and Size-Strain Refinement by the Rietveld Method. *J. Appl. Cryst.*, **23**, P. 246–252 (1990).

NANOSYSTEMS: PHYSICS, CHEMISTRY, MATHEMATICS, 2013, 4 (2), P. 206–213

SPATIAL-TIME PATTERN OF ELECTRICAL FIELD OF TERAHERTZ PULSE IN THE FAR FIELD

M. S. Kulya[1], Ya. V. Grachev[1], V. G. Bespalov[1], V. P. Kujanpaa[2]
[1]St. Petersburg National Research University of Information Technologies,
Mechanics and Optics, Saint Petersburg, Russia
[2]VTT Technical Research Centre of Finland, Finland
maxk2350@yandex.ru, grachev_y@mail.ru, victorbespaloff@gmail.com, veli.kujanpaa@vtt.fi

The spatial and temporal dependence of the electric field amplitude of a terahertz (THz) pulse of several oscillations in the far field near the focal plane of a parabolic mirror was experimentally obtained. During experimentation a space-time anomaly was discovered in the diffraction patterns. In the wave front of the field the amplitude decreases to zero, and going through this spatial plane, the phase of oscillations changes, while in the integrated intensity, there is a dip in the curve. The results can be applied in pulsed terahertz optics and spectroscopy.

Keywords: THz electric field pulsed THz radiation, diffraction, pulses of a few electromagnetic field oscillation.

1. Introduction

Terahertz (THz) radiation lies in the frequency range 0.1–10 THz, which corresponds to wavelengths between the infrared and millimeter/submillimeter range from 0.03–3 mm. The physics and technology of THz radiation is not new [1], however, the development of femtosecond optics and microelectronics has permitted significant progress in this field. Correspondingly, interest in basic and applied research has increased, and recent monographs have been published [2, 3]. Methods for obtaining and detecting THz radiation were established using femtosecond pulses of light when excited charge carriers of semiconductors and superconductors [2–5], with optical detection in $\chi(2)$ nonlinear media [6], in optical breakdown of gases and radiation of first and second harmonic of a femtosecond laser [7, 8] .

One of the fundamental phenomena of optics is the diffraction of light, but experimental studies of the spatial and temporal structure of ultra short broadband pulses, which have a complex amplitude-phase structure, have not been sufficiently carried out [9–12]. Experimentally, it is difficult to study the diffraction of a few electromagnetic field oscillation pulses for the wavelengths of visible and infrared ranges of the spectrum. This is because there is practically no possibility for the direct detection of the amplitude and phase, and only iterative calculation procedures can be used to recover the original temporal or spatial profile [13].

The experimental study of the diffraction of an ultra short pulse with a complex amplitude-phase structure became possible only with the advent of methods for recording temporal forms of an electric field pulse of broadband THz radiation. The THz wave front usually has only a few oscillations of the electromagnetic field. The wave front also has a complex amplitude-phase structure, which is connected with the process of its generation, further diffraction on the formed aperture, and with the influence of the medium's dispersion [14, 15].

The aim of this work was to obtain the spectral and temporal shape of the electric field of a THz pulse from a few oscillations with a broadband spectrum and of picoseconds duration. The particular feature of this research is the direct detection of the spatial-time form of extremely short pulses, which was difficult in the optics of long pulses, as the photodetectors measure only field intensity. This study may be useful in interpreting the results of measurements in pulsed THz optics and spectroscopy.

2. Experimental Setup

The scheme of experimental arrangement is shown in Fig. 1. A femtosecond laser beam *Yb:KYW* laser *FL-1* (wavelength $\lambda p = 1040$ nm, beam diameter $d = 2$ mm, the pulse width at half-width $\tau \geq 120$ fs, repetition rate of 80 MHz, average power $W = 1.2$ W) with use of a beam splitter *BS* is divided into a probe beam and a pump beam. The pump beam passes through an optical delay line (Delay). It falls on a semiconductor crystal *InAs*, placed in a constant magnetic field M, where THz radiation is generated [5]. The plane of the crystal coincides with the focal plane of a parabolic mirror *PM1* with focal length of 90 mm and an optical aperture of 60 mm. THz radiation is collimated by a parabolic mirror *PM1* behind which there is a teflon filter *F*, transmitting THz radiation and scattering powerful femtosecond laser infra-red radiation. In addition, horizontal polarization is separated by a polarizer *P*. After passing along the optical path in the air $L = 25$ cm, THz radiation is focused by a parabolic second mirror *PM2* on the electro-optical crystal *CdTe*, with an area of 10×10 mm^2 and a thickness of 2 mm. This crystal is most suitable for electro-optic detection of THz radiation due to its dispersion properties [16, 17].

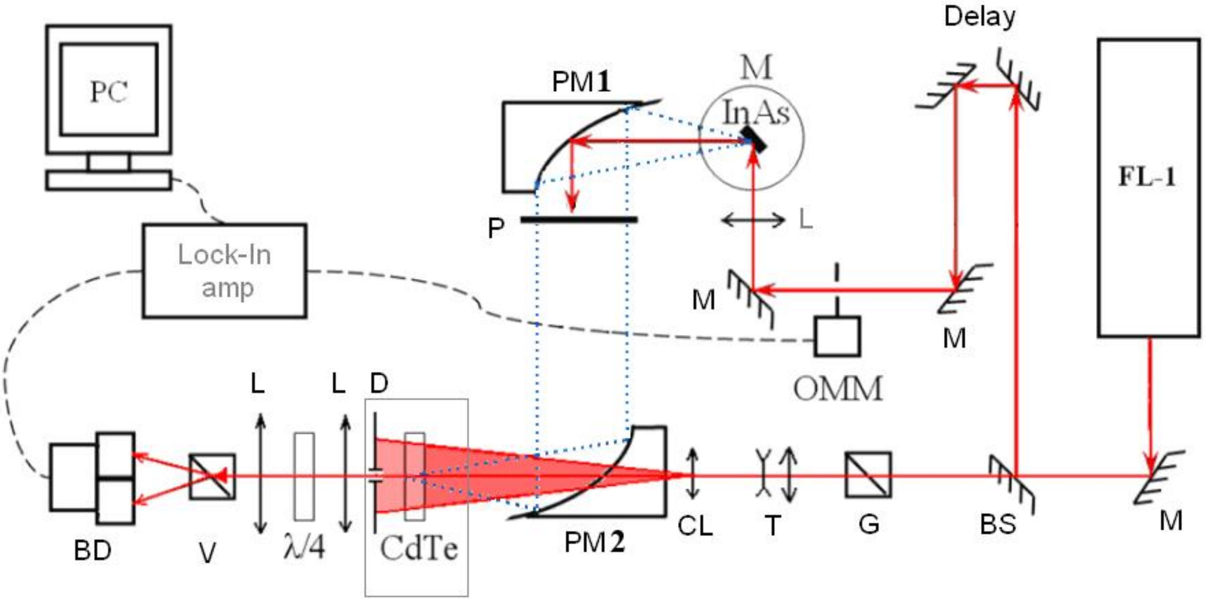

FIG. 1. The experimental scheme: *Yb: KYW* laser *FL-1* ($\lambda = 1040$ nm, $\tau \approx 200$ fs, repetition rate of 80 MHz, $W = 1.2$ W); *BS* —beam splitter; *G* — Glan prism; *M* —magnet; *CL* —cylindrical lens; *T* —telescopic system; *D* — diaphragm; *L* — lens; *PM* —parabolic mirror; *OMM* —optical-mechanical modulator; *P* — Teflon filter; *V* — Wollaston prism; *BD* — balanced detector. Solid lines — femtosecond laser infra-red radiation; dot lines — THz radiation

After the femtosecond laser probe beam passes a Glan prism *G*, its radiation obtains horizontal linear polarization with an accuracy of 10^{-4}. Then, the telescope *T* increases the diameter of the beam to about 5 mm, and the cylindrical lens *CL* focuses the radiation on the central region of the crystal *CdTe*. Thus a rectangular shaped spot of the probe radiation is formed on the crystal, the larger being directed dimension towards the horizontal axis x. When the probe beam propagates through the electro-optical crystal *CdTe*, it is influenced by the constant electric field of collinearly propagating THz pulse, which affects the linear polarization of the probe beam and change it to elliptical polarization. A quarter-wave plate $\lambda/4$ transforms the probe beam polarization to near-circular polarization. The beams with different polarization states are separated by a Wollaston prism *V* and they fall on the balanced detector *BD*. Since the magnitude of the birefringence is directly proportional to the electric field, the intensity difference on the balanced circuit photodiodes is also proportional to the field of THz radiation. The signal from the balanced detector enters the lock-in amplifier, consistent with the optical modulator *OMM* and then the signal goes to an analog-to-digital converter built into the *PC*.

The optical delay line *Delay* changes the crossing time of THz radiation and the probe beam in the crystal. Thus, by measuring the effect of birefringence for various delays, the dependence of the amplitude of the electric field of the terahertz pulse on time $E_{THz}(t)$ can be recorded.

A firmly fixed aperture with a diameter of 1 mm was placed after the crystal *CdTe*, in order to study the spatial and temporal form of the THz pulse, Fig. 2. With movement of the recording system in the horizontal x and vertical y directions the point-to-point detection of the THz field in the focal plane of the cylindrical lens $E_{THz}(x, y, t)$ was provided.

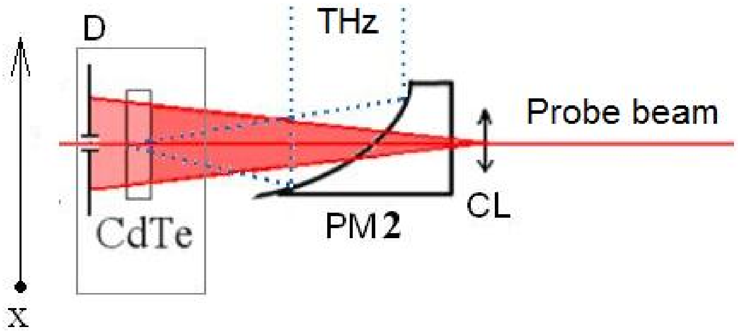

FIG. 2. Scheme of point-to-point measurement of THz field. Solid lines — femtosecond laser infra-red radiation; dot lines — THz radiation

The optical system of two parabolic mirrors (*PM1, PM2*) transfers the image (size d) illuminated by the beam of femtosecond laser on the crystal *InAs* into the plane of the electro-optical crystal *CdTe*. As THz radiation is formed only in the illuminated region [2,3], a far field THz radiation is formed in the focal plane of a parabolic mirror *PM2* (electro-optical detector plane of *CdTe*). The dimensions of the far field THz radiation are defined by the size of the generation region and THz wavelength range. The spectrum covered by the THz generator includes 0.1 – 1.7 THz (wavelengths 3,000–176 μm) [18], with a maximum of intensity at 0.6–0.7 THz ($\lambda \sim 500$ μm $< d$). The maximum size of the diffraction pattern of THz radiation in the plane of the electro-optical detector *CdTe* can be estimated to be equal to d. As the spectrum contains wavelengths larger than d, the size of the area will increase accordingly.

The measurements of the spatial-time pattern of the diffraction were made with different pump beam geometries, illuminating the *InAs* crystal generating the THz radiation. Fig. 3 shows the spatial profiles with different apertures. Fig. 3a describes the pump beam profiles of the femtosecond laser of aperture $d = 2$ mm and Fig. 3b shows a focused laser beam with aperture value $d = 1$ mm. Fig. 3c and d show the rectangular beams created by the introduction of a cylindrical lens in the scheme of the laser beam. It should be noted that by focusing with the cylindrical lens, the generated area on the x-coordinate is a sub-wavelength for THz radiation, which affects the distribution of the far field.

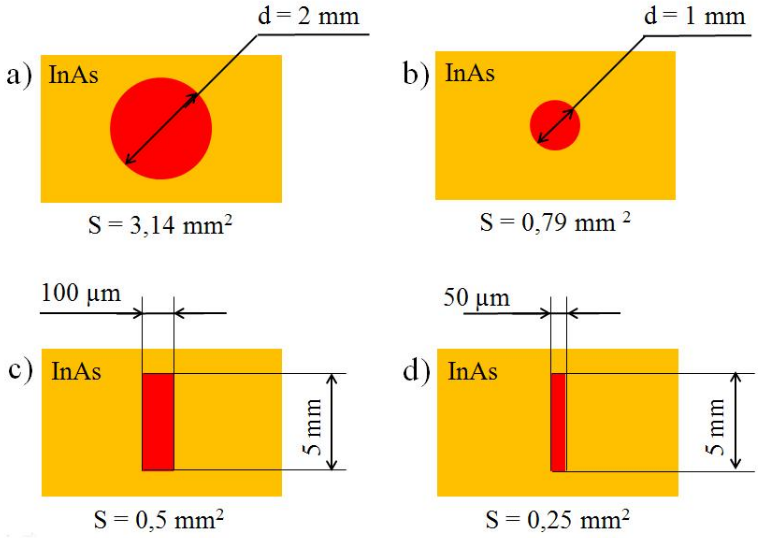

FIG. 3. Spatial profile of the pump beam incident on the crystal *InAs* generating THz radiation: a femtosecond laser source aperture $d = 2$ mm (a), a focused laser beam diameter of 1 mm (b), beams of quasi-rectangular forms created by the introduction of a cylindrical lens in the scheme of the laser beam (c, d)

3. Experimental Results

By moving the mobile measurement system, Fig. 2, the point where the value of the THz field was in its maximum $\max[E_{THz}(x, y, t)]$ was found. The vertical coordinates of the given maximum point was taken as $y = 0$. The zero horizontal coordinates as $x = 0$ when the system was put into the edge position. Fig. 4 and Fig. 5 show the time dependence of the THz electric field E_{THz} $(x = 1$ cm, $y = 0, t)$ and $E_{THz}(x = 2$ cm, $y = 0, t)$, respectively. Fig. 6 depicts a two-dimensional spatial-time picture of the distribution of the amplitudes of THz field E_{THz} $(x, y = 0, t)$ using the spatial profile of the pump beam incident on the generating *InAs* crystal with $d = 2$ mm (Fig. 3a).

From Fig. 6, it can be seen that the wave front of THz radiation has a spatial-time anomaly. In the time plane E_{THz} $(x = 1.7$ cm, $y = 0, t)$ there is a reduction of the field amplitude to zero. In addition, there is a transition point where the phase of the oscillation changes. For visual demonstration, Fig. 7 shows the normalized integrated intensity of THz radiation pattern of the coordinate x:

$$I_{THz}(x, y = 0) = \int |E_{THz}(x, y = 0, t)|^2 \, dt. \tag{1}$$

A similar spatial-temporal anomaly was observed in the case of the excitation by focused laser beam with diameter value of $d = 1$ mm (Fig. 8 on the right), and a beam of quasi-rectangular form (Fig. 8 on the left).

It should be noted that when decreasing the size of the excitation spot of THz radiation the wave front curvature is increased, and the area of maximum intensity of the THz field in the x axis decreases. When comparing the measured energy in a variety of fields of spots illuminating the crystal *InAs* it was found that the highest values of the electric field for THz radiation were achieved by focusing of the pump beam into a circular aperture with a diameter of 1 mm, which corresponds approximately to the maximum power density of the femtosecond

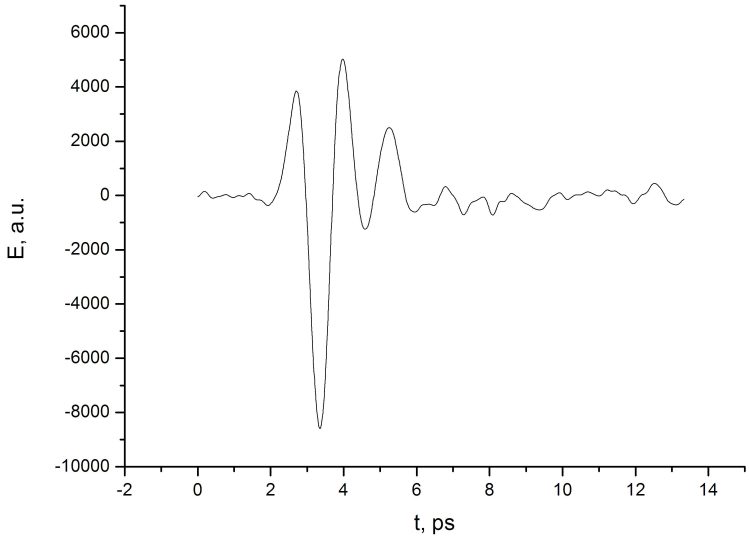

FIG. 4. Temporary form of the THz field in the focal plane of the spatial point E_{THz} $(x = 1$ cm, $y = 0, t)$

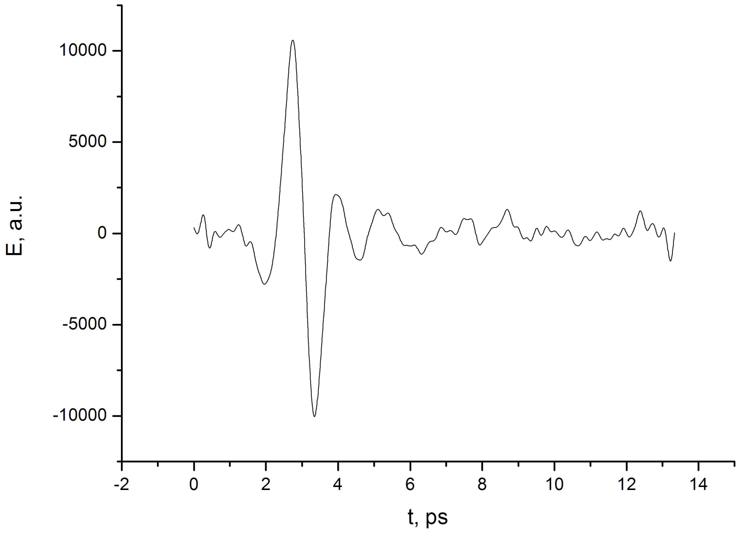

FIG. 5. Temporary form of the THz field in the focal plane of the spatial point E_{THz} $(x = 2$ cm, $y = 0, t)$

radiation. Thus, it is also the maximum efficiency of the energy transform from IR to the THz [2,3].

The presence of the spatial-time anomaly in the diffraction pattern can be explained by the appearance of the phase shift larger than $\pi/2$ in the plane of the beam of THz radiation, which leads to an intensity dip in the far field [19]. A spatial phase shift can be caused by localized heating of the Teflon filter (*P* in Fig. 1), due to the powerful absorption of high intensity femtosecond laser beam. Additional studies are needed for explanation of this phenomenon.

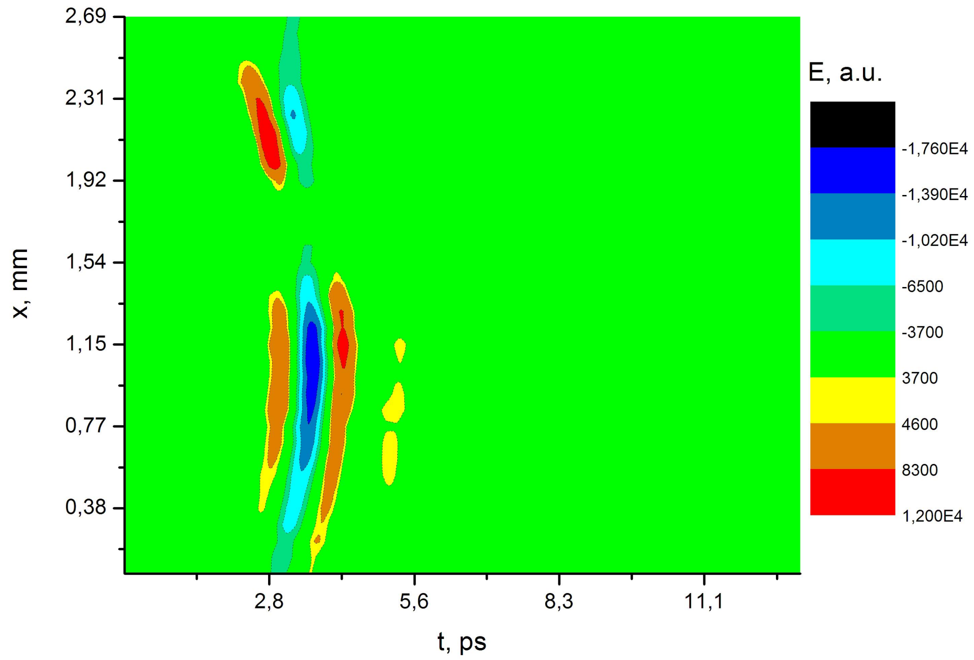

FIG. 6. Spatial-time picture of the amplitude distribution of THz field E_{THz} $(x, y = 0, t)$

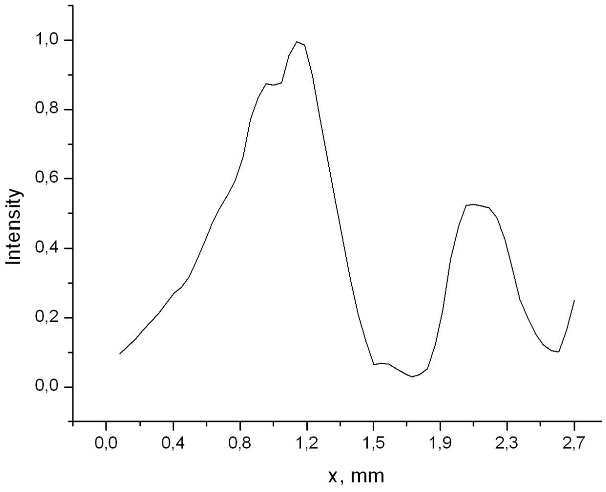

FIG. 7. Integrated picture of the intensity of THz radiation to the coordinate x I_{THz} $(x, y = 0)$

4. Conclusion

The scheme was proposed for an experimental setup, which was then assembled for measurements of the spatial and temporal patterns of the electric field amplitudes of THz radiation near a parabolic mirror focal plane. In these experiments different pump beam geometries of a femtosecond laser were used. Experimentally a spatial-time anomaly was observed in the diffraction patterns. In the wave front of the field the amplitude decreased to zero, and after going through this spatial plane, the phase of the oscillations changed. On the other hand, there was a dip in the integrated intensity curve. A spherical wave front in the observed diffraction patterns was observed, and by reducing the diameter of the excitation spot, the curvature of

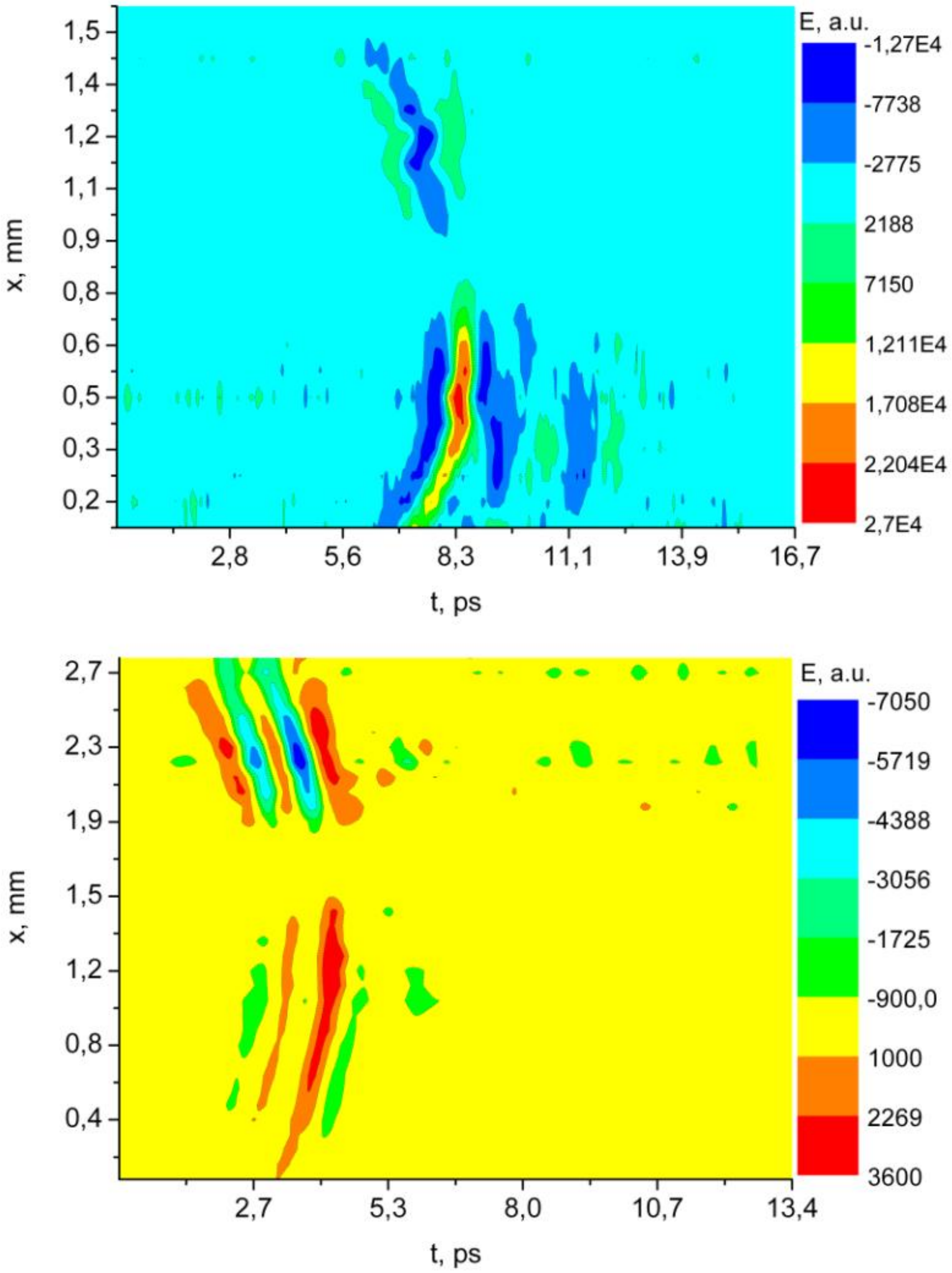

FIG. 8. Spatial-time picture of the amplitude distribution of THz field E_{THz} $(x, y = 0, t)$ in the case of the excitation laser focused beam with diameter $d = 1$ mm (right), and a beam of quasi-rectangular form 5×0.1 mm (left)

the THz wave front increased. So, the experiments show that the spatial non-uniformity of the THz field must be taken into consideration for correct spectroscopic measurements. It is also important to scan the THz pulse through the central peak of the diffraction pattern and the center of the sphere of the wave front, otherwise, the shape of the measured pulse will undergo a temporary distortion and the corresponding spectrum will be changed.

Acknowledgments

This work was supported by grant from the Ministry of Education and Science of the Russian Federation (projects No. 14.512.11.0020).

References

[1] A. Glagolewa-Arkadiewa. Short electromagnetic waves of wave-length up to 82 microns. *Nature*, **113** (2844), P. 640 (1924).

[2] X.C. Zhang, J. Xu. *Introduction to THz wave photonics*. NY., Springer, 246 pp. (2009).

[3] Y.-S. Lee. *Principles of terahertz science and technology*. Springer Science+Business Media, LLC, XII, 340 pp. (2009).

[4] B.B. Hu, X.C. Zhang, D.H. Auston. Terahertz Radiation Induced by Subbandgap Femtosecond Optical Excitation of gas. *Phys. Rev. Lett.*, **67**, P. 2709 (1991).

[5] V.G. Bespalov, V.N. Krylov, S.E. Putilin, D.I. Stasel'ko. Lasing in the far IR spectral range under femtosecond optical excitation of the inas semiconductor in a magnetic field. *Optics and Spectroscopy*, **93** (1), P. 148–152 (2002).

[6] Q. Wu, X.C. Zhang. Free-space electro-optic sampling of terahertz beams. *Appl. Phys. Lett.*, **67**, P. 3523 (1995).

[7] D.J. Cook, R.M. Hochstrasser. Intense terahertz pulses by four-wave rectification in air. *Optics Letters*, **25** (16), P. 1210–1212 (2000).

[8] V.G. Bespalov. Superbroad-band pulsed radiation in the terahertz region of the spectrum: production and application. *Journal of Optical Technology*, **73** (11), P. 764-771 (2006).

[9] N.N. Rozanov. On the diffraction of ultrashort pulses. *Optics and Spectroscopy*, **95** (2), P. 299–302 (2003).

[10] L. Sereda, A. Ferrari, M. Bertolotti. Spectral and time evolution in diffraction from a slit of polychromatic and nonstationary plane waves. *J. Opt. Soc. Am. B*, **13**, P. 1394–1402 (1996).

[11] X. Jingzhou, W. Li, Y. Guozhen. Effects of spectral linewidth of ultrashort pulses on the spatiotemporal distribution of diffraction fields. *Chinese Science Bulletin*, **46** (11), P. 901 (2001).

[12] A.A. Ezerskaya, D.V. Ivanov, V.G. Bespalov, S.A. Kozlov. Diffraction of single-period terahertz electromagnetic waves. *Journal of Optical Technology*, **78** (8), P. 551–557 (2011).

[13] C. Iaconis, I.A. Walmsley. Spectral phase Interferometry for direct electric-field reconstruction of ultrashort optical pulses. *Optics Letters*, **23**, P. 792–794 (1998).

[14] B.B. Hu, X.C. Zhang, D.H. Auston. Terahertz Radiation Induced by Subbandgap Femtosecond Optical Excitation of gaas. *Phys. Rev. Lett.*, **67**, P. 2709 (1991).

[15] N. Llombart, A. Neto. Thz Time-Domain Sensing: The Antenna Dispersion Problem and a Possible Solution. *Terahertz Science and Technology*, **2** (4), P. 416–423 (2012).

[16] D.T.F. Marple, H. Ehrenreich. Dielectric Constant Behavior Near Band Edges in CdTe and Ge. *Phys. Rev. Lett.*, **8**, P. 87–89 (1962).

[17] E.D. Palik, et al. *Handbook of Optical Constants of Solids*. Elsevier, 3227 pp. (1998).

[18] M.S. Kulya, Ya.V. Grachev, V.G. Bespalov. Obtaining topograms with use of pulsed terahertz reflectometr. *Nanosystems: Physics, Chemistry, Mathematics*, **3** (5), P. 33–41 (2012).

[19] J.W. Goodman. I*ntroduction To Fourier Optics*. McGraw-Hill, 441 pp. (1996).

NANOSYSTEMS: PHYSICS, CHEMISTRY, MATHEMATICS, 2013, 4 (2), P. 214–217

CRYSTALLIZATION PROCESS IN OXYFLUORIDE NANO-GLASS-CERAMICS DOPED WITH NEODYMIUM IONS

R. K. Nuryev, A. O. Trofimov, A. Y. Bibik, V. A. Aseev, E. V. Kolobkova, N. V. Nikonorov

Saint Petersburg National Research University of Information Technologies,
Mechanics and Optics, Saint Petersburg, Russia

Nuryev@oi.ifmo.ru, Aseev@oi.ifmo.ru

PACS 42.70.-a, 61.05.cf, 61.05.cp

Oxyfluoride nano-glass-ceramics doped with neodymium ions have been developed and synthesized. The precipitation of crystalline phase in neodymium nano-glass-ceramics after heat treatment has been experimentally investigated. The neodymium ions are incorporated into the nanosize crystalline phase of $PbY_{(1-x)}Nd_{(x)}OF_3$.

Keywords: x-ray diffraction, crystalline phase, glassceramics.

1. Introduction

Transparent nano-glass-ceramics doped with rare earth ions (Er, Eu, Tm, Nd, and Pr) are of the great interest for photonics. They occupy an intermediate state between glasses and crystals. The thermal and mechanical properties of glass-ceramics are superior to those of the parent glass while having spectral and luminescence characteristics that are similar to crystal analogues [1,2]. Rare-earth ions (REI) in a fluoride environment have lower phonon energies, especially in the case of heavy metal fluoride glasses (HMFG). REI in this type of oxygen-free environment have a lower probability of non-radiative excitation relaxation, thus leading to an increase in the luminescence quantum yield in comparison with the case of the oxygen environment [3]. Therefore the transparent fluorine-containing nano-glass-ceramics doped with rare-earth ions are promising media for up-conversion lasers and broadband optical amplifiers.

2. Results and Discussion

Included in this report are studies of the precipitation of crystalline phases in oxyfluoride nano-glass-ceramics and a survey of their spectral and luminescence properties.

2.1. Sample Preparation

Samples of parent glasses were prepared with the following composition: $30SiO_2$–$15AlO_{3/2}$–$29CdF_2$–$18PbF_2$–$5ZnF_2$–$x NdF_3$–$(3-x)YF_3$, where x varied from 0 to 3.0 mol%. The parent glass was synthesized in an alumina cup at 1050 °C under an argon atmosphere. Tg was determined using simultaneous thermal analysis (Netzsch STA 449). To obtain transparent nano-glass-ceramics the glass samples were heated in an electric muffle furnace at 500 °C for 120 minutes. Experimental diffraction patterns were obtained using the wavelength of CuKα = 1.5418 Å(X-ray diffractometer Rigaku Ultima IV).

2.2. X-ray and Spectroscopic Investigations

The heat treatment resulted in the precipitation of crystalline phase in the glass matrix. X-ray diffraction (XRD) and simultaneous thermal analysis (DSC) observation of nano-glass-ceramics doped with 3 mol% yttrium revealed the precipitation of $PbYOF_3$ crystallites [4]. The volume crystallization was accomplished after 120 minutes of thermal treatment. The size of the crystals was determined by Sherrer's equation:

$$l = \frac{K^* \lambda}{\beta^* \cos\theta}.$$

The precipitated crystals were approximately 20 nm in size. The lattice constant was equal to 5.74 Å.

The introduction of neodymium ions qualitatively changes the character of glass crystallization. The XRD analysis of nano-glass-ceramics doped with NdF3 in concentration from 0.1 to 2.9 mol% revealed that the crystalline phase was of the composition $PbYOF_3$ (fig. 1). Thus, the secondary heat treatment of the parent glass resulted in the growth of a crystalline phase of the same chemical composition, which was independent from the dopant concentration.

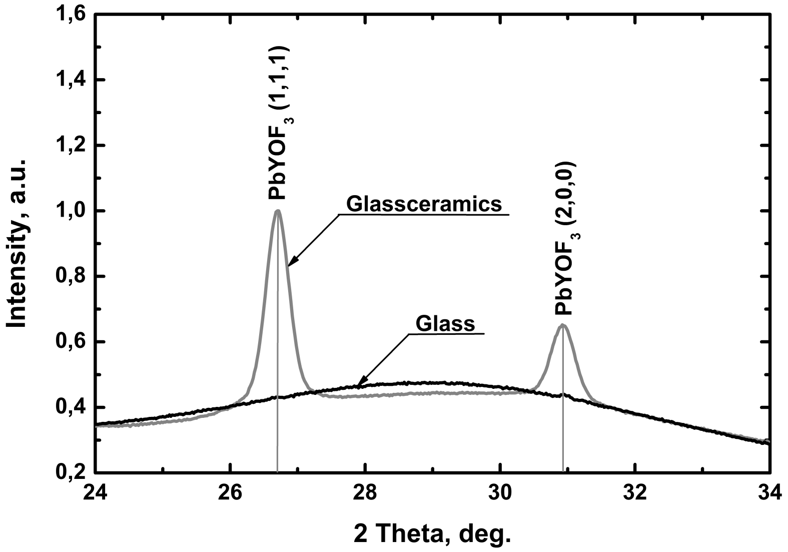

FIG. 1. X-ray diffraction patterns of virgin glass and glassceramics doped NdF_3 of 0.5 mol% after thermal treatment for 120 minutes

The increasing the heating time did not lead to a meaningful increase in the nanocrystalline phase size. These small sizes appreciably reduced the level of light scattering in heterogeneous nano-glass-ceramics. The high transmittance of nano-glass-ceramics and its homogeneity make it a good candidate for use in optical applications.

Nano-glass-ceramics doped with 3 mol% NdF_3 revealed the precipitation of ca. 25 nm NdF_3 crystallites (fig. 2). Increasing the neodymium concentration resulted in an increase of the lattice constant from 5.74 up to 5.84 Å(fig. 3).

The lattice constant depended on the concentration of neodymium ions because of the yttrium and neodymium ratio in the crystalline phase. Two different linear parts of the lattice constant dependence are explained by the precipitation ratio of $PbY_{(1-x)}Nd_{(x)}OF_3$ and $PbYOF_3$ crystalline phases.

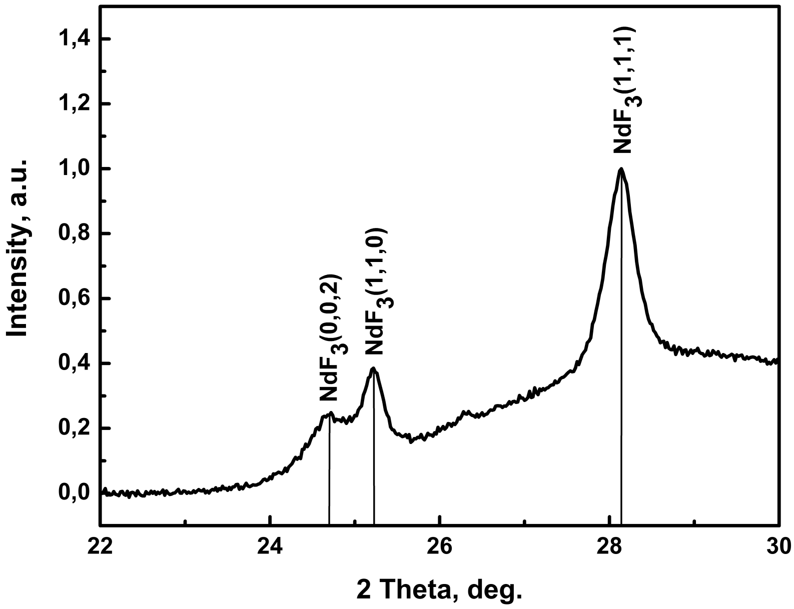

FIG. 2. X-ray diffraction patterns of virgin glass and glass-ceramics doped with 3 mol% NdF_3 after 120 mins thermal treatment

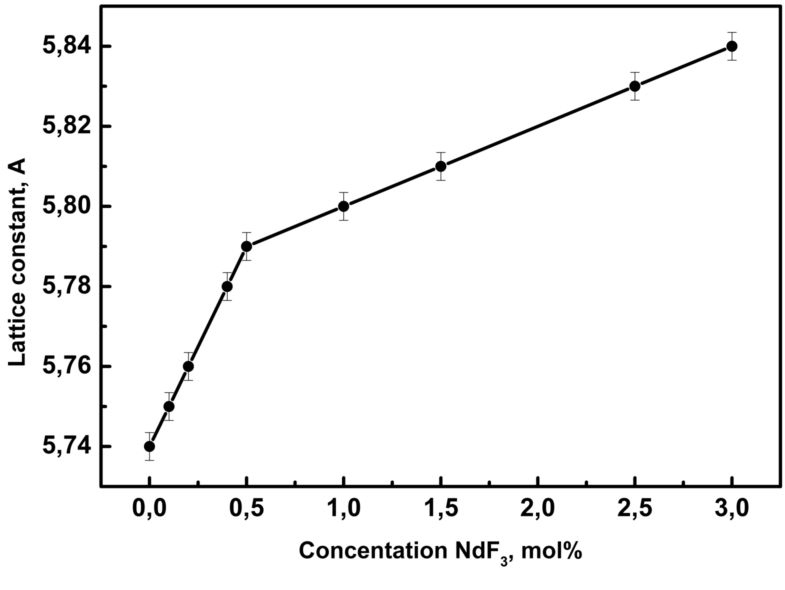

FIG. 3. Relationship between lattice constant and neodymium ions concentration

Thermal treatment results in the appearance of the fine Stark structure in luminescence spectra (fig. 4). The combination of spectral and fluorescent measurements with the XRD and DSC analysis allowed us to conclude that neodymium ions are incorporated into the crystalline phase of $PbY_{(1-x)}Nd_{(x)}OF_3$.

3. Conclusion

The oxyfluoride nano-glass-ceramics doped with neodymium ions have been developed and synthesized. The precipitation of crystalline phases of $PbY_{(1-x)}Nd_{(x)}OF_3$ and $PbYOF_3$ in

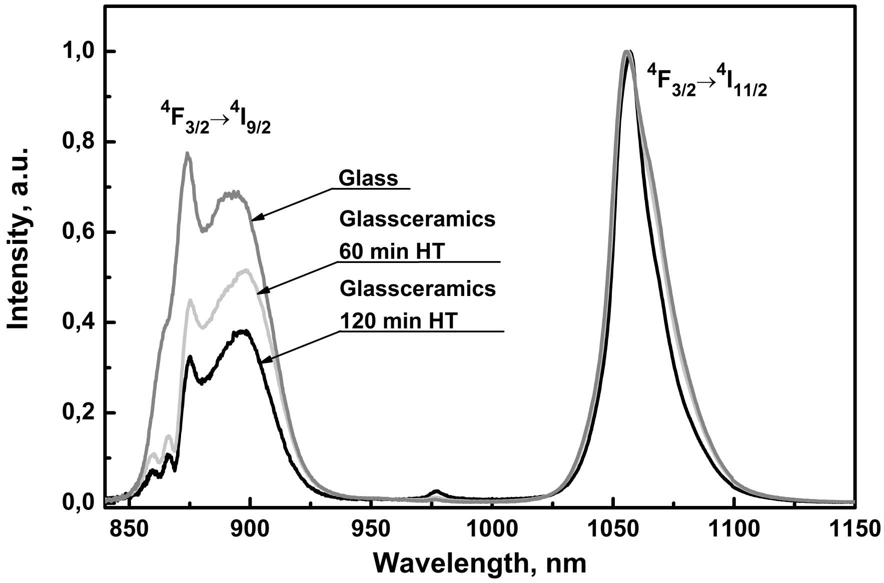

FIG. 4. Luminescence spectra of parent glass and glassceramics after heat treatment

the glass host after heat treatment has been experimentally investigated. The neodymium ions are incorporated into the nanosize crystalline phase of $\mathrm{PbY}_{(1-x)}\mathrm{Nd}_{(x)}\mathrm{OF}_3$. The size of crystalline phase achieves to 30 nm. The lattice constants of nanocrystals were shown to be dependent upon the concentration of neodymium ions.

Acknowledgments

The given research was conducted with the support of the Federal Target Program of "Scientific and pedagogical staff of innovation Russia" for 2009–2013 (contract of Ministry of Education and Science of Russian Federation No. 14.132.21.1751) as well as the Federal Target Program of "Research and engineering in the line of priority directions of development of scientific and technological complex of Russia for 2007–2013" contract of Ministry of Education and Science of Russian Federation No. 14.513.11.0019).

References

[1] F. Lahoz, I.R. Martin, U.R. Rodriguez-Mendoza, I. Iparraguirre. Rare earths in nanocrystalline glass–ceramics. *Optical Materials*, **27**, P. 1762–1770 (2005).

[2] C. Daqin, W. Yuansheng, Y. Yunlong, H. Zhongjian. Crystallization and fluorescence properties of Nd^{3+}-doped transparent oxyfluoride glass ceramics. *Materials Science and Engineering B*, **123**, P. 1–6 (2005).

[3] V.A. Aseev, V.V. Golubkov, E.V. Kolobkova, N. V. Nikonorov. Lead lanthanide oxyfluorides in a glasslike matrix. *Glass Physics and Chemistry*, **38** (2), P. 212–217 (2012).

[4] V.A. Aseev, P.A. Burdaev, E.V. Kolobkova, N.V. Nikonorov. Fluorophosphate glasses activated by rare-earth ions and AgBr. *Glass Physics and Chemistry*, **38** (4), P. 366–372 (2012).

NANOSYSTEMS: PHYSICS, CHEMISTRY, MATHEMATICS, 2013, 4 (2), P. 218–224

EFFECT OF HIGH ENERGY ELECTRON BEAM IRRADIATION ON THE OPTICAL PROPERTIES OF NANOCRYSTALLINE TiO_2

K. P. Priyanka[1], Sunny Joseph[1], AnuTresa Sunny[2], Thomas Varghese[1]*

[1]Nanoscience Research Centre (NSRC), Dept. of Physics, Nirmala College,
Muvattupuzha - 686 661, Kerala, India
[2]School of Chemical Sciences, Mahatma Gandhi University,
Kottayam - 686 560, Kerala, India

*nanoncm@gmail.com

The effect of high energy electron beam irradiation on the optical properties of TiO_2 nanoparticles was studied in order to improve the optical absorption performance and photo-activity. Electron beam irradiation may have resulted in size reduction, which in turn caused an increase of the optical band gap and photoluminescence intensity. Irradiation at a suitable dose rate was found to enhance the optical absorption performance and photo-activity of the tested TiO_2 nanoparticles.

Keywords: TiO_2, electron beam irradiation, optical properties, photoluminescence.

1. Introduction

Nanocrystalline TiO_2 is a well-known semiconductor with photocatalytic activities, having great potential as photoelectric converters with applications in solar cells, environmental purification and for the generation of hydrogen gas. TiO_2 exists in three polymorphic phases: rutile (tetragonal, density = 4.25 g/cm^3), anatase (tetragonal, 3.894 g/cm^3) and brookite (orthorhombic, 4.12 g/cm^3). The low-density solid phases are less stable and undergo transition to rutile in the solid state. The transformation is accelerated by thermal treatment and occurs at temperatures between 450–1200 °C. This transformation is dependent on several parameters, such as initial particle size, initial phase, dopant concentration, reaction atmosphere and annealing temperature [1–5].

The absorption spectrum of a semiconductor defines its possible uses. The useful semiconductors for photocatalysis have a band gap comparable to the energy of the photons of visible light, having a value of $Eg < 3.0$ eV. Eg value ranges from 2.86 to 3.34 eV have been reported in the literature for the anatase phase. Thus, TiO_2 would prove to be the most efficient if it would exhibits the unique ability to absorb visible light significantly. Unfortunately, however, TiO_2 is a poor visible light absorber, requiring a large band gap energy (3.2 eV) for the excitation of electrons from the filled valence band to the vacant conduction band. In order to enhance the photo-response and the photo-activity of TiO_2, a variety of approaches have been employed: e.g. (i) doping with transition metals or nonmetals into TiO_2, (ii) reducing TiO_2 using hydrogen plasma, (iii) adsorbing metal complexes] or organic dyes onto the surfaces of TiO_2 [6–9] and (iv) high energy electron beam irradiation of TiO_2 nanoparticles [10].

The sol-gel method [11] is one of the most suitable routes to synthesize various metal oxides due to low cost, ease of fabrication and low reaction temperatures. This method is widely used to fabricate TiO_2 for films, particles or monoliths. The optimum fabrication conditions are provided for the narrow size distribution of the nanocrystalline TiO_2. In this work, the sol-gel synthesis route has been employed for the preparation of TiO_2 nanoparticles.

The prepared TiO_2 nanoparticles were characterized by x-ray diffraction (XRD), transmission electron microscopy (TEM), UV-Visible and photoluminescence (PL) spectroscopy. In addition, the optical properties of the synthesized nanocrystalline TiO_2 samples and the electron beam irradiated samples were evaluated in context of the band gap.

2. Materials and Methods

Titanium (IV)-n-butoxide ($Ti(OBu)_4$) (98%, Alfa Aesar), isopropyl alcohol (99%, Fisher Scientific) and HNO_3 (Merck) were used without further purification for the synthesis of nanocrystalline TiO_2. Distilled water was used in all synthesis procedures .

The scheme for preparing the nanocrystalline TiO_2 used in this work has been presented schematically as shown in fig. 1. The precursor solution was a mixture of 5 ml titanium (IV)-n-butoxide ($Ti(OBu)_4$) and 10 ml isopropyl alcohol. This solution was then added dropwise to a pH 2 solution of HNO_3. The hydrolysis was performed at room temperature while stirring for 3 hours. After complete consumption of $Ti(OBu)_4$, the solution was refluxed at 70 °C for 20 hours and a sol was formed. Finally, the formed sol was dried at 60 °C for 36 hours to obtain TiO_2 powders. The obtained powder samples were calcined for 3 hours in a furnace at 300–800 °C in an aerobic atmosphere.

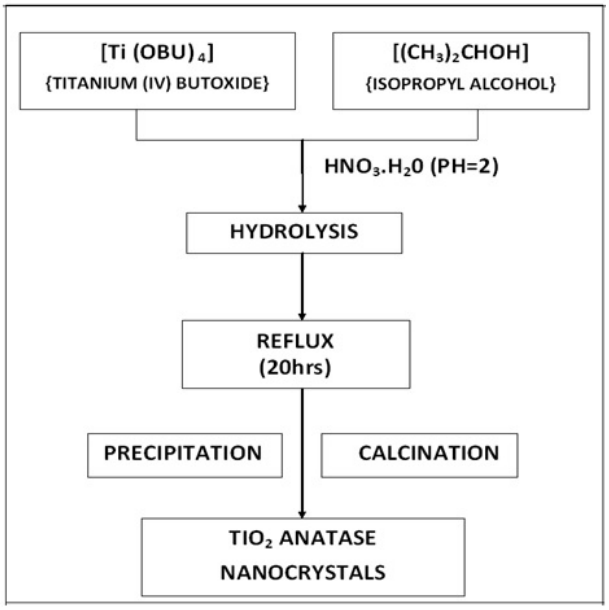

FIG. 1. The scheme of preparation of nanotitania by sol-gel method

The 800 °C calcined TiO_2 nanoparticles were irradiated with an 8 MeV electron beam obtained from a variable energy Microtron, (Department of Physics, Mangalore University, Mangalagangotri, Karnataka State). The rutile samples of TiO_2 nanoparticles were irradiated at a dose rate of 0.5, 1.5, 2.5 and 3.5 kGy, and characterized by UV-Visible absorption spectroscopy and PL spectroscopy. It is of interest to note that the samples with 2.5 and 3.5 kGy dose rates had significant modifications on both their UV and PL spectra.

The structural characteristics of the synthesized titania nanoparticles were also studied by X-ray powder diffraction using a Bruker D8 Advance X-ray diffractometer ($\lambda = 1.5406$ Å) with Cu-Kα radiation in 2θ range from 20 ° to 70 °. From the X-ray diffraction analysis all the peaks of pure TiO_2, were well matchedwith the X-ray pattern of JCPDS Card No. 21-1272. These analyses were performed to determine both the crystal phase and the average crystallite size.

The latter value was estimated from the Debye–Scherrer equation [11]. The Debye–Scherrer equation is given by

$$t = 0.9\lambda/\beta\cos\theta, \tag{1}$$

where λ is the X-ray wavelength, β is the full width at half maximum (FWHM) of the peak and θ is the Bragg's angle.

Transmission electron microscopy is a unique tool to get a direct image of the nanoparticles, revealing the distribution in the nanocrystal and on its surface. High magnification imaging with lattice contrast allows the determination of individual crystal morphology. For TEM studies, the TiO_2 powder was dispersed in ethanol using an ultrasonic bath. A drop of the suspension was placed on a copper grid coated with carbon film. After drying, the copper grid containing the nanoparticles was placed on a holder for the imaging process. TEM photographs of the prepared nanocrystalline rutile TiO_2 powder samples were taken using a Tecnai 30 G2 S-twin (model), FEI make 300 KV High Resolution Transmission Electron Microscope (HRTEM). The TEM images in fig. 2 provide good reviews of the sample surface.

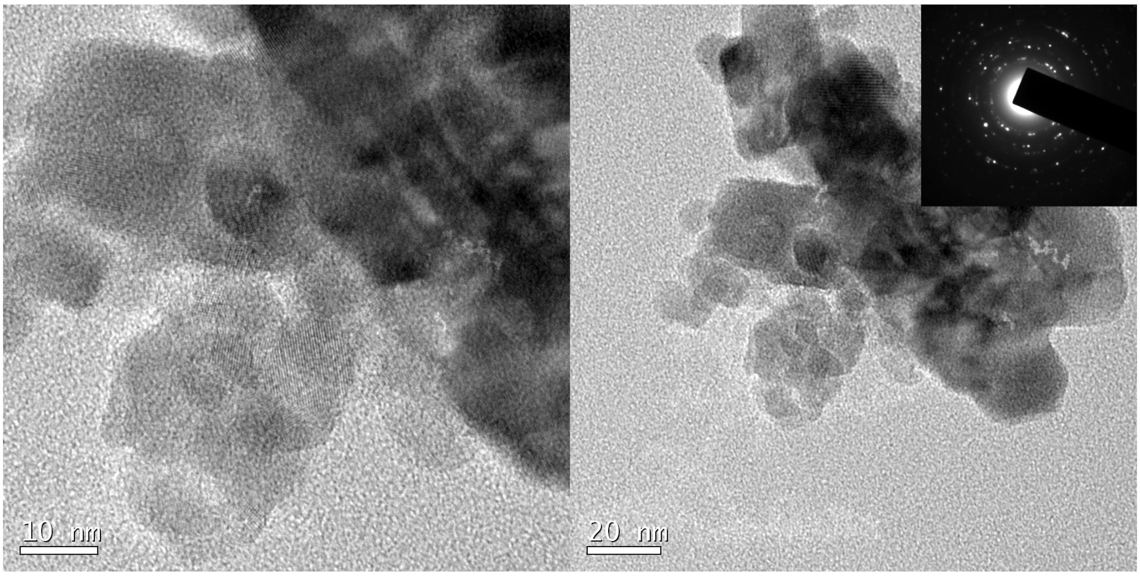

FIG. 2. TEM images of TiO_2 nanoparticles calcined at 800 °C

The absorption spectra of the pure and irradiated samples were recorded with a Shimadzu UV-Visible Spectrophotometer-UV 2600 model with ISR attachment. For measurement, the nanoparticles were pressed into a thick pellet, and placed at the entrance port of the integrating sphere using a sample holder. Calibration of the absorbance scale was done using standard reference materials. The wavelengths tested ranged from 200–800 nm.

Photoluminescence spectroscopy is an effective way to investigate the electronic structure and optical characteristics of semiconductor nanomaterials. This analytical technique reveals information such as surface defects and oxygen vacancies as well as the separation and recombination of photo-induced charge carriers [12]. Photoluminescence spectra were measured at room temperature by a Fluoromax-3 spectrophotometer. The effect of electron beam irradiation on PL spectra was investigated. The photo activity of electron beam irradiated TiO_2 samples can be evaluated by the measurement of PL spectra, since stronger PL intensities were associated with higher photo activities.

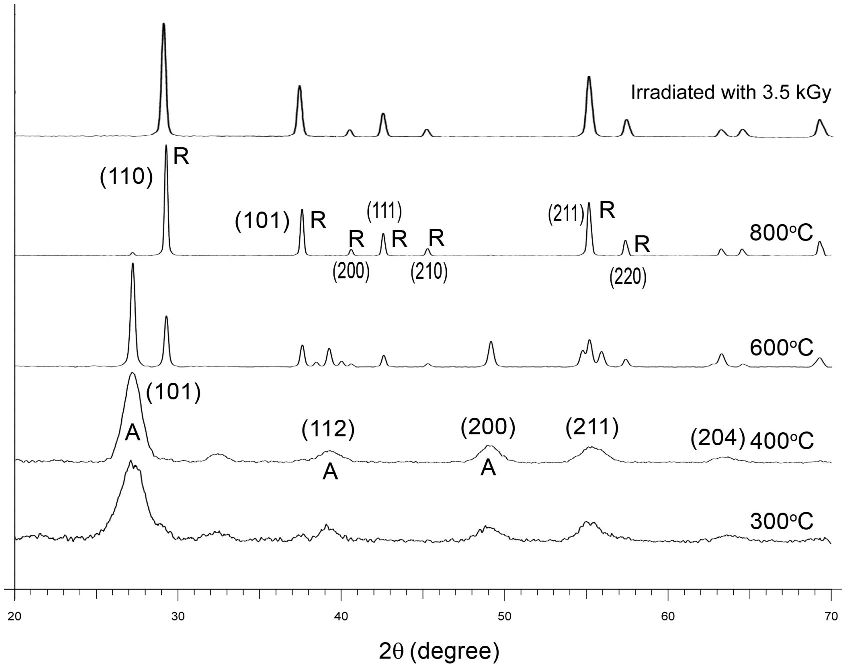

FIG. 3. The XRD spectra of TiO_2 nanoparticles calcined at different temperatures (A — Anatase; R — Rutile)

3. Results and Discussion

Figure 3 shows the X-ray diffraction patterns of uncalcined and calcined TiO_2 samples (A — anatase, R — rutile). The XRD pattern of the sample calcined at 300 °C revealed the presence of the anatase phase. Above 400 °C rutile peaks started to appear and a mixture of both the anatase and rutile phases of TiO_2 existed up to 800 °C. When the calcination temperature was 600 °C, sharp peaks associated with the rutile phase were observed. This suggests that there was a phase transition from anatase to rutile at temperatures lower than 600 °C. The residual anatase phase still exists in the samples up to 800 °C. At 800 °C, the transition to the rutile phase is almost complete. Fig. 3 shows that the diffraction peaks become intense and their FWHM gradually decreases with increasing calcination temperatures, verifying the increase in both the particle size and pertinent phase. The crystallite size obtained using equation (1) was 6 nm in the case of anatase TiO_2 calcined at 400 °C and 33 nm in the case of rutile TiO_2 calcined at 800 °C.

TEM was used to further examine the particle size, crystallinity and morphology of titania samples. TEM bright field images of TiO_2 nanoparticles in rutile (calcined at 800 °C) phase are shown in fig. 2. The TEM image revealed that particles were spherical or near-spherical in shape. Selected area electron diffraction (SAED) is shown in the inset of fig. 2, which clearly indicates that the TiO_2 nanoparticles were highly crystalline in nature. As can be seen from the TEM image, the average particle size is about 30 nm, which is in agreement with the crystallite size obtained from XRD data.

Figure 4 shows the UV-Visible absorbance spectra of pure and irradiated samples of rutile TiO_2 nanoparticles. S1 is pure sample, S2 and S3 are irradiated rutile samples at a dose rate of 2.5 kGy and 3.5 kGy respectively. The figure shows that the absorbance spectrum of rutile TiO_2 is shifted to the blue region, attributed to the quantum size effect [9]. Similar observations were reported for anatase TiO_2 samples [10]. The band gap values obtained for rutile samples

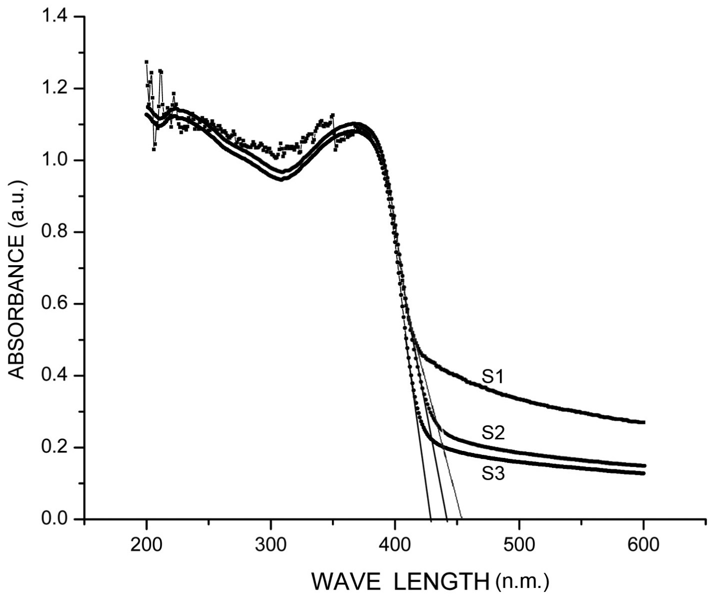

FIG. 4. UV-Vis absorption spectra of rutile TiO_2 samples

were 2.81 eV (S1), 2.85 eV (S2) and 2.88 eV (S3) respectively. This increase in the band gap might occur due to size reduction of the nanoparticles resulting from electron beam irradiation. An additional advantage of size reduction is that the large surface area to volume ratio makes possible timely utilization of photogenerated carriers in interfacial processes [10]. Moreover, beam irradiation appeared to improve the optical absorption performance of TiO_2 nanoparticles. In addition, both non- and irradiated TiO_2 nanoparticles were useful for photocatalytic activities because their band gap energy values were comparable to the energy of visible or UV light photons. As a result, these materials may be well-suited for the fabrication of efficient solar cells.

Figure 5 shows the room temperature photoluminescence emission spectra of pure and irradiated samples of rutile TiO_2 nanoparticles. S1 is pure rutile TiO_2, S2 and S3 are irradiated rutile samples with dose rates of 2.5 kGy and 3.5 kGy respectively. The rutile TiO_2 nanoparticles exhibited a strong and wide PL signal at 400–500 nm with the excited wavelength of 300 nm as shown in fig. 5. The figure shows two obvious PL peaks at about 420 and 485 nm respectively. The former peak will be mainly resulting from band edge free excitons and the latter a result of binding excitons [13]. Both pure and irradiated TiO_2 nanoparticles could exhibit obvious PL signal with similar curve shapes. However, there was a small blue shift in the case of irradiated samples because the electron beam irradiation might result in a slight reduction in particle size. The decrease in particle size had an obvious effect, increasing the surface energy, which can be attributed to the quantum confinement [14, 15]. As a result, a slight blue shift (≈ 0.0139 eV) in the emission peak was observed. The PL spectra of irradiated samples were shown to have much larger intensities relative to non-irradiated samples. Sample S3, which was irradiated at 3.5 kGy, showed a large intensity PL spectrum. However, Jun and co-workers reported that the PL intensity decreased with beam irradiation [16]. The increase in PL intensity for an irradiated sample is attributed to the recombination of self-trapped excitons, which is a combined effect of defect centers generated by oxygen vacancies, small particle size, growth of the brookite phase and increased absorption over the UV and visible range [17]. The increase in PL intensity is an

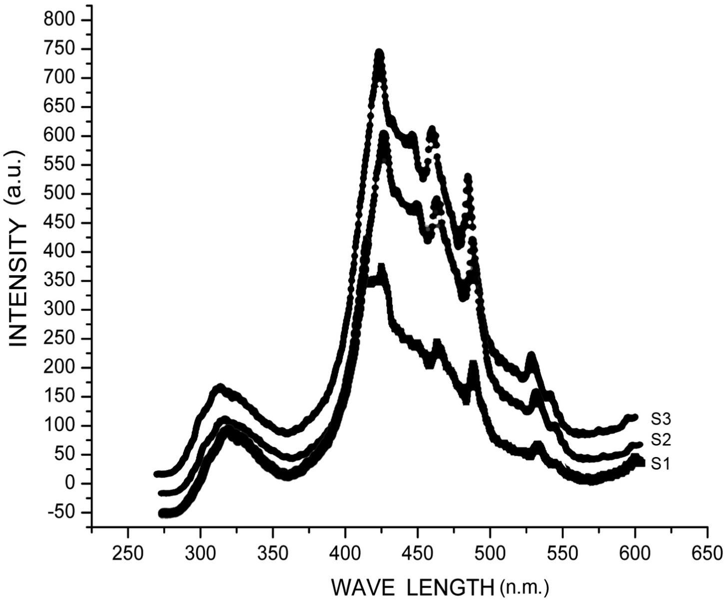

FIG. 5. Room temperature PL spectra of rutile TiO_2 samples

indication of higher photocatalytic activity. Moreover, the beam irradiation with suitable dose rate can help to enhance the photo-activity of TiO_2 nanoparticles. Similar observations have been reported for anatase TiO_2 nanoparticles [10].

4. Conclusion

TiO_2 nanoparticles were synthesized by the sol-gel method and then irradiated with high energy electron beams. The optical properties of the pure and the beam-irradiated samples of rutile TiO_2 were investigated in context of the band gap. The absorption spectra of the irradiated samples were shifted to the blue region, which was attributed to the quantum size effect. The band gap obtained for the irradiated rutile TiO_2 samples were larger as compared to their pure samples. This increase of band gap might occur due to size reduction of the nanoparticles caused by the beam irradiation. The PL intensity of the irradiated samples was more, which was thought to arise from defects and particle size variation. Furthermore, the data obtained here would seem to show that the high energy electron beam irradiation at a suitable dose rate helps to enhance the optical response and photo-activity of TiO_2 nanoparticles.

Acknowledgments

The authors acknowledge their thanks to Nirmala College, Muvattupuzha and Microtron Centre, Mangalore University, Mangalore, Karnataka State for providing the opportunity to undertake this study. The financial support of this work by the KSCSTE, Thiruvananthapuram is gratefully acknowledged.

References

[1] W. Li, S.I. Shah, et al. Metalorganic chemical vapor deposition and characterization of TiO_2 nanoparticles. *Mater. Sci. Eng. B*, **96**, P. 247 (2002).

[2] E. Traversa. Design of ceramic materials for chemical sensors with novel properties. *J. Am. Ceram. Soc.*, **78** (1995).

[3] H. Zhang, J.F. Banfield. Thermodynamic analysis of phase stability of nanocrystalline titania. *J. Mater. Chem.*, **8**, P. 2073–2076 (1998).

[4] H.Z. Zhang, J.F. Banfield. Understanding Polymorphic Phase Transformation Behavior during Growth of Nanocrystalline Aggregates: Insights from TiO_2. *J. Phys. Chem. B*, **104**, P. 3481 (2000).

[5] A. Tsevis, N. Spanos, et al. Preparation and characterization of anatase powders. J. *Chem. Soc. Faraday Trans.*, **94**, P 295–300 (1998).

[6] S. Sahni, B. Reddy, B. Murty. Influence parameters on the synthesis of nano-titania by sol-gel route. *Mater. Sci. Eng. A*, **452–453**, P. 758–62 (2007).

[7] F. Hossain, L. Sheppard, J. Nowotny, G. Murch. Optical properties of anatase and rutile titanium dioxide: Ab initio calculations for pure and anion-doped material. *J Phys. Chem. Solids*, **69**, P. 1820–8 (2008).

[8] L. Palmisano, V. Augugliaro, A. Sclafani, M. Schiavello. Activity of chromium-ion-doped titania for the dinitrogen photoreduction to ammonia and for the phenol photodegradation. *J. Phys. Chem.*, **92**, P. 6710 (1998).

[9] L.Q. Jing, Z.L. Xu, et al. The surface properties and photocatalytic activities of ZnO ultrafine particles. *Appl. Surf. Sci.*, **180**, P 308–314 (2001).

[10] K.P. Priyanka, Sunny Joseph, et al. Surface Modification of Nanotitania Using High Energy Electron Beam Irradiation. *Int. J. Emerg. Tech. Appl. Engg.*, **2** (11), P. 130–134 (2012).

[11] T. Varghese, K.M. Balakrishna. *Nanotechnology: An introduction to synthesis, properties and applications*. Atlantic Publishers, New Delhi, P. 93–96 (2011).

[12] W.F. Zhang, M.S. Zhang, Z.Yin, Q. Chen. Photoluminescence in anatase titanium dioxide nanocrystals. *Appl. Phys. B*, **70**, P. 261–265 (2000).

[13] W.Li, C.Ni, et al. Size dependence of thermal stability of TiO_2 nanoparticles. *J. Appl. Phys.*, **96** (11), P. 6663 (2004).

[14] J. Liqiang, S. Xiaojun, et al. The preparation and characterization of La doped TiO_2 nanoparticles and their photocatalytic activity. *J. Solid State Chem.*, **177**, P. 3375–3382 (2004).

[15] H.K. Bo, H.K. Chang, et al. Electron beam irradiation effect on the photocatalytic activity of TiO_2 on carbon nanofibers. *J. Nanosci. Nanotech.*, **11**, P. 1438–1442 (2011).

[16] J. Jun, J.H. Shin, J.S. Choi, M. Dhayal. Surface Modification of TiO_2 nanoparticles using electron beam radiation. *J. Biom. Nano*, **2** (2), P. 152–156 (2006).

[17] S. K. Gupta, Rucha Desai, et al. Titanium dioxide synthesized using titanium chloride: size effect study using Raman spectroscopy and photoluminescence. *Journal of Raman Spectroscopy*, **41** (3), P. 350–355 (2010).

NANOSYSTEMS: PHYSICS, CHEMISTRY, MATHEMATICS, 2013, 4 (2), P. 225–235

STEPWISE CONFORMATION TRANSITIONS FOR A SEMI-STIFF RING POLYMER CONFINED IN A CONICAL TRAP INDUCED BY THE INCREASING EXTERNAL FIELD OR BY CONE'S OPENING ANGLE VARIATION

[1]A. Siretskiy, [2]C. Elvingson, [3]P. Vorontsov-Velyaminov

[1]Dept. of Informational Technology, SE-751 05, Uppsala University, Uppsala, Sweden

[2]Dept. of Chemistry, Physical Chemistry P.O. Box 523, SE-751 20, Uppsala University, Uppsala, Sweden

[3]Dept. of Molecular Biophysical, Physical Faculty, 198504, Saint Petersburg University, Saint-Petersburg, Russia

alexey.siretskiy@it.uu.se, christer.elvingson@kemi.uu.se, voron.wgroup@gmail.com

PACS 05.10.Ln 05.20.Gg 87.15.A- 64.60.De

In this paper a stepwise compaction process of a ring semi-stiff polymer chain placed in a 3d conical nano-cavity and being under the action of the increasing external field is studied. Compaction from a circle-like shape to several toroidal-like loops for a three-dimensional system was observed. The thermodynamic stability of these toroidal-like structures was investigated by observing a hysteresis of the compaction-extension curves. This study extends our previous work [1] with investigation of the effect of the cone opening angle variation on the distinct shape transitions.

Keywords: semi-stiff ring polymers, Monte Carlo, compact structures, shape transitions, confinement, nanocone.

1. Introduction

It is well known, that confinement can crucially influence the conformational properties of macromolecules [2–4]. The accessible space could be reduced by a spherical cavity [5], a cylindrical pore [6], or a rectangular or circular slit [7]. In all cases, the confinement strongly affects the conformation of the molecule. An important example is the compaction of DNA which has been studied using various methods. It is accomplished for instance by adding of spermin^{+4}, spermidin^{+3} or other highly charged counterions [8, 9]. Microchannels were also used to observe the conformational changes of a single DNA molecule. It has further been found that adding a "crowding agent" also induces compaction for a semi-stiff molecule like DNA [10]. An exhaustive review of the equilibrium behavior of isolated macromolecules confined in cavities of various geometries can be found in [11] and an overview of their dynamical properties is presented in [12]. New types of nanostructures are constantly being obtained synthetically and are also found in biological systems. Specific examples include carbon nano-cones as well as conical cores in some viruses, e.g. the HIV-1 virus encapsulating its RNA content in a conical confinement [13, 14]. Well defined synthetic carbon nano-cones can also be produced during pyrolysis of hydrocarbons [15]. Such conical structures can be used to investigate the role of non-uniform confinement on the stability of e.g. toroidal structures formed by semi-stiff ring polymers, such as DNA.

In this work we investigate how the shape of such a nano-cone will affect the structure of a ring polymer during non-uniform confinement by introducing an external field in the direction toward the tip of the cone. By varying strength of the external field, acting on the polymer, the volume effectively accessible by the polymer will change. It is possible thus to imitate different cone heights in a single computer simulation. Studying stability of several structuresformed during confinement, can provide us better understanding of the structure of RNA(DNA) confined in differently shaped viral capsids, or the properties of synthetic and biopolymers in artificially fabricated confinements.

Simulations are performed in the canonical ensemble within conventional Metropolis Monte Carlo(MC) [17]. Our interest is in the conformational properties of a *semi-stiff chain*, and we show that for the special kind of confinement used here, the external field is able to induce several shape transitions of the semi-stiff polymer in three-dimensions. It should also be mentioned that in the case of the two-dimensional slit, the similar looping with the thermodynamically stable conformations were observed in the computer experiment [1].

The possibility for a semi-stiff circular polymer to have stable looped conformations are shown also analytically using simplifying assumptions. Further, we investigate the relative stability of the polymer at different degrees of compaction as a function of the external field strength. To reveal the role of the shape of the confinement we run simulations for constant external field strength but varying the cone opening angle.

In section 2 we describe the model, in section 3 we introduce the computational methods, and in section 4 the results are presented. The conclusions are made in section 5.

2. Model

The ring polymer consists of N beads connected by N bonds, where the bond length was allowed to fluctuate. We thus include the following interactions in our model: 1) bond stretching, 2) bending rigidity (characterized by the angle between consecutive bonds), 3) repulsion from the wall, confining the polymer, 4) an external potential acting on the center of mass of the polymer, and 5) Lennard-Jones (LJ) interactions between the nonbonded beads. The direction of the external field was chosen to decrease the potential energy of the chain when moving towardsthe towards the cone tip.

So the Hamiltonian of the system is presented as:

$$H = E_{stretch} + E_{bend} + E_{exc} + E_{ext} + E_{LJ}, \tag{1}$$

where $E_{stretch}$ is the energy due to bond length fluctuation, E_{bend} is the bending energy, E_{exc} is the wall repulsion, E_{ext} is the external field contribution, and E_{LJ} is the Lennard-Jones potential included in the three-dimensional case.

Specifically for a chain with N beads, $E_{stretch}$ was calculated using a FENE-type [16] (finitely extensible non-linear elastic) potential:

$$E_{stretch}(b) = \left[\begin{array}{ll} -\gamma \sum_{i=1}^{N} \ln \left[1 - \left(\frac{b_i - b_0}{\Delta b_{max}} \right)^2 \right] & , \quad |b_i - b_0| \leqslant \Delta b_{max} \\ \infty & , \quad |b_i - b_0| > \Delta b_{max}, \end{array} \right. \tag{2}$$

where γ is the stretching constant, Δb_{max} is the maximal bond length fluctuation, $b_i = |\mathbf{b}_i|$, and where $b_0 = |\mathbf{b}_0|$ is the equilibrium bond length. Within the equilibrium length region the FENE behaves similar to the harmonic potential, but unlike the latter it does not allow infinite bond extension. The bending energy is given by

$$E_{bend}(\theta) = \kappa \sum_{i=1}^{N}(1-\cos\theta_i), \tag{3}$$

where $\theta_i = \widehat{\mathbf{b}_i, \mathbf{b}_{i+1}}$ is the angle between successive bond vectors $\mathbf{b}_i$ and $\mathbf{b}_{i+1}$ (or between bond vectors $\mathbf{b}_N$ and $\mathbf{b}_1$ for $i = N$), and κ characterizes the bending stiffness. The confining walls were considered to be hard walls, characterized by:

$$E_{exc} = \left[\begin{array}{l} 0, \text{ all beads are inside the cone} \\ \infty, \text{any of N beads is outside the cone,} \end{array} \right. \tag{4}$$

The interaction with an external force field is given by

$$E_{ext}(x) = \sigma z, \tag{5}$$

where z is the distance between the center of mass of the polymer and the cone tip, in which $z = 0$, see Fig. 1(a), σ is the constant which detemines the force of the external filed. To take into account for the excluded volume interactions, and in order to introduce attraction between the chain monomers-beads to stabilize the ring polymer during compaction we also include a LJ potential:

$$E_{LJ} = \sum_{i=1,j<i}^{N} u(r_{ij}) = 4\epsilon \sum_{i=1,j<i}^{N} \left[(a/r_{ij})^{12} - (a/r_{ij})^{6}\right], \tag{6}$$

where r_{ij} is the distance between bead centers, ϵ is the depth of the potential minimum, and a is the bead diameter. We found, that neglecting the attractive part in the case of three dimensions, could make structures forming toroidal loops unstable.

To simplify notation, we use dimensionless units throughout. The energy is measured in the units of $\epsilon : H = \epsilon H^*$. Distances are given in units of b_0: $b^* = b/b_0$. The bead size is set to be equal to $a = 0.1b_0$, and the maximal bond fluctuation is $\Delta b_{max} = 0.5b_0$. The units of the reciprocal dimensionless temperature β^* is obtained from the relation: $H\beta = H^*\beta^*$, where $\beta = 1/k_BT$ and $\beta^* = 1/T^*$.

The values of the bending constant, κ, the stretching constant γ, and the magnitude of the external field σ are chosen to maintain the property of a (semi)stiff chain, but still flexible enough to show shape transitions. The persistence length, l_p, was equal to $10b_0$. For a chain with $N = 20$, this means that the contour length is approximately $2l_p$. The relation between the bending force constant and the persistence length is given in the Appendix.

3. Method

The Metropolis Monte Carlo method (MC) in the canonical ensemble [17] was used to investigate the equilibrium properties of the system. One MC step corresponding to a single bead displacement or a flip of a segment of the chain (crankshaft move), is presented in Fig. 1(b).

The chain length of $N = 20$ was chosen to investigate shape transitions. The frequency of the crankshaft moves to the single bead displacements were in this case from 1:10 up to 1:1. Our observation has shown that proposed frequency ratio is enough for chain to relax after a large conformational change corresponding to a segment flip. The flip segment length was uniformly chosen in the interval $[1:15]$.

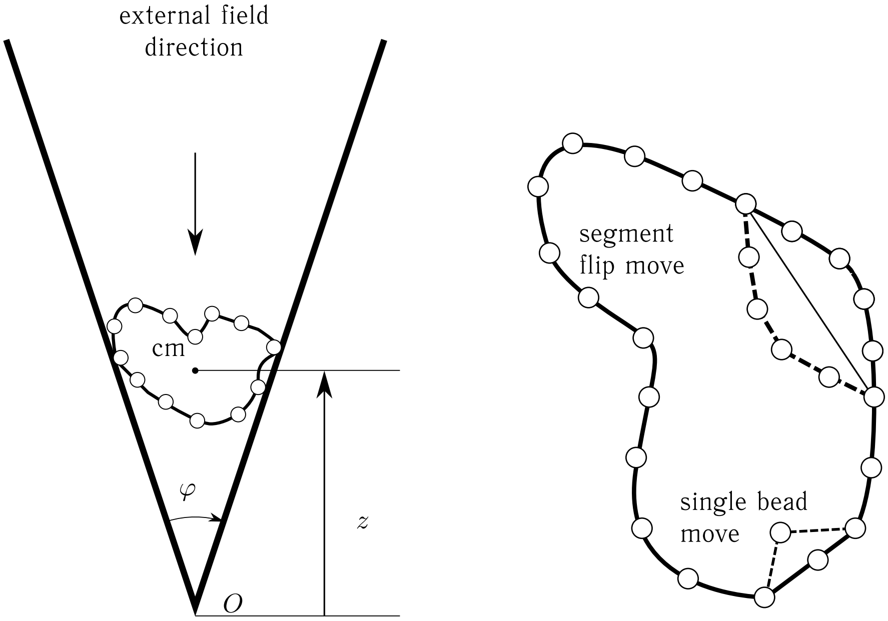

Fig. 1. (a) A sketch of the system used in the simulations. The position of the center of mass of the polymer is denoted by “cm”, and “z” is the distance between the level of the “cm” and the tip of the cone, O, and φ is the cone opening angle. (b) Illustration of the possible moves. The trial configuration for a single bead displacement and for a segment flip (crankshaft move) are shown as dashed curves

The transition probability to accept a trial move is the conventional Metropolis criterion [17]:

$$acc[o \to n] = \min[1, e^{-\beta \Delta H}], \tag{7}$$

where $\Delta H = H(n) - H(o)$ and n and o denote the new and the old configurations respectively.

4. Results

4.1. External field dependence

In order to understand a possibility for a semi-stiff ring polymer to form stable looped structures in the nonuniform confinement, it is feasible to consider a simplification of the proposed model, and evaluate *phantom* semi-stiff ring polymer. That is we drop the Lennard-Jones contribution (6) and therefore allowing the monomers to intersect, while preserving the confining walls interactions (4). All the angles between the monomers θ and all the bond lengths b for all monomers are considered equal, bond length fluctuations are not considered. Under these restrictions the possible conformations are circular, made of integer number of loops.

The Hamiltonian (1) then is reduced to:

$$H = E_{stretch} + E_{bend} + E_{exc} + E_{ext}, \tag{8}$$

It is possible to rewrite the Hamiltonian contributions as functions of z with parameter λ, where z is the distance between the level of the top of the cone and the level of

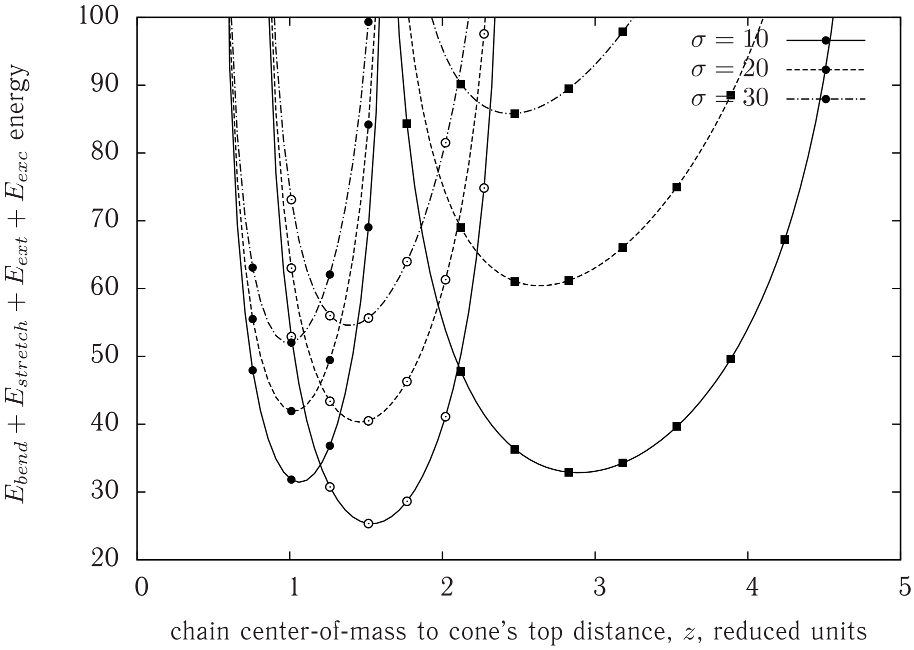

Fig. 2. Analytical curves according to (9): full chain energy H as a function of the distance between the center of mass of the chain and of the cone's tip z for different external fields amplitudes σ. Curves for different σ are marked with different line types: $\sigma = 10$ – solid, $\sigma = 20$ – dashed, and $\sigma = 30$ – dot-dashed. Different symbols denote energy curves for different number of loops: $\lambda = 1$ – filled squares, $\lambda = 2$ – open circles, $\lambda = 3$ – filled circles. Other parameters are: $\tan(\varphi/2) = 1$, $\gamma = 2$, $\kappa = 5$, $\Delta b_{max} = 0.5$, $N = 20$

center of mass (Fig. 1) of the one, two and three loops formed by the ring polymer, and λ is the number of loops:

$$H(z;\lambda) = -N\gamma \ln\left[1 - \frac{1}{\Delta b_{max}^2}\left(2\sin\frac{\lambda\pi}{N}\tan(\varphi/2)z - 1\right)^2\right] + 2\kappa N \sin^2\frac{\lambda\pi}{N} + \sigma z. \qquad (9)$$

The curves of the (9) for $\lambda = 1,2,3$ in Fig. 2 show, how the external field, given by (5) can induce energetically stable loops with the increase of the field amplitude $\sigma = 10, 20, 30$.

For each line type there are three energy wells, marked with different point types, with the minima positions revealing the distances between the cone's top and the mass center position for $\lambda = 1,2,3$ looped structures. One can see, for example, that for $\sigma = 10$, the energy minimum for $\lambda = 2$ (open circles) is lower than for $\lambda = 1$ (filled squares). But at the same time, the energy minimum for $\lambda = 3$ (filled circles) is *higher* than for $\lambda = 2$ (open circles), showing that the three looped structure is less energetically favourable than the two looped one. Situation though changes with the external field strengthens, and for $\sigma = 30$ the three looped structure has a lower energy than the two looped one, providing for the looped structure to be *thermodynamically* stable.

The repulsive part of the LJ interactions provides excluded volume interactions, while the attractive part will add a stabilizing contribution to any compact configuration.

In Fig. 3, we first show the screenshots of the semi-stiff ring polymer in three dimensions at different stages of compaction.

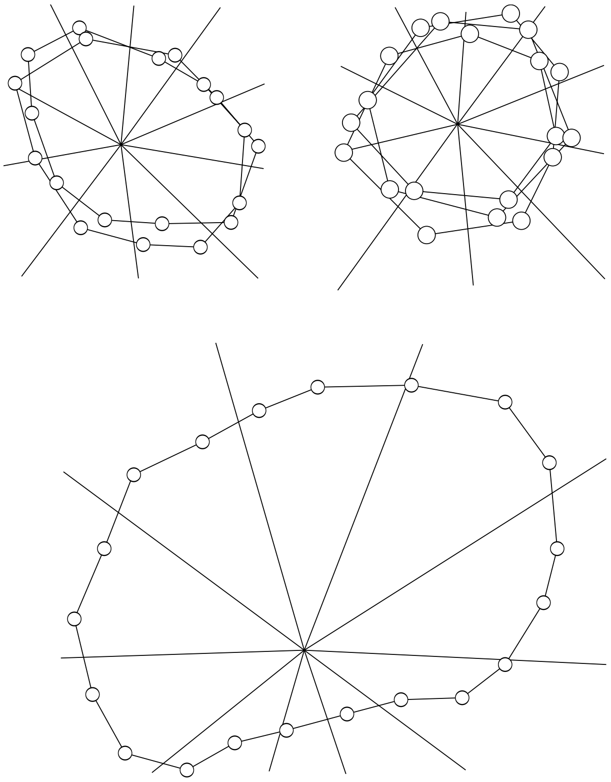

Fig. 3. Examples of different stages of compaction: from 1 to 3 loops. The view is from the top and the tip of the cone is at the center, while the lines originating from the tip are the generatrixes of the cone. The system shown is $N = 20$, $\varphi = \pi/2$, $\beta = 2.0$, and $\gamma = 2.0$, and $\kappa = 5.0$.

To demonstrate the stability of the ring polymer with 2 or 3 loops, we show in Fig. 4 the radius of gyration R_g as a function of the external field strength σ during the compaction process $(1 \to 2 \to 3)$ loops and the expansion process $(3 \to 2 \to 1)$. In Fig. 4, one can clearly observe a hysteresis in the radius of gyration with respect to the external field strength. It is possible to interpret the hysteresis curves as follows: a stronger external field is needed to produce *compaction*, than to *expand* a ring polymer with the same amount of loops.

In Fig. 4 we also show $R_g(\sigma)$ for different temperatures. One can see that the lower is the temperature, the broader is the hysteresis loop. The temperature doesn't play any significant role in the region of the same amount of loops, but does effect on the value of the "threshould" σ, making the hysteresis loop broader.

The graphs can be split into three regions $\sigma \in (0 : 10)$, $\sigma \in (20 : 40)$, and $\sigma > 40$. These regions represent one, two and three loops correspondingly. Within each of the regions the curves show how the radius of gyration changes when the external field strength varies for the molecule forming one, two, and three loops respectively.

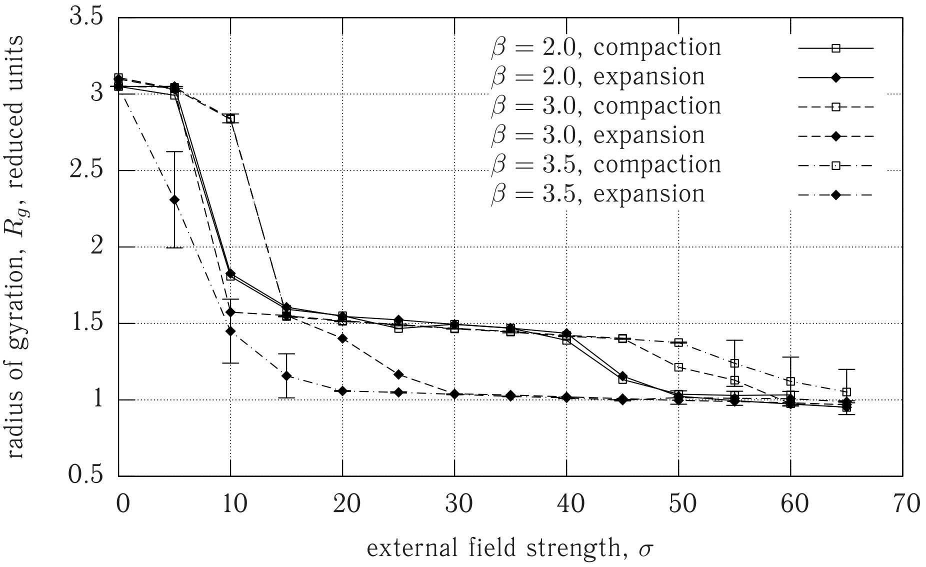

Fig. 4. Hysteresis observed during the compaction-expansion process of a semi-stiff ring polymer. The radius of gyration R_g dependence on the magnitude of the external field σ is shown for the system $N = 20$ for different inversed temperatures, $\beta = 2.0, 3.0, 3.5$ with solid, dashed and dot-dashed curves. The compaction is marked with squares, and the expansion with diamonds. The rest of the parameters are $\varphi = \pi/2$, $\gamma = 2.0$, and $\kappa = 5.0$. Some error bars are also shown.

One can consider an average "slope" of the curves for compaction to notice that the slope is decreasing, showing that with an increasing number of loops it becomes gradually harder to induce further compaction. The error bars are shown to demonstrate, that during the *compaction* of a certain structure, the fluctuations in size are small, while in the *transition region* the fluctuations are large, revealing the *cooperativity* of the transitions.

A simple analysis can also be done to show (in addition to the screenshots in Fig. 3) that the radius of gyration of these loops converges to the values, $R_g = \{3.0, 1.5, 1.0\}$ (Fig. 4) that fits very nicely, up to a scaling factor, the R_g curve for the ideal line of contour length L sequentially packed into 1, 2 and 3 loops: $R_g(k) = \frac{L}{2\pi k} \to R_g = \{3.0, 1.5, 1.0\}$, where i is the number of loops.

4.2. Opening angle dependence

As it was mentioned in [1], the orientation of the loops to the cone's axis depends on the value of the opening angle of the cone. Curves for the simplified model (8), similar to shown in Fig. 2 can be plotted for constant amplitude of the external field, σ, while varying the cone opening angle φ. Number of energetically favourable loops formed by the phantom ring polymer appears to be dependent on the cone's opening angle, φ, as shown on Fig. 5, where the energy curves for $H(z; \lambda)$ from (9) are plotted for the external field strength of $\sigma = 30$, enough to introduce compaction up to 3 loops for $N = 20$ chain, for the three different cone's opening angles: $\varphi = 120°$, $\varphi = 90°$, and $\varphi = 60°$. As one can see too "broad" cones are not very suitable for loop formation.

In order to investigate the change of the orientation of the loops depending on the opening angle we conducted MC-simulations with the full Hamiltonian (1) and observed

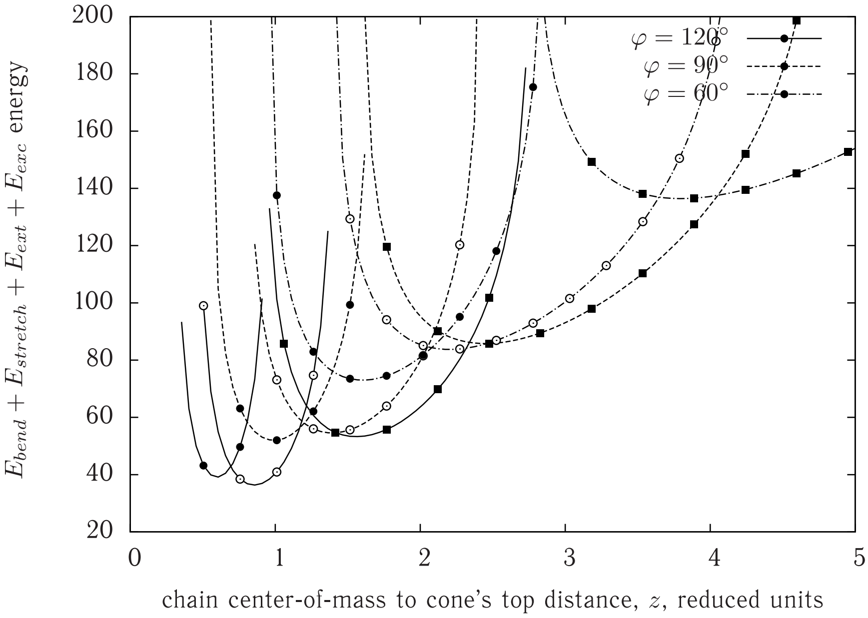

Fig. 5. Analytical curves according to (9): full chain energy H as a function of the distance between the centre of mass of the chain and the cone's tip z for different opening angles φ. Curves for different σ are marked with different line types: $\varphi = 120$ – solid, $\varphi = 90$ – dashed, and $\varphi = 60$ – dot-dashed. Different symbols denote energy curves for different number of loops: $\lambda = 1$ – filled squares, $\lambda = 2$ – open circles, $\lambda = 3$ – filled circles. Other parameters are: $\sigma = 30$, $\gamma = 2$, $\kappa = 5$, $\Delta b_{max} = 0.5$, $N = 20$.

the behaviour of a normalized to unity length vector $\mathbf{n}$ calculated as follows:

$$\mathbf{n} = \left\langle \sum_{i=1}^{N-1} (\mathbf{r}_i - \mathbf{r}_{\mathrm{cm}}) \times (\mathbf{r}_{i+1} - \mathbf{r}_{\mathrm{cm}}) \right\rangle, \tag{10}$$

where $\mathbf{r}_j$ – radius-vector of the bead j, $\mathbf{r}_{\mathrm{cm}}$ – is the position of the center of mass of the chain, "×" – denotes the cross-product, and the canonical ensemble averaging $\langle \cdots \rangle$ being applied. The z-component of $\mathbf{n}$ is directed along the cone's axis. So if the z-component is greater than the other two, located in the plane perpendicular to the cone's axis, then one can conclude that the loops orientation is like shown on the Fig. 3. If all of the components are close to zero due to averaging out, then the loops are oriented as in the two-dimensional case. Figure 6 shows the components length of the $\mathbf{n}$, depending on the opening angle value. It is possible to observe that in the case of strong compacting field, the orientation of the loops of the chain is perpendicular to the cone's axis up to $\varphi \approx 90^*$. After that, however, the orientation changes, that is demonstrated by the graph of the $\mathbf{z}$-component of $\mathbf{n}$. In the opening angle interval $\varphi \in (60° : 90°)$, the number of loops remains constant (i.e. 3), that corresponds to $R_g \approx 1$ in the reduces units, while the orientation of the loops changes, Fig. 6.

Another conclusion from Fig. 6 can be made: not only the orientation of the loops, but also the number of them is dependent on the opening angle. For the "too broad" cones no compaction is possible, since there are effectively no wall left to squeeze the ring polymer.

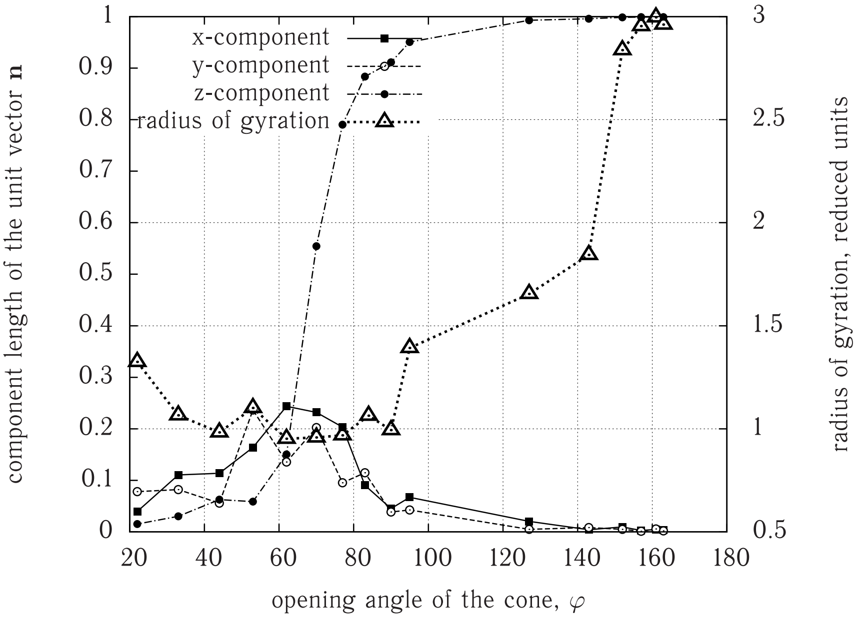

Fig. 6. Components $\mathbf{x}$, $\mathbf{y}$, and $\mathbf{z}$ of the unit vector $\mathbf{n}$, (10), as a function of the opening angle, φ. Radius of gyration, R_g as a function of the φ. The system's parameters are: $N = 20$, $\gamma = 2.0$, $\kappa = 5.0$, $\sigma = 50$, and $\beta = 3.0$.

The snapshots capturing the orientation change for 3-looped structure, and an example of the irregular structure for the very narrow cone are shown on the Fig. 7.

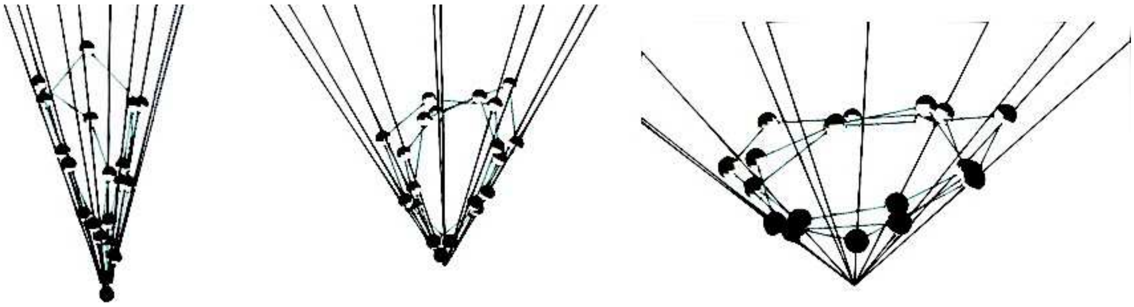

Fig. 7. Printscreens for the cone opening angle $\varphi \approx 30°$, $\varphi \approx 60°$, and $\varphi \approx 90°$ from the left to the right correspondingly. For the most narrow cone, there are no loops formed, but some irregular structure instead. The orientation of the loops changes with the grows of φ. The rest parameters as for the system in the Fig. 6

5. Conclusions

In the present communication, we continued studies of work [1] to investigate discrete shape transitions of a semi-stiff ring polymer confined in a conical trap. The proposed model of a ring polymer including chain stiffness undergoes a set of a distinct shape transitions, starting from a single loop up to several ones. The crucial role of the studied compaction is due to the a conical geometry and a direction of the external field acting on the center of mass of the chain. Such kind of shape transitions is not a specific feature of the dimensionality of the system, as long as the same behaviour can be observed in the two-dimensional slit and in a three-dimensional conical pore.

The two ways of inducing a compaction was considered in the present work: 1) the external field σ change with fixed cone's opening angle φ, 2) and the cone's opening angle change while keeping the external field constant, but sufficient to induce compaction.

From the first hand, a theoretical possibility to form the energetically stable structures was concluded, based on the investigation of the Hamiltonian of the system looped into one, two, and three loops correspondingly.

Both of the considered ways to induce compaction lead to the looping of the semi-stiff ring polymer. The formed configurations while varying the external field strength are shown to be locally thermodynamically stable.

We investigate further the phenomenon observed earlier in [1], namely, the orientation of the loops with the opening angle change. It was shown that the orientation of the loops is changing with the value of the opening angle of the cone. The vector normal to the loop(s), $\mathbf{n}$, as stated in (10) was used to describe the orientation of the loops.

Four regimes were detected: 1) a stick-like, then no loops can be formed in the case of too narrow cone, $\varphi \approx 30^\circ$ 2) a narrow cone regime, with the vector $\mathbf{n}$ oriented perpendicular the cone's axis $\varphi \approx 40^\circ \div 60^\circ$, 3) a broad cone regime, with the vector $\mathbf{n}$ collinear to the cone's axis, $\varphi \approx 60^\circ \div 160^\circ$, and 4) too broad cone, when no looping is possible at all due to the effective absence of the confining walls, $\varphi > 160^\circ$.

Acknowledgement

The authors thank John Grime for his visualisation tool, jgrime@uchicago.edu.

Appendix: persistence length derivation

The persistence length can be evaluated by first calculating the average bending angle using [18]:

$$\langle \cos\theta \rangle = \frac{\int \cos\theta e^{\alpha\cos\theta} ||J|| d\theta}{\int e^{\alpha\cos\theta} ||J|| d\theta}, \tag{11}$$

where $\langle \cdots \rangle$ is the canonical ensemble averaging, θ is the bond angle, and $\alpha = \kappa\beta$ is the bending stiffness constant κ in $k_B T$ units, and $||J||$ – is the determinant of the Jacobian matrix: $||J|| = r^2 \sin\theta$ for the three-dimensions.

The persistence length in terms of b_0 can then be evaluated using [19]:

$$l_p = \frac{1 - \langle \cos\theta \rangle^N}{1 - \langle \cos\theta \rangle}. \tag{12}$$

References

[1] Siretskiy A., Elvingson C. Role of non-uniform confinement in shape transitions of semi-stiff polymers. *Molecular Physics*, **113**(1), P. 1–8 (2013).

[2] Odijk T. Statics and dynamics of condensed DNA within phages and globules. *Phil. Trans. R. Soc. A*, **362**, P. 1479–1517 (2004).

[3] Choi M., Santangelo C. D. et. al., The first experimental observation of the biaxial confinement of semi-flexible filament in a channel. *Macromolecules*, **38**, P. 9882 (2005).

[4] LaMarque J. C., Le T. V. L., Harvey S. C. Packaging double-helical DNA into viral capsids. *Biopolymers*, **73**, P. 348–355 (2004).

[5] Ostermeir K., Alim K., Frey E. Buckling of stiff polymer rings in weak spherical confinement. *Phys. Rev. E.*, **81**(6), P. 1–8 (2010).

[6] Odijk T., The statistics and dynamics of confined or entangled stiff polymers. *Macromolecules*, **16**(8), P. 1340–1344 (1983).

[7] Liu Y., Chakraborty B. Shapes of semiflexible polymers in confined spaces. *Phys. Biol.*, **5**(2), P. 1–8 (2008).

[8] Yoshikawa K., Takahashi M., Vasilevskaya V., Khokhlov A. Large discrete transition in a single DNA molecule appears continuous in the ensemble. *Phys. Rev. Lett.*, **76**, P. 3029–3031 (1996).

[9] Bloomfield V. DNA condensation by multivalent cations. *Biopolymers*, **44**, P. 269–282 (1997).

[10] Zhang C., Shao P. G., van Kan J. A., van Maarel J. C. Macromolecular crowding induced elongation and compaction of single DNA molecules confined in a nanochannel. *PNAS*, **106**, P. 16651–16656 (2009).

[11] Gorbunov A. A., Skvortsov A. M., Statistical properties of confined macromolecules. *Advances in colloid and interface science*, **62**(1), P. 31–108 (1995).

[12] Milchev A. Single-polymer dynamics under constraints: scaling theory and computer experiment. *J. Phys. Cond. Matter.*, **23**(10), P. 3101 (2011).

[13] Li S., Hill C. P., Sundquist W. I., Finch J. T. Image reconstructions of helical assemblies of the HIV-1 CA protein. *Nature*, **407**, P. 409 (2000).

[14] Ganser B. K., Li S., Klishko V. Y., Finch J. T., Sundquist W. I. Assembly and analysis of conical models for the HIV-1 core. *Science*, **283**(80), P. 5398 (1999).

[15] Naess S. N., Elgsaeter A., Helgesen G., Knudsen K. D. Carbon nanocones: wall structure and morphology. *Sci. Technol. Adv. Matter.*, **10**, P. 065002 (2009).

[16] Milchev A., Binder K. Dynamics of Polymer Chains Confined in Slit-Like Pores. *J. Phys. II France*, **6**, P. 21-31 (1996).

[17] Metropolis N., Rosenbluth A., Rosenbluth M., Teller A., Teller E., Equation of State Calculations by Fast Computing Machines. *J. Chem. Phys.*, **21**(6), P. 1087–1092 (1952).

[18] Schellman J. A., Flexibility of DNA. *Biopolymers*, **13**, P. 217 (1974).

[19] Freed K. F. *Renormalization group theory of Macromolecules*. New York.: Wiley&Sons (1987).

NANOSYSTEMS: PHYSICS, CHEMISTRY, MATHEMATICS, 2013, 4 (2), P. 236–240

PERSISTENT CURRENT OSCILLATIONS IN ELECTRON-HOLE QUANTUM DOTS

A. A. Vasilchenko, D. M. Tolkachev

Kuban State Technological University, Krasnodar, Russia

a_vas2002@mail.ru, gendalf373@rambler.ru

PACS 73.21.Fg

A system of Kohn-Sham equations was solved self-consistently for the two-dimensional, spatially separated electrons and holes. A series of magic numbers were found for the total angular momentum of the electrons and holes in a strong magnetic field. The change of the angular momentum of the charge carriers was shown to lead to oscillations of the persistent current.

Keywords: electron-hole quantum dots, the Kohn-Sham equations, persistent current.

1. Introduction

In recent years, quantum effects in mesoscopic and nanoscale structures have been actively studied. The superconducting transition temperature is well documented to have an oscillatory form in thin superconducting rings with a period equal to half of the magnetic flux quantum $\Phi_0 = h/e$. The situation is much more complicated in quantum rings due to electron-electron interactions. Little-Parks oscillations and oscillations of the persistent current in semiconductor quantum rings are associated with the change of the energy in a magnetic field. Particularly, in two-dimensional systems with axial symmetry, both effects are explained by changes in the angular momentum of the electrons in quantum rings and order parameter in superconducting rings. The oscillations of the persistent current in semiconductor quantum rings have been studied actively both theoretically [1] and experimentally [2]. Systems with two-dimensional electron-hole (EH) complexes have been studied to a lesser degree.

2. Theoretical model

In the present paper the total energy of spatially separated EH quantum dots was calculated with a finite number N electron-hole pairs in a transverse magnetic field B. Density functional theory was used to calculate the total energy of the EH system. The total energy is written for a two-component system (electrons and holes) as

$$E_t[n_e, n_h] = T_e[n_e] + T_h[n_h] + E_c[n_e, n_h] + E_{xc}[n_e, n_h], \tag{1}$$

where T_e, T_h — the kinetic energy of the carriers, E_c – electrostatic energy, E_{xc} — exchange-correlation energy, n_e and n_h — the density of electrons and holes.

It should be noted that for a small number of particles it is necessary to exclude their self-interaction in the expression (1). Exclusion of particles self-interaction leads to good agreement with the exact results for quantum dots with a small number of electrons [3].

We obtain Kohn-Sham equations for electrons and holes by varying the expression (1) according to the densities n_e and n_h:

$$\left[-\frac{\mu}{m_e}\frac{1}{r_e}\frac{\partial}{\partial r_e}\left(r_e\frac{\partial}{\partial r_e}\right)+\frac{\mu}{m_e}\frac{k_e^2}{r_e^2}+\frac{\mu}{m_e}\frac{k_e}{L^2}+\frac{\mu}{m_e}\frac{r_e^2}{4L^4}+V_{eff,e}(r_e)\right]\psi_{e,k_e}(r_e)=E_{e,k_e}\psi_{e,k_e}(r_e), \tag{2}$$

$$\left[-\frac{\mu}{m_h}\frac{1}{r_h}\frac{\partial}{\partial r_h}\left(r_h\frac{\partial}{\partial r_h}\right)+\frac{\mu}{m_h}\frac{k_h^2}{r_h^2}+\frac{\mu}{m_h}\frac{k_h}{L^2}+\frac{\mu}{m_h}\frac{r_h^2}{4L^4}+V_{eff,h}(r_h)\right]\psi_{h,k_h}(r_e)=E_{h,k_h}\psi_{h,k_h}(r_h), \tag{3}$$

where k_e (k_h) — the angular momentum of the electron (hole), m_e (m_h) — mass of the electron (hole), L — magnetic length,
$\mu = m_e m_h/(m_e+m_h)$, $V_{eff,e}(r) = -V_h(r,d)+V_e(r,0)-V_{e,k_e}(r,0)+V_{xc,e}(r)$,
$V_{eff,h}(r) = -V_e(r,d)+V_h(r,0)-V_{h,k_h}(r,0)+V_{xc,h}(r)$, $V_e(r,d) = 2\int\frac{n_e(r')dr'}{\sqrt{|r-r'|^2+d^2}}$,
$V_{e,k_e}(r,d) = 2\int\frac{\psi^2_{e,k_e}(r')dr'}{\sqrt{|r-r'|^2+d^2}}$, $V_h(r,d) = 2\int\frac{n_h(r')dr'}{\sqrt{|r-r'|^2+d^2}}$, $V_{h,k_h}(r,d) = 2\int\frac{\psi^2_{h,k_h}(r')dr'}{\sqrt{|r-r'|^2+d^2}}$,
$n_{e,k_e}(r) = \psi^2_{e,k_e}(r)$, $n_e(r) = \sum\limits_{k_e} n_{e,k_e}(r)$, $n_{h,k_h}(r) = \psi^2_{h,k_h}(r)$, $n_h(r) = \sum\limits_{k_h} n_{h,k_h}(r)$,
d — the distance between the electron and hole quantum dots.

Here and below the exciton system units were used: the energy was measured in units of $Ry_{ex} = e^2/2\varepsilon a_{ex}$, and the length in units $a_{ex} = \varepsilon\hbar^2/\mu e^2$.

The electrons and holes were assumed to be spin-polarized. Electron-hole correlations may be neglected for spatially separated quantum dots, then

$$E_{xc} = \int \varepsilon_{x,e}(n_e)n_e(r)dr - \sum_{k_e}\int \varepsilon_{x,e}(n_{e,k_e})n_{e,k_e}dr +$$
$$\int \varepsilon_{x,h}(n_h)n_h(r)dr - \sum_{k_h}\int \varepsilon_{x,h}(n_{h,k_h})n_{h,k_h}dr,$$

where $\varepsilon_{x,e} = \alpha n_e$, $\varepsilon_{x,h} = \alpha n_h$, $\alpha = \pi\sqrt{2\pi}L$

The persistent current was the sum of the paramagnetic and diamagnetic currents:

$$I_e = -\frac{\mu}{m_e}\sum_{k_e}\int\frac{2k_e}{r}\psi^2_{e,k_e}(r)dr + \frac{\mu}{m_e}\frac{N}{2\pi L^2},$$

$$I_h = \frac{\mu}{m_h}\sum_{k_h}\int\frac{2k_h}{r}\psi^2_{h,k_e}(r)dr - \frac{\mu}{m_h}\frac{N}{2\pi L^2}$$

3. Numerical results

Kohn-Sham equations were solved numerically for different values of the magnetic field and the distance between the quantum dots. The calculations were performed for different sets of k_e and k_h and the minimum energy was achieved in a compact configuration of particles (neighboring states are populated). This result is shown in Fig. 1 for $N = 3$ and $m_e = m_h = 0,077m_0$ (m_0 is the free electron mass). The total energy has a minimum when the total angular momentum of the holes is $K_h = 3$ (k_h=0,1,2), $K_h = 6$ ($k_h = 1, 2, 3$) and $K_h = 9$ ($k_h = 2, 3, 4$), i.e. period of magic number is 3. When we increased N (up to ten EH pairs), the period of magic numbers for the total angular momentum of the electrons and holes was equal to N as well. The results presented in Fig. 1 correspond to the magnetic field value, near which occurs transition from one configuration of particles to another. This transition is important to study persistent current oscillations and the fractional quantum Hall effect. At the value of magnetic field $= 3,2$ T, a total energy minimum was achieved for $K_e = 3$ and $K_h = 3$. When the magnetic field was increased, the ground state became the one with $K_e = 6$ and $K_h = 6$.

Changing the angular momentum of the electrons and holes resulted in a jump in the persistent current. Fig. 2 shows the dependence of persistent current of electrons and holes on the magnetic field. The persistent current had an oscillatory form with almost linear segments. Different segments corresponded to different values of K_e and K_h which increased as the magnetic field increased. The first segment in Fig. 2 corresponded to the values of $K_e = K_h = 6$, and for the subsequent segments values K_e and K_h, were equal to 9, 12, 15 and 18. The oscillation period decreased slightly as the magnetic field increased. The amplitude of the oscillations decreased because with largeK_e and K_h the diamagnetic current compensated for the paramagnetic one.

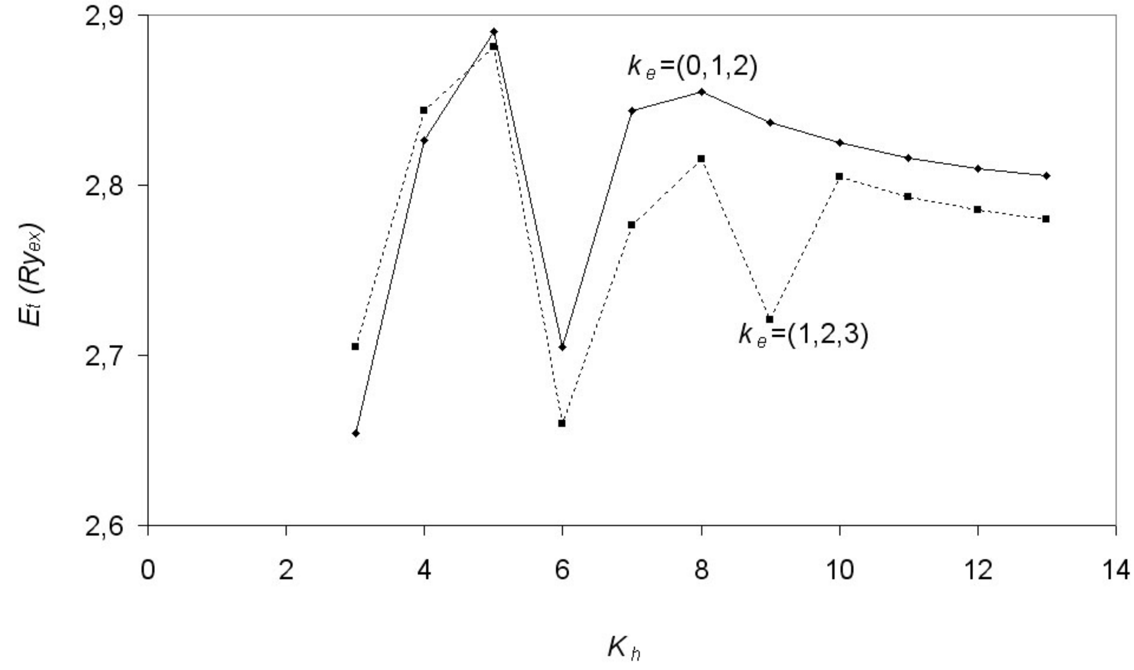

Fig. 1. The total energy versus the total angular momentum of the holes ($N = 3$, $d = 2$, $B = 3,2$ T, $m_e = m_h = 0,077 m_0$). The points are connected by lines for illustrative purposes

Fig. 3 shows the phase diagram for the transition from a state with $K_e = K_h = 3$ into the state with $K_e = K_h = 6$. The transition to a new state for small d was possible only in very strong magnetic fields, and this value of the magnetic field increased along with the mass of the hole. When the mass of the holes was doubled, a transition to a new state occurred also with $K_e = K_h$, so the persistent current oscillation period of the electrons and holes were equal (Fig. 4). It should be noted that the oscillation's amplitude of the persistent current was smaller for holes than for electrons, and the oscillation period became longer than in case of $m_e = m_h$.

4. Conclusion

Thus, the system of Kohn-Sham equations were solved numerically for two-dimensional electrons and holes in a strong magnetic field. The total energy of the electron-hole

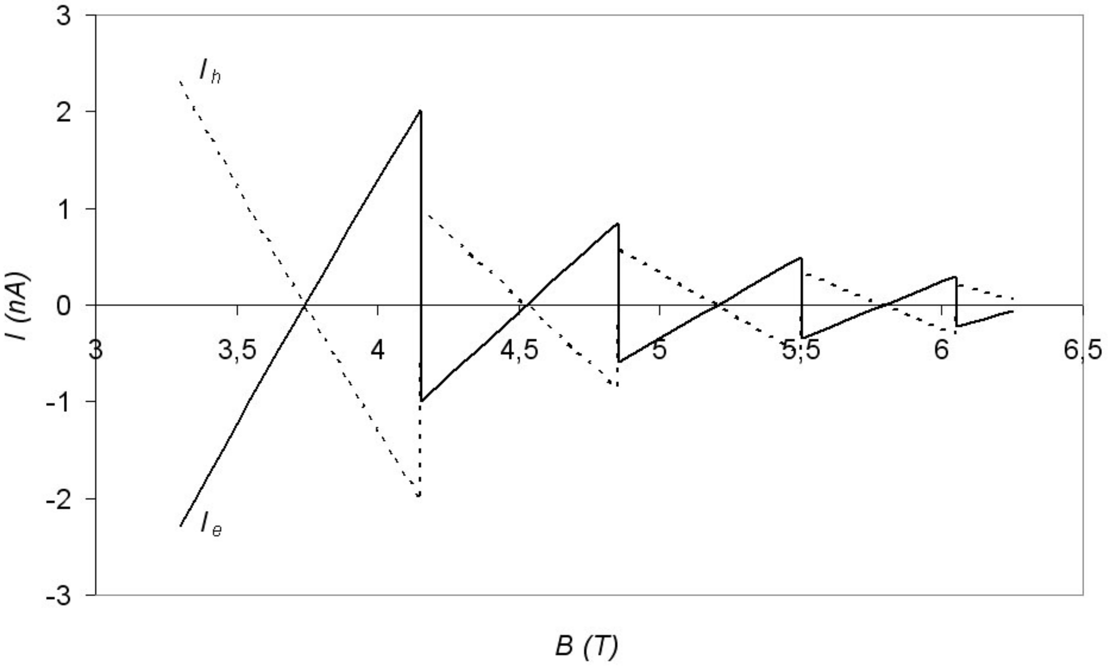

Fig. 2. The persistent current versus the magnetic field ($N = 3$, $d = 2$, $m_e = m_h = 0,077m_0$)

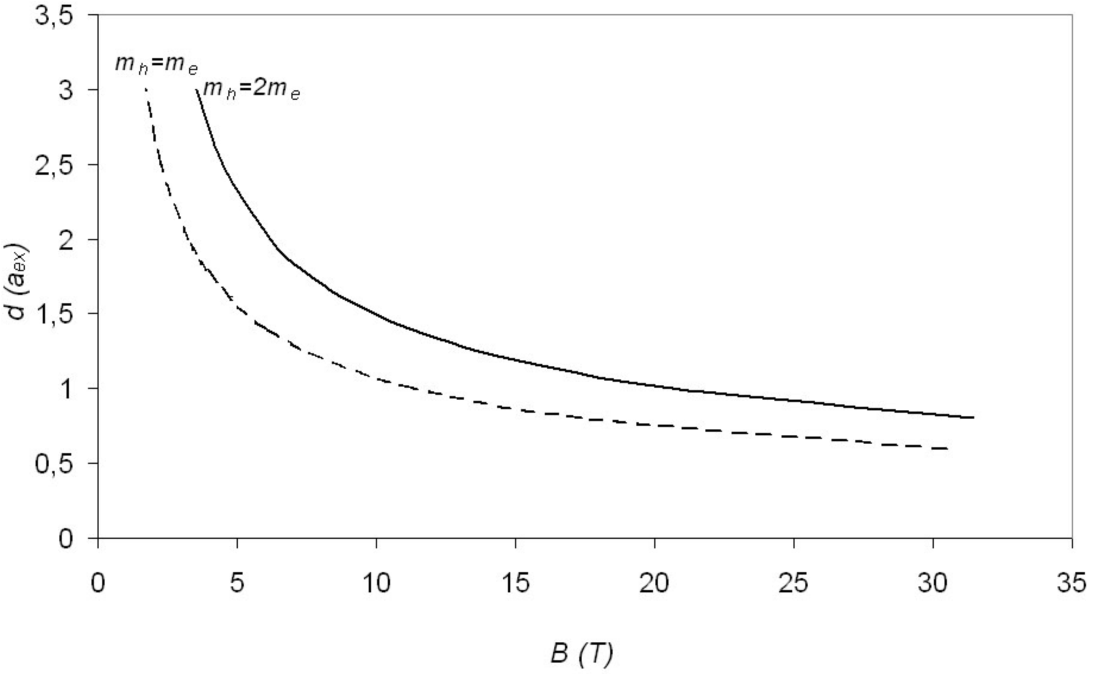

Fig. 3. The phase diagram of transition from state $k_e = (0,1,2)$ and $k_h = (0,1,2)$ to state $k_e = (1,2,3)$ and $k_h = (1,2,3)$ (N=3, $m_e = 0,077m_0$)

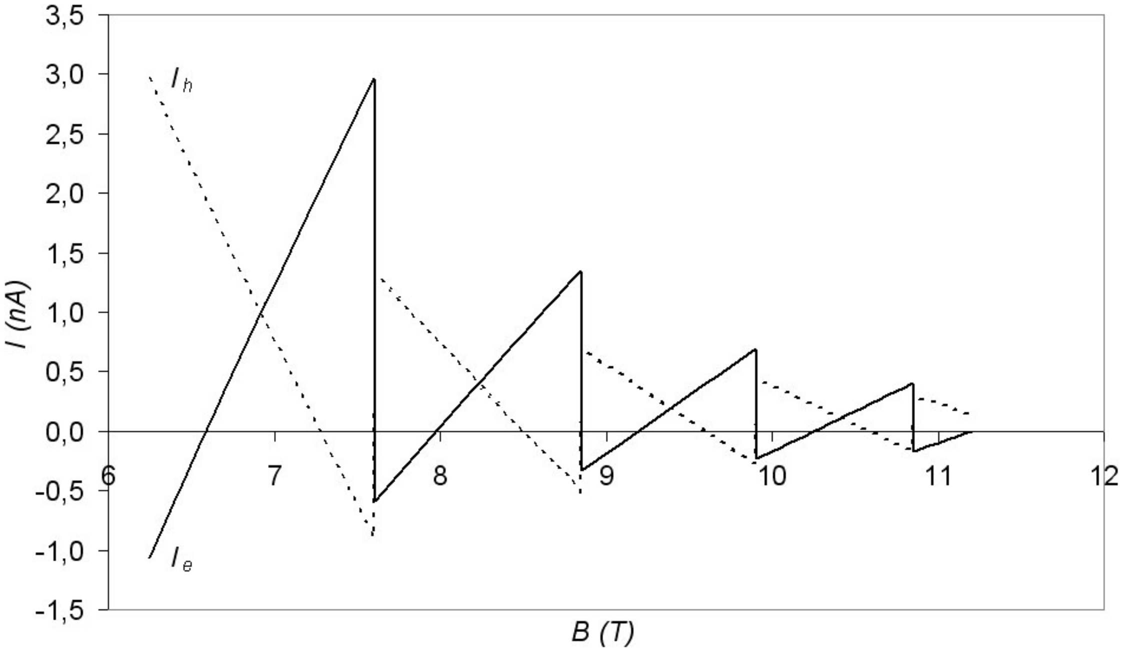

Fig. 4. The persistent current versus the magnetic field ($N = 3$, $d = 2$, $m_h = 2m_e$, $m_e = 0,077m_0$)

system was calculated and a series of magic numbers were found for the total angular momentum of the electrons and holes. Changes in the total angular moment of electrons and holes were shown to lead to oscillations in the persistent current of electrons and holes.

This work was supported by RFBR and Ministry of Education and Science of the Russian Federation.

References

[1] Castelano L. K., et. al. Control of the persistent currents in two interacting quantum rings through the Coulomb interaction and interring tunneling. *Phys. Rev. B.*, **78**, P. 195315 (2008).

[2] Kleemans N.A.J.M. et. al. Oscillatory persistent currents in self-assembled quantum rings. *Phys. Rev. Lett.*, **99**, P. 146808 (2007).

[3] Vasilchenko A.A., Yakovenko N.A. The electronic structure of a quantum dot in a strong magnetic field. *Engineering Physics*, **5**, P. 2-4 (2008).

NANOSYSTEMS: PHYSICS, CHEMISTRY, MATHEMATICS, 2013, 4 (2), P. 241–246

SYNTHESIS OF HEXAGONAL LAF$_3$: ND^{3+}, SM^{3+} NANO CRYSTALS AND STUDIES OF NLO PROPERTIES

S. G. Gaurkhede[1], M. M. Khandpekar[2], S. P. Pati[3], A. T. Singh[4]

[1] Department of Physics, Bhavans College of ASC, Andheri (W) Mumbai-400058.India
[2] Material Research Lab, Department of Physics, Birla College, Kalyan – 421304.India
[3] National Institute of Science and Technology,Palur Hills,Behrampur-761008, Odisha.India
[4] Department of Physics, K. M. Agarwal College of ASC, Kalyan-421301.India
[1]s.gaurkhede@gmail.com

Hexagonal shaped LaF$_3$ nanocrystals (NC) doped by Nd^{3+} and Sm^{3+} ions were synthesized using a domestic microwave oven. The powder XRD study confirmed that the crystalline size of the particle was approximately 20 nm (JCPDS standard card (32–0483) of pure hexagonal LaF$_3$ crystals).The Transmission Electron Microscope (TEM) analysis indicated the size of the primary and secondary particles were between 15–20 nm. The presence of fundamental groups was verified by FTIR spectra. The synthesized nanocrystals were also studied for Non-Linear Optical (NLO) properties. The Second Harmonic Generation (SHG) efficiencies of LaF$_3$: Nd^{3+}, Sm^{3+} containing rare earth elements were found to be less than that of pure Potassium Dihydroxyl Phosphate (KDP) crystals.

Keywords: microwave radiation, hexagonal shape, luminescent properties, x-ray diffraction.

1. Introduction

In recent years, the fields of luminescence and display materials have undergone a revival of sorts with the evolution of nano-sized luminescent particles, driven primarily by an ever-increasing awareness of the unique physical and optical properties that nanometer-scale particles have when compared to their identical bulk material analogs [1]. Studies on the luminescent properties of lanthanide-doped nanoparticles have attracted a great deal of interest, since they have utility in the following applications: phosphors in lamps and display devices [2], components in optical telecommunication equipment [3], active materials in lasers [4], new optoelectronics devices [5], up converters [6–8], magnetic resonance imaging (MRI) [9], and biological fluorescent labels [10–12]. LaF$_3$ nanocrystals are widely used as: lubricants, additives in steel and metal alloys, electrode materials [13] and chemical- and biosensors [14]. LaF$_3$ possesses low phonon energy, adequate thermal and environmental stability [15], and hence, is an excellent host matrix [16–18] for investigating luminescence . Nanoparticles of LaF$_3$ doped with other lanthanide ions, have been studied for their luminescent properties [19–23]. In Several investigations were performed to investigate the optical properties of LaF$_3$:Nd^{3+} [24] for their possible use in optoelectronics devices. This paper presents a study of LaF$_3$:Nd^{3+}, Sm^{3+} nanoparticles synthesized in laboratory with a simple method utilizing microwave irradiation. The nanoparticles synthesized in this manner have hexagonal shape and exhibit luminescence.

2. Experimental

LaF$_3$: Nd^{3+} and Sm^{3+} nanocrystals were synthesized in an aqueous medium using microwave irradiation for low power heating. The method was characterized by its simplicity and cost-effectiveness. Water soluble LaCl$_3$+NdCl$_3$+ SmCl$_3$ (1 unit) and NH$_4$F (3 units) were mixed to obtain a solution in 1:3 molar ratio [25]. A 10 ml solution was prepared with de-ionized water in a 100 ml beaker using 0.064 mol LaCl$_3$+NdCl$_3$+SmCl$_3$. To this, a 10 ml solution of 0.576 mol NH$_4$F was added in a dropwise manner via a funnel fitted with a stopper to control the addition rate. The whole set up can be placed in a conventional microwave oven during reaction. The microwave oven was operated using the low power setting (in on-off mode set at 30 sec) for 30 minutes. The low power range helps to avoid overheating and bumping, thus improving the yield . A white ultrafine crystalline precipitate identified as doped LaF_3 nanocrystals appeared almost instantly at the bottom of the beaker. The precipitate was washed several times with de-ionized water, absolute methanol and acetone, and then dried it in the microwave oven for approximately 15 minutes. The dried sample was then stored in sealed tubes for further characterization.

LaF_3: Nd^{3+} and Sm^{3+} nanocrystals were also prepared using methanol in place of deionized water with the method described above.

3. Characterization

Powder x-ray diffraction (XRD) measurements were performed using a PANALYTICAL X'PERT PROMPD diffractometer model. Transmission electron microscope (TEM) analysis was performed t for different magnifications using a PHILIPS (CM 200). Fundamental groups were verified by FTIR spectra using a Spectrum one: FT-IR Spectrometer. The fluorescence spectrum was measured with a LS 45 luminescence spectrometer (Perkin Elmer Corp). NLO studies, as measured by SHG efficiency, was obtained from the crystalline powder sample by using the method of Kurtz and Perry.

4. Result and Discussion

The XRD results are shown in Fig.1 which indicated that LaF_3: $Nd^{3+}Sm^{3+}$ nanoparticles were well crystallized, and the patterns are in good agreement with hexagonal structure (Space group: P_3cl (165), Cell=$0.7187\times0.7187\times0.735$ nm^3, $\alpha = \beta = 90$ °, $\gamma = 120$ °) known for bulk LaF_3 (JCPDS card No. 32-0483) [26]. The calculated cell parameters $a = b = 0.7126$ nm and $c = 0.7255$ nm for the LaF_3: $Nd^{3+}Sm^{3+}$ nanoparticles, are smaller than those of undoped LaF_3 nanoparticles ($a = b = 0.7187$ nm and $c = 0.735$ nm.

The decrease in the lattice parameters of LaF_3: Nd^{3+} , Sm^{3+} nanoparticles can be attributed to the smaller radius of Nd^{3+} ion (0.99 nm) and Sm^{3+} ion (0.96 nm) in comparison to the La^{3+} ion (0.106 nm) [27–29]. This indicated that Nd^{3+} ions and Sm^{3+} ions were doped into the LaF_3 lattice and occupied the site of La^{3+} ions, with the formation of a LaF_3: Nd^{3+}, Sm^{3+} solid solution. The broadening of diffraction peaks for LaF_3: Nd^{3+}, Sm^{3+} nanoparticles is also shown by Fig. 1, which revealed the nanocrystalline nature of the samples. According to the Scherrer equation, $D = 0.90\lambda/\beta\cos\theta$, where D is the average crystal size, λ is the x-ray wavelength (0.15405 nm); θ and β being the diffraction angle and full width at half maximum of an observed peak, respectively. After subtraction of the equipment broadening, the full width at half maximum (FWHM) of the strongest peak (111) at $2\theta = 27.9$ ° helped to calculate the average crystalline size of LaF_3: Nd^{3+}, Sm^{3+} nanoparticles as 15–20 nm.

The transmission electron microscopy (TEM) image in Fig. 2 showed that the particles were well separated from each other. The nanocrystals had a hexagonal shape and a particle size of 6–20 nm. When these nanocrystals were incorporated into the polymer matrix, these particles were so small that the Rayleigh scattering was negligible. The selected area electron diffraction (SAED) pattern in (Fig. 2 inset) showed three strong diffraction rings corresponding to the (002), (111) and (300) reflections, which is in agreement with the hexagonal LaF_3 structure [30], suggesting that the original structure of LaF_3 was retained even after the modification. The particle sizes derived using TEM were in agreement with the values obtained from XRD studies.

Figure 3 has shown FTIR spectrum of the LaF_3: Nd^{3+}, Sm^{3+} nanocrystals. The characteristic absorption peaks were observed in the 4000–500 cm^{-1} range. The broad absorption band

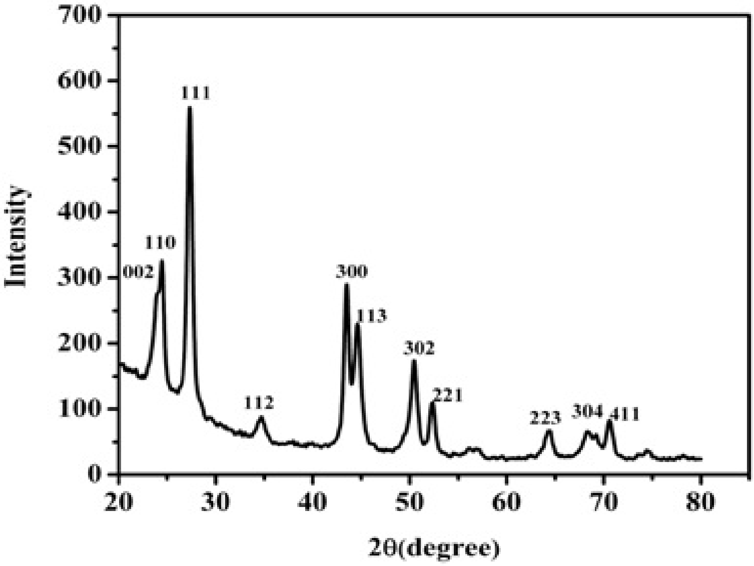

FIG. 1. XRD pattern of LaF_3: Nd^{3+}, Sm^{3+} nanocrystals

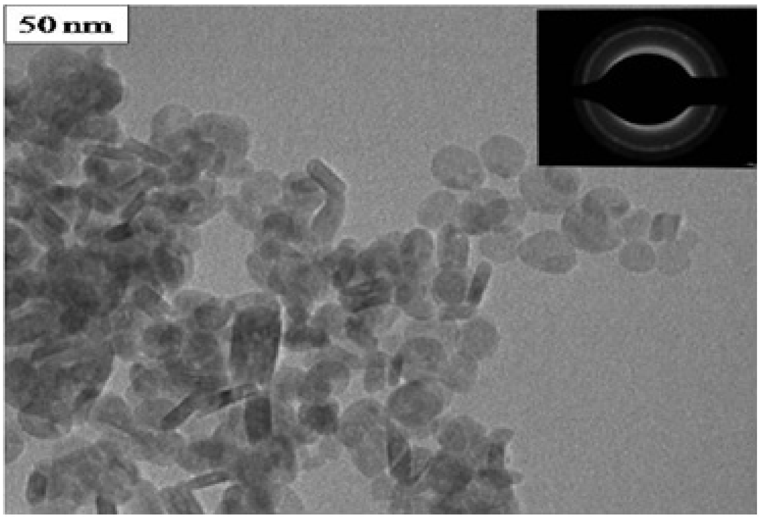

FIG. 2. TEM image of Nd^{3+}, Sm^{3+} doped LaF_3 nanocrystals

at 3434 cm^{-1} can be attributed to ν_{as} (O–H) stretching and bending vibrations. The peaks at 2925 cm^{-1} and 2853 cm^{-1} correspond to the ν_{as} (C–H) group of the long alkyl chain [31–34]. The peak at 1632 cm^{-1} could be assigned to δ (H_2O) bending vibrations from the residual water, while the one at 1439 cm^{-1} can be assigned to the asymmetric (ν_{as}) and symmetric (ν_{as}) bending vibrations of δ (O–H) group from methanol. Other absorptions can be assigned to methanol and acetone as a result of their use in the preparation of the sample.

Nonlinear optics (NLO) is the branch of optics which studies the nonlinear interactions of electromagnetic radiation and the medium through which it is propagated. The nonlinear interactions arise when the medium responds in a nonlinear manner to the incident radiation fields, this being characterized as a change in the wavelength frequency of the incident electromagnetic waves. Typically, these nonlinear interactions are observed only with very high intensity (electric field) light. Second-harmonic generation (SHG) is a second-order nonlinear phenomenon, whereby a fundamental wave is partially converted into a second-harmonic (SH)

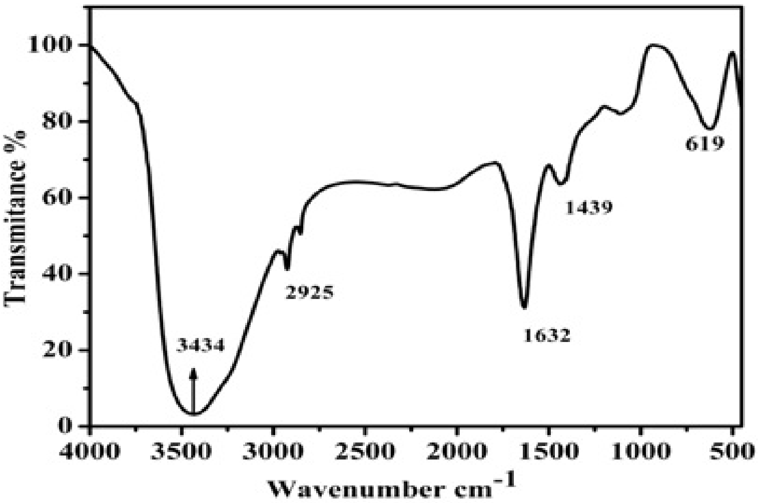

FIG. 3. FTIR spectrum of the of Nd^{3+}, Sm^{3+} doped LaF_3 nanocrystals

wave with twice the initial frequency. The experimental setup for SHG studies used a mirror and a 50/50 beam splitter. A Q – switched Nd: YAG laser (1064 nm) was used with input pulse energy of 6 mJ/pulse and pulse width of 8 ns which is incident on the LaF_3 powder. The particles were grained into fine powder and packed in the micro capillary tube after sieving. The generation of the second harmonic (SHG) was confirmed by the emission of green radiation (532 nm).

SHG is a key technology as frequency doublers of laser light. The second harmonic generation (SHG) efficiency of the LaF_3 doped Nd^{3+}, Sm^{3+} nanocrystals was studied by using modified version of the Kurtz and Perry [35] methodology with Potassium dihydrogen phosphate (KDP) as the reference material. In comparison to the harmonic signal of 22 mV produced from KDP, an SHG efficiency of 0.281 (6.2 mV) was recorded in de-ionized water and 0.513 (11.3 mV) for LaF_3 doped Nd^{3+}, Sm^{3+} in methanol. Less work has been done on SHG efficiency.

5. Conclusions

Nanocrystals of LaF_3: Nd^{3+}, Sm^{3+} have been rapidly synthesized by chemical route in an aqueous medium using domestic microwave oven at low power range. These hexagonal lanthanide-doped nanocrystals had particle sizes varying from 15–20 nm, as confirmed by both TEM and XRD studies. FTIR analysis was used for the identification of fundamental groups present in the materials. The SHG efficiency of LaF_3:Ln^{3+} (Ln^{3+}: Nd^{3+}, Sm^{3+}) containing rare earth elements was determined to be less than the value obtained for pure KDP crystals.

References

[1] B.M. Tissue. Synthesis and luminescence of lanthanide ions in nanoscale insulating hosts. *Chemistry of Materials*, **10** (10), P. 2837–2845 (1998).

[2] H. Song, B. Chen, et al. Ultraviolet light-induced spectral change in cubic nano-crystalline Y_2O_3: Eu^{3+}. *Chemical Physics Letters*, **372** (3), P. 368–372 (2003).

[3] M. Nishi, S. Tanabe, et al. Optical telecommunication- band fluorescence properties of Er^{3+}-doped YAG nanocrystals synthesized by glycothermal method. *Optical Materials*, **27** (4), P. 655–662 (2005).

[4] M.M. Lezhnina, H. Kaetker, U.H. Kynast. Synthesis and optical characterization of rare earth nanofluorides. *Optical Materials*, **30** (2), P. 264–272 (2007).

[5] Y.X. Pan , Q. Su, et al. Synthesis and red luminescence of Pr^{3+} doped $CaTiO_3$ nanophosphor from polymer precursor. *J. Solid State Chem*, **174** (1), P. 69–73 (2003).

[6] P.Y. Jia, J. Lin, M. Yu. Sol-gel deposition and luminescence properties of $LiYF_4$: Tb^{3+} thin films. *Journal of Luminescence*, **122** (1), P. 134–136 (2007).

[7] S. Sivakumar, F.C.J.M. Van Veggel, P.S. May. Near-infrared (NIR) to red and green up-conversion emission from silica sol-gel thin films made with $La_{0.45}Yb_{0.50}Er_{0.05}F_3$ nanoparticles, hetero-looping-enhanced energy-transfer (Hetero LEET): a new up-conversion process. *Journal of the American Chemical Society*, **129** (3), P. 620–625 (2007).

[8] J.S. Zhang, W.P. Qin, D. Zhao. Spectral variations and energy transfer processes on both Er^{3+} ion concentration and excitation densities in Yb^{3+}-Er^{3+} co-doped LaF_3 materials. *Journal of Luminescence*, **122** (2), P. 506–508 (2007).

[9] F. Evanics, P.R. Diamente, et al. Water-soluble GdF_3 and GdF_3/LaF_3 nanoparticles-physical characterization and NMR relaxation properties. *Chemistry of Materials*, **18** (10), P. 2499–2505 (2006).

[10] F. Wang, Y. Zhang, X. Fan, M. Wang. One-pot synthesis of chitosan / LaF_3:Eu^{3+} nanocrystals for bio-applications. *Nanotechnology*, **17** (5), P. 1527–1532 (2006).

[11] P.R. Diamente, F.C.J.M. Van Veggel. Water-soluble Ln^{3+}-doped LaF_3 nanoparticles: retention of strong luminescence and potential as biolabels. *Journal of Fluorescence*, **15** (4), P. 543–551 (2005).

[12] D.Y. Kong, Z.L. Wang, C.K. Lin, Z.W. Quan. Bio-functionalization of CeF_3:Tb^{3+} nanoparticles. *Nanotechnology*, **18** (7), Article ID 075601 (2007).

[13] M. Bralic, N. Radic, S. Brinic, E. Generalic. Fluoride electrode with LaF_3-membrane and simple disjoining solid state internal contact. *Talanta*, **55** (3), P. 581–586 (2001).

[14] N. Miura, J. Hisamoto, et al. Solid-state oxygen sensor using sputtered LaF_3 film. *Sensors and Actuators*, **16** (4), P. 301–310 (2001).

[15] O.V. Kudryavtseva, L.S. Garashina, K.K. Rivkina, B.P. Sobolev. Solubility of LnF_3 in lanthanum fluoride. *Soviet Physics-Crystallography*, **18** (2), P. 531–536 (1974).

[16] H.R. Zheng, X.J. Wang, et al. Up-converted emission in Pr^{3+} doped fluoride nanocrystals-based oxyfluoride glass ceramics. *Journal of Luminescence*, **108** (14), P. 395–399 (2004).

[17] X.J. Wang, S.H. Huang, R. Reeves. Studies of the spectroscopic properties of Pr^{3+} doped LaF_3 nanocrystals/glass. *Journal of Luminescence*, **94**, P. 229–233 (2001).

[18] S. Tanabe, H. Hayashi, T. Hanada, N. Onodera. Fluorescence properties of Er^{3+} ions in glass ceramics containing LaF_3 nanocrystals. *Optical Materials*, **19** (3), P. 343–349 (2002).

[19] M.J. Dejneka. The luminescence and structure of novel transparent oxyfluoride glass-ceramics. *Journal of Non- Crystalline Solids*, **239** (1), P. 149–155 (1998).

[20] S. Fujihara, C. Mochizuki, T. Kimura. Formation of LaF_3 microcrystals in sol-gel silica. *Journal of Non-Crystalline Solids*, **244** (2), P. 267–274 (1999).

[21] B.S. Zhuchkov, V.P. Tolstoy, I.V. Murin. Synthesis of ScF_3, LaF_3 nanolayers and nLaF_3-mScF_3 multinanolayers at the surface of silicon by successive ionic layer deposition method. *Solid State Ionics*, **101** (1), P. 165–170 (1997).

[22] J.F. Zhou, Z.S. Wu, et al. Study on an antiwear and extreme pressure additive of surface coated LaF_3 nanoparticles in liquid paraffin. *Wear*, **249** (6), P. 333–337 (2001).

[23] D.B. Pi, F. Wang et al. Luminescence behavior of Eu^{3+} doped LaF_3 nanoparticles. *Spectrochimica Acta A*, **61** (11), P. 2455–2459 (2005).

[24] J.W. Stouwdam, G.A. Hebbink, et al. Lanthanide-doped nanoparticles with excellent luminescent properties in organic media. *Chemistry of Materials*, **15** (24), P. 4604–4616 (2003).

[25] J.X. Meng, M.F. Zhang, Y.L. Liu. Hydrothermal preparation and luminescence of LaF_3:Eu^{3+} nanoparticles. *Spectrochimica Acta A*, **66** (1), P. 81–85 (2007).

[26] W.T. Carnall, G.L. Goodman, K. Rajnak, R.S. Rana. A systematic analysis of the spectra of the lanthanides doped into single crystal LaF_3. *The Journal of Chemical Physics*, **90** (7), P. 3443–3457 (1989).

[27] Y.F. Liu, W. Chen, et al. X-ray luminescence of LaF_3:Tb^{3+} and LaF_3:Ce^{3+}, Tb^{3+} water-soluble nanoparticles. *Journal of Applied Physics*, **103** (6), Article ID 063105 (2008).

[28] F. Wang, Y. Zhang, X. Fan, M. Wang. Facile synthesis of water-soluble LaF_3:Ln^{3+} nanocrystals. *Journal of Materials Chemistry*, **16** (11), P. 1031–1034 (2006).

[29] J. Wang, J. Hu, et al. Oleic acid (OA)-modified LaF_3: Er,Yb nanocrystals and their polymer hybrid materials for potential optical-amplificationapplications. *Journal of Materials Chemistry*, **17** (16), P. 1597–1601 (2007).

[30] X. Wang, J. Zhuang, Q. Peng, Y. Li. Hydrothermal synthesis of rare-earth fluoride nanocrystals. *Inorganic Chemistry*, **45** (17), P. 6661–6665 (2006).

[31] H. Guo, T. Zhang, et al. Ionic liquid based approach to monodisperse luminescent LaF_3:Ce,Tb nanodiskettes: synthesis, structural and photoluminescent properties. *Journal of Nanoscience and Nanotechnology*, **10** (3), P. 1913–1919 (2010).

[32] W.Y. Feng, T.Y. Wen, et al. Synthesis of LaF_3 superfine powder by microwave heating method. *Trans. Nonferrous Met. Soc. China*, **14** (4), P.738–741 (2004).

[33] P.J. Thistlethwaite, M.S. Hook. Diffuse reflectance fourier transform infrared study of the adsorption of oleate/oleic acid onto titania. *Langmuir*, **16** (11), P.4993–4998 (2000).

[34] P.J. Thistlethwaite, M.L. Gee, D. Wilson. Diffuse reflectance infrared fourier transform spectroscopic studies of the adsorption of oleate/oleic acid onto zirconia, Langmuir, **12** (26), P. 6487–6491 (1996).

[35] S.K. Kurtz, T.T. Perry. A powder technique for the evaluation of nonlinear optical materials. *Journal of Applied Physics*, **39** (8), P. 3798–3813 (1968).

NANOSYSTEMS: PHYSICS, CHEMISTRY, MATHEMATICS, 2013, 4 (2), P. 247–259

SOME ASPECTS OF CARBON NANOTUBES TECHNOLOGY

A. V. Melezhyk, A. V. Rukhov, E. N. Tugolukov, A. G. Tkachev

Tambov State Technical University, Russian Federation, 392000, Tambov, Sovetskaya str., 106.

nanocarbon@rambler.ru, artem1@inbox.ru, tugolukov.en@mail.ru, nanotam@yandex.ru

Different carbon sources (e.g. hydrocarbons, oxygen containing organic compounds) were evaluated for their use in the chemical vapor deposition (CVD) process of carbon nanotube (CNT) production with regards to their efficiency and environmental safety. The effects of both the carbon source and gas feed rates on the yield of the obtained CNT's were determined. The data obtained indicate that intermediate species formed in gas-phase thermal transformations of carbon sources play important roles in the CVD process of CNTs growth. Particularly, it is supposed that ketene, which is an intermediate species in the thermal decomposition of acetone , is the immediate source of carbon for CNTs growth in the CVD processes utilizing acetone as a carbon source.

Keywords: carbon nanotubes, CVD, source of carbon, acetone, ketene, mass yield, conversion.

1. Introduction

Carbon nanotubes (CNTs) are promising materials which have applications in various technological fields. Due to improved technology and the increased scale of CNTs production at present their cost has dropped to a level where the application of CNTs could be economically viable in many areas. The large scale production and wide application of CNTs makes the selection of raw materials important. Among the factors which should be considered when selecting a carbon source are the yield and quality of the CNTs produced, the environmental impact and the overall safety of the CVD process.

Hydrocarbons were most frequently used as carbon sources for the production of CNTs by the CVD method at ambient pressure, however, there have been few articles published concerning the analysis and relative efficiency of different hydrocarbon sources for CNTs synthesis via the CVD process [1,2].

Methane is the most readily available hydrocarbon, being the main component of "natural gas", which is widely used as an energy source. The use of methane for CNTs production has been amply documented [3–9]. The use of methane as a carbon source for CNTs synthesis has two distinct disadvantages. First, only high purity methane is acceptable for this synthesis. Ethane and propane, which usually are present in natural gas as admixtures, are much more reactive than methane and can complicate the synthetic process, yielding non-reproducible results and low quality CNTs. Methane of high purity is relatively expensive, because cryogenic temperature rectification and/or adsorption technologies are necessary for the refining of crude methane. Secondly, methane usually demands higher temperature for conversion into CNTs (850–1000 °C compared to 600–700 °C for higher alkanes and unsaturated hydrocarbons). This is of minor importance for laboratory settings, however, for industrial applications, increasing reaction temperature necessitates the use of more expensive construction materials and thermal insulation; the durability of the construction drops because of increased thermal stresses; problems arise from increased heat transfer by radiation, which is proportional to 4th power of absolute temperature; consumption of energy increases. In spite of these disadvantages, methane is still suitable for the generation of high quality single- and double-wall nanotubes

(SWNTs and DWNTs) provided that appropriate catalysts and optimal technological regimes are implemented.

Higher saturated hydrocarbons, such as propane, butane, and hexane have been used in the synthesis of CNTs via the CVD process. For these hydrocarbons, the optimal reaction temperature usually ranges from 600–700 °C. However, Ajayan et al. describe how long strands of SWNTs were grown from n-hexane with floating catalyst (ferrocene + thiophene) at much higher temperatures, 1100–1200 °C [10]. In several works, liquefied petroleum gas, consisting of propane and butane (sometimes containing an admixture of sulfur-containing organic compounds) was successfully used for the production of multiwalled CNTs [11–17].

Regarding the application of saturated hydr °Carbons in the CVD method of CNTs synthesis, it is well known that saturated hydrocarbons at ca. 700 °C or above rapidly undergo a series of non-catalytic gas phase free-radical reactions resulting in the formation of a complex mixture of hydrogen, methane, ethylene, propylene, and higher saturated and unsaturated hydrocarbons [18]. With longer reaction times, heavy hydrocarbons (condensed aromatics) appear in significant amounts.

When these facts are considered, the nature of the original saturated hydrocarbon seems to be of minor importance when compared to the optimal reaction temperature. Due to the fast thermal transformations of the starting hydrocarbons, the species which react with the catalyst of CVD process may be the products, or intermediates of hydrocarbon pyrolysis. So, if n-hexane was used by Ajayan et al [10] as the carbon source for obtaining long strands of SWNTs, undoubtedly the n-hexane molecules were not the species directly reacting with the catalyst to grow CNTs, because at 1100–1200 °C thermal transformations of n-hexane are extremely fast. In all likelihood, one could obtain similar results by supplying the reactor with a gas mixture containing methane, hydrogen, ethylene and other hydrocarbons.

Unsaturated hydrocarbons, such as acetylene, ethylene, and propylene have been frequently used for CNTs production. It follows from analysis of published data that all these hydrocarbons permit the generation of high quality carbon nanotubes, provided that optimal catalysts and conditions were used. For instance, Hao et al utilized propylene (diluted with nitrogen) as the carbon source for large-scale fluidized-bed CVD process of CNTs production [19].

The published results from numerous studies and our data would seem to indicate that the dilution of unsaturated hydrocarbons with an inert gas is necessary to retard their cycloaromatization with the unwanted formation of heavy hydrocarbons. When these gas phase reactions are not diluted, they tend to form tar-like products which condense on cold walls at the reactor outlet. The longer the reactants are in the hot zone of the reactor, the more dilute these hydrocarbons must be to avoid tar formation. Through experimentation, it was shown that the unsaturated hydrocarbons listed above can be arranged in following order by their tendency to give tar: acetylene > ethylene > propylene. Hence, from these findings, propylene appears to be most suitable as a carbon source for the CVD process. Additionally, propylene can be easily transported in a liquefied state at relatively low pressure (nearly 1 MPa), while ethylene is transported in high pressure balloons.

Aromatic hydrocarbons (benzene, toluene, and xylene) were also studied as carbon sources for CNTs production however, they do not seem to offer substantial advantages over alkanes and alkenes and thus, were not widely used.

The principal disadvantage of using hydrocarbons for CNTs production (with exception of methane) is the formation of harmful by-products such as condensed poly-nuclear aromatics. Conversion of a carbon source to CNTs in any case does not reach 100%. Practically, conversion to CNTs usually amounts 30–80% in CVD processes of multi-walled nanotube synthesis

(MWNTs) and is much less (1–10%) in cases of SWNTs and DWNTs production. Thus, the formation of harmful by-products is unavoidable even if optimal conditions are used.

Oxygen-containing organic compounds may be used as an alternative to hydrocarbons for CNTs production. Among these, ethanol was the most widely studied [20–44]. Ethanol is most suitable for obtaining SWNTs and DWNTs and less acceptable for MWNTs synthesis. In SWNTs or DWNTs synthesis via CVD, the starting material (carbon source) is usually diluted with inert gas (argon, nitrogen) to a volume content of ethanol vapor not more than several %. Dilution of the carbon source, together with the application of a catalyst with low mass content of catalytically active metals, favors the formation of thin nanotubes (SWNTs and DWNTs). One of the pyrolysis products of ethanol is water. Water vapor in low concentrations favors the formation of and increases the yield of both SWNTs and MWNTs [45–47]. Evidently, any oxygen-containing compound, even CO_2 [48] for instance, in low concentration should exhibit the same effect because of the reversible nature of reactions of oxygen-containing organic compounds in a hydrocarbon-containing atmosphere at high temperatures. However, if there is too much water in the reacting gas mixture, the growth of nanotubes is suppressed, because at high temperatures water reacts with carbon. Hence, ethanol is less suitable as a carbon source for the generation of multi-walled carbon nanotubes because usually a more concentrated carbon source is needed for efficient growth of MWNTs, and, if so, too much water is generated from the decomposition of ethanol.

Other oxygen-containing organics, such as camphor [49] and phenol [50] have been used as carbon source for CVD synthesis of carbon nanotubes, however, the advantages of these compounds as carbon sources are uncertain.

Different alcohols and ketones were studied as carbon sources for CNTs CVD synthesis and the highest quality nanotubes were obtained from acetone [51]. In view of this, acetone appears to be a promising raw material for CNTs production.

The present work evaluated different organic compounds as carbon sources for the CVD process of CNTs production.

2. Experimental

CNTs were obtained by the CVD method using a fixed bed laboratory reactor. A horizontal quartz tube reactor (inner diameter 37 mm, length 1150 mm, volume of hot zone nearly 0.5 L) was used in our experiments. Samples of catalysts were placed into the reactor on a semi-cylindrical Graflex (flexible graphite foil) support. The feed rates of gases were measured and regulated with a "MassFlow" (Bronkhorst HIGH TECH) and are given below at standard conditions. A tubular ceramic furnace PT-1.2-70 was used for precision temperature control. Mass yields of CNTs were calculated as ratio of mass of the crude product minus mass of starting catalyst divided by mass of catalyst. It was found from SEM and TEM images that in all cases the products were nanotubes without visible admixture of other particles. Conversion of carbon compounds into CNTs was calculated in % from theoretical assuming that theoretical yield corresponds to conversion of all carbon atoms of a starting compound into CNTs.

Following compounds were used as sources of carbon:

Liquefied propane-butane — technical grade (Russian standard);
Liquefied propylene — 99.95% purity;
Ethanol — 96% (water 4%);
Acetone — "Pure for analysis" (Russian standard);
Argon was used of 99.96% purity, hydrogen — 99.98%.

Electron images of CNTs were recorded with using two-beam scanning electron microscopy complex Neon 40, Carl Zeiss. Raman spectra were obtained with using Integra Spectra spectrometer.

3. Results and Discussion

In Fig. 1 and 2 there are plots of CNTs mass yield and propane-butane to CNTs conversion on argon feed rate. Multicomponent metal oxide (Co,Mo)/MgO–Al_2O_3 was used as a catalyst, the process of CNTs growing was carried out over 30 min at 650 °C. One can see that at constant volume ratio of argon to propane-butane and at constant feed rate of propane-butane, CNTs yield and conversion of propane-butane to CNTs decrease with increasing gas flow speed, with a maximum in one case.

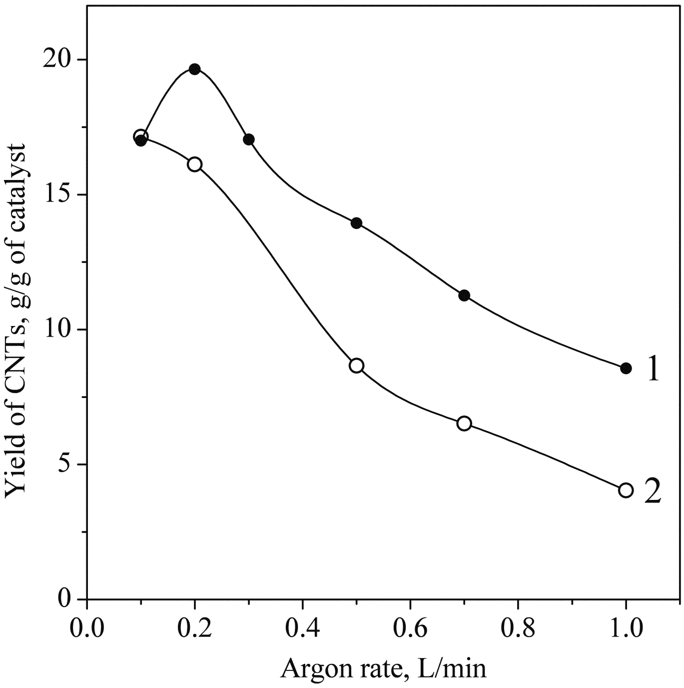

FIG. 1. Dependence of CNTs yield on argon feed rate. (Co,Mo)/MgO–Al_2O_3 catalyst, 30 min, 650 °C. 1 — constant volume ratio of argon to propane-butane (1:1); 2 — constant rate of propane-butane (0.2 L/min)

A much more expressed maximum was observed for the dependence of CNTs yield on propane-butane rate with (Fe,Co,Mo)/Al_2O_3 catalyst (Fig. 3, propane-butane not diluted with argon).

The plots Fig. 1–3 can be explained if we assume that the species which directly reacts with the catalyst is ethylene and/or propylene which is formed via free-radical thermal transformations of propane and butane prior to contact with the catalyst. If the gas flow rate is too high, the concentration of these reactive species and yield of CNTs decreases. Conversely, low gas flow rates can also result in decreased CNTs production because of, (1) deficiency of carbon source, and (2) further transformation (polymerization) of ethylene and propylene to heavier hydrocarbons.

In Fig. 4 the dependence of CNTs yield on the flow rate of propylene diluted with argon at constant volume ratio of argon to propylene (6:1) was determined using the same conditions as in Fig. 3 (catalyst (Fe,Co,Mo)/Al_2O_3, 30 min, 650 °C). In this case, some decrease in the

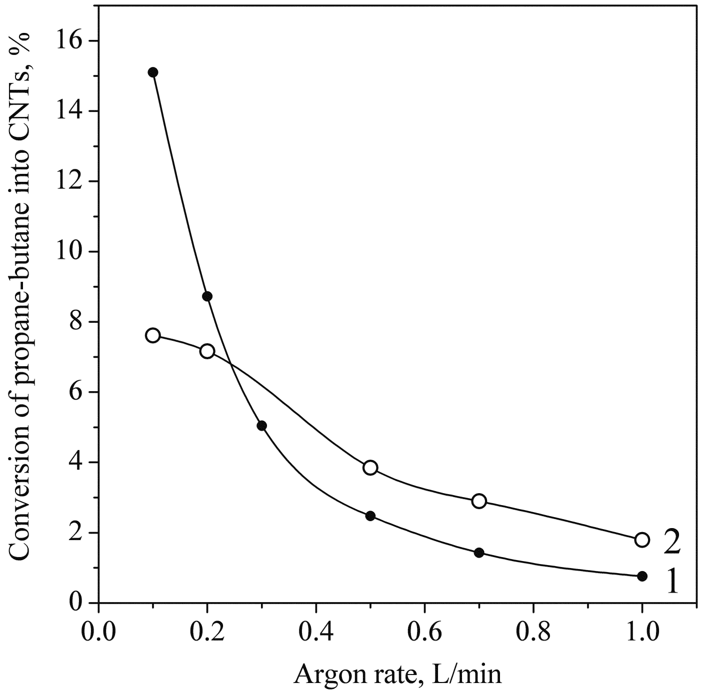

FIG. 2. Dependence of conversion of propane-butane to CNTs (% of theoretical) on argon feed rate. (Co,Mo)/$MgO–Al_2O_3$ catalyst, 30 min, 650 °C. 1 — constant volume ratio of argon to propane-butane (1:1); 2 — constant rate of propane-butane (0.2 L/min)

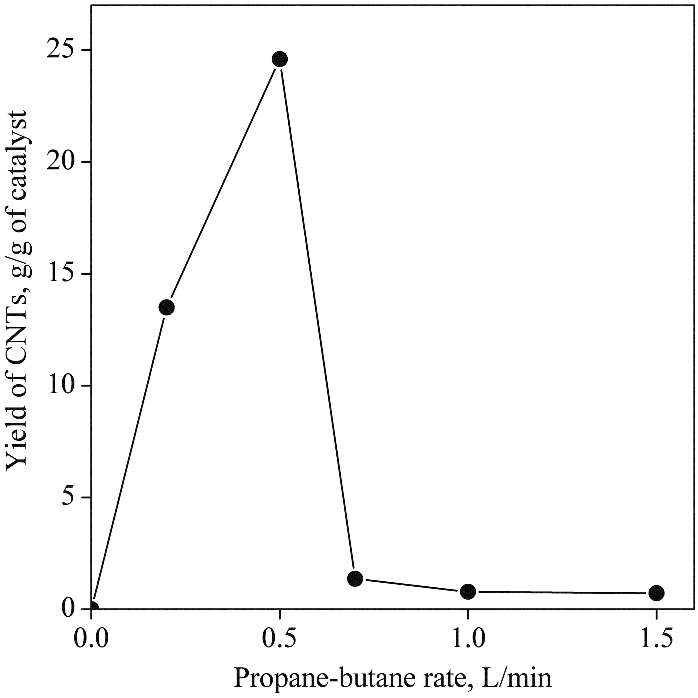

FIG. 3. Dependence of CNTs yield on the propane-butane feed rate. (Fe,Co,Mo)/Al_2O_3 catalyst, 30 min, 650 °C. Propane-butane not diluted with argon

yield with increasing argon rate was also observed, however, the decrease in the yield was not as drastic as in Fig. 3. These data indicate that in the CVD process with propylene, some gas phase reactions also be occurring, but for now, it is difficult to identify them.

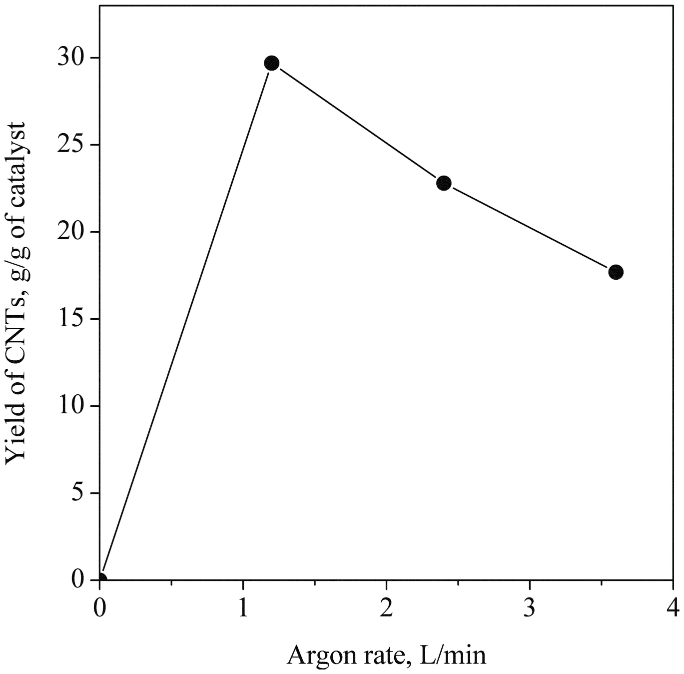

FIG. 4. Dependence of CNTs yield upon argon feed rate. (Fe,Co,Mo)/Al_2O_3 catalyst, 30 min, 650 °C. Constant volume ratio of argon to propylene = 6:1

The data given above prove that gas phase hydrocarbon transformations can play a valuable and even critical role in the CVD synthesis of CNTs. Particularly, the time a gas species remains in the hot zone of a reactor is of critical importance. Proper identification of these transformations is valuable for adjusting the optimal synthesis of CNTs. These parameters should be taken into consideration when designing the CVD reactor.

Inevitably carcinogenic heavy aromatics form as by-products when hydrocarbons are used as raw materials for CNTs synthesis, therefore, some oxygen-containing organic compounds, namely, ethanol and acetone, were studied as alternative sources of carbon.

Experiments with ethanol were conducted at 750 °C, which was found to be optimal (by mass yield) for the catalyst used ((Co,Mo)/MgO–Al_2O_3). As it follows from Fig. 5 and 6, it is impossible to achieve a good mass yield of MWNTs together with good conversion of ethanol into MWNTs. This is most likely due to the formation of large amounts of water via the thermal decomposition of ethanol.

The thermal decomposition of acetone is principally different from that of hydrocarbons and alcohols. The pyrolysis of acetone, which occurs at 500–700 °C, gives ketene in up to 80% yield if the ketene is quickly removed from the heating zone via the following process:

$$\mathrm{CH_3 - CO - CH_3 \rightarrow \dot{C}H_3 + CH_3 - \dot{C} = O \rightarrow CH_4 + CH_2 = C = O.}$$

The formation of ketene can occur either via a free-radical mechanism, as written above, or as a heterogeneous reaction of acetone molecule on the Lewis acid catalysts (e.g., alumina).

Ketene is toxic, but, as an unstable gas, it quickly polymerizes with the formation of diketene first, and then predominantly 3-acetyl-2-hydroxy-6-methyl-4H-pyran-4-one.

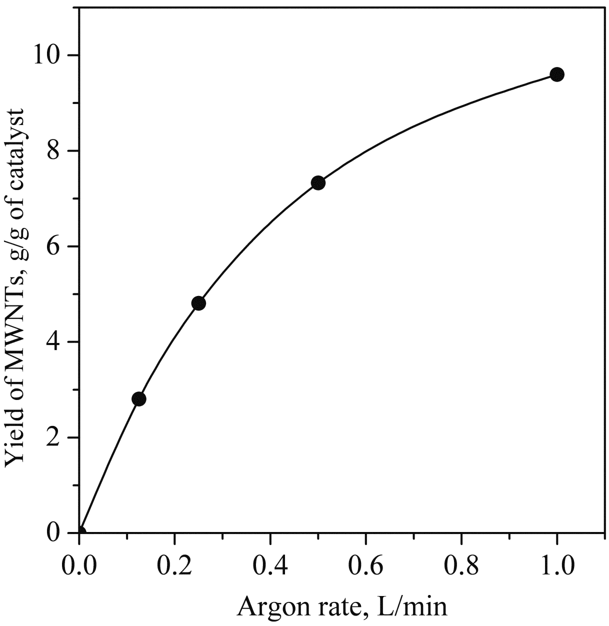

FIG. 5. Dependence of MWNTs yields upon argon flow rate. Catalyst (Co,Mo)/MgO–Al_2O_3, 750 °C, 30 min. The feed rate of argon is proportional that of ethanol, 1 L/min argon (gas) at 40 ml/h ethanol (liquid)

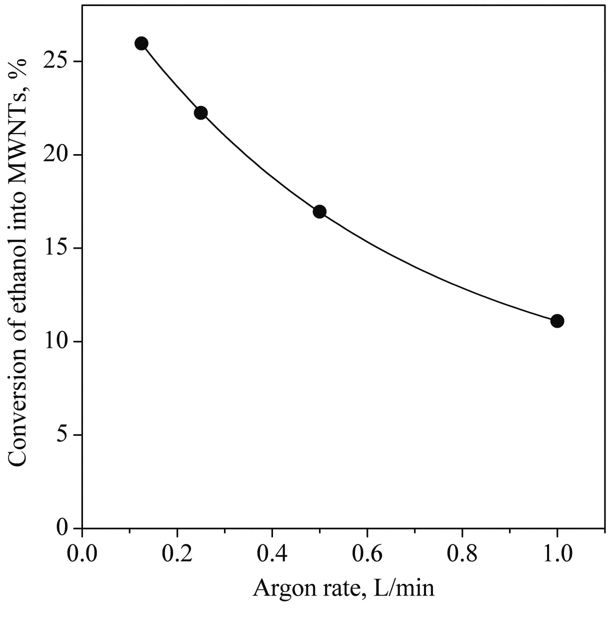

FIG. 6. Dependence of ethanol conversion into MWNTs upon argon feed rate. Catalyst (Co,Mo)/MgO–Al_2O_3, 750 °C, 30 min. The feed rate of argon is proportional to feed rate of ethanol, 1 L/min argon (gas) at 40 ml/h ethanol (liquid)

Ketene reacts rather quickly with water to form acetic acid. Diketene is toxic liquid which is insoluble in water, and as a result, reacts slowly with that medium. The last compound is not harmful and is used for the impregnation of antibacterials onto foodstuff packing materials. Due to high reactivity of ketene and its derivatives it is unlikely that they can remain in nature for a long time and thus, are not likely to accumulate in living organisms, unlike condensed poly-nuclear aromatics which are known to acumulate in organisms.

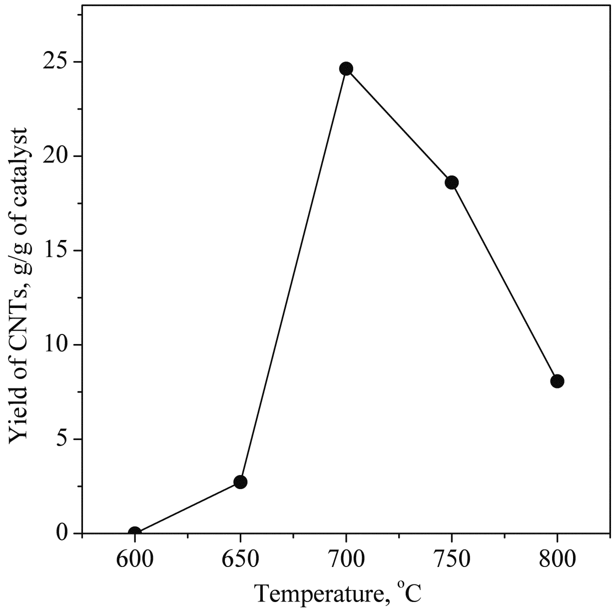

FIG. 7. Dependence of CNTs yield from acetone on temperature. The catalyst is (Co,Mo)/MgO–Al_2O_3. Feed rate of acetone (liquid) was 18.3 ml/h, argon (gas) 1 L/min, duration of synthesis 30 min

Thus, one can hope that the neutralization of acetone pyrolysis by-products, if it used as a raw material for CNTs production, is simpler than sequestering poly-nuclear aromatics, the by-products obtained from hydrocarbons.

A series of experiments were performed in a laboratory reactor in order to evaluate possibility of using acetone for the CVD production of CNTs. Multicomponent metal oxide (Co,Mo)/MgO–Al_2O_3 was used as the catalyst. The preliminary reduction of catalyst with hydrogen (10–15 min) was essential for obtaining good yields of nanotubes when using acetone. On contrary, in cases of hydrocarbons or ethanol, the prior reduction of this and other catalysts was not required. Presumably, these hydrocarbons themselves quickly reduce the catalysts in situ.

As shown in Fig. 7, the maximum yield of CNTs from acetone on this catalyst was obtained at 700 °C. Subsequent experiments were conducted at this temperature.

The yield of acetone-derived CNTs passes through a maximum with increased argon feed rate and decreases with increased substrate in the feeder gas (Fig. 8) as is the case for CNTs synthesis from propane-butane. Fig. 9 shows that a similar dependence was observed for the conversion of acetone into CNTs, but the maximum was observed only at a constant feed rate of acetone. The conversion value at low argon feed rates is sufficiently high, which proves the efficiency of acetone as a feedstock for production of carbon nanotubes. The optimal combination of mass yield and the conversion of acetone to carbon nanotubes was observed at an argon feed rate of ca. 0.3–0.5 L/min.

One can assume that ketene is an intermediate species involved in the growth process of CNTs in this system, however, the decreases in yield and conversion with increased argon feed rate in acetone-based syntheses is less pronounced than in cases of propane-butane systems. Molecules of acetone may also be able to participate in the process of CNTs growth together with ketene. In prior work [51] it was assumed that transient methyl radicals were the source of carbon for CNTs growth in this system. However, in view of the very short lifetime of

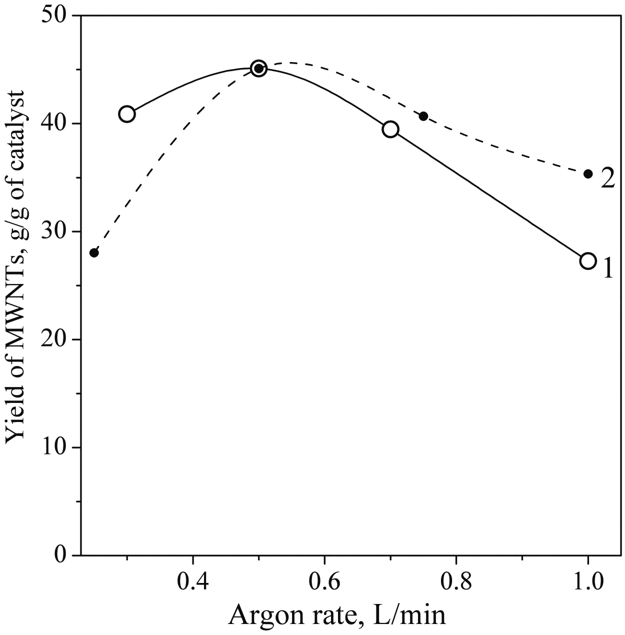

FIG. 8. Dependence of mass yield of CNTs from acetone on argon feed rate. The catalyst (Co,Mo)/MgO–Al_2O_3, 700 °C, duration of synthesis 30 min. 1 — constant feed rate of acetone, 18.3 ml/h (liquid); 2 — feed rate of acetone is proportional to feed rate of argon, 18.3 ml/h acetone (liquid) at 0.5 L/min argon (gas)

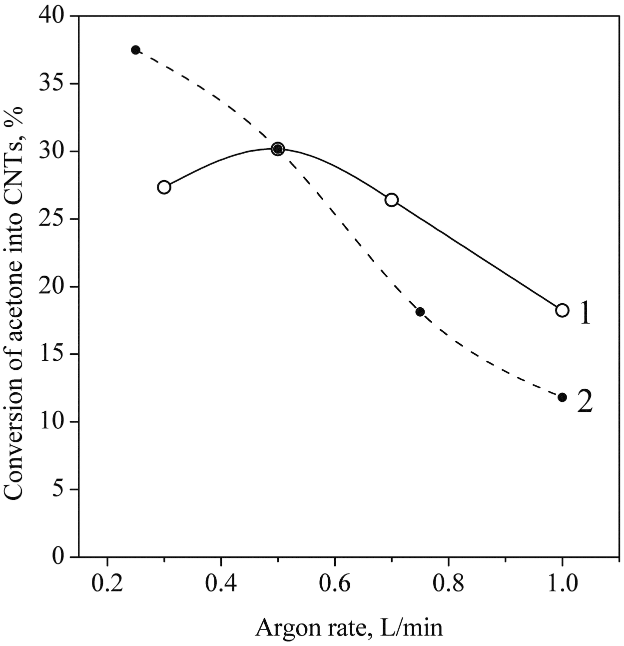

FIG. 9. Dependence of acetone conversion into CNTs on argon feed rate. The catalyst (Co,Mo)/MgO–Al_2O_3, 700 °C, duration of synthesis 30 min. 1 — constant feed rate of acetone, 18.3 ml/h (liquid); 2 — feed rate of acetone is proportional to feed rate of argon, 18.3 ml/h acetone (liquid) at 0.5 L/min argon (gas)

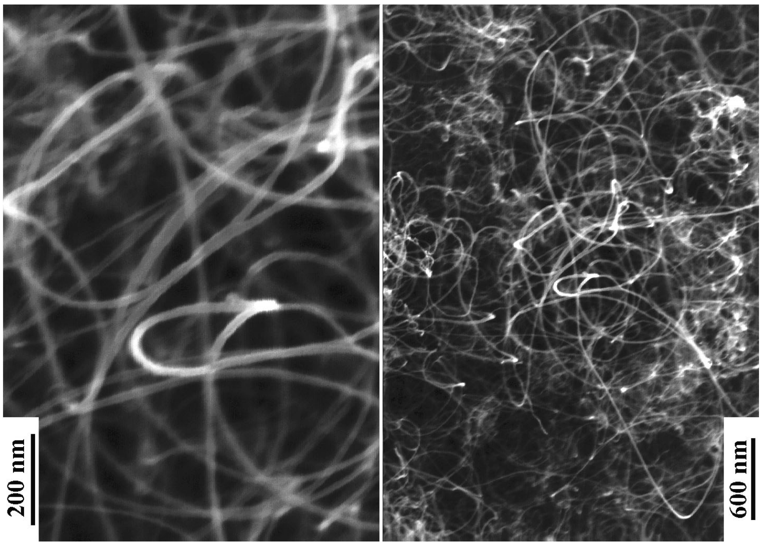

FIG. 10. SEM images of CNTs obtained from acetone. Catalyst (Co,Mo)/MgO–Al_2O_3. 700 °C, duration of synthesis 30 min. Argon feed rate 0.7 L/min (gas), acetone 18.3 ml/h (liquid). Mass yield of CNTs is 39.5 g/g of catalyst

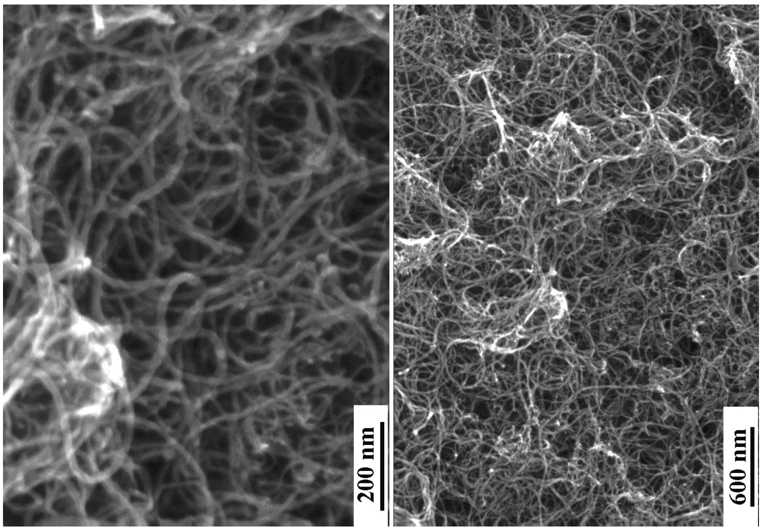

FIG. 11. SEM images of CNTs obtained from propylene. Catalyst (Co,Mo)/MgO–Al_2O_3. 650 °C, duration of synthesis 30 min. Hydrogen feed rate 1.2 L/min, propylene 0.2 L/min (gas). Mass yield of CNTs is 24.5 g/g of catalyst

methyl radicals, their participation in this heterogeneous process of CNTs growth seems to be less probable than the participation of ketene molecules.

Participation of free radical intermediates ("polycyclic free radical condensate") is thought to occur in the CVD process of CNTs synthesis from hydrocarbons [52]. In reality, the formation of liquid, tar-like condensates or deposits on cold walls at the outlet of CVD reactor was often observed. These condensates may be adsorbed on growing nanotubes, however, it is open to question whether they are an intermediate or a by-product in the CVD synthesis of CNTs. It should be noted that the cycloaromatization of unsaturated hydrocarbons can proceed on the same catalysts at the same temperatures which are usually used for CNTs synthesis.

In our investigations to obtain carbon nanofibers from acetylene (which is especially prone to cycloaromtization reactions), condensates were predominantly formed on "bad" catalysts, when the yields of CNTs were low.

The data obtained prove that acetone can be a suitable source of carbon for the production of CNTs by the CVD method.

SEM images of MWNTs obtained using acetone and propylene on the same catalyst, (Co,Mo)/MgO–Al_2O_3, are shown in Fig. 10, 11. CNTs obtained from acetone are less deformed, which indicates higher quality. As is known, Raman spectra are often used for estimation of disorder-order ratio of CNTs structure. The D/G ratio in Raman spectra for different samples of MWNTs obtained from acetone in these experiments ranged from 0.60 to 0.76. This is close to the D/G value of 0.67 found in prior work for high-quality MWNTs obtained from acetone on a (Mn,Co)/zeolite catalyst [51].

4. Conclusions

Intermediate species, which are formed in gas-phase thermal transformations of hydrocarbons, participate in the CVD process of CNTs synthesis. The temperature, flow rate and time present in the reactor are critical factors determining yield of CNTs and conversion of a carbon source into CNTs.

Acetone is a promising source of carbon for an environmentally-benign CVD process for CNTs production. It is possible that ketene, which is an intermediate in the thermal decomposition of acetone, participates in the CVD process of CNTs growth.

References

[1] F. Danafar, A. Fakhru'l Razi, M.A.M. Salleh, D.R.A. Biak. Fluidized bed catalytic chemical vapor deposition synthesis of carbon nanotubes—A review. *Chemical Engineering Journal*, **155**, P. 37–48 (2009).

[2] Q. Li, H. Yan, J. Zhang, Z. Liu. Effect of hydrocarbons precursors on the formation of carbon nanotubes in chemical vapor deposition. *Carbon*, **42**, P. 829–835 (2004).

[3] S. Zhan, Y. Tian, et al. Effect of process conditions on the synthesis of carbon nanotubes by catalytic decomposition of methane. *China Particuology*, **5**, P. 213–219 (2007).

[4] Z. Niu, Y. Fang. Effect of temperature for synthesizing single-walled carbon nanotubes by catalytic chemical vapor deposition over Mo-Co-MgO catalyst. *Mater. Res. Bull.*, **43**, P. 1393–1400 (2008).

[5] Z. Niu, Y. Fang. Effects of synthesis time for synthesizing single-walled carbon nanotubes over Mo-Fe-MgO catalyst and suggested growth mechanism. *J. of Crystal Growth*, **297**, P. 228–233 (2006).

[6] M. Inoue, K. Asai, et al. Formation of multi-walled carbon nanotubes by Ni-catalyzed decomposition of methane at 600–750 °C. *Diamond and Related Materials*, **17**, P. 1471–1475 (2008).

[7] H. Ago, N. Uehara, et al. Gas analysis of the CVD process for high yield growth of carbon nanotubes over metal-supported catalysts. *Carbon*, **44**, P. 2912–2918 (2006).

[8] W. Gac, A. Denis, T. Borowiecki, L. Kepinski. Methane decomposition over Ni-MgO-Al_2O_3 catalysts. *Appl. Catal. A: General*, **357**, P. 236–243 (2009).

[9] V.Z. Mordkovich, E.A. Dolgova, et al. Synthesis of carbon nanotubes by catalytic conversion of methane: Competition between active components of catalyst. *Carbon*, **45**, P. 62–69 (2007).

[10] P.M. Ajayan, B. Wei. Direct synthesis of long single-walled carbon nanotube strands. United States Patent 7615204, D01F 9/12 (20060101), B82B 1/00 (20060101) (2009).

[11] W. Qian, H. Yu, et al. Synthesis of carbon nanotubes from liquefied petroleum gas containing sulfur. *Carbon*, **40**, P. 2968–2970 (2002).

[12] P.M. Akbarzadeh, A. Shafiekhani, M.A. Vesaghi. Hot filament CVD of Fe-Cr catalyst for thermal CVD carbon nanotube growth from liquid petroleum gas. *Appl. Surface Science*, **256**, P. 1365–1371 (2009).

[13] J. Huang, Q. Zhang, et al. Liquefied petroleum gas containing sulfur as the carbon source for carbon nanotube forests. *Carbon*, **46**, P. 291–296 (2008).

[14] P. Ndungu, A. Nechaev, et al. Carbon nanomaterials synthesized using liquid petroleum gas: Analysis toward applications in hydrogen storage and production. *Int. J. of Hydrogen Energy*, **33**, P. 3102–3106 (2008).

[15] J.-M. Zhou, G.-D. Lin, H.-B. Zhang. Efficient growth of MWCNTs from decomposition of liquefied petroleum gas on a $Ni_xMg_{1-x}O$ catalyst. *Catal. Comm.*, **10**, P. 1944–1947 (2009).

[16] S.W. Jeong, S.Y. Son, D.H. Lee. Synthesis of multi-walled carbon nanotubes using Co-Fe-Mo/Al_2O_3 catalytic powders in a fluidized bed reactor. *Advanced Powder Technology*, **21**, P. 93–99 (2010).

[17] P. Ndungu, Z.G. Godongwana, et al. Synthesis of carbon nanostructured materials using LPG. *Micropor. and Mesopor. Materials*, **116**, P. 593–600 (2008).

[18] T.N. Mukhina, N.L. Barabanov, et al. *Pyrolisis of hydrocarbon raw*. Moscow, "Khimiya", 240 pp. (1987).

[19] Y. Hao, Z. Qunfeng, et al. Agglomerated CNTs synthesized in a fluidized bed reactor: Agglomerate structure and formation mechanism. *Carbon*, **41**, P. 2855–2863 (2003).

[20] G. Ortega-Cervantez, G. Rueda-Morales, J. Ortiz-Lpez. Catalytic CVD production of carbon nanotubes using ethanol. *Microelectronics Journal*, **36**, P. 495–498 (2005).

[21] Y. Murakami, Y. Miyauchi, S. Chiashi, S. Maruyama. Characterization of single-walled carbon nanotubes catalytically synthesized from alcohol. *Chemical Physics Letters*, **374**, P. 53–58 (2003).

[22] A. Botello-Mendez, J. Campos-Delgado, et al. Controlling the dimensions, reactivity and crystallinity of multiwalled carbon nanotubes using low ethanol concentrations. *Chemical Physics Letters*, **453**, P. 55–61 (2008).

[23] W. Li, H. Wang, et al. Co-production of hydrogen and multi-wall carbon nanotubes from ethanol decomposition over Fe/Al_2O_3 catalysts. *Appl. Catal. B: Environmental*, **84**, P. 433–439 (2008).

[24] S. Inoue, Y. Kikuchi. Diameter control and growth mechanism of single-walled carbon nanotubes. *Chemical Physics Letters*, **410**, P. 209–212 (2005).

[25] Y. Murakami, Y. Miyauchi, S. Chiashi, S. Maruyama. Direct synthesis of high-quality single-walled carbon nanotubes on silicon and quartz substrates. *Chemical Physics Letters*, **377**, P. 49–54 (2003).

[26] J. Diao, H. Wang, et al. Effect of C-supported Co catalyst on the ethanol decomposition to produce hydrogen and multi-walled carbon nanotubes. *Physica E: Low-dimensional Systems and Nanostructures*, **42**, P. 2280–2284 (2010).

[27] Y. Chen, B. Wang, et al. Effect of different carbon sources on the growth of single-walled carbon nanotube from MCM-41 containing nickel. *Carbon*, **45**, P. 2217–2228 (2007).

[28] Q. Liu, Y. Ouyang, et al. Effects of argon flow rate and reaction temperature on synthesizing single-walled carbon nanotubes from ethanol. *Physica E: Low-dimensional Systems and Nanostructures*, **41**, P. 1204–1209 (2009).

[29] G. Wang, H. Wang, et al. Efficient production of hydrogen and multi-walled carbon nanotubes from ethanol over Fe/Al_2O_3 catalysts. *Fuel Processing Technology*, Article in Press, Corrected Proof, doi:10.1016/j.fuproc.2010.11.008.

[30] E. Einarsson, Y. Murakami, M. Kadowaki, S. Maruyama. Growth dynamics of vertically aligned single-walled carbon nanotubes from *in situ* measurements. *Carbon*, **46**, P. 923–930 (2008).

[31] A. Gruneis, M.H. Rummeli, et al. High quality double wall carbon nanotubes with a defined diameter distribution by chemical vapor deposition from alcohol. *Carbon*, **44**, P. 3177–3182 (2006).

[32] H. Sugime, S. Noda. Millimeter-tall single-walled carbon nanotube forests grown from ethanol. *Carbon*, **48**, P. 2203–2211 (2010).

[33] M. Wienecke, M.-C. Bunescu, et al. MWCNT coatings obtained by thermal CVD using ethanol decomposition. *Carbon*, **44**, P. 718–723 (2006).

[34] Q. Liu, Y. Fang. New technique of synthesizing single-walled carbon nanotubes from ethanol using fluidized-bed over Fe-Mo/MgO catalyst. *Spectrochimica Acta Part A: Molecular and Biomolecular Spectroscopy*, **64**, P. 296–300 (2006).

[35] S. Chaisitsak, J. Nukeaw, A. Tuantranont. Parametric study of atmospheric-pressure single-walled carbon nanotubes growth by ferrocene–ethanol mist CVD. *Diamond and Related Materials*, **16**, P. 1958–1966 (2007).

[36] L. Zheng, X. Liao, Y.T. Zhu. Parametric study of carbon nanotube growth via cobalt-catalyzed ethanol decomposition. *Mater. Letters*, **60**, P. 1968–1972 (2006).

[37] F. Li, X.-P. Zou, et al. Preparation of carbon nanotubes by ethanol catalytic combustion technique using nickel salt as catalyst precursor. *Transactions of Nonferrous Metals Society of China*, **16**, P. 381–384 (2006).

[38] H. Igarashi, H. Murakami, et al. Purification and characterization of zeolite-supported single-walled carbon nanotubes catalytically synthesized from ethanol. *Chemical Physics Letters*, **392**, P. 529–532 (2004).

[39] F. Gao, L. Zhang, Y. Yang, S. Huang. Quality of horizontally aligned single-walled carbon nanotubes: Is methane as carbon source better than ethanol. *Appl. Surface Science*, **256**, P. 3357–3360 (2010).

[40] G. Wang, H. Wang, et al. Simultaneous production of hydrogen and multi-walled carbon nanotubes by ethanol decomposition over Ni/Al_2O_3 catalysts. *Appl. Catal. B: Environmental*, **88**, P. 142–151 (2009).

[41] Q. Zhao, Y. Li, et al. Synthesis of multi-wall carbon nanotubes by the pyrolysis of ethanol on Fe/MCM-41 mesoporous molecular sieves. *Superlattices and Microstructures*, **47**, P. 432–441 (2010).

[42] S. Inoue, T. Nakajima, Y. Kikuchi. Synthesis of single-wall carbon nanotubes from alcohol using Fe/Co, Mo/Co, Rh/Pd catalysts. *Chemical Physics Letters*, **406**, P. 184–187 (2005).

[43] C.T.M. Kwok, B.J. Reizman, et al. Temperature and time dependence study of single-walled carbon nanotube growth by catalytic chemical vapor deposition. *Carbon*, **48**, P. 1279–1288 (2010).

[44] A. Bachmatiuk, F. Borrnert, et al. The formation of stacked-cup carbon nanotubes using chemical vapor deposition from ethanol over silica. *Carbon*, **48**, P. 3175–3181 (2010).

[45] X. Li, A. Westwood, et al. Water assisted synthesis of clean single-walled carbon nanotubes over a Fe_2O_3/Al_2O_3 binary aerogel catalyst. *New Carbon Materials*, **23**, P. 351–355 (2008).

[46] L. Zhu, Y. Xiu, D.W. Hess, C.-P. Wong. Aligned Carbon Nanotube Stacks by Water-Assisted Selective Etching. *Nano Letters*, **5**, P. 2641–2645 (2005).

[47] K. Hata, D.N. Futaba, et al. Water-Assisted Highly Efficient Synthesis of Impurity-Free Single-Walled Carbon Nanotubes. *Science*, **306**, P. 1362 (2004).

[48] J. Huang, Q. Zhang, M. Zhao, F. Wei. Process Intensification by CO_2 for High Quality Carbon Nanotube Forest Growth: Double-Walled Carbon Nanotube Convexity or Single-Walled Carbon Nanotube Bowls. *Nano Res*, **10**, P. 872–881 (2009).

[49] S.P. Somani, P.R. Somani, et al. Carbon nanofibers and multiwalled carbon nanotubes from camphor and their field electron emission. *Current Applied Physics*, **9**, P. 144–150 (2009).

[50] L. Yu, Y. Lv, Y. Zhao, Z. Chen. Scalable preparation of carbon nanotubes by thermal decomposition of phenol with high carbon utilizing rate. *Mater. Letters*, **64**, P. 2145–2147 (2010).

[51] L.A. Montoro, P. Corio, J.M. Rosolen. A comparative study of alcohols and ketones as carbon precursor for multi-walled carbon nanotube growth. *Carbon*, **45**, P. 1234–1241 (2007).

[52] P.T.A. Reilly, W.B. Whitten. The role of free radical condensates in the production of carbon nanotubes during the hydrocarbon CVD process. *Carbon*, **44**, P. 1653–1660 (2006).

NANOSYSTEMS: PHYSICS, CHEMISTRY, MATHEMATICS, 2013, 4 (2), P. 260–268

EFFECT OF OXIDE COMPOSITION (V_2O_5+Al_2O_3) VIA GAS PHASE ON THE THERMAL OXIDATION OF InP

B. V. Sladkopevtcev, N. N. Tretyakov, A. I. Dontsov, E. V. Tomina, I. Ya. Mittova
Voronezh State University, Voronezh, Russia
inorg@chem.vsu.ru

The effect of the oxide-chemostimulator V_2O_5 and the inert component Al_2O_3 binary compositions on the thermal oxidation of InP have been studied. The area of negative deviation of nanoscale oxide film thickness on InP from the additive joint effect has been established with a minimum for a composition of 20% Al_2O_3 + 80% V_2O_5. A decrease in the transit efficiency effect of V_2O_5 chemostimulator in composition with Al_2O_3 has been associated with an intensification of the transformation of V_2O_5 into V_2O_3, which is not an oxygen transitor.

Keywords: indium phosphide, thermal oxidation, transitor, chemostimulator, vanadium oxides, nanoscale films.

1. Introduction

Mutual increase or decrease of chemostimulating activity by the cooperative influence of two activator oxides have been observed during $A^{III}B^{V}$ thermal oxidation [1,2]. The phenomenon is due to the chemical interaction of the oxides and products of their transformations while present in the solid and gas phases. Oxides may be introduced through the gas phase or directly deposited on the surface of the semiconductor. The influence of non-chemical factors (size, diffusion, surface, etc.) can be detected when the active oxide is introduced into the system via the gas phase jointly with an inactive oxide, which is inert to both oxidizable semiconductor and the first oxide. A linear relationship between the oxide film thickness on GaAs and the activator oxide's composition was discovered during thermal oxidation processes of GaAs with compositions of a chemostimulating oxide (Sb_2O_3, Bi_2O_3, MnO, MnO_2, V_2O_5) and an inert oxide (Al_2O_3) [3,4]. The realization of such an additive dependence in practice allows one to adjust the chemostimulator concentration and to create nanoscale films doped with precisely controlled gas sensitive properties as shown with the GaAs example [3]. The chemostimulator leads to accelerated oxidation of the semiconductor components on the transit mechanism [5], and the inert oxide can affect both the conversion of oxide-chemostimulator and the above-mentioned non-chemical processes. In addition, one can expect InP to exert an influence on the secondary processes in the resulting film (e.g. formation of phosphate and changing the "polymer" structures [6] of formed phosphates). V_2O_5 is one of the most interesting chemostimulators, which is capable of having both a transit and catalytic effect on $A^{III}B^{V}$ thermal oxidations. This effect is dependent upon the method of chemostimulator introduction [7–9].

The purpose of this research is to establish the interaction characteristics of oxide compositions V_2O_5 + Al_2O_3 and their roles in the processes of the thermal oxidation of InP.

2. Experimental

For these studies, monocrystalline polished FIE-1A (doped by Sn) n-InP(100) wafers were used with a 300 K concentration of majority carriers no lower than 5×10^{16} cm^{-3}. Before thermal oxidation, the wafer surfaces were treated in H_2SO_4 (reagent grade, Russian State Standard GOST 4204-77, 92.80%): H_2O_2 (analytical grade, Russian State Standard GOST 177-88, 56%): H_2O = 2:1:1 etchant for 10 minutes and then rinsed repeatedly in bi-distilled water. The oxide films were obtained by thermal oxidation in a horizontal quartz reactor with a diameter of 30 mm (flow system) furnace MTP-2M-50-500, pre-heated to 530 °C operating temperature. The temperature in the reactor was controlled with an accuracy of ±1 °C (TRM-10). The oxygen flow rate was 30 l/h.

Mixed oxide compositions were made using V_2O_5 and Al_2O_3 (analytical grade, specification TU 6-09-4093-88 and TU 6-09-426-75 respectively) powders with an average particle size of 150–200 μm. After mechanical grinding in an Arden shaker for 15 minutes, each of the powders was passed through a series of sieves with a mesh size of 200 and 150 microns. The mass of each oxide present in a 0.2 g of sample was then calculated using the following formulas:

$$m_{\mathrm{V_2O_5}} = \frac{0.2}{\left[\left(\frac{1}{X_{\mathrm{V_2O_5}}}-1\right)\frac{M_{\mathrm{V_2O_5}}}{M_{\mathrm{Al_2O_3}}}\right]+1}, \qquad m_{\mathrm{Al_2O_3}} = \frac{0.2}{\left[\left(\frac{1}{X_{\mathrm{Al_2O_3}}}-1\right)\frac{M_{\mathrm{Al_2O_3}}}{M_{\mathrm{V_2O_5}}}\right]+1},$$

where X is the amount of V_2O_5 and Al_2O_3 in mole %. Samples were thoroughly mixed for at least 3 minutes.

The activator composition was placed in a quartz container, covered by the InP wafer with its working side facing the flow of activator vapor at a distance of 10 mm. The container with the wafer and activator mixture was placed in the work zone of a furnace and kept in an oxygen flow for 10–40 minutes. Oxide composition was changed every 10 minutes, in each experiment a freshly prepared oxides composition was used.

The oxidation conditions were chosen to compare the results with those previously obtained for GaAs with different chemostimulator compositions [3]. The optimal distance between the surface of wafers and the mixed oxides composition was determined empirically by the maximum value of oxidation acceleration when compared with the native InP thermal oxidation and strictly controlled for all experiments.

The thickness of the oxide films were determined after every 10 minutes of oxidation by laser ellipsometer LEF-754 (λ = 632.8 nm) with an absolute accuracy of ±1 nm. This methodology (with additional oxidation) allowed measurement of the film thickness on the same sample at different reaction times with a constant temperature and oxides mixture composition. This excluded the uncontrolled errors associated with InP surface treatment (before thermal oxidation) and changes in its properties from sample to sample.

Transformations in the oxides and their compositions was established by X-ray diffraction (XRD, X-ray diffractometer DRON-4, Co-Kα radiation, λ = 1.79021 Å). The elemental composition of the oxide films on InP and distribution of component thickness was investigated by Auger electron spectroscopy (AES, ESP-3 analyzer DESA-100, an accuracy of ±10%). Surface morphology of the samples was measured by scanning tunneling microscopy (STM, complex of nanotechnological equipment “UMKA”), the data were processed using the microscope software. A quantitative analysis of the elemental composition of thin films was performed on CamScan (EPMA, ±0.1%).

3. Results and Discussion

The main reason for the nonlinear dependence of the oxide film thickness on the GaAs surface on the composition of the mixture is the pronounced acid-base and redox interactions of the oxides-chemostimulators in both the solid and gas phases [1]. Individual V_2O_5 and Al_2O_3 powders and their compositions were annealed at 530 °C for 10 and 60 mins (conditions corresponding to studied oxidation process of InP) in order to investigate the possibility of any

TABLE 1. X-ray powder diffraction data for individual oxides and their compositions

Sample	Annealing conditions	Identified phases
Al_2O_3	530 °C, 10 minutes	γ-Al_2O_3
V_2O_5	530 °C, 10 minutes	V_2O_5
$(Al_2O_3)_{0.8}(V_2O_5)_{0.2}$	530 °C, 10 minutes	γ-Al_2O_3; V_2O_5
$(Al_2O_3)_{0.2}(V_2O_5)_{0.8}$	530 °C, 10 minutes	γ-Al_2O_3; V_2O_5; V_2O_3; V_6O_{13}
$(Al_2O_3)_{0.5}(V_2O_5)_{0.5}$	530 °C, 10 minutes	γ-Al_2O_3; V_2O_5; V_2O_3
$(Al_2O_3)_{0.5}(V_2O_5)_{0.5}$	530 °C, 60 minutes	γ-Al_2O_3; V_2O_5; V_2O_3

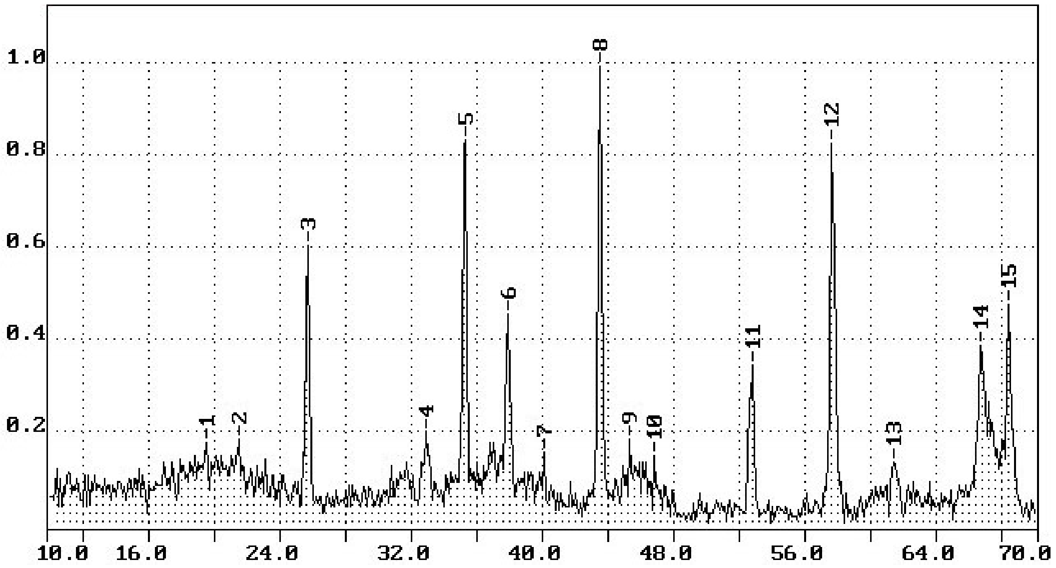

FIG. 1. The XRD pattern of composition 80% V_2O_5 + 20% Al_2O_3 annealed at 530 °C for 10 minutes

additional interactions and transformations. The results of XRD analysis are shown in Tab. 1 and fig. 1.

According to the results of XRD, after 10 minutes of annealing, individual oxides have not changed. The diffractograms of V_2O_5+Al_2O_3 compositions showed peaks corresponding to V_2O_3 (peaks No. 4, 12 and 14, $d = 2.722$, 1.600 and 1.402, respectively), both for 10 min annealing, and for 60 minutes. Consequently, the components of V_2O_5 and Al_2O_3 mixtures react with one another, as shown in the partial conversion of V_2O_5 to V_2O_3.

Although, the joint phase and solid solutions were not detected for these annealing conditions by XRD, however, according to [10], there should be bronze types α ($Al_xV_2O_5$) and ν ($Al_xV_6O_{12}$), solid solution $Al_zV_{2-z}O_4$ and bronze $Al_{0.33}V_2O_5$ phases formed in the Al_2O_3–V_2O_5–V_2O_3 system. The absence of these phases in our systems may be due to insufficient duration and relatively low annealing temperatures.

In reactions performed at 530 °C over 10–40 minutes (fig. 2), it was shown that the oxide film thickness on InP was dependent upon the oxide composition. Furthermore, the addition of small amounts of Al_2O_3 to V_2O_5 resulted in a negative deviation from the additive dependence with a minimum for a composition of 20% Al_2O_3 + 80% V_2O_5. This deviation was reduced with increasing amounts of Al_2O_3 in the composition. Starting from 40% Al_2O_3, there is an additive dependence between the oxide film thickness on InP and the composition of the oxide mixture. The same relationship was observed with negative deviation from linear dependence of the oxide film thickness for the thermal oxidation of a semiconductor under the influence of 20% Al_2O_3 + 80% MnO_2 composition [4].

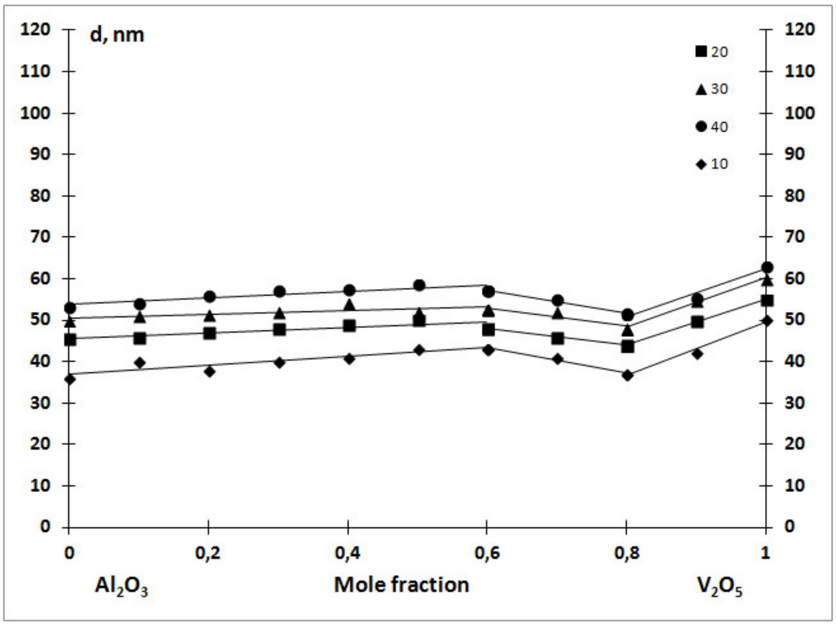

FIG. 2. Plots of the oxide films thickness grown on InP at 530 °C at 10, 20, 30, 40 minutes versus concentration

The relative integral films thickness (dR), defined as the difference between the thickness *d* of the oxide layer on the InP surface actually achieved under the influence of the oxide composition and the expected thickness calculated by the addition rule, assuming their independent parallel influence. This characteristic, previously introduced for the interpretation of similar processes [11], can quantify characterized non-linear effects during the thermal oxidation of $A^{III}B^{V}$ semiconductors in the presence of mixed oxide compositions (Fig. 3).

As shown on fig. 3, in a region with up to 40% concentration of Al_2O_3 there is a negative deviation from additive dependence which increases with time. The thickness of the oxide film is increased linearly when the content of Al_2O_3 was higher than 40%. This is evidence of the additive effects of the composition of V_2O_5 + Al_2O_3 upon InP oxidation.

Since the composition of the activator influences the gas-phase InP thermal oxidation, and transitional interactions can occur too, one should consider that a possible decomposition and transformation of the corresponding oxides may occur during the experiments. Mittova et al. found that for equilibrium conditions at 800 K, the percentage of V_4O_{10} did not exceed 0.3% in the vapor phase above the V_2O_5(s) [12]. At 800 K, the vapor over V_4O_8 has a V_4O_{10} content of about 0.06% and it decreased with increasing temperature. Under these experimental conditions, which are far from equilibrium, the chemostimulator in oxide composition can be in different phases . The relative amount of the chemostimulator will depend on the amount of the second component. Transit opportunities for various forms of vanadium oxide during InP thermal oxidation did differ (XRD, table 1). In the first approximation, they can be estimated by changes in the equilibrium values of the Gibbs free energy of oxygen transit reactions at the experimental temperature:

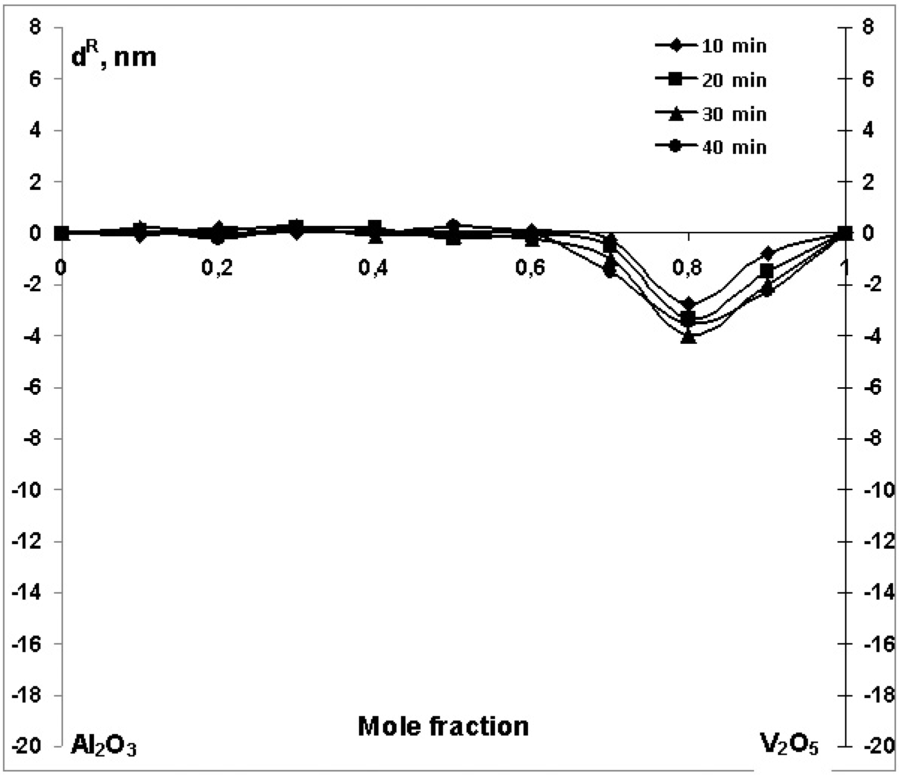

FIG. 3. Relative integral oxide film thickness dR grown on InP at 530 °C at 10, 20, 30, 40 minutes as a function of the V_2O_5+Al_2O_3 composition

$$4/3\mathrm{In}_{(s)} + \mathrm{V}_4\mathrm{O}_{10(g)} \to 2/3\mathrm{In}_2\mathrm{O}_{3(s)} + 2\mathrm{V}_2\mathrm{O}_{4(s)}, \qquad \Delta G_{800\mathrm{K}} = -589.2\,\mathrm{kJ/mol}; \qquad (1)$$

$$8/3\mathrm{In}_{(s)} + \mathrm{V}_4\mathrm{O}_{10(g)} \to 4/3\mathrm{In}_2\mathrm{O}_{3(s)} + 2\mathrm{V}_2\mathrm{O}_{3(s)}, \qquad \Delta G_{800\mathrm{K}} = -597\,\mathrm{kJ/mol}; \qquad (2)$$

$$2\mathrm{In}_{(s)} + 3/10\mathrm{V}_4\mathrm{O}_{10(g)} \to \mathrm{In}_2\mathrm{O}_{3(s)} + 12/10\mathrm{V}_{(s)}, \qquad \Delta G_{800\mathrm{K}} = -12.3\,\mathrm{kJ/mol}. \qquad (3)$$

Similar reactions for phosphorus are also accompanied by a significant negative change of ΔG, comparable to that of the above.

V_2O_3 produced during the annealing of V_2O_5 + Al_2O_3 composition (Table 1), evaporates at temperatures of about 1800 K accordingly to the reaction [4]:

$$\mathrm{V}_2\mathrm{O}_{3(s)} = \mathrm{VO}_{2(g)} + \mathrm{VO}_{(g)}. \qquad (4)$$

The transfer of oxygen to indium from VO_2 and VO is thermodynamically impossible and therefore, these oxide forms cannot act as an oxygen transistor:

$$2\mathrm{In}_{(s)} + 3/2\mathrm{VO}_{2(s)} \to \mathrm{In}_2\mathrm{O}_{3(s)} + 3\mathrm{V}_{(s)}, \qquad \Delta G_{800\mathrm{K}} = 793\,\mathrm{kJ/mol}, \qquad (5)$$

$$2\mathrm{In}_{(s)} + 3\mathrm{VO}_{(s)} \to \mathrm{In}_2\mathrm{O}_{3(s)} + 3\mathrm{V}_{(s)}, \qquad \Delta G_{800\mathrm{K}} = 919\,\mathrm{kJ/mol}. \qquad (6)$$

The inclusion of these oxides in the film is also not possible because the temperature of InP oxidation was far below the point where V_2O_3 evaporation occurs .

Al_2O_3 does not affect the oxidation process under experimental conditions due to thermodynamic restrictions; it is incapable of transferring oxygen to semiconductor components (its evaporation becomes noticeable only at 2440 K [12]). Aluminum was not detected in the oxide films grown on InP in the presence of V_2O_5 + Al_2O_3 compositions (EPMA data).

STM data show a fairly homogeneous surface of oxide films formed on InP in the presence of V_2O_5 + Al_2O_3 (height of the relief is in the range of 20–30 nm). The relief of the surface is much more pronounced for films prepared during the thermal oxidation of InP with directly pre-deposited V_2O_5 nanoislands (order of 60 nm [13]). A slight relief of the film surface in case of exposure to the V_2O_5 + Al_2O_3 composition through the gas phase is the result of evaporation of volatile phosphorus oxides during InP thermal oxidation (correlation with the AES data). The height of the surface relief naturally increases with the oxidation time (fig. 4a and 4b).

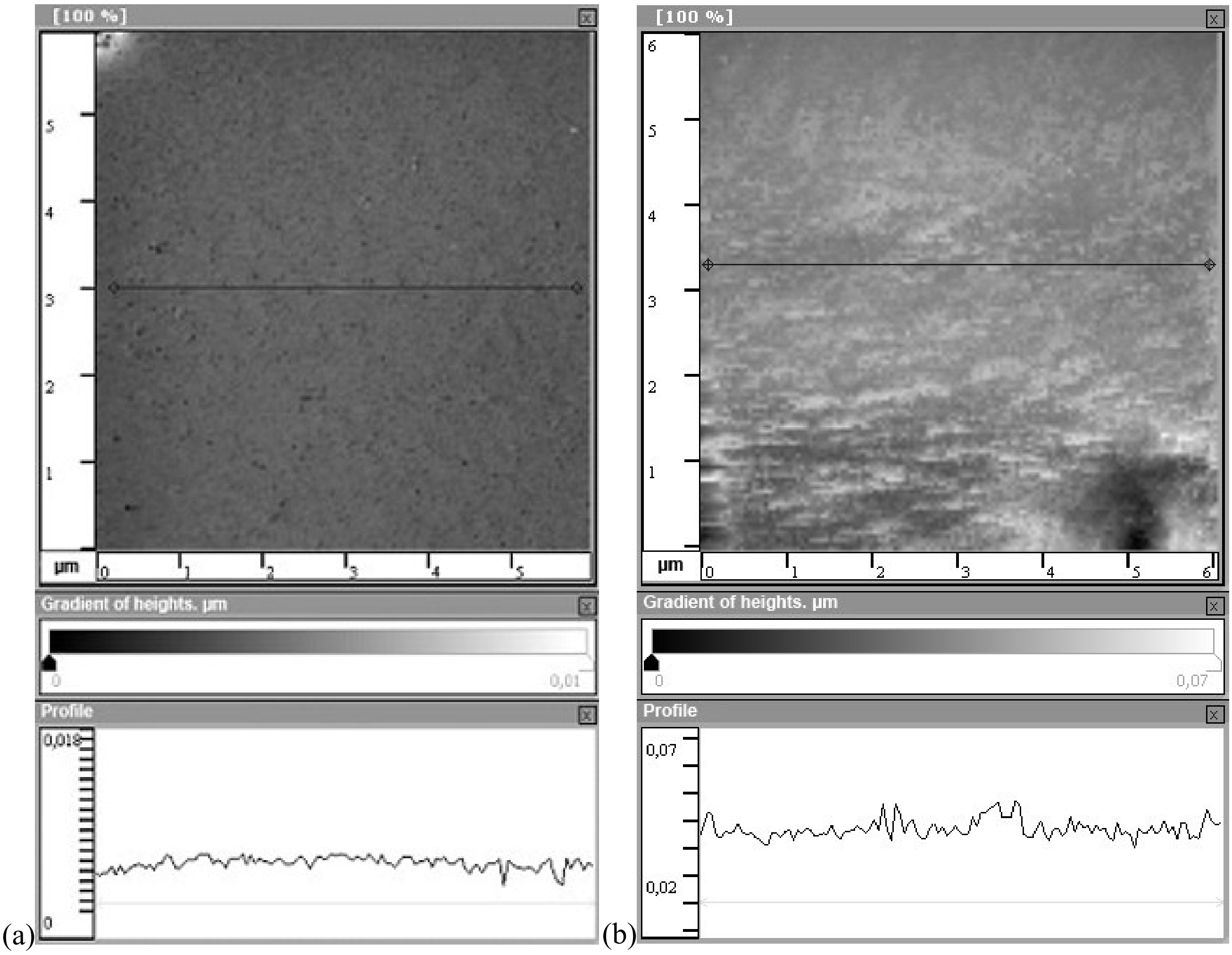

FIG. 4. STM image and profile of surface of oxide films formed by thermal oxidation of InP in the presence of composition 80% V_2O_5 + 20% Al_2O_3 at 530 °C at 10 (*a*) and 40 (*b*) minutes

The kinetic curves “oxide film thickness — oxidation time” were taken at a temperature range of 500–550 °C (fig. 5) in order to establish the mechanism of InP thermal oxidation in the presence of a V_2O_5 + Al_2O_3 mixture (60% V_2O_5 + 40% Al_2O_3). This composition lies in a linear range, see fig. 3.

By processing the kinetic data using the equation $d = (k\tau)^n$ [14], it was found that the index n was 0.26, and the effective activation energy (EAE) was 219 kJ/mol. This value is between the EAE of InP oxidation with V_2O_5 introduced via the gas phase (164 kJ/mol) and native InP oxidation (273 kJ/mol). $n < 0.5$, implying that the process of thermal oxidation was

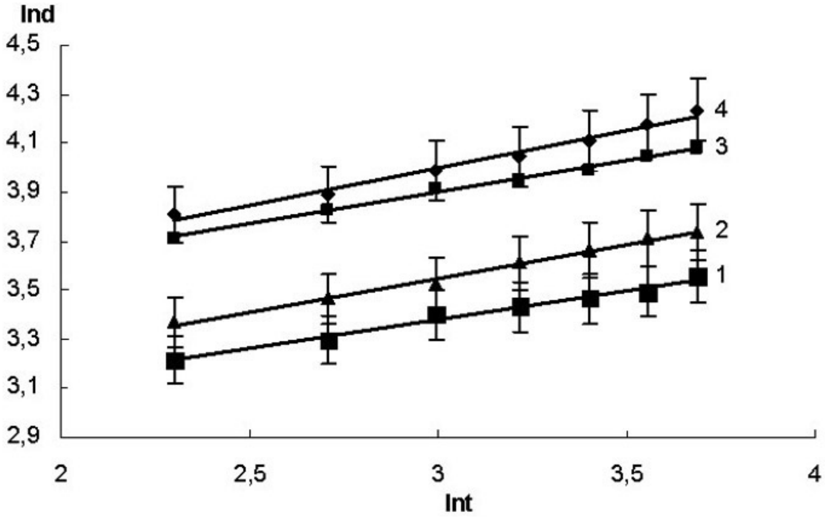

FIG. 5. Log-log plots of the oxide layers thickness vs. time for the thermal oxidation of InP in the presence of 80% V_2O_5 + 20% Al_2O_3 at 500 °C (1), 520 °C (2); 530 °C (3); 550 °C (4)

controlled by diffusion in the solid phase. The relative increase in the film thickness in the presence of a chemostimulator composition compared with its own oxidation, was calculated as:

$$b = \frac{\Delta d_{(\mathrm{V_2O_5+Al_2O_3})-\mathrm{InP}} - \Delta d_{\mathrm{InP}}}{\Delta d_{\mathrm{InP}}} \cdot 100\%,$$

where Δd is the change in the film thickness and is 15–20%. Thus, the transit nature [5] of InP oxidation saved under the influence of V_2O_5 in the gas phase with addition of Al_2O_3.

According to AES data (fig. 6a) indium, phosphorus and oxygen were detected on the surface of the film in the sample oxidized at 530 °C for 40 min in the presence of a composition containing 30% V_2O_5 (linear region, see Fig. 2). For the components of the substrate contained in the oxidized state, the highest oxygen content among of all the elements was at a depth of 15 nm from the surface.

The amount of vanadium was 5–6 atom % in the films on InP, obtained in the presence of the composition with 80% V_2O_5, corresponding to the region of the negative deviation from the additive dependence (fig. 3). Indium and oxygen were present on the surface, however, the presence of phosphorus became noticeable from a depth of 20 nm, which was due to its evaporation, probably in the forms of oxides (fig. 6b). The presence of vanadium in the film, for which there is a negative deviation from the additive d^R dependence, may arise from the inclusion of transit-inactive forms of vanadium (e.g. VO_2) in the growing layers of vanadium oxide. A similar situation was observed for GaAs oxidation in the presence of a similar composition of 80% V_2O_5 + 20% Al_2O_3, where it was shown by XRD that a negative deviation of the oxide film thickness on semiconductor and that VO_2 was present [3]. The absence of aluminum in the films was confirmed by its inertness to InP thermal oxidation.

Negative deviation in the concentration dependence of the relative integrated film thickness on InP (established by the addition of up to 40% Al_2O_3 to V_2O_5) may arise from the change of the temperature range and the nature of chemostimulator's ability to undergo self-transformations. In this case, the dissociation of V_2O_5 to V_2O_3 was facilitated (V_2O_3 is not transistor of oxygen). This weakening of the chemostimulating effectiveness is due to the increased conversion to compounds of lower oxidative activity towards GaAs oxide, as evidenced by Mn_3O_4 in the case of manganese oxides (II) and (IV) in compositions with Al_2O_3 [4]. In

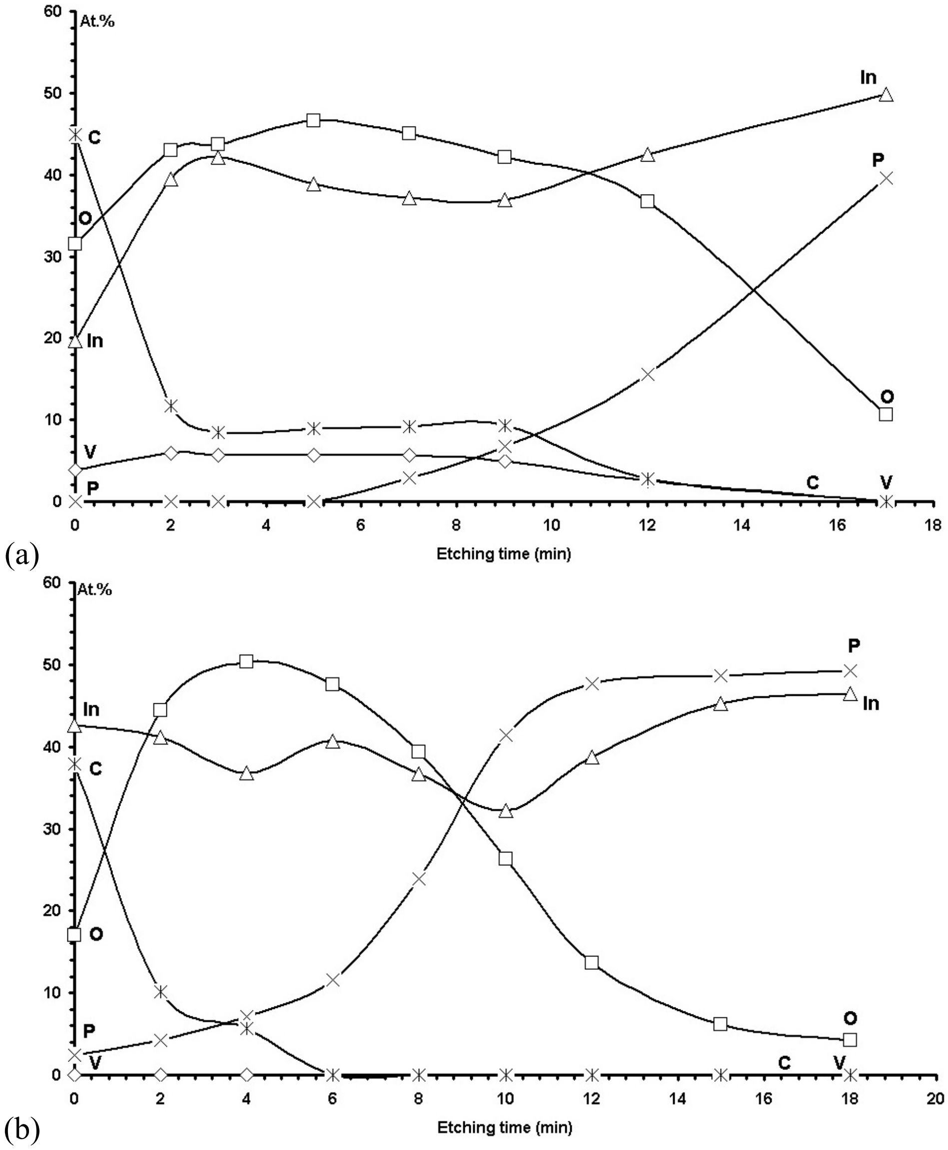

FIG. 6. AES depth profiles, obtained after 40 min of InP oxidation at 530 °C in presence of compositions: (a) —30% V_2O_5 + 70% Al_2O_3; (b) — 80% V_2O_5 + 20% Al_2O_3

addition, the chemostimulating effect of vanadium oxide can be reduced due to possible interactions between Al_2O_3 and V_2O_5, leading to the formation of aluminum vanadate. Although vanadate in an annealed aluminum oxide composition is not found (XRD data), according to [15], incongruent melting of $AlVO_4$ at 760 °C, present in the system Al_2O_3 – V_2O_5, can be obtained by heating a mixture of oxides Al_2O_3 and V_2O_5 at 500 °C.

Evidence for a transit mechanism of the process are: oxidation state of indium and phosphorus in the films; the inclusion of vanadium; the relative increase in the film thickness 15% to 20% in the presence of V_2O_5 + Al_2O_3 composition; EAE value close to that of the native oxidation of InP. In the case of the catalytic effect of V_2O_5 on InP thermal oxidation, the EAE was almost an order of magnitude lower in comparison with the value for their native oxidation [16]. The role of Al_2O_3 is to intensify the transition of V_2O_5 into V_2O_3. Al_2O_3 is a non-transistor of oxygen and is not included in the growing film on InP and reduces the chemostimulating effect of vanadium oxide (V).

4. Conclusions

The influence of the inert component Al_2O_3 on V_2O_5 chemostimulating action during the thermal oxidation of InP in the presence of a mixture of these oxides in the gas phase was identified. Negative deviation from linearity of the nanoscaled oxide film thickness on InP with a minimum 20% Al_2O_3 + 80% V_2O_5 for the composition correlated with the transformation of V_2O_5 into V_2O_3, which does not have the ability to act as an oxygen transit. Thus, Al_2O_3 which is inert to the process of InP oxidation (AES, EPMA) changes the temperature range and the nature of V_2O_5 transformations. This is the ultimate reason for the deviation from linear dependence of the oxide film thickness formed on InP.

Acknowledgments

This research was supported by the Russian Foundation for Basic Research, grant No. 13-03-00705-a.

References

[1] P.K. Penskoi, V.F. Kostryukov, V.R. Pshestanchik, I.Ya. Mittova. Joint effect of chemostimulator (Sb_2O_3, Bi_2O_3, MnO_2) compositions with an inert component (Al_2O_3) on gallium arsenide thermal oxidation. *Doklady Chemistry*, **414** (2), P. 152–154 (2007).

[2] I.Ya. Mittova, E.V. Tomina, et al. Thermal oxidation of InP surfaces modified with NiO + PbO mixtures. *Inorganic Materials*, **41** (4), P. 323–330 (2005).

[3] P.K. Penskoi, V.F. Kostryukov, et al. Effect of inert components (Y_2O_3, Al_2O_3, and Ga_2O_3) on the chemistimulating effect of the Sb2O3 activator of GaAs thermal oxidation. *Russian Journal of Inorganic Chemistry*, **54** (10), P. 1564–1570 (2009).

[4] T.V. Kozhevnikova, P.K. Penskoi, et al. Role of an inert component in compositions with manganese(II) and manganese(IV) oxides in studying nonlinear effects in GaAs thermal oxidation. *Russian Journal of Inorganic Chemistry*, **55** (12), P. 1857–1862 (2010).

[5] I.Ya. Mittova, V.R. Pshestanchik. The chemistry of processes which create dielectric layers with functional group substituents on semiconductors by impurity thermo-oxidation. *Russian chemical reviews*, **60** (9), P. 967–979 (1991).

[6] M. Yamaguchi. Thermal oxidation of InP and properties of oxide films. *Journal of Applied Physics*, **51** (9), P. 5007–5012 (1980).

[7] V.M. Ievlev, A.A. Samsonov, et al. Catalytic effect of a nanolayer of the (V_2O_5 + PbO) composite in the thermal oxidation of InP crystals. *Doklady Chemistry*, **417** (2), P. 277–281 (2007).

[8] I.Ya. Mittova, E.V. Tomina, A.A. Lapenko, B.V. Sladkopevtsev. Synthesis and catalytic performance of V_2O_5 nanoislands produced on the surface of InP crystals by electroexplosion. *Inorganic Materials*, **46** (4), P. 383–388 (2010).

[9] I.Ya. Mittova, E.V. Tomina, A.A. Lapenko, A.O. Khorokhordina. Solid-state reactions during thermal oxidation of vanadium-modified GaAs surfaces. *Inorganic Materials*, **40** (5), P. 441–444 (2004).

[10] *Phase diagrams of refractory oxides*: Handbook. Nauka, Leningrad, P. 1–2, (1986).

[11] I.Ya. Mittova, V.R. Pshestanchik, V.F. Kostryukov. Alternating nonlinearity of the joint activating effect of binary mixtures of p-element oxides on the chemically activated thermal GaAs oxidation. *Doklady Chemistry*, **378** (4–6), P. 165–167 (2001).

[12] E.K. Kazenas, Y.V. Tsvetkov. *Thermodynamics of evaporation of oxides*. LKI, Moscow, 474 pp. (2007).

[13] I.Ya. Mittova, B.V. Sladkopevtsev, E.V. Tomina, A.I. Dontsov. Effect of V_2O_5 nanoislands on the surface composition and structure of InP during thermal oxidation. *Inorganic Materials*, **47** (8), P. 811–815 (2011).

[14] I.Ya. Mittova, G.V. Borzakova, V.A. Terekhov. Growth of native oxide layers on indium phosphide. *Izv. Akad. Nauk SSSR*, *Inorganic Materials*, **27** (10), P. 2047–2051 (1991).

[15] A.A. Fotiev. *Vanadates. Composition, synthesis, structure, properties*. Nauka, Moscow, 272 pp. (2008).

[16] O.V. Krilov, B.R. Shub. *Nonequilibrium processes in catalysis*. Chimiya, Moscow, 284 pp. (1990).

[17] I.Ya. Mittova, E.V. Tomina, A.A. Lapenko, B.V. Sladkopevtsev. The catalytic action of vanadium and its oxides (V) in the oxidation process of $A^{III}B^{V}$ semiconductors. *Nanosystems: physics, chemistry, mathematics*, **3** (2), P. 116–138 (2012).

NANOSYSTEMS: PHYSICS, CHEMISTRY, MATHEMATICS, 2013, 4 (2), P. 269–275

PHOTOLUMINESCENCE IN Fe^{3+} ION DOPED BARIUM TITANATE NANOPARTICLES

P. Barik[1], T. K. Kundu[1]

[1] Department of Physics, Visva-Bharati University, Santiniketan-731235, W.B., India
pbarik_mid1983@yahoo.co.in, tapaskumar.kundu@visva-bharati.ac.in

PACS 78.67.Bf, 78.55.Qr

Fe^{3+} ion doped barium titanate (BT) nanopowders were synthesized by the sol gel route. The average size of tetragonal bariun titanate (t-BT) powders lies in the range 16–40 nm. The specimens show ultraviolet (UV) emission (peak at 376 nm) along with emission in violet, blue, green and yellow color. The blue band (peak at 452 nm) is seen to grow significantly with annealing temperature. This band arises due to Ti^{3+} defects which are stabilized by Fe^{3+} ions in BT specimens. The samples show two distinct Electron Paramagnetic Resonance (EPR) bands of g-value around 4.11 and 1.98, which originated from Fe^{3+} ions and Ti^{3+} defects respectively. A correlation between the photoluminescence (PL) and EPR band intensity, grown from same species, was found.

Keywords: barium titanate, photoluminescence, nanoparticles.

1. Introduction

Pure Barium Titanate ($BaTiO_3$, BT) and transition metal ion-doped BT have important applications in electromechanical devices such as capacitors, transducers, thermistors, actuators, humidity sensors etc [1-4]. BT also has interesting optical properties with potential application in high-density optical data storage, laser power combining and optical computing [5]. Of all the known defects in BT, iron is easily soluble and has a significant effect on the optical properties of BT [6-8]. Katyar et al observed a structure-less visible emission band in BT at 500 nm at low temperature revealing lower emission energy than its band gap [9]. BT nanocrystals (nc-BT) show relatively enhanced photoluminescence (PL) emission [9, 10]. Various reports were published to describe the origin of the visible emission shown by BT [11-13]. It was reported that the emission is related to the charge transfer between titanium and oxygen atoms. The luminescence from bulk BT was ascribed to the presence of self-trapped excitons (STE) within TiO_6 octahedra, viz $Ti^{3+} - O^-$ STE [10]. Zhang et al established that the PL of BT is due to localized states promoted by the intrinsic defect distribution (oxygen vacancy) [14]. Those states essentially decrease the band gap energy of BT. Recently, a group has established that both five-fold and six-fold oxygen-Ti coordination exist in amorphous BT systems, which is responsible for PL in disorder materials [15-17]. Therefore, from the above discussions it seems that more investigations are required in this field to understand the origin of the emission shown by BT.

PL emission from an acceptor doped or Fe-doped BT system are of particular interest in this work. Here, we report the emission from Fe^{3+}-doped nc-BT powders. The emission appears both in ultraviolet and visible range of wavelength. PL emissions have correlation with electron paramagnetic resonance (EPR) signals shown by the specimens.

2. Experimental

Iron ion doped BT ultrafine powder were synthesized by the sol-gel hydroxide method using barium hydroxide [$Ba(OH)_2 \cdot 8H_2O$, Merck], tetraisopropyl orthotitanate [$Ti(C_3H_7O)_4$, Merck] and iron(III) nitrate [$Fe(NO_3)_3 \cdot 9H_2O$, Merck] as starting materials [18]. Here, the powders were doped with 2 mole% of Fe^{3+}. The concentration of the dopant was chosen within the solubility limit of Fe^{3+} in BT [19]. $Ba(OH)_2 \cdot 8H_2O$ was dissolved in ethanol and glacial acetic acid (1:1 volume ratio) by stirring and heating the solution at 50-70 °C. After cooling the solution to room temperature a stoichiometric amount of tetraisopropyl orthotitanate was added drop wise. Then, a calculated amount of iron nitrate, prepared separately, was added to the above solution. The clear solution, which was obtained after stirring for a few minutes, was allowed to gel at room temperature. The dried gel-powders were calcined at different temperatures between 400-700 °C for two hours in a tube furnace to obtain doped nc-BT powders. XRD patterns of the specimens were recorded using Phillips powder Diffractometer. The microstructures of the samples were investigated by a TEM of JEOL. A Perkin-Elmer luminescence spectrometer was used to study the light emission from the samples. The EPR spectra were recorded at an X-band frequency (~9.43 GHz) with a Varian Associates spectrometer.

3. Results and discussions

Figure 1 shows X-ray diffraction patterns of 2 mole % iron ion doped BT powders obtained by heating the gel-powders at different temperatures. We have calculated interplanar spacing (d_{hkl}) values, corresponding to each of the diffraction peaks. Specimen 'a', gel-powders annealed at 400 °C, shows a set of d_{hkl} values that matches with an orthorhombic (o-BT-II) crystal structure (P_{nma} space group), with average lattice parameters a=0.6435 nm, b=0.5306 nm, and c=0.8854 nm. The observed d_{hkl} values are reproduced with a standard deviation of ±0.0005 nm. The orthorhombic phase (o-BT-II) is structurally different from conventional orthorhombic BT. A thorough analysis by the Rietveld method was given in our previous reports [19, 20]. Specimens 'b' and 'c', heating the gel-powders at 600 °C and 700 °C respectively, contain two sets of d_{hkl} values. One set is due to standard tetragonal BT phase and other set of d_{hkl} values arise due to orthorhombic crystal structure. A large fraction of the o-BT-II is promoted to t-BT at a temperature of 700 °C via a surface diffusion limited o→t transformation process. The average diameter (D) of the grains was determined from the FWHM values in the XRD peaks by using Debye-Scherrer relation $d_{XRD} = k\lambda/\beta(\theta)\cos(\theta)$, where λ is the wavelength of X-ray, β the FWHM of the (200) peak, θ the diffraction angle and the constant $k \approx 1$. The average sizes of 16 nm and 40 nm were obtained for the t-BT samples annealed at 600 °C and 700 °C respectively.

The grain size of the nanocrystalline ceramics was also estimated using transmission electron microscope (TEM). A typical micrograph from specimen 'c' is shown in Fig. 2a. The corresponding diffraction patterns are shown in Fig. 2b. There is a distribution of particle sizes in the specimens. The results estimated from TEM reasonably agree with those obtained from XRD.

Figure 3 shows EPR spectra of the specimens after heating the powders at (a) 400 °C, (b) 600 °C, and (c) 700 °C for 2 h in air. The samples show two distinct EPR bands (Band I and Band II) of g-value around 4.11 and 1.98. The intensity of Band-II increases by 55% as the sintering temperature rises from 400 °C to 700 °C. The positions of the signals are not altered significantly. The reverse trend is observed for the Band I

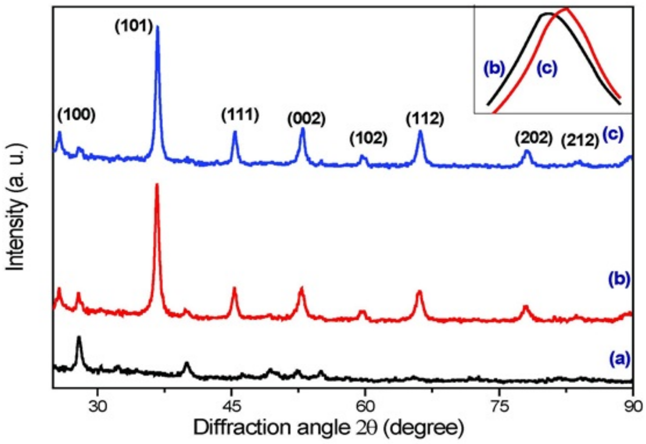

Fig. 1. XRD patterns for 2% Fe-doped BT nanopowders after heating a sol-gel precursor at (a) 400 ° C and (b) 600 ° C (c) 700 ° C for 2 hr in air. A close-up in the inset compares the shift in (101) peak of sample (b) and (c)

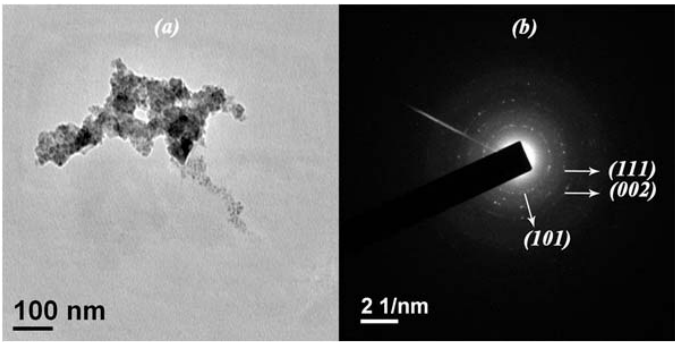

Fig. 2. A typical (a) TEM image and (b) Diffraction pattern taken from specimen 'c' heat-treated at 700 ° C for 2hr. The diffraction rings in the pattern (from center to edge) can be indexed as the (101), (111), and (002) peaks of a tetragonal (P_{4mm}) BT phase

signal, as its intensity is decreased by 58% with the same change in sintering temperature. Thus, when the Band I signal is strong, the Band II signal is weak and vise versa. The O_i^- is a common EPR sensitive species ($g \sim 2$) in oxides [21, 22]. A peak at g=1.97 was reported in BT due to localized Ti^{3+} states [23]. In the present case, intensity of the signal at g = 1.98 have increased with the annealing temperature and the doped specimens show an extra EPR peak (g = 4.11). EPR studies of Fe^{3+} ($3d^5$, $S = 5/2$) in the tetragonal phase have been reported previously [24-26]. In a large number of Fe^{3+}-containing materials, a symmetric and isotropic line at g ≈4.0–4.2 as well as a line at $g = 2.0$ was observed. In our case, the g-value at 4.11 indicates that the iron ions are trivalent and the site symmetry is slightly distorted octahedral. Here, the Fe^{3+} occupies the Ti^{4+} sites which produce distorted octahedral symmetry. This case produces a low symmetry site structure. As the Fe^{3+} ions occupy the Ti^{4+} sites, EPR response of Fe^{3+} doped BT may be expected to exhibit changes upon crystallization due to removal of distortion around various ions in the BT. This argument is supported by our experimental observation where the signal intensity of Band I decreases with annealing temperature. Band II that grows with annealing temperature can originate either due to species Fe^{3+} or Ti^{3+}. In the absence of Fe^{3+} ions, the same signal is eliminated with increased annealing temperatures. The appearance of a few emission bands from the doped BT specimens, when excited properly, corroborates the EPR results.

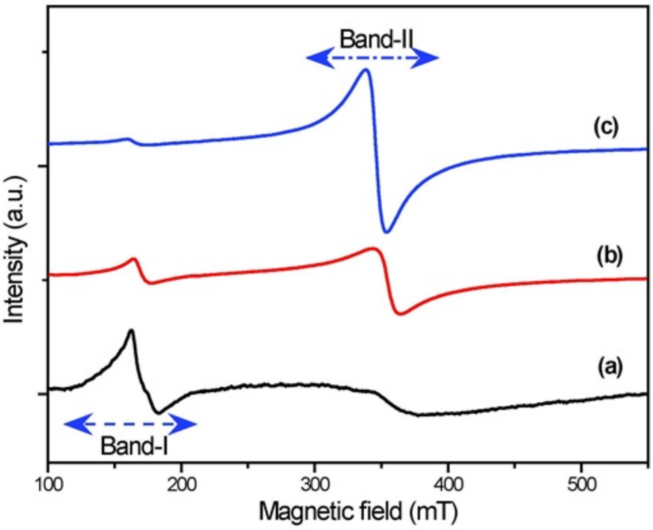

Fig. 3. EPR spectra for 2% Fe doped BT nanopowders after heating a sol-gel precursor at (a) 400 ° C, (b) 600 ° C, and (c) 700 ° C for 2 hr in air

The emission spectra from the specimens, irradiated at 250 nm by a xenon lamp, are shown in Fig. 4. The excitation energy was chosen from the excitation spectra of the specimens which show an intense peak at 250 nm. The spectra are analyzed by fitting with multiple Gaussian curves. A typical Gaussian fitting of PL spectrum from the specimen '*c*' is shown in Fig. 5. The composite specimens, '*b*' and '*c*', also show same bands with different intensity level and shifted peak positions. The UV emission peak shifts significantly to higher wavelengths with increasing annealing temperatures. Typically the peak at 376 nm in specimen '*a*' is shifted to 395 nm in specimen '*c*'. It is evident from Gaussian fitting data that the band intensity of 421 nm and 619 nm line decreases and other bands grow on annealing the powder at temperature as high as 600 ° C or above. Among the bands, the growth of 452 nm line is distinct and significant.

The band gap of BT lies between 3–3.2 eV, as obtained from optical absorption edges [27]. Thus, the energy corresponding to the 250 nm line makes a direct transition and the UV emission band is assigned to a direct band gap transition. The band gap energy of nc-BT has increased to 4.9 eV according to the excitation maxima. Luminescence at ∼2.96 eV (421–424 nm) is caused by the transition from the near conduction band edge to the valance band. It is argued that the electronic band structure of BT has a low-lying narrow conduction bands resulting from defects [28]. In amorphous materials, nonbridging oxygens (i.e. ones which are bonded to a single main group atom) participate in ionic interactions to form a typical network like Ti-O. Crystallization into a single o- or t-BT polymorph can lead to the elimination of defects or imperfections, particularly of nonbridging oxygen of a TiO_5 group, in which Ti is penta-coordinated by oxygen. A decrease in the intensity of the 421 nm line, as observed experimentally, supports these statements. The recombination process corresponding to the charge transfer from the central Ti^{3+} to adjacent V_0^+ states in the TiO_5 groups leads to a luminescence peak centered at 452 nm.

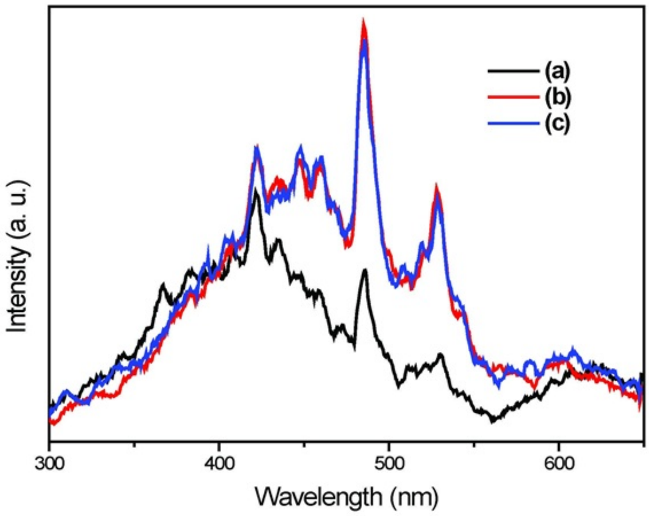

Fig. 4. Photoluminescence spectra for 2% Fe doped BT nanopowders after heating a sol-gel precursor at (a) 400 ° C, (b) 600 ° C, and (c) 700 ° C for 2 hr in air

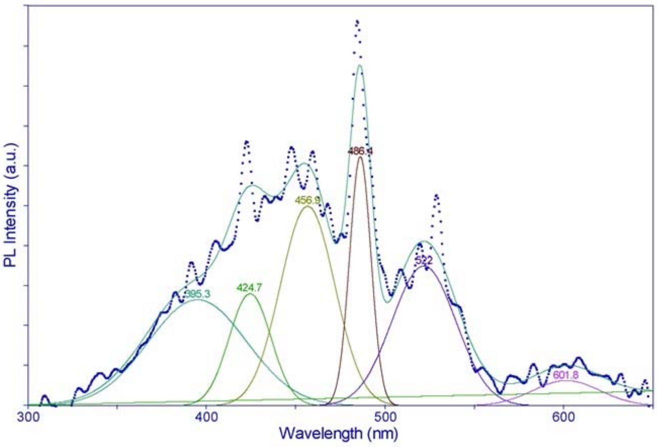

Fig. 5. Photoluminescence emission spectra of the specimen heated at 700 ° C for 2 hr fitted with Gaussian curves

The energy interval (~2.75 eV) between Ti^{3+}($3d^1$)- and V_0^+ states supports the emission at a wavelength of 452 nm. Experimentally, the band is observed to grow considerably with annealing at higher temperatures. If it is considered that EPR Band II originates from Ti^{3+} species then a correlation between the PL band and EPR band intensity is found. The intensities of both signals increase with higher annealing temperatures. In that case, Fe^{3+} ions certainly play an important role in stabilizing Ti^{3+} defects in BT, even samples sintered at higher temperatures. In amorphous and composite materials, a large amount of "broken" surfaces or dangling bonds and color centers intrinsically exist either in a distorted structure or a highly strained lattice (as in this example of o-/t-BT-nanocrystals) and involve a series of E_{em} levels localized within the forbidden gap. They very sensitively tailor the light emission in multiple bands at room temperature. The blue emission at 485 nm (~2.57 eV) is attributed to the intraband transitions from self-trapped excitons [28, 29]. It is also evident from Gaussian fitting data that a prominent yellow emission is centered at ~2.38 eV (520–524 nm) and its intensity increases as the sintering temperature increases. The electrons' polarons interact with holes, possibly trapped near crystal defects or impurities, and form an intermediate state: self-trapped exciton (STE). These self-trapped excitons contributed to the 485 nm and 520 nm emissions [10, 30]. The band at 620–600 nm is explained in terms of the transition from Fe^{3+} states to the valence band of BT. The intensity of this band decreases with annealing temperature and a correlation with EPR band I grown from the same species is found. The existence of Fe^{3+} energy states in BT was earlier established from optical absorption data [8]. PL measurements and optical absorption studies of nc-BT powders that are heat-treated under different atmospheres would provide much useful information.

4. Conclusions

BT nanopowders doped with 2 mole % Fe^{3+} ions were synthesized by the sol gel route. The gel-powders annealed at 400 °C show orthorhombic BT (o-BT-II) crystal structure. The o-BT-II phase begins to transform to t-BT on heating the specimens at temperatures as high as 600 °C. The average size of t-BT powders range from 16–40 nm. The samples show two distinct EPR bands (Band I and Band II) of g-value around 4.11 and 1.98. The Band I signal (g=4.11) originates due to isolated Fe^{3+} ions in low symmetry site at low temperatures. As the Fe^{3+} ions occupy the Ti^{4+} sites, the EPR response exhibits changes upon crystallization due to removal of distortion around various ions in the BT. Band II, which grows with annealing temperature, originates due to Ti^{3+} defects stabilized by Fe^{3+}. The specimens show UV emission (peak at 376 nm) along with the emission in violet, blue, green and yellow color (421, 452, 485, 526, 619 nm). The redshift of the UV emission band is primarily caused by quantum size effects. The blue band (452 nm) is seen to grow with annealing temperatures due to Ti^{3+} defects which are stabilized by Fe^{3+} in the doped specimens. A correlation between the PL band and EPR band intensity, grown from same species, was found.

Acknowledgement

The work was supported by the grant from the Nano Science and Technology Initiative of the Department of Science and Technology, and University Grant Commission, New Delhi.

References

[1] Sahoo T., Tripathy S.K., et al. Microstructural and photo luminescence studies on hydrothermally synthesized Ce-doped barium titanate nanocrystals. *Materials Science and Engineering: B.*, **131**(1-3), P. 277–280 (2006).

[2] Yu J., Sun J., et al. Light-emission properties in nanocrystalline $BaTiO_3$. *Applied Physics Letters.*, **77**(18), P. 2807–2809 (2000).

[3] Pizani P.S., Basso H.C., et al. Visible photoluminescence in amorphous ABO_3 perovskites. *Applied Physics Letters*, **81**(2), P. 253–255 (2002).

[4] Pizani P.S., Leite E.R., et al. Photoluminescence of disordered ABO_3 perovskites. *Applied Physics Letters*, **77**(6), P. 824–826 (2000).

[5] Gunter P., Huignard J.P., *Photorefractive materials and Their Application I and II. Topic in Applied Physics*, Vol. 61 and 62. Springer-Verlag, Berlin, (1988 and 1989).

[6] Klein M.B., Schwartz R.N., Photorefractive effect in $BaTiO_3$: microscopic origins. *Journal of the Optical Society of America B: Optical Physics*, **3**(2), P. 293–305 (1986).

[7] Schunemann P.G., Temple D.A., et al. Role of iron centers in the photorefractive effect in barium titanate. *Journal of the Optical Society of America B: Optical Physics*, **5**(8), P. 1685–1696 (1988).

[8] Mazur A., Schirmer O.F., et al. Optical absorption and light-induced charge transport of Fe^{2+} in $BaTiO_3$. *Applied Physics Letters*, **70**(18), P. 2395–2397 (1997).

[9] Katiyar R.S., Meng J.F., et al. Effect of grain size and Pb dopant on luminescence in $BaTiO_3$. *Journal of Vacuum Science & Technology A*. **15**(6), P. 2945–2948 (1997).

[10] Meng J., Huang Y., et al. Photoluminescence in nanocrystalline $BaTiO_3$ and $SrTiO_3$. *Physics Letters A*, **205**(1), P. 72–76 (1995).

[11] Dey S.K., Leeg R.Z., Processing and parameters of sol-gel PZT thin-films for GaAs memory applications. *Ferroelectrics*, **112**(1), P. 309–319 (1990).

[12] Leonelli R., Brebner J.L., Time-resolved spectroscopy of the visible emission band in strontium titanate. *Physical Review B*, **33**(12), P. 8649–8656 (1986).

[13] Bouma B., Blasse G., Dependence of luminescence of titanates on their crystal structure. *Journal of Physics and Chemistry of Solids*, **56**(2), P. 261–265 (1995).

[14] Zhang M.S., Yin Z., et al. Study of structural and photoluminescent properties in barium titanate nanocrystals synthesized by hydrothermal process. *Solid State Communications*, **119**(12), P. 659–663 (2001).

[15] Souza I.A., Gurgel M.F.C., et al. Theoretical and experimental study of disordered $Ba_{0.45}Sr_{0.5}5TiO_3$ photoluminescence at room temperature. *Chemical Physics*, **322**(3), P. 343–348 (2006).

[16] Orhan E., Varela J.A., et al. Room-temperature photoluminescence of $BaTiO_3$: Joint experimental and theoretical study. *Physical Review B*, **71**(8), P. 085113–085119 (2005).

[17] Silva M.S., Cilense M., et al. The nature of the photoluminescence in amorphized PZT. *Journal of Luminescence*, **111**(3), P. 205–213 (2005).

[18] Beck H.P., Eiser W., et al. Pitfalls in the synthesis of nanoscaled perovskite type compounds. Part I: Influence of different so-gel preparation methods and characterization of nanoscaled $BaTiO_3$. *Journal of the European Ceramic Society*, **21**(6), P. 687–693 (2001).

[19] Jana A., Kundu T.K., et al. Dielectric behavior of Fe-ion-doped $BaTiO_3$ nanoparticles. *Journal of Applied Physics*, **97**(4), P. 044311–044316 (2005).

[20] Jana A., Ram S., et al. $BaTiO_3$ nanoparticles of orthorhombic structure following a polymer precursor. Part I. X-ray diffraction and electron paramagnetic resonance. *Philosophical Magazine B*, **87**(35), P. 5485–5495 (2007).

[21] Hoffmann K., Hahn D., Electron Spin Resonance of Lattice Defects in Zinc Oxide. *Physica status solidi (a)*, **24**(2), P. 637–648 (1974).

[22] Ram S., Kundu T.K., Synthesis and Unusual Electron Paramagnetic Resonance Spectrum of Metastable Nanoclusters of ZnO Semiconductor Crystallites. *Journal of Nanoscience and Nanotechnology*, **4**(8), P. 1076–1080 (2004).

[23] Kutty T.R.N., Murugaraj P., EPR study on the role of Mn in enhancing PTC of $BaTiO_3$. *Materials Letters*, **3**(5-6), P. 195–199 (1985).

[24] Hornig A.W., Rempel R.C., et al. Interpretation of Electron Paramagnetic Resonance in $BaTiO_3$. *Physical Review Letter*, **1**(8), P. 284–286 (1958).

[25] Kirkpatric E.S., Muller K.A., et al. Strong Axial Electron Paramagnetic Resonance Spectrum of Fe^{3+} in $SrTiO_3$ Due to Nearest-Neighbor Charge Compensation. *Physical Review*, **135**(1A), P. A86–A90 (1964).

[26] Maartense I., Magnetic Properties of Fe^{2+}-Doped $MnCO_3$. *Physical Review B*, **6**(11), P. 4324–4331 (1972).

[27] Cordona M., Optical Properties and Band Structure of $SrTiO_3$ and $BaTiO_3$. *Physical Review*, **140**(2A), P. A651–A655 (1965).

[28] Kim S.W., Fujita S., et al. Self-organized ZnO quantum dots on SiO_2/Si substrates by metalorganic chemical vapor deposition. *Applied Physics Letters*, **81**(26), P. 5036–5038 (2002).

[29] Brus L., Electronic wave functions in semiconductor clusters: experiment and theory. *The Journal of Physical Chemistry*, **90**(12), P. 2555–2560 (1986).

[30] Cho W.S., Hamada E., Planar defects and luminescence of $BaTiO_3$ particles synthesized by a polymerized complex method. *Journal of Alloys and Compounds*, **268**(1-2), P. 78–82 (1998).

NANOSYSTEMS: PHYSICS, CHEMISTRY, MATHEMATICS, 2013, 4 (2), P. 276–287

PARTICIPATION OF NANOCRYSTALLINE $\mathbf{TiO_2}$ SURFACE IN THE ELECTRON TRANSFER BETWEEN SEMICONDUCTOR SOLID AND ADSORBED COBALT(III)-*R*PY COMPLEX

A. S. Ganeshraja[1], K. Anbalagan[1]

[1] Department of Chemistry, Pondicherry University Kalapet, Pondicherry 605 014, India
asgchem84@gmail.com, kanuniv@gmail.com

PACS 81.20.-n, 61.72.uj

Cis-[$\mathrm{Co^{III}(tn)_2}$(Rpy)Br]$\mathrm{Br_2}$, ($R = $ 4-CN, H, 4-Bz, 4-Me, 4-Et, and 4-MeNH), in aqueous 2-propanol exhibit varying adsorption characteristics and led to surface compound formation. UV (λ = 254) excitation of the nano-$\mathrm{TiO_2}$//cobalt(III)-(Rpy) surface compound resulted in interfacial electron transfer (IFET) reaction. The IFET has been found to be dependent upon the coordination environment of the complex, more precisely due to the Rpy ligand. In addition, the proposed mechanism of the IFET reaction includes the formation of a $\mathrm{Co^{II}}$ ion implanted in nanocrystalline $\mathrm{TiO_2}$. This photoreduction was found to be solvent controlled. The photoefficiency of the $\mathrm{Co^{II}_{aq}}$ formation was spectrally analyzed simultaneously as $\mathrm{Co^{II}:TiO_2}$ was isolated from the photolyte solution. The isolated solid was subjected to FTIR, DRS, PXRD, and SEM-EDX instrumental analysis. It is concluded that the removal of metal ion in the form of a complex is coordination structure dependent, hence, seems more specific in removal efficiency and in doping the anatase lattice.

Keywords: surface adsorption, interfacial electron transfer reaction, cobalt doped nano-$\mathrm{TiO_2}$.

1. Introduction

Interfacial electron transfer (IFET) between sensitizer molecular adsorbates and semiconductor materials has been a subject of intense research in recent years. Examples include, among others, photocatalysis [1], surface photochemistry [2,3], dye-sensitized solar cells (DSSCs) [4], organic semiconductor-based photovoltaics [5], and nanoscale optoelectronics based on a single molecule or a small group of molecules [6]. This is a fundamental process in surface chemistry, relevant to a broad range of practical applications, including effective mechanisms of solar energy conversion [7,8], photoelectrochemistry [9], artificial photosynthesis and imaging [10]. Despite its great technological significance, IFET remains poorly understood [1,2] compared to electron transfer in homogeneous solutions [11].

At present, $\mathrm{TiO_2}$ is considered as the most promising photocatalyst because of its low cost, nontoxicity, excellent stability, and high efficiency [12]. However, it can be activated only through irradiation with ultraviolet (UV) light (4–5 % of solar light) because of its large band gap of 3.0 eV to 3.2 eV [13]. Thus, many attempts have been made to enhance the photocatalytic activity of $\mathrm{TiO_2}$ in the visible light range. Doping with transition metals (Cr, Co, V, Fe, etc.) is one of the promising approaches [14]. Co(II) is considered as one of the more promising candidates because of its effect in reducing the electron–hole recombination rate and in shifting the absorption edge into the visible light region. Co-doped $\mathrm{TiO_2}$ has shown high activities for degradation of acetaldehyde, 2-chlorophenol, and 2,4- dichlorophenol in aqueous solutions [15]. Transition metal-doped

TiO_2 photocatalysts are active under visible light irradiation. However, these materials have certain disadvantages, such as thermal instability as well as low quantum efficiency of the photoinduced charge carriers [16,17]. To overcome these drawbacks, considerable effort has been exerted to modify the properties of transition metal-doped TiO_2 using nonmetal impurities [18]. In this work, the luminescence properties of anatase TiO_2 samples doped with different amounts of Co^{2+} when were excited using a source with energy (2.54 eV), well below the TiO_2 bandgap, is reported. The effect of introducing defects through the incorporation of Co atoms in the TiO_2 lattice is discussed. With this approach the electron–hole recombination, which is excitonic in nature, is not excited because laser energies greater or on the order of the bandgap are required; instead, this study is focused on the defects-related emission band observed by Sekiya et al. [19] at 1.95eV (77 K). In our sol–gel samples, this band was observed at 2.02eV at room temperature [20].

Understanding the photophysics of transition metal complexes attached to semiconductor surfaces is essential for the design of artificial systems for solar energy conversion. In particular, Cobalt(III)-pyridyl complexes have attracted a great deal of attention as a promising class of compounds with long-lived charge-separated states and rich photochemical properties. However, their electronic excitations and photoconversion mechanisms remain only partially understood. This paper builds upon our recent work [21,22] and addresses the study of TiO_2 nanoparticles sensitized with *cis*-$[Co^{III}(tn)_2(R\text{py})Br]Br_2$ (where R=*4*-CN, H, *4*-Bz, *4*-Me, *4*-Et, and *4*-MeNH) adsorbates. Our study includes the characterization of the electronic excitations, electron injection time scales, and IFET mechanisms [23] IFET photoefficiency and photo degradation of 2-propanol. Here, we focus on TiO_2 surfaces modified by Co(III)-pyridyl complexes attached by nitrogen linkers. Emphasis is given to the characterization of the electronic excitations and injection time scales as determined by the nature of the molecular adsorbates and the attachment modes.

2. Experimental

2.1. Materials and methods

$CoCl_2.6H_2O$ (99%), R-pyridine (Rpy), ferric chloride, potassium oxalate, sodium acetate, ammonium thiocyanate, nanocrystalline titanium dioxide (surface area = 200–220 m^2/g and particle size = 25 nm) and DMSO-d_6 (NMR solvent) were purchased from Sigma Aldrich. 1,3-diamino propane (LR), pyridine, 1,10-phenanthroline and all other chemicals were purchased from Himedia and SD. Fine Chemicals (India). All the solvents and 1,3-diamino propane were purified by distillation and water was triply distilled over alkaline $KMnO_4$ in an all glass apparatus. Analytically pure crystals of *cis*-$[Co^{III}(tn)_2(R\text{py})Br]Br_2$ adsorbates (where R = *4*-CN, H, *4*-Bz, *4*-Me, *4*-Et, and *4*-MeNH) were synthesized by a modified procedure [24] and recrystallized.

2.2. Instrumentation

Cobalt(III) complexes were photolysed using a 254 nm, 6 watt low pressure mercury vapor lamp as the light source (Germicidal G4T5, 3H, model 3006) in a small quartz immersion well (model 3210, 80 mL cap. Photochemical Reactors Ltd, UK). Electronic absorption spectral studies were undertaken on a double beam spectrophotometer (Shimadzu 2450, Japan) with integrating sphere attachment (ISR-2200). UV-vis diffuse reflectance spectra (UV-vis DRS) were recorded in absorbance mode at room temperature in the 200–1000 nm range on a Shimadzu, (UV 2450) double-beam spectrophotometer equipped with integrating sphere attachment (ISR-2200) using $BaSO_4$ as the reference. The instrument is interfaced with a computer for data collection and analysis. Fourier transform infrared (FTIR) spectra were recorded in the 4000–400 cm^{-1} range using a Thermo Nicolet 6700 FTIR spectrophotometer using KBr wafer with resolution 0.1 cm^{-1}. ^1H NMR measurements were made on a Bruker instrument; model Avance-II in 400 MHz Fourier transform-nuclear magnetic resonance with DMSO-d_6 solvent. PXRDs were collected on an 800 W Philips (PANANALYTICAL, Almelo, The Netherlands) powder diffractometer equipped with an etched glass plate sample holder by rotating anode diffractometer in the 2θ range 10–80 ° with step size of 0.02 ° using Cu Kα (λ = 1.5406 Å) radiation to determine the identity of any phase and their crystalline size. Surface morphology and chemical mapping were examined by SEM (Hitachi, S-3400N microscope), operating at 0.3-30 kV. Microanalyses (energy dispersive X-ray analysis, EDX) were performed with Thermo SuperDry II attachment of SEM.

2.3. Photocatalytic activity measurement

The photocatalytic activity of nano-TiO_2 was evaluated by measuring the efficiency of the reduction of the $Co^{III}(tn)_2(R py)Br^{2+}$ complex in neat water/aqueous 2-propanol solutions under 254 nm light irradiation. The photoefficiency was calculated by estimating photogenerated Co^{II} by Kitson's method [25]. Photoreduction was carried out in a reactor vessel using a 254 nm low pressure mercury vapor lamp, which were housed in a fume hood (Lab Guard), covered with black polythene sheet to prevent extraneous light. The photoreactor is a double walled quartz vessel, in which, photolyte mixture (100 mg of nano-TiO_2 crystals in 80 mL of *cis*-$Co^{III}(tn)_2(R py)Br^{2+}$ (1.68×10^{-3} M) solution and 1M $NaNO_3$) was taken in the inner jacket and cool water in the outer jacket. Prior to irradiation, the suspension of the catalyst was achieved by ultrasonic treatment and continued magnetic stirring in the dark to attain cobalt(III) complex ion adsorption/desorption equilibrium on the catalyst. The photolyte suspension was irradiated with 254 nm light for defined periods (0, 2–16 min). About 4 mL aliquots were sampled and centrifuged to remove the semiconductor particles and then spectrally analyzed. In order to diminish experimental error, experiments were repeated at least two-three times for the same sample and the mean value was calculated. Photoefficiency of Co(II) formation in terms of percentage, PE (%) was computed using the formula: PE (%) = $[(A_t - A_i)/A_t] \times 100$ where A_i and A_t are the absorbances of the photolysed solutions initially and at definite time interval 't' respectively.

3. Results and discussion

3.1. Photocatalytic reduction of $Co^{III}(tn)_2(R py)Br^{2+}$

Cobalt(III)-*R*pycomplex is a good UV light absorber, however, it decomposes on exposure to light over a long period of time due to ligand to metal charge transfer (LMCT) bands ($\lambda = \sim 356$ nm). Surprisingly, the addition of nano-TiO_2 (anatase) provoked the complex to degrade more efficiently and a higher amount of cobalt(II) was generated. Figure 1 depicts repetitive scan spectra of $Co^{III}(tn)_2(4\text{-Etpy})Br^{2+}$ complex observed at defined irradiation time intervals; there is a blue shift in the absorption maxima at $\lambda = 357 \rightarrow 351$ nm and red shift at $\lambda = 512 \rightarrow 518$ nm. The absence of an isosbestic point in the repetitive scan spectra indicates the decomposition of the complex during the reduction process suggesting, perturbation of the Co^{III} centre due to IFET. The photoefficiency of Co(II) formation by TiO_2 (e^-_{cb}/h^+_{vb})/scavenger of $Co^{III}(tn)_2(4\text{-Etpy})Br^{2+}$ is increased with respect to the concentration of 2-propanol and more active at higher concentrations in the photolytic solutions. This implies the observed photoefficiency (Table 1) for the formation of Co^{II} is a summation of the individual electron transfer reactions due to (i) excited nano-TiO_2: $Co^{III}(tn)_2(R\text{py})Br^{2+}$ + nano-TiO_2 + hν (λ = 254 nm) $\rightarrow$ Co^{II} + products and (ii) ligand to metal charge transfer transition in cobalt(III) complex: $Co^{III}(tn)_2(R\text{py})Br^{2+}$ + hν (λ = 254 nm) $\rightarrow$ Co^{II} + products. However, the former path is predominant and requires a thorough investigation.

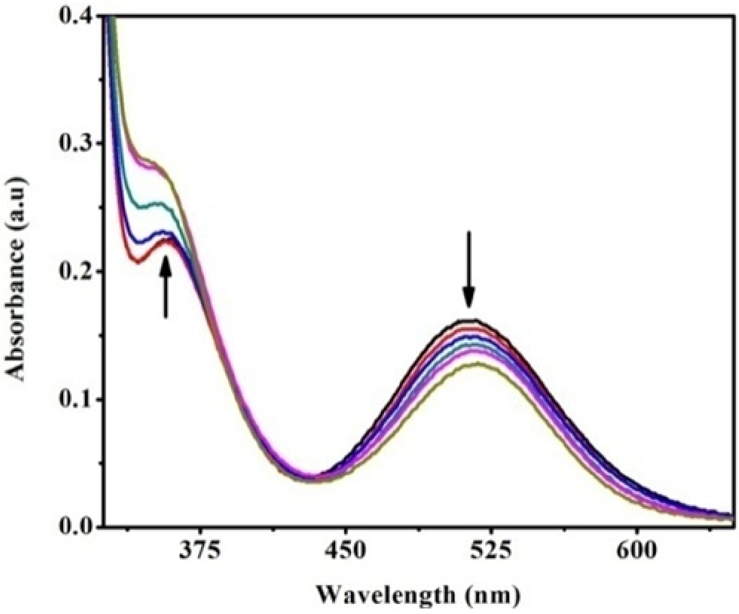

Fig. 1. Repetitive scan spectra recorded for the photocatalysed $Co^{III}(tn)_2$ (4-Etpy)Br^{2+} complex ion in nano-TiO_2 suspension in neat water at various time intervals: 0, 2, 4, 8, 12 and 16 min respectively. Complex concentration = 1.68×10^{-3} M, ionic strength = 1M $NaNO_3$, pH $\sim$ 7 and at 298 K

In the case of photoreduction of $Co^{III}(tn)_2(R\text{py})Br^{2+}$ complex with nanocrystalline titania influence than that of polycrystalline titania. Nanocrystalline materials are single- or multi-phase polycrystalline solids with a grain size of a few nanometers (1 nm = 10^{-9} m = 10 Å), typically less than 100 nm. Since the grain sizes are so small, a significant volume of the microstructure in nanocrystalline materials is composed of interfaces, mainly grain boundaries, i.e., a large volume fraction of the atoms resides in grain boundaries. Consequently, nanocrystalline materials exhibit properties that are significantly different from and often improved over, their conventional coarse-grained polycrystalline counterparts [26]. In polycrystalline wide band gap oxide semiconductors such as ZnO and TiO_2, the photoconductivity (PC) has been observed to decay very slowly, over a period of many hours to several days [27,28]. This slow decay is often referred to as 'persistent PC' and different possible explanations have been proposed [29-31]. In some cases, models have been fitted to the experimental data for the determination of electronic parameters of the materials, such as the energy distribution of charge carrier traps [32,33] Photocatalytic degradation studies of pollutants using either Co(II)-tetrasulfophthalocyanine grafted on TiO_2 via a silane reagent or polycrystalline TiO_2 samples impregnated with Cu(II)-phthalocyanine [32] were reported in the literature.

Table 1. Photoefficiency P.E (%) of formation of Co(II) upon $\lambda = 254$ nm irradiation of *cis* $Co^{III}(tn)_2(Rpy)Br^{2+}$ in aqueous 2-propanol at 298 K. ionic strength 1M $NaNO_3$, complex concentration = $1.68 \times 10^{-3}M$

Rpy	PE (%) in water/Pr^{i}OH(w/w)%								pKa value of Rpy
		100/0	95/5	90/10	85/15	80/20	75/25	70/30	
4-CN	-	14±0.5	18±1.0	19±1.0	21±0.7	26±0.8	28±0.9	32±0.6	1.90
	poly-TiO_2	16±1.0	17±0.5	21±1.0	24±0.8	29±0.7	31±0.6	37±0.5	
	nano-TiO_2	17±0.7	20±0.9	24±0.5	29±0.8	31±0.6	37±1.0	41±1.4	
H	-	15±0.8	21±0.7	29±1.0	34±0.5	38±1.4	40±0.9	42±1.2	5.25
	poly-TiO_2	14±0.6	24±1.0	32±0.8	35±0.8	41±0.7	44±0.9	48±1.2	
	nano-TiO_2	18±1.0	25±0.7	34±0.6	39±1.0	45±0.5	51±0.9	55±0.5	
4-Bz	-	12±0.8	19±1.0	24±0.6	28±0.7	32±0.8	38±0.5	41±1.2	5.59
	poly-TiO_2	16±0.6	23±0.8	28±1.0	30±1.4	34±0.5	38±0.9	49±0.8	
	nano-TiO_2	18±0.6	21±0.8	29±0.7	31±0.5	36±1.0	44±0.9	57±1.4	
4-Me	-	12±1.0	19±1.0	26±0.5	29±0.8	34±0.9	38±0.8	49±1.4	6.02
	poly-TiO_2	17±1.0	23±0.5	29±0.6	34±0.8	37±0.9	45±0.9	52±0.7	
	nano-TiO_2	19±0.7	26±0.5	33±1.0	38±0.6	46±0.8	54±1.4	57±0.9	
4-Et	-	18±1.2	24±0.6	28±1.0	31±0.5	36±1.4	41±0.8	49±0.5	6.02
	poly-TiO_2	19±1.0	27±1.0	32±0.9	37±0.8	45±0.5	48±0.8	53±1.4	
	nano-TiO_2	21±0.6	28±0.5	35±1.0	39±0.9	49±0.8	58±0.5	64±0.7	
4-MeNH	-	19±0.8	24±0.5	29±0.5	32±1.0	46±1.0	52±0.8	53±0.9	9.70
	poly-TiO_2	23±0.7	28±0.8	32±0.5	38±0.6	49±1.0	58±0.9	61±0.5	
	nano-TiO_2	26±0.8	31±0.6	37±0.7	44±0.5	54±1.0	63±0.9	69±0.8	

3.2. Photo-oxidation of 2-propanol to acetone by ^{1}H NMR

The photoreduction was systematically followed by NMR measurements which indicate the growth of acetone peak progressively appearing in signal intensity as a function of dosage of light [34]. Table 2 exhibits ^{1}H NMR signals due to 2-propanol appearing at $\delta = 1.0$ to 1.1 ppm ($-CH_3$) and $\delta = 3.8$ to 3.93 ppm (-CH) before the initiation of photoreduction and after defined irradiation periods. There is a steady growth of the signal due to photo released acetone and the signal intensity increases with respect to the level of light irradiation. That is, a new ^{1}H NMR signal at $\delta = 2.04$ ppm indicates the formation of acetone and the signal strength (Table 2) increases considerably with increased irradiation times [35]. In fact, the integrated intensity of the acetone signals gradually increase, whereas the -CH and $-CH_3$ (2-propanol) signals gradually decrease. The origination of acetone is from the oxidation of 2-propanol resulting from the scavengingof valence band holes by the alcohol: nano-TiO_2 (h^+) + $(CH_3)_2CHOH \rightarrow CH_3COCH_3$.

3.3. Mechanism of photoinduced electron transfer reaction

It is apparent from Table 1 that excited nanocrystalline TiO_2 shows better catalytic activity, which critically depends upon the surface-substrate interaction. Surface affinity of molecules/ions is a competing feature of the surface, therefore, formation of poly (or) nano-TiO_2//cobalt(III)-(Rpy) surface compound is inevitable. Therefore, an enhancement

Table 2. ^{1}H NMR data for the generator of acetone upon λ = 254 nm irradiation of $Co^{III}(tn)_2(4\text{-}Etpy)Br^{2+}$ at 298 K in DMSO-d_6. Photocatalyst nano-TiO_2, ionic strength 1N $NaNO_3$, complex 1.86×10^{-3}M. 'A' and 'P', respectively, denote acetone and 2-propanol

Irradiating time (min)	2x -CH_3(d) P δ ppm		-CH(m) P δ ppm							2x -CH_3(s) A δ ppm
0	0.98	0.99	3.72	3.73	3.75	3.61	3.78	3.79	3.81	-
8	0.98	0.99	3.72	3.73	3.75	3.76	3.78	3.79	3.81	2.02
16	0.98	0.99	3.72	3.73	3.75	3.76	3.78	3.79	3.81	2.02
45	0.98	0.10	3.71	3.73	3.75	3.76	3.77	3.79	3.80	2.02

in the photocatalytic reduction originates from (i) Rpy can modify the surface affinity of $Co^{III}(tn)_2(R py)Br^{2+}$ ion with the nano-TiO_2 surface and (ii) photoexcitation can prompt the formation of microdomains in nano-TiO_2 with characteristic hydrophobic/hydrophilic behavior. Therefore, accumulation of adsorbate is varied, and hence, available for reduction. In addition, charge relaxation/recombination processes of nano-TiO_2 (e^-, h^+) pair are altered due to the formation of compact nano-TiO_2//cobalt(III)-(Rpy) surface compound, (Co^{III}_{ad}). Such processes provide a favorable negative charge potential for reduction of the Co(III) center. Thus, the overall efficiency of heterogeneous photocatalysis is determined by the adsorbate content and population/lifetime of the charge carriers for interfacial charge-transfer processes [36,37]. Sixth ligand (Rpy) in $Co^{III}(tn)_2(R py)Br^{2+}$ with a hydrophobic tail imparts variation in surface adherence of the complex ion on the surface of nano-TiO_2, however, the adsorption process is restricted by thermodynamic aspects. To rationalize these observations, one must invoke a mechanism that incorporates several complementary routes as given in eqs. (1-7).

Surface compound formation: $\text{nano-}TiO_2 + Co^{III}(tn)_2(R py)Br^{2+} \rightarrow \text{nano-}TiO_2//Co^{III}(tn)_2(R py)Br^{2+}$ (1)

Photoexcitation: $\text{nano-}TiO_2 + h\nu \rightarrow \text{nano-}TiO_2(e^-, CB) + \text{nano-}TiO_2(h^+, VB)$ (2)

Charge trapping: $(e^-, CB) \rightarrow (e^-, tr)$ (3)

$(h^+, VB) \rightarrow (h^+, tr)$ (4)

Electron-hole recombination: $(e^-, tr)/(e^-,CB) + (h^+,tr)/(h^+, VB) \rightarrow (e^-,tr) + \text{heat}$ (5)

Electron transfer: $\text{nano-}TiO_2\ (e^-, CB)/\ (e^-, tr) + (Co^{III}_{ad}) \rightarrow Co^{II}_{surf} + Co^{II}_{aq}$ (6)

Hole transfer: $\text{nano-}TiO_2(h^+, VB)/\ \text{nano-}TiO_2\ (h^+, tr) + (CH_3)_2CHOH \rightarrow CH_3COCH_3$ (7)

Where (e^-, tr) and (h^+, tr) represent charge trapped surface states while Co^{III}_{ad}, Co^{II}_{surf}, and Co^{II}_{aq} represent surface compound, surface implanted species and aqueous species respectively. It is unlikely that the photoreduction of Co(III) proceeds through multielectron process, but it should occur in one electron step. The predominant reduction path of the metal centre is as given in eqs. 1-7 with a limited contribution from charge transfer population states like: $\sigma(N) \rightarrow d\sigma^*(Co)$ and $\sigma(Cl) \rightarrow Co$.

3.4. *p*Ka dependent photoreduction

In this investigation, a linear dependence of photoefficiency(%) of $Co^{III}(tn)_2(R py)$ Br^{2+}/TiO_2 suspension with respect to the Rpyligand in terms of acidity constant (pKa) as shown in Figure 2 is observed. Linear regression analysis of PE% versus pKa yields a slope indicating that electron donating groups in Rpy ($p\text{Ka} > 5.25$) enhances photo efficiency (%) and that electron withdrawing groups in Rpy ($p\text{Ka} = 1.90$) reduces the photo catalytic behavior. Therefore, it can be concluded that coordination environment of the metal centre of a transition metal ion can greatly influence the photochemical character of the complex.

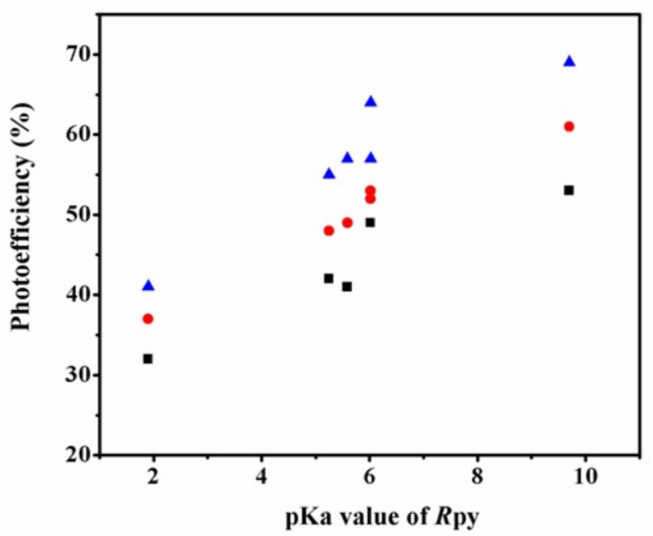

Fig. 2. Linear plot of photoefficiency *vs.* pKa value of aryl amine (R) in $\text{Co}^{\text{III}}(\text{tn})_2(R\text{py})\text{Br}^{2+}$; ■ absence of nano-$TiO_2$, ● presence poly-$TiO_2$, and ▲ presence nano-$TiO_2$ in 70/30 (w/w)% water/$\text{Pr}^{\text{i}}\text{OH}$

It is interesting to note that the PE (%) of Co^{II} generation is (i) linearly increasing with 2-propanol content and (ii) showing some relationship with variation in the Rpy ligand of the complex. This non-consistency can be attributed to nanoparticle (or polycrystalline) surface//cobalt(III)-Rpy affinity and subsequent interfacial electron transfer. Accumulation of cobalt(III) complex on the surface of nano-TiO_2 to form a compact layer is mainly dependent upon the blocking effect of Rpy due to electron withdrawing and electron donating properties. Pellizzetti and co-workers showed a significant alteration in the distribution of aromatic intermediates on the surface of TiO_2 in their study [38]. Figure 2 shows photoefficiency *vs* pKa of the aryl amine of the Rpy ligand of six $\text{Co}^{\text{III}}(\text{tn})_2(R\text{py})\text{Br}^{2+}$ complexes. It is interesting that, within this limited set of complexes at least, there is an obvious relationship between PE and the pKa value of the ligand. There is a reasonable enhancement in the PE with aromatic ring electronic nature of the Rpy ligand, which appears to asymptotically approach a limiting value.

3.5. Characterizations of cobalt-doped nano-TiO_2

The isolated solids were subjected to spectral, macrostructural, microstructural, and surface morphological analyses. Therefore, the irradiated $\text{Co}^{\text{III}}(\text{tn})_2(R\text{py})\text{Br}^{2+}$ with nanocrystalline TiO_2 were subjected to FTIR, DRS, PXRD and SEM-EDX analyses. The experimental results yield the characteristic features on the inclusion of cobalt ion in anatase lattice, which was confirmed by XRD patterns. XRD and SEM results revealed that the particle size of Co-doped nano-TiO_2 is enhanced as the result of the UV-light irradiation method. Here, we focus on TiO_2 surfaces modified by $\text{Co}^{\text{III}}(\text{tn})_2(R\text{py})\text{Br}^{2+}$

complexes attached by nitrogen linkers. Emphasis is given to the characterization of the electronic excitations and injection time scales as determined by the nature of the molecular adsorbates and the attachment modes.

3.6. FTIR, DRS and powder X-ray difraction analysis of Co/nano-TiO_2

Transmittance peaks observed between 450–600 cm^{-1} can be assigned to the Ti-O-Ti bond as shown in Figure 3(A). Both pure and Co-doped nano-TiO_2 showed a characteristic band at 511 cm^{-1} corresponding to a Ti-O bond of the anatase phase. Ti-O vibration tends to shift to lower energy regions with Co content in nano-TiO_2. The DRS of undoped anatase [39] showed 100% reflectance, and doped samples absorb more effectively from 480–600 nm. Nano-TiO_2 with low cobalt density absorbs at ~563 nm, and the λ_{max} shifts towards ~574 nm (Figure 3(B)). The red shift is attributed to the 3d Co^{2+} electrons into the conduction band of nano-TiO_2. The absorption spectrum of TiO_2 consists of a single broad intense absorption around 400 nm due to the charge-transfer from the valence band (mainly formed by $2p$ orbitals of the oxide anions) to the conduction band (mainly formed by $3d$ t_2g orbitals of the Ti^{4+} cations) [40]. Pure TiO_2 showed absorbance in the shorter wavelength region while Co/TiO_2 and the DRS results showed a red shift in the absorption onset value in the case of Co-doped titania. The doping of various transition metal ions into TiO_2 could shift its optical absorption edge from the UV into the visible light range, but no prominent change in the TiO_2 band gap was observed [40].

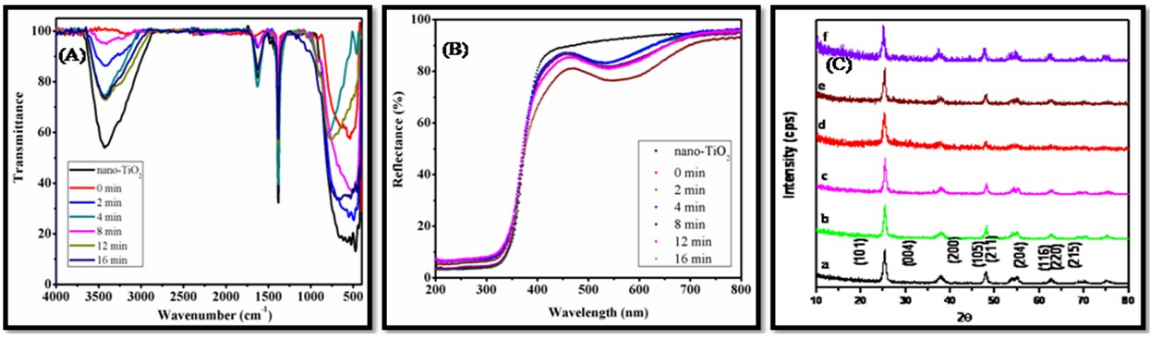

Fig. 3. (A) Diffuse reflectance spectra, (B) FT-IR spectra and (C) PXRD pattern of the pure nano TiO_2 and x%Co:nano-TiO_2

Figure 3(c) shows the X-ray diffraction patterns of the undoped and cobalt-doped TiO_2 samples. The nanocrystalline anatase structure was confirmed by (1 0 1), (0 0 4), (2 0 0), (1 0 5) and (2 1 1) diffraction peaks [41,42]. The XRD patterns of anatase have a main peak at $2\theta = 25.2^\circ$ corresponding to the 101 plane (JCPDS 21-1272) while the main peaks of rutile and brookite phases are at $2\theta = 27.4^\circ$ (110 plane) and $2\theta = 30.8^\circ$ (121 plane), respectively. Therefore, rutile and brookite phases have not been detected [43,44]. The XRD patterns didn't show any Co phase (even for 5% Co/TiO_2 sample) indicating that Co ions were uniformly dispersed among the anatase crystallites. In the region of $2\theta = 10–80^\circ$, the diffractive peak shapes of pure TiO_2 crystal planes are quite similar to that of Co/TiO_2 with different concentrations of Co. The XRD patterns indicate pure anatase phase [45] form and confirm the absence of phase transformation to other related crystalline phases like rutile and brookite. This indicates that only a small amount of the elements are substituted into the Ti^{4+} sites, while interstitially incorporated Co(II) cannot be discounted as shown in Figure 3(C).

Table 3. The chemical content of cobalt doped TiO_2 samples, recorded for nano-TiO_2/Co,x% prepared by UV sensitized photoreduction of (1.63×10^{-3} M) $Co(tn)_2(4\text{-}Mepy)Br^{2+}$ in water at various time interval of irradiation and at 27 ° according to the Energy Dispersive X-ray analysis

Irradiation Time(min)	Abbreviation of Sample	Content Weight % (atm. %)		
		Ti	O	Co
-	nano-TiO_2	59.95 (33.33)	40.05 (66.67)	-
0	nano-TiO_2/Co,0.26 atm. %	60.05 (33.40)	40.32 (67.12)	0.26(0.12)
2	nano-TiO_2/Co, 0.53 atm. %	51.29 (26.18)	48.17 (73.60)	0.53 (0.22)
4	nano-TiO_2/Co, 0.68 atm. %	35.89 (15.86)	63.43 (83.90)	0.68 (0.25)
12	nano-TiO_2/Co, 0.50 atm. %	30.66 (12.93)	68.85 (86.90)	0.50 (0.17)
16	nano-TiO_2/Co, 0.71 atm. %	36.97 (16.49)	62.32 (83.25)	0.71 (0.26)

3.7. Surface Morphology of cobalt doped nano-TiO_2

The morphology of the undoped TiO_2 sample is shown in Figure 4, revealing that the agglomeration of nanocrystals form particles or grains, which are expected to contribute more grain boundary effects. The chemical compositions of undoped and doped samples are very essential to know the exact concentration of the dopant (Co here) and the defects. The EDAX spectrum of undoped TiO_2 shows the presence of Ti and O elements alone in the sample, confirming the absence of any impurities. The atomic percentage of Ti and O elements in undoped TiO_2 sample is 59.95 and 40.05, respectively, but actual stoichiometric atomic percentage of Ti is 36.97 and O is 62.32, which shows oxygen deficiency in the undoped TiO_2 sample. Likewise, all the doped samples show oxygen deficiency. Table 3 gives the atomic percentage of Ti, O, and Co. SEM images illustrate that the particles, which mainly belong to anatase phase, are loosely agglomerated, spherical and a few hundred nm in size (Figure 4(A)). Homogeneous and continuous surface structure with well dispersed spheres appear as the dopant density in Co/TiO_2 is increased (Figure 4(B)(C)).

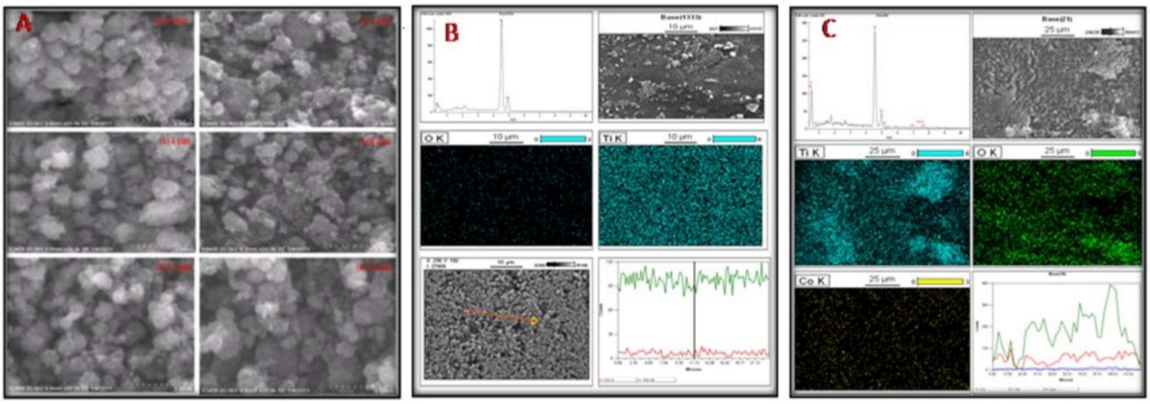

Fig. 4. (A) SEM images and (B), (C) EDX spectra, mapping, line spectra of pure nano-TiO_2 and x%Co:nano-TiO_2 particles

4. Conclusion

We have demonstrated that *cis*-$[Co^{III}(tn)_2(R\text{py})Br]Br_2$ complexes are photocatalytically reduced into Co^{II}_{sol}. The photoreduction is found to be solvent dependent. The photoproduced acetone illustrates the scavenging effect of isopropanol. The IFET reaction mechanism is important to understand the functioning and construction of nano-TiO_2 photocatalysed photochemical energy conversion systems. It is concluded that the removal of metal ion, hence, seems more specific in removal efficiency and in doping the anatase lattice.

Acknowledgment

KA is thankful to the CSIR (sanction order: No. 01(2570)/12/EMR-II/3.4.2012), New Delhi for financial support through major research project. ASG is thankful to Mr. S. Thirumurugan and Mr. Kanniah Rajkumar, Department of Chemistry, Pondicherry University for their help in data measurement. The authors are thankful to CIF, Pondicherry University for instrumental facility.

References

[1] Kamat P. V. Photochemistry on Nonreactive and Reactive (Semiconductor) Surfaces. *Chem. Rev.*, **93**, P. 267–300 (1993).

[2] Guo H., Saalfrank P., Seideman T. Theory of Photoinduced Surface Reactions of Admolecules. *Prog. Surf. Sci.*, **62**, P. 239–303 (1999).

[3] Zimmermann F. M., Ho W. State Resolved Studies of Photochemical Dynamics at Surfaces. *Surf. Sci. Rep.*, **22**, P. 127–247 (1995).

[4] Hagfeld A., Gratzel M. Molecular Photovoltaics. *Acct. Chem. Res.*, **33**, P. 269–277 (2000).

[5] Forrest S. R. The Limits to Organic Photovoltaic Cell Efficiency. *MRS Bull.*, **30**, P. 28–32 (2005).

[6] Galperin M., Nitzan A. Current-Induced Light Emission and Light-Induced Current in Molecular-Tunneling Junctions. *Phys. Rev. Lett.*, **95**, P. 206802-1–4 (2005).

[7] O'Regan B., Gratzel M. A Low-cost, High-efficiency Solar Cell based on Dye-sensitized Colloidal TiO_2 films. *Nature*, **353**, P. 737–740 (1991).

[8] O'Regan B., Gratzel M. Photoelectrochemical Cells. *Nature*, **414**, P. 338–344 (2001).

[9] Yang L., Jiang X., Yang M. Improvement of Surface-enhanced Raman Scattering Performance for Broad Band Gap Semiconductor Nanomaterial (TiO_2): Strategy of Metal Doping. *Appl. Phys. Lett.*, **99**, P. 111114-1–3 (2011).

[10] Kalayanasundaram K., Gratzel M. Applications of Functionalized Transition Metal Complexes in Photonic and Optoelectronic Devices. *Coord. Chem. Rev.*, **77**, P. 347– 414 (1998).

[11] Boroda Y. G., Calhoun A., Voth G. A. A Theory for Electron Transfer Across the Electrode/electrolyte Interface Involving more than one Redox Ion. *J. Chem. Phys.*, **107**, P. 8940–8954 (1997).

[12] Cong Y., Tian B. Z., Zhang J. L. Improving the Thermal Stability and Photocatalytic Activity of Nanosized Titanium Dioxide via La^{3+} and N co-doping. *Appl. Catal. B*, **101**, P. 376–381 (2011).

[13] Rengifo-Herrera J. A., Pierzchaa K., Sienkiewicz A., Forr L., Kiwi J., Moser J. E., Pulgarin C. Synthesis, Characterization, and Photocatalytic Activities of Nanoparticulate N, S-codoped TiO_2 having Different Surface-to-volume Ratios. *J. Phys. Chem. C*, **114**, P. 2717–2723 (2010).

[14] Liu S., Xie T. H., Chen Z., Wu J. T. Highly active V-TiO_2 for Photocatalytic Degradation of Methyl Orange. *Appl. Surf. Sci.*, **255**, P. 8587–8592 (2009).

[15] Yang Q. J., Choi H., Chen Y. J., Dionysiou D. D. Heterogeneous Activation of Peroxymonosulfate by Supported Cobalt Catalysts for the Degradation of 2,4- dichlorophenol in water: The Effect of Support, Cobalt Precursor, and UV Radiation. *Appl. Catal. B*, **77**, P. 300–307 (2008).

[16] Liu Y., Wei J. H., Xiong R., Pan C. X., Shi J. Enhanced visible light photocatalytic properties of Fe-doped TiO_2 nanorod clusters and monodispersed nanoparticles. *Appl. Surf. Sci.*, **257**, P. 8121–8126 (2011).

[17] Han C., Pelaez M., Likodimos V., Kontos A.G., Falaras P., O'Shea K., Dionysiou D.D. Size-Tunable Hydrothermal Synthesis of SnS(2) Nanocrystals with High Performance in Visible Light-Driven Photocatalytic Reduction of Aqueous Cr(VI). *Appl. Catal. B*, **107**, P. 77–87 (2011).

[18] Asahi R., Morikawa T., Ohwaki T., Aoki K., Taga Y. Visible-Light Photocatalysis in Nitrogen-Doped Titanium Oxides. Science, P. 269–271 (2001).

[19] Sekiya T., Kamei S., Kurita S. Luminescence of Anatase TiO_2 Single Crystals Annealed in Oxygen Atmosphere. *J. Luminescence*, **1140**, P. 87–89 (2000).

[20] Rodríguez R., Jiménez-Sandoval S., Estevez M., Vargas S. Defec-Induced Luminescence in Co(II)-doped Anatase TiO_2 Prepared by the Sol-Gel Method. *J. Non-Crystalline Solids*, **351**, P. 167–172 (2005).

[21] Anbalagan K., Ganeshraja A. S., Maharaja Mahalakshmi C. Excited Nanoscale-TiO_2 Induced Interfacial Electron Transfer Reaction of Redox Active Cobalt(III)-alkyl Amine Complex and the Solid Surface. *Met. Chem. Phys.*, **134**, P. 747–754 (2012).

[22] Anbalagan K. UV-Sensitized Generation of Phasepure Cobalt-Doped Anatase: $Co_xTi_{1-x}O_{2-\delta}$ Nanocrystals with Ferromagnetic Behavior Using Nano-TiO_2/cis- $[Co^{III}(en)_2(MeNH_2)Cl]^{2+}$. *J. Phys. Chem. C*, **115**, P. 3821–3832 (2011).

[23] Kelly C. A., Meyer G. J. Excited State Processes at Sensitized Semiconductor- Interfaces Characterized by Nanosecond Absorption Spectroscopy. *Coord. Chem. Rev.*, **211**, P. 295–315 (2001).

[24] Anbalagan K., Maharaja Mahalakshmi C., Ganeshraja A. S. Synthesis and Spectroscopic Characterization of Cobalt(III)-Alkyl Amine Complexes Showing Surface Affinity: Single Crystal X-ray Structure Determinations. *J. Mol. Struct.*, **1005**, P. 45–52 (2011).

[25] Kitson R. E. Simultaneous Spectrophotometric Determination of Cobalt, Copper and Iron. *Anal. Chem.*, **22**, P. 664–667 (1950).

[26] Suryanarayana C. Nanocrystalline Materials. *Inter. Mater. Rev.*, **40**, P. 41-64 (1995).

[27] Moazzami K., Murphy T. E., Phillips J. D., Cheung M. C-K., Cartwright A. N. Sub- Bandgap Photoconductivity in ZnO Epilayers and Extraction of Trap Density Spectra. *Semicond. Sci. Technol.*, **21**, P. 717–723 (2006).

[28] Comedi D., Heluani S. P., Villafuerte M., Arce R. D., Koropecki R. R. Power-law Photoconductivity Time Decay in Nanocrystalline TiO_2 Thin Films. *J. Phys.: Condens. Matter*, **19**, P. 486205 (10pp) (2007).

[29] Shimakawa K., Murata K., Matsunomo S., Naito H. Photo-Carrier Transport in Disordered Organic TPD Films. *J. Non-Cryst. Solids*, **352**, P. 1671–1674 (2006).

[30] Anbalagana K., Lydia I. S. Solvent Control on the Electron Transfer Reaction between $Co^{III}(en)_2Br(L)^{2+}$–$Fe(CN)_6^{-4}$ (L = aryl amines) by Regression Relationships: the PXRD and Electrochemical Investigations. *J. Phys. Org. Chem.*, **24**, P. 45–53 (2011).

[31] Xie Z., Burkalov V. M., Henry B. M., Kirov K. R., Smith H. E., Grovenor C. R. M., Assender H. E., Briggs G. A. D., Kano M., Tsukahara Y. Intensity-Dependent Relaxation of Photoconductivity in Nanocrystalline Titania Thin Films. *Phys. Rev. B*, **73**, P. 113317 (2006).

[32] Mele G., Ciccarella G., Vasapollo G., Garcia-Lopez E., Palmisano L., Schiavello M. Photocatalytic Degradation of 4-nitrophenol in Aqueous Suspension by using Polycrystalline TiO_2 Samples Impregnated with Cu(II)-phthalocyanine. *Appl. Catal. B*, **38**, P. 309–311 (2002).

[33] Anbalagana K., Lydia I. S. Homogeneous Solvation Controlled Photoreduction of Cobalt(III) Complexes in Aqueous 2-methyl-2-propanol Solutions Linear Solvation Energy Relationship and Cyclic Voltammetric Analyses. *Spectrochim. Acta A*, **69**, P. 964–970 (2008).

[34] Matsuo S., Sakaguchi N., Yamada K., Matsuo T., Wakita H. Role in Photocatalysis and Coordination Structure of Metal Ions Adsorbed on Titanium Dioxide Particles: A Comparison between Lanthanide and Iron Ions. *Appl. Surf. Sci.*, **228**, P. 233–244 (2004).

[35] Ardo S., Meyer G. J. Direct observation of Photodriven Intermolecular Hole Transfer Across TiO_2 Nanocrystallites: Lateral Self-exchange Reactions and Catalyst Oxidation. *J. Am. Chem. Soc.* **132**, P. 9283–9285 (2010).

[36] Creutz C., Brunschwig B. S., Sutin N. Interfacial Charge Transfer Absorption: 3. Application to Semiconductor-Molecule Assemblies. *J. Phys. Chem. B*, **110**, P. 25181–25190 (2006).

[37] Ardo S., Sun Y., Staniszewski A., Castellano F. N., Meyer G. J. Stark-like Effects after Excited State Interfacial Electron Transfer at Sensitized TiO_2 Nanocrystallites. *J. Am. Chem. Soc.*, **132**, P. 6696–6709 (2010).

[38] Minero C., Mariella G., Maurino V., Pellizzetti E. Photocatalytic Transformation of Organic Compounds in the Presence of Inorganic Anions. 1. Hydroxyl-Mediated and Direct Electron-Transfer Reactions of Phenol on a Titanium Dioxide Fluoride System. Langmuir, **16**, P. 2632–2641 (2000).

[39] Ohko Y., Hashimoto K., Fujishima A. Kinetics of Photocatalytic Reactions under Extremely Low-Intensity UV Illumination on Titanium Dioxide Thin Films. *J. Phys. Chem. A*, **101**, P. 8057–8062 (1997).

[40] Wu J. C. S., Chen C. H. A Visible-Light Response Vanadium-Doped Titania Nanocatalyst by Sol–Gel Method. *J. Photochem. Photobiol. A*, **163**, P. 509–515 (2004).

[41] Hamadanian M., Reisi-Vanani A., Majedi A. Sol–Gel Preparation and Characterization of Co/TiO_2 Nanoparticles: Application to the Degradation of Methyl Orange. *J. Iran. Chem. Soc.*, **7**, P. S52–S58 (2010).

[42] Anbalagan K., Stephen L. D. UV-Sensitized Nanomaterial Semiconductor Catalytic Reduction of $Co^{III}(N{-}N)_3^{3+}$/nm-TiO_2 and Co:TiO_2 Formation: SEM-EDX and HRTEM Analyses. *Transition Met. Chem.*, **34**, P. 915–923 (2009).

[43] Baiju K.V., Shajesh P., Wunderlich W., Mukundan P., Kumar S. R., Warrier K. G. K., Effect of Tantalum Addition on Anatase Phase Stability and Photoactivity of Aqueous Sol–Gel Derived Mesoporous Titania. *J. Mol. Catal. A*, **276**, P. 41–46 (2007).

[44] Srivatsa K. M. K., Chhikara D., Senthil Kumar M. Synthesis of Anatase Titania Nanostructures at Room Temperature by PECVD Technique. *J. Mater. Sci. Technol.*, **27**, P. 696–700 (2011).

[45] Santhosh, S. M., Swetha S., Geetha, S., Balakrishna R. Erratum to “Structure and Photocatalytic Activity of $Ti_{1-X}M_xO_2$(M = Zr, Co and Mo) Synthesized by Pulverized Solid State Technique”. *Cent. Eur. J. Chem.*, **8**, P. 453–460 (2010).

NANOSYSTEMS: PHYSICS, CHEMISTRY, MATHEMATICS, 2013, 4 (2), P. 288–293

MISCIBILITY STUDIES OF PVC/PMMA BLENDS IN TETRAHYDROFURAN BY VISCOSITY, DENSITY, REFRACTIVE INDEX AND ULTRASONIC VELOCITY METHOD

Gautam kumar sah[1], Ashok kumar Gupta[1]

[1] University Department of Chemistry (Physical Chemistry section),
Lalit Narayan Mithila University, Darbhanga, India
gautamdar@gmail.com, ashokkumargupta80@gmail.com

PACS 81.05.Lg

The density and Coefficient of Viscosity for Polyvinyl chloride/poly(methyl methacrylate) (PVC/PMMA) blends in tetrahydrofuran at 303.15 K and 313.15 K were measured. These measured parameters were then used to estimate few other related physical quantities like Huggin's constants and the interaction parameters μ and α proposed by Chee and Sun et al. to identify the molecular interaction arising in the mentioned polymer blend solutions. The peculiar deviation confirms the structural changes in the solution of blends.

Keywords: viscosity, polymer blends, poly(methyl methacrylate), poly (vinyl chloride), molecular interaction.

1. Introduction

Polymers play an important role in all branches of industry today. Many notable advances in technology have followed the exploitation of properties offered by new polymeric materials like blends, composites, etc. Polymer blends are prepared by physical mixing of two or more polymers. The resulting system often exhibits properties that are superior to any one of the component polymers [1-5]. However, the manifestation of superior properties depends upon the miscibility of homo-polymers at the molecular scale. The miscibility results in different morphology of the blends, ranging from a single phase system to two phase or multiphase systems [2]. The basis of polymer-polymer miscibility may arise from several different interactions, such as hydrogen bonding, dipole-dipole forces, and charge transfer complexes for homo-polymer mixtures [1].The importance of polymer blending has increased in recently, because of the preparation of polymeric materials with desired properties, low basic cost and improved processability. Polymer blends are physical mixtures of structurally different polymers or copolymers, which interact through secondary forces with no covalent bonding (Krause, 1978) and are miscible at the molecular level. As stated above, several factors contribute to polymer–polymer miscibility, including the aorementioned hydrogen bonding, dipole– dipole forces and charge transfer complexes for homopolymer mixtures (Varnell & Coleman, 1981; Varenell, Runt, & Coleman, 1983; Woo, Barlow, & Paul, 1986). There are several techniques for studying the miscibility of the polymer blends (Cabanclas, Serrano, & Baselga, 2005; Crispim, Rubira, & Muniz,1999; Jiang & Han, 1998; Patel, 2004; Ping, 1997). Some of these techniques are complicated, costly and time consuming, hence it is desirable to identify simple, low cost and rapid techniques to study the miscibility of polymer blends. Chee (1990) and Sun, Wang, and Fung (1992) have suggested a viscometric method for the study of polymer–polymer miscibility in solution, while Singh and Singh (1983, 1984)) have suggested the use of ultrasonic velocity and viscosity measurements for testing the same properties. Palladhi and Singh (1994a, 1994b) have shown that the variation of ultrasonic velocity and viscosity with blend composition is linear for miscible blends and non-linear for immiscible blends. Recently, (Varada Rajulu, Reddy, and Ranga Reddy (1998) and Varada Rajulu, Siddaramaiah, and Reddy (1998) have used ultrasonic and refractometric techniques to study the miscibility of polymer blends.

2. Experimental

PVC (Chemplast Sanmar limited Chennai) and PMMA (grade LG 2 Sumitomo chemical Singapore), tetrahydrofuran from Fisher Scientific were used after purification by fractional distillation. A dilute polymer solution of 1% w/v was prepared for viscometric studies. Stock solutions of polymers and the blends of PVC/PMMA of different compositions, 20/80, 30/70, 40/60, 50/50, 60/40, 70/30 and 80/20, were prepared in tetrahydrofuran. Viscosity measurements at 303.15K and 313.15K were made using an Ostwald viscometer. The total weight of the two components in the solution was always maintained at 1 g/dL. Different temperatures were maintained in a thermostat bath, with a thermal stability of ±0.05 K.

3. Results and discussion

Viscometry is a simple and effective technique for monitoring the interactions in polymer blend solutions. From viscometric measurements, the relative and reduced viscosities of pure polymers and their blends were obtained. Figures 1 and 2 shows the Huggin's plots for the PVC/PMMA at 303.15 K and 313.15 K for different weight fractions of polymer 1 and polymer 2 (W_1: W_2), respectively. The values of K_H were determined by extrapolation to infinite dilution of the Huggin's plots and the values of 'b' are the slopes of the plots. This has been compared by results obtained from calculation from Huggin's equation. The figure indicates the considerable higher slope variation for PVC/PMMA blend compositions. This may be attributed to the mutual attraction of macromolecules in solution, because of the increase of hydrodynamic and thermodynamic interaction. Hence, the PVC/PMMA blend is found to be miscible. Below this critical concentration, a sharp decrease in the slope is observed in the Huggin's plot, because of the phase separation. To quantify the miscibility of the polymer blends Chee (1990) [4] suggested that the general expression for interaction parameter when polymers are mixed in weight fractions W_1 and W_2 is as follows:

$$\Delta B = \frac{b - \bar{b}}{2w_1 w_2},$$

where $\bar{b} = W_1 b_{11} + W_2 b_{22}$ in which, b_{11} and b_{22} are the slopes of the viscosity curves for the pure components. The coefficient b is related to the Huggin's coefficient K_H as

$$b = K_H [\eta]^2,$$

for ternary system, the coefficient b is also given by

$$b = w_1^2 b_{11} + w_2^2 b_{22} + 2 w_1 w_2 b_{12},$$

where b_{12} is the slope for the blend solution. Using these values, Chee (1990) defined a more effective parameter as follows:

$$\mu = \frac{\Delta B}{\{[\eta]_2 - [\eta]_1\}^2},$$

where $[\eta]_1$ and $[\eta]_2$ are the intrinsic viscosities for the pure component solutions. The blend is miscible when $\mu \geqslant 0$ and immiscible $\mu < 0$.

The reduced viscosity data for the PVC/PMMA blends at different compositions at 303.15 K and 313.15 K have been recorded in tables 1 and 2 respectively. Recently, Sun et al. (1992) have suggested a new formula for the determination of polymer miscibility as follows:

$$\alpha = Km - \frac{K_1[\eta]_1^2 w_1^2 + K_2[\eta]_2^2 w_2^2 + 2\sqrt{K_1 K_2}[\eta]_1[\eta]_2 w_1 w_2}{\{[\eta]_1 w_1 + [\eta]_2 w_2\}^2}$$

where K_1, K_2 and Km are the Huggins's constants for individual component 1, 2 and the blend respectively. The long-range hydrodynamic interactions are considered while deriving this equation. Sun et al. (1992) have suggested that a blend will be miscible when $\alpha \geqslant 0$ and immiscible when $\alpha < 0$.

Table 1. The reduced viscosity data for PVC/PMMA and their blends in tetrahydrofuran at 303.15 K at different concentrations

Concentration (g/dl)	Reduced viscosity of different composition (dl/gm)					
	100/0 (PVC)	80/20	60/40	40/60	20/80	0/100 (PMMA)
0.2	0.70892	0.54775	0.50596	0.41444	0.26903	0.24045
0.4	0.71498	0.61076	0.549721	0.41869	0.3072	0.24592
0.6	0.76668	0.61561	0.593481	0.44595	0.31992	0.25133
0.8	0.82374	0.68196	0.637241	0.45928	0.3378	0.25681
1.0	0.85206	0.71755	0.681002	0.4697	0.36366	0.28308

Table 2. The reduced viscosity data for PVC/PMMA and their blends in tetrahydrofuran at 313.15 K at different concentrations

Concentration (g/dl)	Reduced viscosity of different composition (dl/gm)					
	100/0 (PVC)	80/20	60/40	40/60	20/80	0/100 (PMMA)
0.2	0.62975	0.50467	0.46226	0.37212	0.25176	0.22441
0.4	0.66873	0.53613	0.48616	0.39112	0.27847	0.23009
0.6	0.7077	0.56759	0.51165	0.41013	0.30519	0.23577
0.8	0.74668	0.59905	0.53078	0.42913	0.33191	0.24145
1.0	0.78564	0.61095	0.55945	0.44814	0.35863	0.27543

The Huggins's plots for the pure components (PVC and PMMA) and their blends at 303.15 K and 313.15 K are shown in Fig. 1 and Fig. 2 respectively. The figure indicates the considerable higher slope variation for 80/20 and 60/40 PVC/PMMA blend compositions. This may be attributed to the mutual attraction of macromolecules in Solution, because of the increase of hydrodynamic and thermodynamic interaction. Hence PVC/PMMA blend is found to be miscible, Below this critical concentration, a sharp decrease in the slope is observed in the Huggins's plot because of the phase separation.

Blends are miscible in all compositions except the (40/60) at both temperatures mentioned above. Immisciblity of the blend (40/60) has been supported by the fact that both interaction parameters μ and α were found to be negative at both temperatures. μ and α parameters for the (60/40) blend at 313.15 K have been found to be slightly negative,

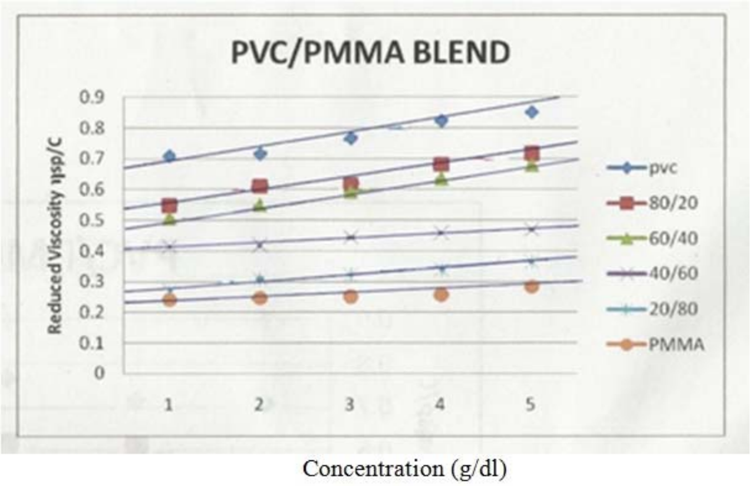

Fig. 1. Plot of ηsp/C *vs.* concentration for PVC/PMMA/THF ternary systems at 303.15 K

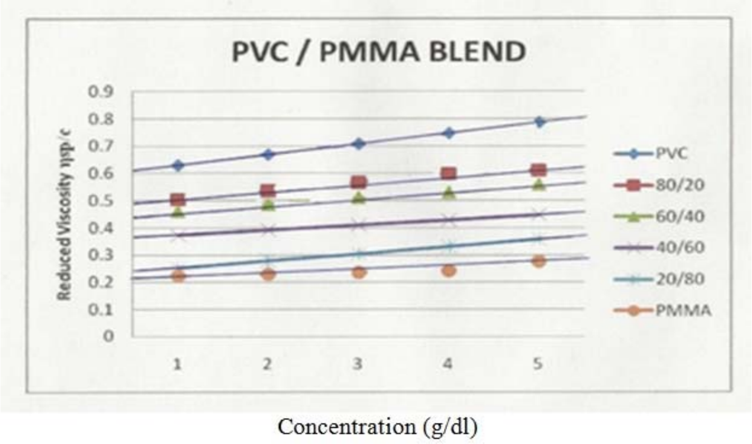

Fig. 2. Plot of ηsp/C *vs.* concentration for PVC/PMMA/THF ternary systems at 313.15 K

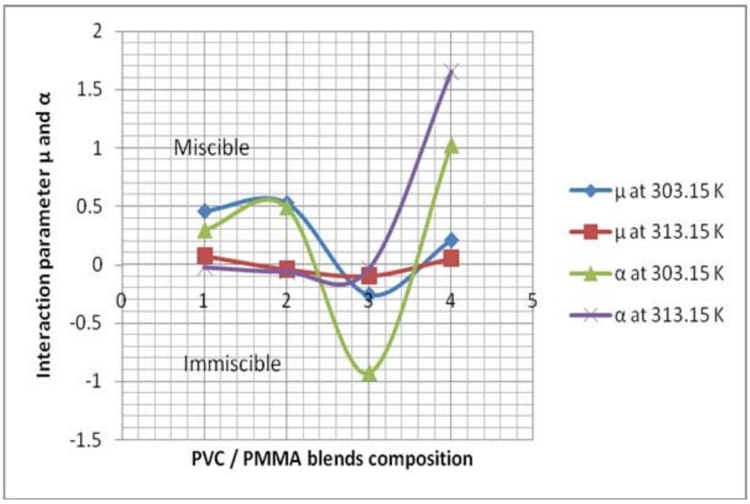

Fig. 3. Effect of temperature on the interaction parameter μ and α of PVC/PMMA blend in at 303.15 K and 313.15 K

Table 3. Interaction parameters and Huggins's constants of PVC/PMMA blends at 303.15 K

PVC/PMMA	$[\eta]$	K_H	μ	α
100/0(PVC)	0.656462	0.4517727	-	-
80/20	0.5146216	0.7798907	0.4575677	0.2949006
60/40	0.4622	1.0242064	0.5261955	0.492312095
40/60	0.39692792	0.472713180	-0.25565	-0.9242617
20/80	0.2527247	1.7430205	0.2102835	1.0213427
0/100(PMMA)	0.2261522	0.9569496	-	-

Table 4. Interaction parameters and Huggins's constants of PVC/PMMA Blends at 313.15 K

PVC/PMMA	$[\eta]$	K_H	μ	α
100/0(PVC)	0.590784	0.5582969	-	-
80/20	0.481523	0.59053915	0.071553727	-0.0189689
60/40	0.4381608	0.6241702	-0.04432155	-0.0581165
40/60	0.353113	0.558296996	-0.10198976	-0.0310992
20/80	0.2250383	2.6379087	0.048943006	1.65734316
0/100(PMMA)	0.2067026	1.3546565	-	-

approximately zero showing the miscibility to some extent. Fig. 3 shows the variation of interaction parameters as a function of blend composition and temperature. The interaction parameter α for blend (40/60) is highly negative at 313.15 K in comparison to that at 303.15 K. Variation of μ parameter, on the other hand, is less pronounced.

4. Conclusion

Viscometric method shows that the polymer blend of PVC/PMMA is found to be miscible. It is also observed that temperature has no significant effect on the miscibility of these blends except in the case of the (40/60) composition, considering the α parameter. As it can be seen, interaction parameter (μ) has been found more satisfactory in dealing with miscibility of blends at both temperatures. The above-mentioned techniques are simple, low cost, rapid and efficient methods for determining the miscibility windows of PVC/PMMA blends in solution.

References

[1] Stephen A.M., Kumar T.P., Renganathan N.G., Pitchumani S., Thirunakaran R., Muniyandi N. Ionic conductivity and FT-IR studies on plasticized PVC/PMMA blend polymer electrolytes. *J.Power Sources*, **89**(1), P. 80-87 (2000).

[2] Subban R.H.Y., Arof A.K. Plasticizer interactions with polymer and salt in PVC–LiCF3SO3–DMF electrolytes. *Eur. Polym. J.*, **40**(8), P. 1841–1847 (2004).

[3] Sun Z., Wang W., Feng Z. Criterion of polymer-polymer miscibility determined by viscometry. *Eur. Polym. J.*, **28**(10), P. 1259–1261 (1992). Tang M., Liau W.R. Solvent effect on the miscibility of poly(4-hydroxystyrene)–poly(ethylene oxide) blends. *Eur. Polym. J.*, **36**(12), P. 2597–2603 (2000).

[4] Chee, Sun et al., Sun Z., Wang W., Feng Z. Criterion of polymer-polymer miscibility determined by viscometry. *Eur. Polym. J.*, **28**(10), P. 1259–1261 (1992).

[5] Wu W., Luo X., Ma D. Miscibility of the segmented polyurethane blends with chlorinated poly(vinyl chloride). *Eur. Polym. J.*, **35**(6), P. 985–990 (1999).

[6] Zhao Y., Prud'homme R.E. A nonradiative energy transfer fluorescence spectroscopy study of poly (vinylchloride)/poly (methyl methacrylate) blends. *Polym Bull*, **26**(1), P. 101 (1991).

[7] Honeycutt J.D. A Theoretical study of tacticity effects on poly(vinylchloride) poly(methyl methacrylate) miscibility. *Macromolecules*, **27**(19), P. 5377–5381 (1994).

[8] Karlou K., Schneider H.A. DSC and PVT study of PVC/PMMA blends. *J. Therm. Anal. Calorim.*, **59**(1–2), P. 59 (2000).

[9] Oh B., Kim Y.R. (1999). Evaluation and characteristics of a blend polymer for a solid polymer electrolyte. *Solid state Ionics*, **124**(1-2). P. 83–89.

[10] Ohno N., Kumanotani J. Synthesis and Physical Properties of Blends of Donor Polymers from 2-(*p*-Dimethylaminobenzyl)-1,3- propanediol and Acceptor Polymers from 2-(3,5-Dinitrobenzyl)-1,3- propanediol: A New Phase Composed of Donor and AcceptorPolymers. *Polym J.*, **11**(12), P. 947–954 (1979).

[11] Singh R.P., Paladhi R. Miscibility and interaction studies on some aqueous polymer blend solutions by ultrasonic and rheological techniques. *J. Appl. Polym. Sci.*, **51**(9), P. 1559–1565 (1994).

[12] Paul D.R., Newman S. *Polymer blends*, vol. 1. Academic Press, New York (1978).

[13] Pingping Z., Haiyang Y., Yiming Z. Viscosity behavior of incompatible poly(vinyl chloride) (PVC)/polystyrene (PS) blends in various solvents. *Eur Polym J*, **35**(5), P. 915–921 (1999).

NANOSYSTEMS: PHYSICS, CHEMISTRY, MATHEMATICS, 2013, 4 (2), P. 294–298

EFFECT OF ANCHORING ATOMS ON TRANSPORT PROPERTIES OF A CARBON-DIMER BASED MOLECULAR JUNCTIONS: A FIRST PRINCIPLES STUDY

RM. Hariharan[1], D. John Thiruvadigal[1*]

[1]Centre for Materials Sciences and Nanodevices, Department of Physics
and Nanotechnology, SRM University, Kattankulathur-603203, India

*john.d@ktr.srmuniv.ac.in

PACS 73.23.-b

The conductance of a molecular device is sensitive to the contact geometry between the molecules and the probing electrodes. Combining the density functional theory calculations (DFT) for molecular electronic structure with a non-equilibrium Green's function (NEGF) method for electron transport, we calculate the molecular conductance of carbon dimer connected between Au leads through two different anchoring atoms Se and Te. The current-voltage characteristics and transmission spectra of two systems are studied. The results exhibit that, depending on the anchoring groups and the subsequent different metal-molecule chemical bonds, the current varies over more than four times of magnitude under the same bias. Furthermore, the system exhibits negative differential resistance (NDR) effect, when anchored with Te atom. This emphasizes the great importance of the anchoring groups in molecular devices.

Keywords: anchoring group effects, electronic transport, first-principle, I-V characteristics.

1. Introduction

Over the past decade, molecular devices have received significant attention due to their great potential in the practical applications of atomic-scale circuits [1]. Many interesting physical properties of molecular devices have been predicted theoretically and verified experimentally, such as single-electron characteristics [2], negative differential resistance (NDR) [3,4], molecular rectification [5], and field-effect characteristics [6], etc.

A basic goal in molecular electronics is to measure and control electron transport through a molecule attached to two electrodes. To reach this goal, one must not only synthesize molecules with the desired functionality, but also design proper molecule-electrode contacts. This is because the contacts play a critical role in the electron-transport properties of molecules [7-9]. One way to optimize the molecule-electrode contacts is to select the proper anchoring groups at the two ends of a molecule so that they can bind to the electrodes and in turn, provide efficient electronic coupling between the molecule and the electrodes. So, the key issue in such molecular electronic devices is to find suitable anchoring groups and to construct contact structures that provide both stability and high contact transparency [10]. Therefore, the extensive and profound understanding of these effects in molecular devices is quite necessary. Using a combined density functional theory-non-equilibrium Green's function (DFT+NEGF) method, Zeng et al [11] performed transport calculations on carbon dimer sandwiched between Au electrodes, with anchoring groups of H, Cu and S.

In this present work, we focus our concentration on the anchoring group effect in molecular devices. Specifically, the transport properties of a carbon-dimer C_2 cluster sandwiched between two Au (111) electrodes were investigated. The anchoring groups connecting the cluster and the electrodes are chosen as Se and Te respectively. Thus, equivalently, we study the transport properties of two different molecules C_2Se_2 and C_2Te_2, since both contain a C_2 unit and they are all of a linear chain structure. The reason for choosing selenium and tellurium as anchoring atoms because they serves as an efficient alligator clip connection to Au other than sulfur [12,13].

Also, we show that asymmetric molecular junctions, such as carbon dimer with appropriately chosen anchoring group, gives rise to I-V curve showing NDR effects.

2. Computation method

The simulation model adopted in this work is presented: a C_2 molecule is sandwiched between two Au (111) bulk electrodes via different anchoring atoms. And in the present work, the central sandwiched molecules are C_2Se_2 and C_2Te_2, which are all linear and symmetrical molecules. The C–C and C–Se bond lengths in C_2Se_2 molecule and C–C and C–Te bond lengths in C_2Te_2 molecule are obtained by fully optimizing the respective molecules. For the left and right electrodes, we select a 3 × 3 unit cell in the x and y directions to avoid the interaction between the molecules and their mirror images. The terminating atoms of the molecules are located symmetrically at the hollow sites above the Au (111) surface. By full optimization, we obtain the equilibrium distances between the central molecules and the electrodes.

Our calculations are carried out using the Atomistix Toolkit (ATK 11.2.3 version) [14] program which combines DFT and NEGF methods to simulate the transport properties of two-probe systems. The exchange-correlation functional is described by the generalized gradient systems. The exchange-correlation functional is described by generalized gradient approximation (GGA) in the form of the Revised Perdew – Burke – Ernzerh (revPBE) in the present calculations [2]. The valence wave functions are expanded by localized numerical atomic orbital (LNAO), with the single zeta plus polarization basis set (SZP) for Au element and the double zeta plus polarization basis set (DZP) for C, H, Se and Te atoms. The Brillouin zone of the leads is sampled by 1 × 1 × 80 k points in the directions of x, y and z (z is the electron transport direction), which is enough to produce the results.

In the NEGF theory, the transmission function $T(E,V)$ [15] of the system is the sum of transmission probabilities of all channels available at energy E under external bias voltage V:

$$T\left(E,V\right)=Tr\left[\Gamma_L\left(E,V\right)G^R\left(E,V\right)\Gamma_R(E,V)G^A(E,V)\right]$$

where $G_{R/A}$ are the retarded and advanced Green's functions, and coupling functions $\Gamma_{L/R}$ are the imaginary parts of the left and right self-energies, respectively. Self-energy depends on the surface Green's functions of the electrode regions and comes from the nearest-neighbor interaction between the extended molecule region and the electrodes.

The I-V characteristics of the two probe system can be obtained by using the Landauer–Buttier formula [11], the current is the integration of the transmission function over the bias window around the Fermi level:

$$I=\frac{2e}{h}\int_{\mu_1}^{\mu_2}T(E,V)[f(E-\mu_1)-f(E-\mu_2)]dE$$

where $T(E, V)$ is the transmission function through the device at energy E and function $f(E - \mu_{1/2})$ are the Fermi distribution functions of electrons in the left / right electrodes. $\mu_{1/2} = \mu \pm eV/2$ are the chemical potentials of the left/right electrodes, with μ the Fermi level of the electrodes in equilibrium and V the bias applied to the device.

3. Results and discussion

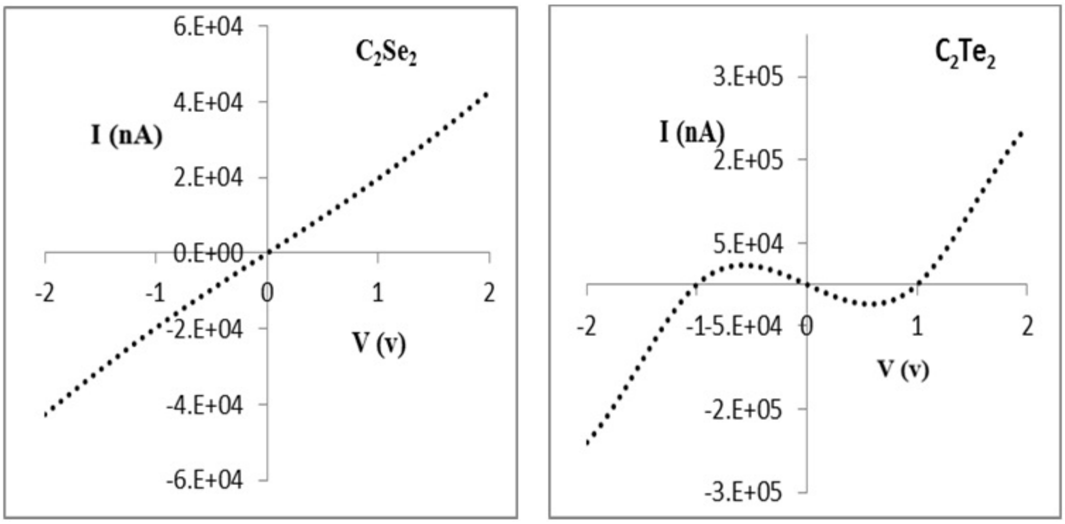

Fig. 1. The I-V characteristics of C_2Se_2 and C_2Te_2 molecules respectively

The I–V curves of two systems are presented in Fig 1. As can be seen from this figure, the current for C_2Se_2 linearly increases with the voltage increasing from 0.0 V to 2.0 V, while the current of C_2Te_2 increases in the opposite direction, reaches maximum in 0.58V and drops to zero at 1.0 V. Further the current for C_2Te_2 rapidly increases from 1.0 V to 2.0V. This indicates evident NDR behavior, which can be clearly observed in the I–V curve for C_2Te_2 system at zero bias range as shown Fig 1.

On the whole, the amplitude of the I–V curves of two different systems varies over more than four times of magnitude. For example, when the bias is 1.5 V, the currents are 30,638 nA for C_2Se_2, and 1,36,254 nA for C_2Te_2 respectively. Obviously, NDR behavior and the change in magnitude of current are originated from the contact atoms Se and Te linked to the C_2 cluster to the electrodes. Thus, it shows the importance of different linking atoms which result in such a big difference of the currents through the same molecule with different linking atoms.

In order to understand the difference in I-V characteristics of C_2Se_2 and C_2Te_2 systems, the transmission spectra of those systems at zero bias respectively are shown in Fig. 2. As can be seen from figure 2, the transmission function of C_2Te_2, has very large gap near the fermi level, the transmission spectrum in the zero bias window becomes smaller and smaller, which results in NDR behavior. This NDR behavior may arise due to the coupling between the Te molecule and electrodes. The transmission coefficient can be related to the molecular orbitals which have been modified by the electrodes when connected to different anchoring groups [16].

Thus when a Te molecule is connected to gold electrodes, the energy levels and spatial distribution of molecular orbitals are modified due to the molecule–electrode interaction and leads to NDR behavior. NDR behavior is not reported in the earlier work on carbon dimer by Zeng et al. with three different anchoring groups H, Cu and S [9].

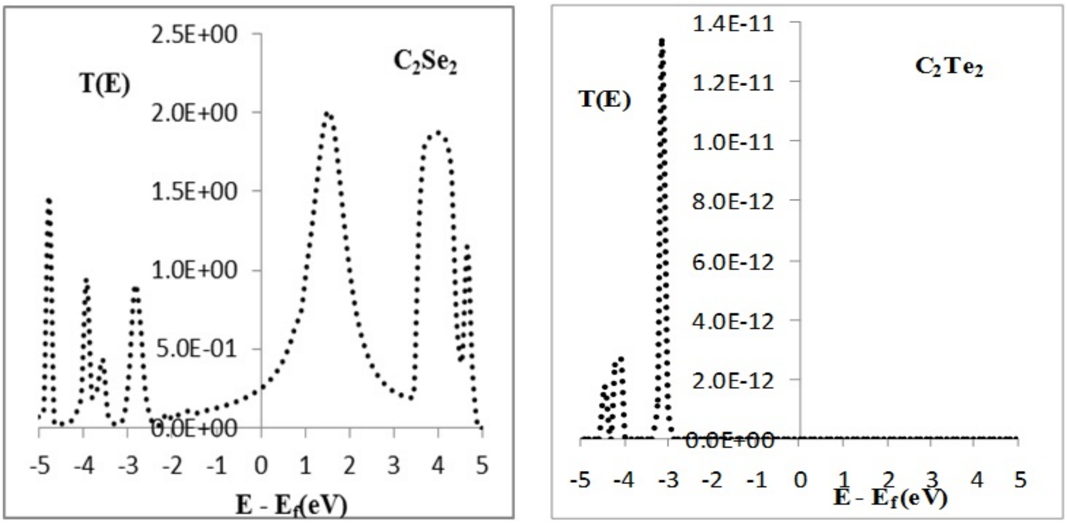

Fig. 2. The Transmission spectra of C_2Se_2 and C_2Te_2molecules at 0V respectively

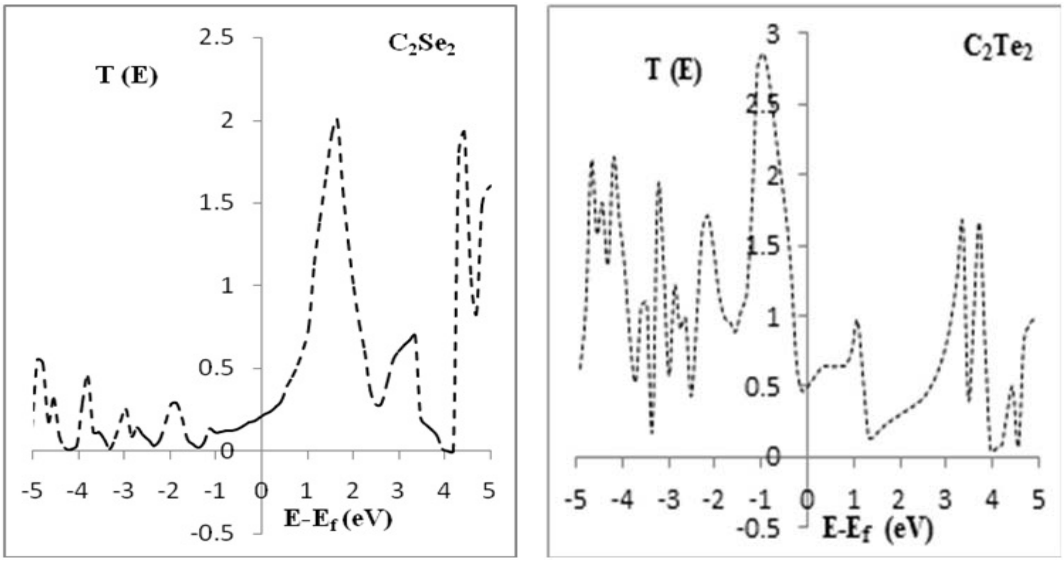

Fig. 3. The Transmission spectra of C_2Se_2 and C_2Te_2molecules at 1V respectively

Whereas, the transmission function of C_2Se_2, has sharp peaks near Fermi level which results in linear conductance of the molecule. The results show that the anchoring group plays a crucial role in the NDR effect and the overall conductivity of molecular junctions.

However, as can be seen from figure 3, with an increase in the bias, much transmission energy enters into bias windows which results in the increasing of current for C_2Te_2. For the C_2Te_2, there is a large platform around the Fermi level, so the current is very big when the bias voltage is applied to the device. However, we hardly find any new transmission entering into the bias window when the bias voltage is applied for C_2Se_2. So a current progresses in the same way as that zero bias for C_2Se_2.

4. Conclusions

Using the DFT+NEGF approach, the electron transport properties of molecular junctions containing carbon dimer molecules with two different anchoring groups, Se and Te, were calculated. The current in these two different systems varies by more than four times of magnitude under the same bias range. Furthermore, the system exhibits negative differential resistance (NDR) effect, when anchored with Te atom at zero bias range. The results show that the anchoring group and the subsequent different metal-molecule chemical bonds play a significant role in determining the overall conductivity of the molecular junctions.

Acknowledgements

This work was supported by the DST- FIST programme (Govt. of India) under Grant No. SR/ FST / PSI-010/2010. The work was carried out in the Centre for Materials Sciences and Nanodevices, Department of Physics and Nanotechnology, SRM University.

References

[1] C. Joachim, J.K. Gimzewski and A. Aviram. Electronics using hybrid-molecular and mono-molecular devices. *Nature*, **408**, P. 541–548 (2000).

[2] H.W.C. Postma, T. Teepen, Z. Yao, M. Grifoni, C. Dekker. Carbon nanotube single-electron transistors at room temperature. *Science*, **293**(5527), P. 76–79 (2001).

[3] J. Chen, W. Wang, M.A. Reed, A.M. Rawlett, D.W. Price, J.M. Tour. Room-temperature negative differential resistance in nanoscale molecular junctions. *Applied Physics Letters*, **77**(8), P. 1224–1226 (2000).

[4] M.Q. Long, K.Q. Chen, L. Wang, B.S. Zou, Z. Shuai. Negative differential resistance induced by intermolecular interaction in a bimolecular device. *Applied Physics Letters*, **91**(23), P. 233512 (2007).

[5] A. Aviram, M.A. Ratner. Molecular rectifiers. *Chemical Physics Letters*, **29**(2), P. 277–283 (1974).

[6] J. Lu, S. Yin, L.M. Peng, Z.Z. Sun, X.R. Wang. Proximity and anomalous field-effect characteristics in double-wall carbon nanotubes. *Applied Physics Letters*, **90**, P. 052109 (2007).

[7] Fang Chen, Xiulan Li, Joshua Hihath, Zhifeng Huang, Nongjian Tao. Effect of Anchoring Groups on Single-Molecule Conductance: Comparative Study of Thiol-, Amine-, and Carboxylic-Acid-Terminated Molecules. *Journal of American Chemical Society*, **128**(49), P. 15874–15881 (2006).

[8] Yeonchoo Cho,Woo, Youn Kim,and Kwang S.Kim. Effect of Electrodes on Electronic Transport of Molecular Electronic Devices. *Journal of Physical Chemistry A*, **113**(16), P. 4100–4104 (2009).

[9] Manabu Kiguchi. Electrical conductance of single C_{60} and benzene molecules bridging between Pt electrodes. *Applied Physics Letters*, **95**(7), P. 073301 (2009).

[10] Jorge M. Seminario, Angelica G. Zacarias, and James M. Tour. Molecular Alligator Clips for Single Molecule Electronics. Studies of Group 16 and Isonitriles Interfaced with Au Contacts. *Journal of American Chemical Society*, **121**(2), P. 411–416 (1999).

[11] R.N. Wang, X.H. Zheng, Z.X. Dai, H. Haoa, L.L. Song and Z. Zeng. Anchoring group effects in molecular devices: An ab initio study on the electronic transport of a carbon-dimer. *Physics Letters A*, **375**(3), P. 657–660 (2011).

[12] Shundong Yuan, Chunlei Dai, Jiena Weng, Qunbo Mei, Qidan Ling, Lianhui Wang and Wei Huang. Theoretical Studies of Electron Transport in Thiophene Dimer: Effects of Substituent Group and Heteroatom. *Journal of Physical Chemistry A*, **115**(17), P. 4535–4546 (2011).

[13] S. Jalili and R. Ashrafi. A first principles study on transport properties of benzene-based molecular junctions: The effect of side groups and anchoring atoms. *PhysicaE*, **43**(4), P. 960-965 (2011).

[14] ATK-VNL Tool Kit 11.2.3 Version, www.quantumwise.com.

[15] Yi-Peng An, Zhongqin Yang and M.A. Ratner. High-efficiency switching effect in porphyrin-ethyne-benzene conjugates. *Journal of Chemical Physics*, **135**(4), P. 044706 (2011).

[16] Ming-Jun Li, Hui Xua, Ke-Qiu Chen and Meng-Qiu Long. Electronic transport properties in benzene-based heterostructure: Effects of anchoring groups. *Physics Letters A*, **376**(20), P. 1692-1697 (2012).

N A N O
Ф&Х&М

НАНОСИСТЕМЫ:

ФИЗИКА, ХИМИЯ, МАТЕМАТИКА

Журнал зарегистрирован
Федеральной службой по надзору в сфере связи, информационных технологий и массовых коммуникаций
(свидетельство ПИ № ФС 77 - 49048 от 22.03.2012 г.)
ISSN 2220-8054

Учредитель: федеральное бюджетное образовательное учреждение высшего профессионального образования «Санкт-Петербургский национальный исследовательский университет информационных технологий, механики и оптики»

Издатель: федеральное бюджетное образовательное учреждение высшего профессионального образования «Санкт-Петербургский национальный исследовательский университет информационных технологий, механики и оптики»

Отпечатано в типографии «Фалкон Принт»
Адрес: 197101, г. Санкт-Петербург, ул. Большая Пушкарская, 54

Подписка на журнал НФХМ
На 2013 год подписка осуществляется через ОАО Агентство «Роспечать»
Подписной индекс 57385 в каталоге «Издания органов научно-технической информации»